Generic and specific computational principles for visual anticipation of motion trajectories

Selma Souihel

UNIVERSITÉ CÔTE D'AZUR

ÉCOLE DOCTORALE
SCIENCES ET TECHNOLOGIES DE L'INFORMATION ET DE LA COMMUNICATION

THÈSE DE DOCTORAT

Principes computationnels génériques et spécifiques à l'anticipation visuelle du mouvement

Selma Souihel

INRIA Sophia Antipolis

Présentée en vue de l'obtention du grade de docteur en Informatique **d'**Université Côte d'Azur

Dirigée par : Bruno Cessac

Soutenue le : 18/12/2019

Devant le jury, composé de :

Laurent Perrinet, Dr., Aix Marseille Université
Matthias Hennig, Dr., University of Edinburgh
Michael J. Berry II, Dr., Princeton University
Frédéric Chavane, Dr., Aix Marseille Université
Stephanie Palmer, Dr., University of Chicago
Olivier Marre, Dr., Institut de la Vision
Benoit Miramond, Dr., Université Côte d'Azur

PROJET FINANCÉ PAR L'ANR - PROJECT FUNDED BY THE ANR

Principes computationnels génériques et spécifiques à l'anticipation visuelle du mouvement.

Jury :

Président du jury
Benoît Miramond, Professeur, Université Côte d'Azur

Rapporteurs
Laurent Perrinet, Chercheur, Université Aix Marseille
Matthias Hennig, Reader, University of Edinburgh
Michael J. Berry II, Associate Professor, Princeton University

Examinateurs
Bruno Cessac, Directeur de Recherche, Inria Sophia Antipolis
Frédéric Chavane, Directeur de Recherche, Université Aix Marseille Université

Invités
Stephanie Palmer, Assistant Professor, University of Chicago
Olivier Marre, Chercheur, Institut de la Vision

French abstract

La vision commence dans la rétine, où la lumière est convertie en signaux électriques par les photorécepteurs. Les signaux sont envoyés aux cellules bipolaires puis aux cellules ganglionnaires, responsables de la formation des trains de potentiels d'action. L'information visuelle est ensuite transmise au thalamus par le nerf optique, qui la relaie au cortex visuel. La phototransduction seule nécessite du temps, jusqu'à 150 ms, auxquelles s'ajoutent les délais introduits par les transmissions synaptiques entre les trois unités . Cela montre la nécessité d'avoir des mécanismes compensatoires pour réduire les délais de traitement. Ces mécanismes sont connus sous le terme d'anticipation.

L'anticipation se produit d'abord au niveau de la rétine et se poursuit ensuite dans le cortex visuel primaire. Dans la rétine, elle se caractérise soit par un décalage du pic de réponse des cellules ganglionnaires, soit par une onde d'activation à courte portée. Dans le cortex, elle se caractérise par une onde d'activation à plus grande portée.

La première contribution de cette thèse est le développement d'un modèle d'anticipation dans la rétine, avec trois types de cellules ganglionnaires : les cellules Fast OFF avec contrôle de gain, les cellules sélectives à la direction avec connectivité via les synapses électriques et les cellules sensibles au mouvement différentiel couplées via les cellules amacrines. La deuxième contribution consiste à utiliser notre modèle comme entrée d'un modèle cortical capable de reproduire l'anticipation telle qu'observée dans d'imagerie optique. Nous avons étudié en particulier les phénomènes non linéaires impliqués dans l'anticipation, ainsi que la connectivité, tant au niveau de la rétine que du cortex visuel primaire.

Le modèle intégré rétine-cortex nous a permis d'étudier les effets de l'anticipation sur des stimuli en deux dimensions, et mettre en avant l'aspect collaboratif des méchanismes d'anticipation dans la rétine et dans le cortex.

Mots-clés : Rétine, cortex, connectivité, modélisation, anticipation.

English abstract

Vision is initiated in the retina, where light is converted into electrical signals by photoreceptors, sent to bipolar cells then ganglion cells, generating spike trains. Visual information is then transmitted to the thalamus via the optic nerve which in turn transmits it to the visual cortex. The retinal processing alone takes time, up to 150 ms, not to mention the time lags introduced by synaptic transmissions between the three processing units. This shows that the existence of compensatory mechanisms to reduce processing delays is absolutely essential. These compensatory mechanisms are known as anticipation.

Anticipation first occurs at the level of the retina and is further carried out by the primary visual cortex. In its first occurrence, anticipation is either characterized by a shift in the the peak response, or a short range wave of activation. In the second case, it is characterized by a wider range wave of activation.

The first contribution of this thesis is the development of a generalized 2D model of the retina, mimicking three types of ganglion cells : Fast OFF cells with gain control, direction selective cells with gap junction connectivity, and differential motion cells connected through an upstream amacrine circuit, able of anticipating different kind of moving stimuli. The second contribution is to use our retina model as an input to a mean field cortical model to reproduce motion anticipation as observed in voltage sensitive dye imaging recordings. Throughout our work, we will study the effect of non linear phenomena involved in anticipation, as well as connectivity, both at the level of the retina and the primary visual cortex.

The integrated retinocortex model allowed us to study the effects of anticipation on two-dimensional stimuli, and to highlight the collaborative aspect of anticipation mechanisms in the retina and the cortex.

Keywords : Retina, cortex, connectivity, modeling, anticipation.

Acknowledgment

I would first like to deeply thank my advisor, Bruno Cessac, who gave me the opportunity to pursue this PhD. Throughout these three years, he has been of tremendous support, both at the professional and the personal level. I'm proud of being able to consider him as my mentor. I would also like to thank Frédéric Chavane and Olivier Marre, who highly contributed to define the "Trajectory" of my thesis. I am very grateful to Frédéric and Olivier along with Benoit Miramond, Laurent Perrinet, Michael J. Berry, Matthias Hennig and Stephanie Palmer, for accepting to examine this thesis.

Many thanks to all the Inria Biovision team past and current members : Pierre, Marie-Cécile, Teva, Dora, Marco, Josselin, Iliann, Hui Yin, Simone, Iganacio, who have always made sure the work atmosphere is pleasant. Special thanks to Jenny, my office-mate and friend, who was supportive along the way ... Warm thanks to all my Inria friends and colleagues.

On a more personal note, I would like to thank my dear friend Clément, for his almost perpetual good mood, the morrocan squad, Ayoub, Ichrak, Zineb and Simo, who were home far from home, and the music band past and current members, mainly Nathalie, Marco and Ben, for the bless I have been having playing with them.

Enfin, je dédie cette thèse à mes parents, dont le soutien et l'encouragement m'ont toujours poussée à donner le meilleur de moi-même. J'espère vous rendre fiers. Je la dédie également à mes frères et soeur, Yassine, Siham et Simo, et ma nièce la petite Nour, en espérant qu'elle en fera une un jour :)

Funding body : ANR project "Trajectory"

This thesis has been entirely funded by the ANR project "Trajectory" (ANR-15-CE37-0011). **Coordinator of the project** : Dr. Frédéric Chavane (Aix-Marseille Université Institut de Neurosciences de la Timone)

Partners :

- AMU INT : Aix Marseille Université Institut de Neurosciences de la Timone
- INSERM IDV : INSERM Institut de la Vision
- INRIA : Institut National de Recherche en Informatique et en Automatique
- USM UV : Universidad Santa Maria & Universidad de Valparaiso

Contents

Résumé

Abstract

French introduction **2**

English introduction **6**

What is the thesis about ? **10**

1 Introduction to the visual system **12**

1.1 The retina 13

1.1.1 General organization of the retina 13

1.1.2 Motion processing in the retina 16

1.2 The visual cortex 22

1.2.1 General organisation of the visual cortex 22

1.2.2 Motion processing in the visual cortex 26

2 Anticipation in the retina and the primary visual cortex **29**

2.1 The flash lag effect 30

2.2 Anticipation in the retina 31

2.2.1 Experimental evidence 32

2.2.2 Anticipation models 34

2.3 Anticipation in the primary visual cortex 36

2.3.1 Experimental evidence 37

3 Developing a 2D retina model **41**

3.1 Retina organization 42

3.2 Bipolar cells layer 42

3.2.1 Stimulus integration . . . 42
3.2.2 Bipolar cells voltage . . . 47
3.2.3 Gain control . . . 48
3.3 Amacrine cells layer . . . 49
3.3.1 Bipolar to amacrine cells connections . . . 49
3.3.2 Dynamics . . . 50
3.3.3 Probabilistic model of amacrine connectivity . . . 51
3.4 Ganglion cells . . . 58
3.4.1 Bipolar cells pooling . . . 58
3.4.2 Ganglion cells response . . . 58
3.4.3 Fast OFF cells . . . 59
3.4.4 Direction selective ganglion cells and gap junctions connectivity 62

4 Mathematical results 66
4.1 Anticipation time in the gain control model . . . 66
4.1.1 Peak times in the ganglion cell activity . . . 68
4.1.2 Anticipation time in a simple example . . . 68
4.1.3 Peak time without bipolar gain control and without lateral connectivity . . . 70
4.1.4 Peak time with bipolar gain control and without lateral connectivity . . . 71
4.2 The role of gap junctions . . . 72
4.2.1 Propagating wave of activity . . . 72
4.2.2 Effect of gain control after gap junctions . . . 73
4.2.3 Effect of gain control before gap junctions . . . 75
4.3 Differential motion sensitive ganglion cells : Amacrine connectivity . . . 76
4.3.1 General mechanisms . . . 76
4.3.2 Nearest neighbours interactions . . . 87

5 Simulations results of the retina model 93
5.1 Anticipation variability with bar's characteristics . . . 93
5.2 Amacrine connectivity . . . 94
5.2.1 Anticipation variability : Laplacian connectivity . . . 94
5.2.2 Probabilistic connectivity . . . 105

5.3 Gap junction connectivity . . . 109
5.3.1 The model equations . . . 109
5.3.2 Anticipation variability . . . 109
5.4 Response to 2D stimuli . . . 114
5.4.1 Flash lag effect . . . 114
5.4.2 Gain control accounts for angular anticipation . . . 115
5.4.3 Retina response to a parabolic trajectory . . . 116

6 Primary visual cortex model **119**
6.1 General introduction to the mean field model . . . 119
6.1.1 Mean field equations . . . 121
6.1.2 Transfer function . . . 122
6.1.3 Application to the Adaptive Exponential IF model . . . 124
6.1.4 Application to the Hodgkin Huxley model . . . 124
6.2 Cortical representation of apparent motion . . . 130
6.2.1 Experimental and modeling results . . . 130
6.2.2 Reproducing apparent motion results . . . 131
6.3 Studying anticipation in V1 . . . 133
6.3.1 Experimental measures (Courtesy of F. Chavane) . . . 133
6.3.2 Studying anticipation with the mean field cortical model . . . 134
6.3.3 Understanding the origin of the "shoulder" effect . . . 138
6.3.4 Studying the latency and time to peak . . . 140
6.3.5 Concluding remarks . . . 144

7 Results of the retino-cortical model **145**
7.1 Connecting the retina and the cortex models . . . 145
7.2 Latency and time to peak using a retinal drive . . . 146
7.2.1 LN retina drive . . . 146
7.2.2 Gain control retina drive . . . 148
7.2.3 Amacrine connectivity retina drive . . . 149
7.2.4 Gap junction connectivity retina drive . . . 151
7.2.5 Removing edge effects . . . 153
7.2.6 Synthetic view of the spatio-temporal . . . 158
7.2.7 The effect of velocity . . . 159

8 Perspectives **163**

8.1 On spike train correlations 163

8.1.1 Pairwise correlations algorithm 163

8.1.2 Correlations results on experimental recordings 171

8.2 Macular : a simulation platform of the retina and V1 176

8.2.1 General presentation 176

8.2.2 Development process 176

English conclusion **181**

French conclusion **184**

9 Appendix **187**

9.1 Parameters of the retina model 187

9.2 Parameters of the cortical model 188

9.3 Anticipation time 189

9.3.1 Kernel form 189

9.3.2 General equation for the anticipation time 189

9.3.3 Moving bar 190

9.3.4 Time of the response peak without gain control 194

Publications **202**

Bibliography **204**

French introduction

Le système visuel est une des machines d'encodage de l'information les plus évoluées qui existent, de part son efficacité, à la fois en termes de traitement et de consommation d'énergie. La vision commence au niveau de la rétine, récepteur qui est improprement assimilé à une caméra, mais qui est en réalité capable d'effectuer des opérations bien plus élaborées, notamment d'extraction et de compression des caractéristiques utiles de la scène visuelle, dans le but de coder l'information avec le plus d'efficience. Contraste, orientation, mouvement, sont autant d'éléments que la rétine est capable d'extraire. L'information ainsi codée par la rétine est ensuite transmise au thalamus, relais central du système visuel, qui la transmet à son tour au cortex visuel, la partie du cerveau spécialisé dans le décodage et le traitement de l'information visuelle. Le traitement visuel requiert du temps cependant: une barre en mouvement projetée sur la rétine génère une activité qui arrivera au moins 200 ms plus tard au cortex, le temps pour une voiture roulant à 50 km/h de parcourir environ 3m. Il va sans dire que de tels délais de traitement peuvent avoir de graves conséquences sur la sécurité des personnes, notamment leur capacité à éviter des obstacles en mouvement. Plus généralement, les délais introduits par le système visuel peuvent impacter la survie des espèces qui ont besoin d'une représentation exacte des mouvements ayant lieu dans le monde les entourant, pour avoir la capacité de fuir d'éventuels prédateurs ou de pourchasser leur proies. Comment les êtres vivants font-ils donc pour compenser ces retards? Une des pistes de réponse consiste à considérer l'anticipation et l'extrapolation du mouvement par la rétine puis par le cortex visuel primaire, V1. C'est l'objet de cette thèse, effectuée dans le cadre du projet ANR «Trajectory», en collaboration avec F. Chavane et S. Chemla de l'Institut des Neurosciences de la Timone à Marseille, Olivier Marre de l'Institut De la Vision à Paris, et Alain Destexhe et Matteo Di Volo de l'Institut des Neurosciences de Paris Saclay.

Dans un premier temps, nous nous sommes intéressés aux différents mécanismes pouvant expliquer l'anticipation au niveau de la rétine. Nous choisissons dans la suite de modéliser la sortie rétinienne en termes de fréquences de décharge, nombre moyen d'impulsions électriques générés par les cellules ganglionnaires. Dans la rétine, nous faisons la distinction entre deux types d'anticipation: le premier est marqué par un maximum de fréquence de décharge en réponse à un objet en mouvement arrivant en avance par rapport au pic obtenu lorsque le même objet est seulement "flashé". Le second type d'anticipation consiste, quant à lui, en une montée de l'activité d'une cellule ganglionnaire avant que l'objet n'arrive dans son champ récepteur. Berry et al. [1] ont montré que le premier type d'anticipation peut être modélisé par un modèle linéaire-non linéaire, implémentant un mécanisme de contrôle de gain au niveau des cellules ganglionnaires, et qui a pour effet d'avancer le pic de réponse des cellules. Ce modèle a été repris par Chen et al. [2], qui ont implémenté le même mécanisme au niveau des cellules bipolaires, pour reproduire deux effet supplémentaires: la réponse à l'apparition d'une barre, ainsi qu'à la réponse au mouvement après un temps d'immobilité. Le modèle original étant unidimensionel, nous avons dans un premier temps étendu et implémenté le modèle à contrôle de gain en 2 dimensions, et étudié comment le temps d'anticipation et le maximum de fréquence de décharge dépendaient des caractéristiques du stimulus: contraste, taille et vitesse de la barre. Notre modèle implémente également la sensibilité à l'orientation, en adaptant une méthode de vision par ordinateur au filtrage spatio-temporel anisotrope du stimulus. Les modèles à contrôle de gain reproduisent des effets locaux d'anticipation, qui trouvent leurs origine biophysique dans l'adaptation, expliquée par l'inactivation de canaux ioniques. Néanmoins, l'anticipation peut également être étudiée du point de vue collectif, en tenant compte des interactions entre les différentes cellules. Il est dans ce cas nécessaire de comprendre comment les cellules rétiniennes sont connectées et communiquent entre elles. Des études ont mis en évidence le couplage des cellules ganglionnaires sensibles à la direction à travers les synapses électriques. Nous avons intégré ce couplage, basé sur le sur le modèle développé par Trendholm et al. [3], dans notre modèle et étudié en quoi il améliore l'anticipation. Puis nous nous sommes intéressés à un circuit rétinien capable d'expliquer le mouvement différentiel: un objet ayant un mouvement différent de celui de l'arrière-plan induit une activité plus saillante. Ce circuit introduit une connectivité via les cellules amacrines agissant en amont des cellules ganglionnaires. La mise en équations de ce circuit a permis de comprendre

le rôle des temps caractéristiques et des poids synaptiques dans le comportement du système couplé, et de déterminer le régime de paramètres dans lequel cette connectivité latérale permet d'améliorer l'anticipation. Enfin, dans les deux cas de connectivité, nous avons mis en évidence l'existence d'une onde de propagation, à même d'extrapoler différentes formes de trajectoires.
Afin d'ancrer notre modèle de connectivité dans la réalité biologique, nous avons développé un modèle probabiliste de connectivité entre les cellules amacrines et bipolaires, s'inspirant de la forme de l'arbre dendritique des cellules amacrines. Nous explorons dans ce cas le changement des propriétés d'anticipation des cellules ganglionnaires couplées par les cellules amacrines.
Le modèle 2D, implémentant le contrôle de gain, la sélectivité à l'orientation et les deux formes de connectivité, nous permet d'étudier l'anticipation dans le cas de stimuli plus complexes que le stimulus classique : une barre en translation rectiligne uniforme. Pour cela, nous concevons des stimuli avec des trajectoires curvilignes, des mouvements accélérés, et des objets plus complexes qu'une simple barre. Loin de faire une étude exhaustive de l'anticipation dans le cas de ces stimuli complexes, nous extrayons des propriétés qualitatives permettant d'évaluer l'anticipation rétinienne et ces effets.

Dans la deuxième partie de cette thèse, nous avons examiné les mécanismes d'anticipation dans le cortex visuel primaire. Des études expérimentales se basant sur l'imagerie optique ont mis en évidence un mécanisme d'anticipation dans le cortex. Ce mécanisme peut être expliqué par la propagation de l'activité via la connectivité latérale, qui a pour effet d'augmenter l'activité des colonnes corticales avant l'arrivée de l'objet dans leurs champs récepteurs.
Comment la répartition des tâches se fait-elle donc entre la rétine et le cortex et en quoi l'anticipation rétinienne impacte-t-elle l'anticipation corticale?Pour répondre à cette question, nous partons d'un modèle de champs moyen du cortex primaire, développé par M. Di Volo et A. Destexhe de l'Institut des Neurosciences de Paris Saclay, avec lesquels nous avons collaboré. Ce modèle a initialement été proposé pour reproduire les résultats de l'imagerie optique concernant le stimulus du mouvement apparent, entre deux tâches gaussiennes spatialement distants, et apparaissant de façon successive. Nous avons étendu la validité de ce modèle en montrant qu'il permet également de reproduire partiellement l'anticipation corticale, en termes de latence et de temps au pic, en accord avec les résultats obtenus expérimentalement.

Nous avons ensuite connecté le modèle de rétine que nous avons développé au modèle cortical, en omettant le thalamus. Le but n'était pas d'avoir un modèle exhaustif du système visuel, mais bien de considérer une entrée rétinienne réaliste au cortex, en contraste avec les modèles communément développés qui prennent généralement des entrées qui ne sont pas biologiquement réalistes (activité constante, bruit blanc). C'est à notre connaissance le premier modèle de ce type, intégrant des mécanismes sophistiqués à la fois au niveau de la rétine et du cortex. Pour connecter le modèle rétinien au modèle cortical, nous avons utilisé des conversions spatiales et des densité cellulaires spécifiques aux primates. Le modèle intégré rétine-cortex nous a permis d'évaluer l'effet de l'anticipation dans la rétine sur l'anticipation corticale notamment en termes de latence et de temps au pic, et de mettre en évidence l'aspect collaboratif de ces deux effets.
Le modèle 2D intégré rétine-cortex nous permet également d'étudier l'anticipation de stimuli plus complexes, et d'émettre des hypothèses quant à la coopération entre la rétine et le cortex dans l'anticipation des trajectoires.

Enfin, dans un travail en cours, nous avons développé une méthode de calcul des corrélations entre les trains de spikes dans le cas non stationnaire, et l'avons appliqué à des données expérimentales de rétine de salamandre et de souris (avec la permission d'Olivier Marre). Nous avons mis en évidence une variation des corrélations au cours du mouvement, liées aux interactions entre les cellules. Ces interactions suggèrent que le mouvement d'un objet peut être extrapolé, non seulement par les fréquences de décharge, mais aussi par les corrélations des spikes qui reflètent les corrélations spatio-temporelles dans la trajectoire d'un objet en mouvement.

Nos résultats peuvent à l'avenir être utilisé pour motiver des travaux théoriques et expérimentaux qui auront pour but de mieux comprendre la prédiction au sens large, à la fois au niveau de la rétine et du cortex.

English introduction

The visual system is an incredibly efficient information encoding machinery, both in terms of data processing and energy consumption. Vision begins in the retina, a receptor that is often and improperly thought of as a camera. However, it is actually able to perform much more elaborate operations than a camera, such as extracting and compressing useful features of the visual scene, in order to code information as efficiently as possible. Contrast, orientation, movement, these are all elements the retina is able to infer. The information encoded by the retina is then transmitted to the thalamus, the central relay of the visual system, which in turn transmits it to the visual cortex, the part of the brain specialized in decoding and processing visual information.
Visual processing requires time : a moving bar projected on the retina generates an activity that will reach the cortex at least 200 ms later; a car traveling at 50 km/h can cross about 3m during this time. It is evident that such processing times can have serious consequences for the safety of people, including their ability to avoid moving obstacles. More generally, the delays introduced by the visual system can impact the survival of species that need an accurate representation of the movements taking place in the surrounding world, in order to have the ability to escape predators or to hunt their prey. So how do living beings compensate for these delays? One of the possible responses consists in considering the anticipation and extrapolation of movement occurring at the level of the retina and the primary visual cortex, V1. This is the purpose of this thesis, carried out as part of the ANR (French Research Agency) project "Trajectory", in collaboration with F. Chavane and S. Chemla from Institut des Neurosciences de la Timone Marseille, Olivier Marre from Institut De la Vision in Paris and Alain Destexhe and Matteo di Volo from Institut des Neurosciences Paris Saclay.

First, we focused on the different mechanisms that can explain anticipation at the retina level. We have modeled the retina output in terms of firing rate, the average

number of spikes emitted by a ganglion cell. In the retina, we distinguish between two types of anticipation: the first is denoted by a peak firing rate response to a moving object occurring before the peak response to the same object when flashed. The second type of anticipation consists in a rise in the cell's activity before the object enters in its receptive field. Berry et al. [1] have shown that the first type of anticipation can be modeled by a linear-non-linear model, implementing a gain control mechanism at the level of ganglion cells, and which has the effect of advancing the peak response of the cells. This model was later used by Chen et al. [2] who implemented the same mechanism at the level of bipolar cells to reproduce two additional effects: the response to the appearance of the bar, and to its motion onset. The original model being one-demensional, we first extended the gain control model in 2 dimensions, and studied how anticipation time and maximum firing rate depend on the characteristics of the stimulus: contrast, bar size and speed. Our model also implements orientation selectivity, by adapting a computer vision method to anisotropic spatial-temporal filtering of the stimulus.

In the feed-forward pathways, gain control models reproduce local anticipatory effects, which can be biophysically explained by adaptation, which in turns is explained by the inactivation of ion channels. Nevertheless, anticipation can also be studied from the point of view of the population, taking into account the interactions between the different cells. In this case, it is necessary to understand how retinal cells are connected and communicate with each other. Studies have shown a class of ganglion cells, selective to directions, is coupled through gap junctions. We have integrated this coupling into our model and studied how it improves anticipation. Then, we focused on a retinal circuit capable of explaining differential motion: an object with a different motion from its background induces more salient activity. This circuit introduces a connectivity pathway involving amacrine cells, acting upstream of ganglion cells. In order for our connectivity model to be biologically plausible, we developed a probabilistic connectivity model between amacrine and bipolar cells, inspired by the shape of the synaptic arbor of amacrine cells. The study of this circuit equations has made it possible to highlight and understand the role of characteristic times and synaptic weights in the behavior of the coupled system, and to determine the parameters regime in which amacrine connectivity outperform gain control, in terms of anticipation. We also explored the change in the anticipation properties of the system, when using the probabilistic connectivity. Finally, in both connectivity pathways, we have highlighted

the existence of a propagation wave, able to extrapolate different trajectories.
The coupled 2D model allows us to study anticipation in the case of stimuli that are more complex than a bar in smooth motion. To do this, we design stimuli with curved trajectories, accelerated movements, and more complex objects. Far from making an exhaustive study of anticipation in these complex stimuli, we extract qualitative properties to evaluate anticipation and its effects.

In the second part of this thesis, we examined anticipation mechanisms in the primary visual cortex. Experimental studies conducted by the laboratory of F. Chavane and based on optical imaging have shown an anticipation mechanism in V1 that can be explained by the propagation of activity via lateral connectivity. This propagation has the effect of increasing the activity of cortical columns before the bar reaches their receptive field.
How is the division of labor between the retina and the cortex organized and how does retinal anticipation impact cortical anticipation? To answer this question, we have used a mean field model of the primary cortex, developed by M. Di Volo and A. Destexhe from Institut des Neurosciences de Paris Saclay, with whom we have collaborated. Their model has initially been proposed to reproduce the results of optical imaging in the case of the apparent motion stimulus : a motion illusion occurring between two spatially distant Gaussian spots, which appear successively. We have extended the validity of this model by showing that it is partially able to reproduce cortical anticipation, in terms of latency and time to peak, in accordance with the results obtained experimentally.
We then connected the retina model we developed in the first part of the thesis to the cortical model, omitting the thalamus. The goal here is not to have an exhaustive model of the visual system, but to consider a realistic retinal entry to the cortex, in contrast to commonly developed cortical models which generally take non biologically realistic entries. To the best of our knowledge, this is the first model of its kind, integrating advanced mechanisms in both the retina and the cortex. In order to connect the retina model to the cortical one, we used spatial and density conversions specific to primates. The integrated retino-cortical model allowed us to evaluate the effect of retinal anticipation on cortical anticipation, particularly in terms of latency and peak time, and to highlight their collaborative aspect. The integrated 2D retino-cortical model allows us to study the anticipation of more complex stimuli, and to make hypotheses

about the cooperation between the retina and the cortex in the anticipation of trajectories. In particular, we explored the changes in the cortical wave of activation properties, when V1 is driven by a retina output implementing the anticipation mechanisms above-mentioned.

Finally, in an ongoing work, we developed a method for calculating correlations between spike trains in the non-stationary case, and applied it to experimental data from salamander and mice retina, then to Poissonian spike trains generated from our retina model. We found a variation in correlations during movement, related to interactions between cells. These interactions suggest that the motion of an object can be extrapolated, not only through firing rates, but also by the spike trains correlations that reflect the spatio-temporal correlations in its trajectory.

Our results can be used in the future to motivate theoretical and experimental work aiming at a better understanding of prediction in a broader sense, both in the retina and in the visual cortex.

What is the thesis about ?

This thesis is first and foremost a computer science thesis, based on a computational development, implementation and study of an integrated retino-cortical model.

We will show throughout this thesis that the retina is a complex neural entity, which does not only transform incoming light into a simple neural code, but also performs complex processing tasks. We will also emphasize the role that lateral connectivity, both at the level of the retina and the primary visual cortex, plays in motion anticipation.

Chapters description

In the introductory chapters (I and II), we will review the characteristics of retinal encoding and feature extraction capacity, as well as cortical processing, mainly in terms of motion detection. We will then emphasize the anticipatory mechanisms occurring at the level of the retina and the primary visual cortex, and review some models that have been used to account for these effects.
In the modeling chapters (III and VI), we introduced the 2D phenomenological model we have developed for retina anticipation, implementing gain control and lateral connectivity through gap junctions and an amacrine cell circuit. The model also accounts for orientation selectivity, through a method inspired from computer vision. We will then introduce the mean field model we have used to reproduce cortical anticipation. The novelty of our work lies in the use of the retina model output as an input to the cortical model.
In the results chapters (IV, V and VII), we will discuss the mathematical and simulation results of motion anticipation, and emphasize the role that lateral connectivity both in the retina and V1 is likely playing. In particular, we will show how lateral connectivity

can improve anticipation in the retina. We will also emphasize the existence of a propagating wave with different characteristics, both in the retina and in the cortex, as an outcome of this connectivity.

Finally, in the last chapter, we will introduce a method for correlation evaluation, and test it on recordings of ganglion cells . We will also present the simulation platform that is currently being developed within the Inria team Biovision, and discuss the perspective of implementing our work in the software.

Chapter 1

Introduction to the visual system

Handling the conversion of light into visual concepts is a complex problem that only a fully developed biological system can handle [4]. Vision tasks involve recognizing objects, discriminating them from the backgrounds, interpreting spatial cues such as orientation and contrast ... These tasks become all the more difficult to attend to when dealing with moving objects. The neural computations underlying the processing of moving visual scenes are still not fully understood. Beyond the utility of expanding the global knowledge of biological vision, a better understanding of the involved mechanisms would also allow bio-inspired vision systems to optimize their visual information processing and improve their performance.

Vision starts when light passes through the cornea and the lens, and is then focused on the retina, the first milestone of neural visual processing. As in a camera, the retinal representation of the visual scene is reversed. The retina transforms incoming photons into neural signals and transmits them to several brain regions, via the optic nerve. The well functioning of the retina is therefore fundamental for seeing, and the loss of information at this level could have dramatic consequences on vision. This explains the growing interest to study how the retina encodes visual information, and understand the specificities of its underlying circuitry. [4]

The output cells of the retina are retinal ganglion cells, whose axons gather to form the the fibers of the optic nerve. Ganglion cells encode and extract relevant features of the visual scene, and send them in parallel streams to the thalamus through the optic nerve, in the form of spike trains. The thalamus relays the visual information to the visual cortex, ultimately enabling us to see.

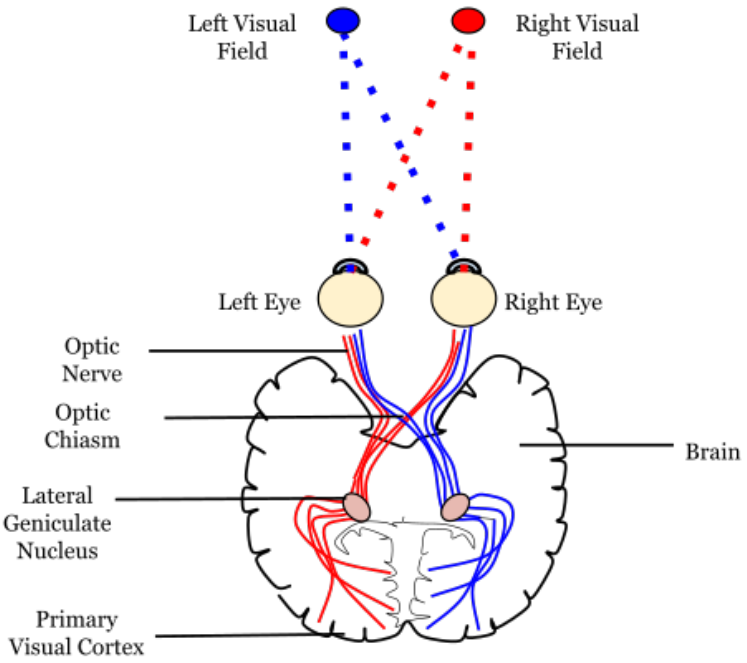

Figure 1.1: General representation of the visual pathway. Vision starts at the level of the eye, where the retina converts the incoming light to an electrical neural signal. This signal is then transmitted to the LGN via the optic nerve which in turn sends it to the primary visual cortex. [5] .

1.1 The retina

1.1.1 General organization of the retina

Photoreceptors

Light is first absorbed by the photoreceptors, located in the outer nuclear layer. These cells that have the ability to perform phototransduction, i.e. the conversion of light into electrical signal. Photoreceptors are divided into two types, rods and cones. Rods are more sensitive to faint light, which makes them responsible for our night vision. They are mostly located in the periphery of the retina. Cones on the other hand are concentrated in the central part of the retina, also known as the fovea, and are at the origin of color vision. They can generally be differentiated into three subtypes, responding to either red, green or blue light. Their combination allows us to perceive colors. Most mammals and rodent retinas have however a preponderance of rods[6].

Photoreceptors hyperpolarize with light and depolarize in darkness, releasing glutamate, an excitatory neurotransmitter. Their signals is then transmitted to downstream cells, horizontal and bipolar cells.

In the second cell layer, known as the inner nuclear layer, are located horizontal, bipolar and amacrine cells.

Horizontal cells

Horizontal cells have AMPA and glutamate receptors, and consequently hyperpolarize to light. Theses cells influence bipolar cells, but it is still unclear whether they do it directly or through a feedback mechanism, via photoreceptors. As they release GABA, an inhibitory neurotransmitter, horizontal cells are accountable for the antagonistic center surround receptive field of bipolar cells.

Bipolar cells

Bipolar cells receive signals from the photoreceptors along with inhibitory feedback from horizontal cells. They then transmit the visual information to ganglion cells, which is also modulated by the activity of amacrine cells. Their intermediate position makes them essential to understand how signals are transmitted from the photoreceptors to ganglion cells, but it also makes it more challenging to record their neural activity. As a consequence, little is known about the response properties of bipolar cells, whose activity is often modeled as a linear filter applied to the stimulus, followed by a non-linearity. Bipolar cells don't uniformly respond to the glutamate release of photoreceptors. According to the type of receptor they express, they are either hyperpolarized or deporalized by light, which gives rise to two major classes of bipolar cells, ON-center and OFF-center bipolar cells. Bipolar cells also receive GABAergic inhibitory input from horizontal cells, shaping their center-surround receptive field. [7]

Amacrine cells

Amacrine cells are the most diverse retinal cell class, they however remain very insufficiently understood. This cell family consists of two major types, small-field and wide-field cells, based on the size of their dendritic arbor. They are involved in both feed-forward and lateral connectivity pathways [8].

Amacrine cells are activated through glutamatergic input from bipolar cells. They conversely release two types of inhibitory neurotransmitters : GABA and glycine, onto bipolar cells and ganglion cells, and can also provide a feedback to other amacrine cells. They are also connected to bipolar cells and ganglion cells via gap junctions.

Ganglion cells

Ganglion cells, whose axons form the fibers of the optic nerve, are the output layer of the retina. They integrate the visual information processed by the upstream layers and transmits it to the brain, in the form of action potentials. They receive excitatory glutamatergic input from bipolar cells, and inhibitory GABAergic and glycinergic inputs from amacrine cells. Ganglion cells have a wide diversity of dentritic field morphologies, yielding different sizes of receptive fields. These receptive field are mainly characterized by the receptive field's configuration of upstream bipolar cells. According to their retinal location, ganglion cells will either communicate with a small number of photoreceptors (as few as five in the fovea), or a large number (up to many thousands in the periphery)[6] [9]. Ganglion cells play an essential role in objects shape and motion detection.

A small number of ganglion cells is photosensitive, and contribute to circadian rhythms and light reflex. These cells contain their own photopigment, melanopsin, which makes them sensitive to light even when photoreceptors are not responding.

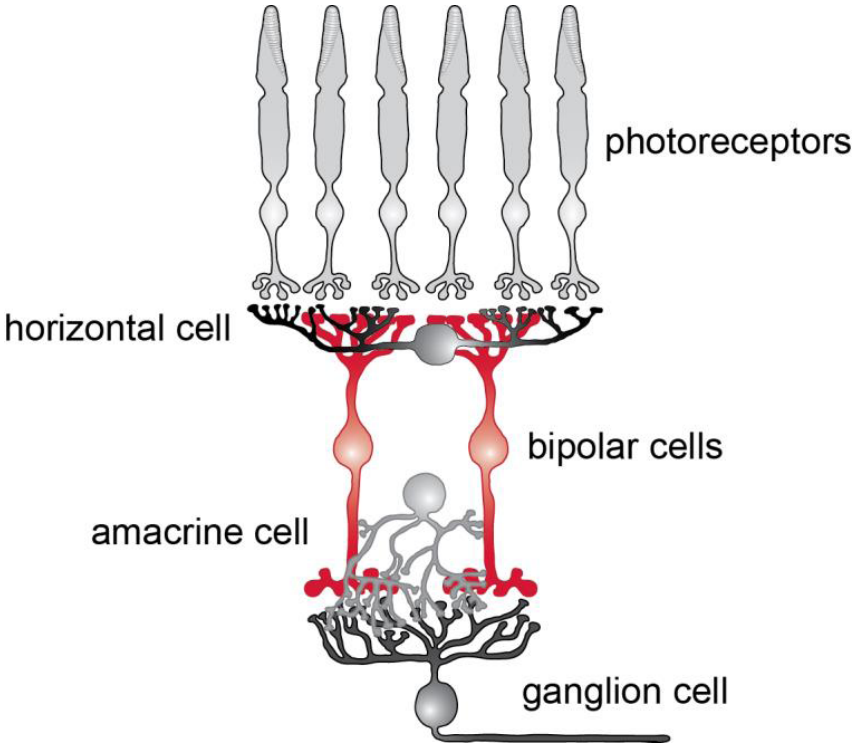

Figure 1.2: Simple retina representation. The photoreceptors transform the light into an electrical signal transmitted to the bipolar cells. These neuronal signals are modified by horizontal cells which also ensure the lateral connectivity of photoreceptors and bipolar cells. Bipolar cells then forward the signal to ganglion cells, taking into account the lateral interactions afforded by amacrine cells. [5] .

1.1.2 Motion processing in the retina

While color vision and binocular vision are not shared between all the species, motion detection is an essential visual capability common to all of them. As a consequence, studying visual motion processing has been one of the fundamental challenges facing systems neuroscience. Studies have revealed that sensitivity to motion starts already at the level of the retina, allowing different species to navigate the world, and detect the possible presence of mates, predators or preys. We will review in this section some aspects of the understanding of motion detection by the retina, giving as examples direction selectivity, speed tuning and lag normalization.

1.1.2.1 Direction selectivity

There exists a wide range of theoretical and biological approches to studying retinal processing of motion. Moving stimuli are generally considered as a spatiotemporal pattern of light intensity projected on the retina, from which retina extracts relevant information, such as the direction of image motion. Detecting motion requires neural networks able to process in a non-linear fashion moving stimuli, asymmetrically in time. [10] [11] [12] [13]
Direction sensitivity is the first mechanism involved in motion sensitivity, achieved through the interaction of On and Off pathways [14] (See Fig. 1.3).

Direction selective ganglion cells (DSGCs) are triggered differentially by the direction of a visual stimulus, responding more strongly when the motion of the object corresponds to their preferred direction. This feature is not dependent on the stimulus shape, size or color. There exists three types of DS cells in the retina : ON/OFF DSGCs, which respond both to the leading and the trailing edge of the stimulus, ON DSGCs, which only respond to the leading edge, and OFF DSGCs, which only respond to the trailing edge.

ON/OFF DCGCs are divided into 4 major types, according to their prefered direction : ventral, dorsal, nasal or temporal. Cells of different types differ in their dendritic configuration and synaptic projections. For instance, nasal cells have a dentritic arbor with an asymmetry toward the nasal direction.
From a mechanistic point of view, DSGCs receive their inputs from bipolar and starbust amacrine cells, responding to their directional preference with a large excitatory postsynaptic potential followed by a small inhibition. Conversely, when stimulated by

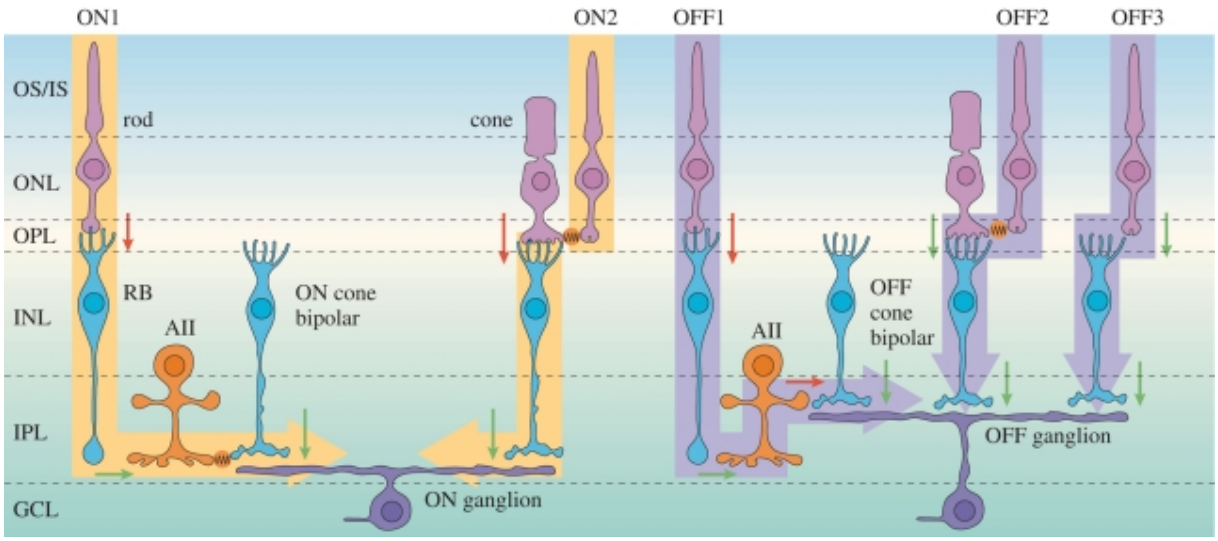

Figure 1.3: Schematic of the mammalian retina wiring, highlighting the rod and cone pathways. Left, ON pathways. Right, OFF pathways. The cone circuitry is illustrated using two cone photoreceptors : on the left hand side, the photoreceptor is connected to the ON ganglion cell through an ON cone bipolar cell. On the right hand side, the cone photoreceptor is connected to the OFF ganglion cell via an OFF cone bipolar cell. The rod pathways are more diverse : they can be either direct (OFF3); connected through a rod bipolar, an amcrine cell, and an ON or an OFF cone bipolar cell (ON1, OFF1); or connected through a cone photoreceptor and an ON or an OFF cone bipolar cell (ON2, OFF2).[14]. .

an object moving in their null direction (i.e the opposite of their preferred direction), they respond with a small excitatory postsynaptic potential followed by a large inhibition. Starbust amacrine cells (SACs), whose dendrites emerge radially from the soma, have been shown to express important direction selectivity properties. Optical calcium imaging has specifically revealed that SACs respond strongly to centrifugal motion, while they are inhibited by the centripetal motion. More generally, when SACs were silenced with toxins, direction selectivity was strongly undermined.

SACs possess two types of neurotransmitters, acetylcholine, allowing excitation and GABA, allowing inhibition. Studies have shown an uneven repartition of gabaergic and cholinergic SACs synapses onto the dendritic arbor of DSGCs, providing direction sensitivity. (See Fig. 1.4)

As stated before, direction selectivity could also be an intrinsic feature of DSGCs, due to the asymmetry of their dendritic field. Trenholm [3] showed the existence of DSGCs that conserve their direction selectivity even in the presence of cholinergic and GABAergic inhibitors. This property is further enhanced by the presence of gap junctions between cells that are tuned to the same direction, increasing the response of

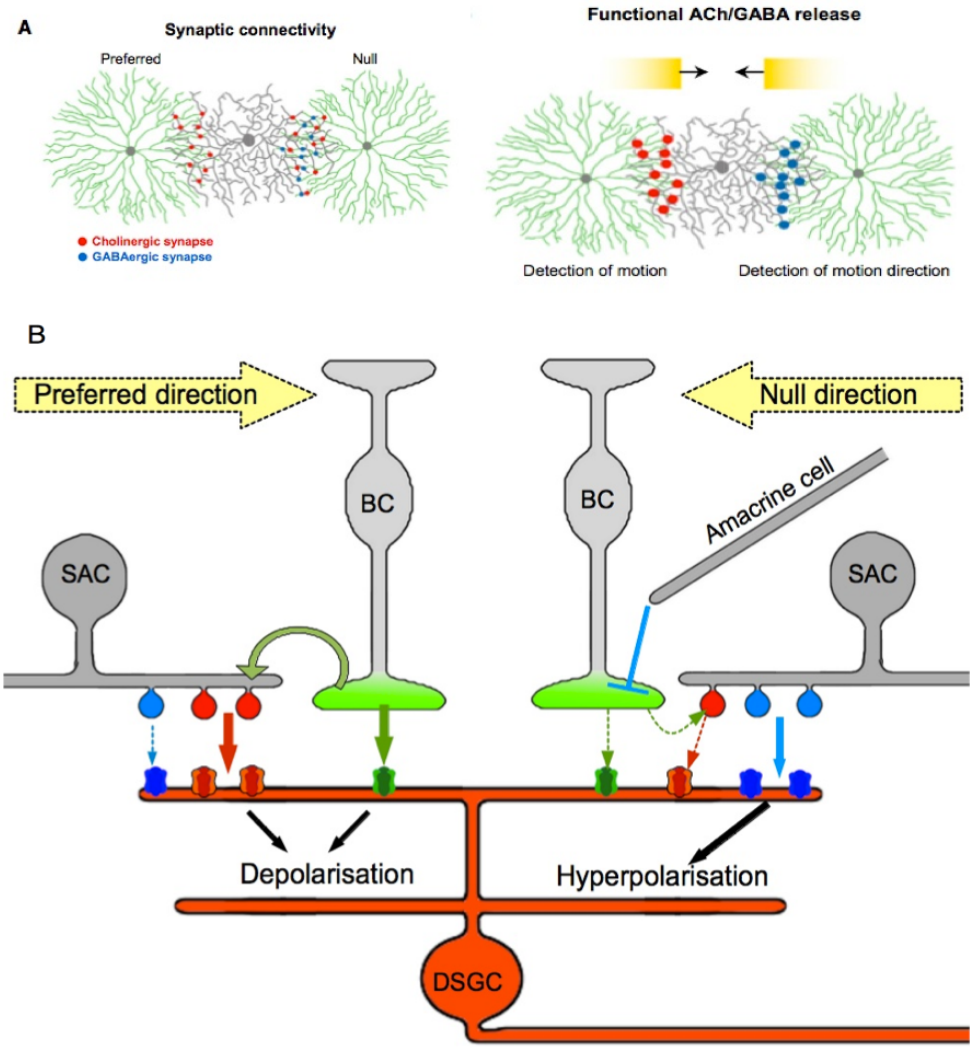

Figure 1.4: A) Distribution of the excitatory (cholinergic) synapses and inhibitory (gabaergic) synapses along the motion axis. On the null side of the dendritic arbor of SACs, more inhibitory synapses are present, reducing as a consequence the activity of DSGCs along the non preferred axis. Conversely, on the preferred side of the dendritic tree, more cholinergic and glutamatergic synapses are present, facilitating the emergence of action potentials at the level of DSGCs. B) Details of the neurotransmitter exchanges between SACs, bipolar cells and DSGCs involved in the direction selectivity pathway. Glutamate is represented in green, Acetylcholine in red and GABA in blue [15]. .

downstream cells (cells that are located further in the connectivity graph) to an object moving in their preferred direction.

1.1.2.2 Speed processing

Speed tuning has been recently identified as a property inherent to a certain class of ganglion cells. Ravello et al. [16] have studied speed selectivity of RGCs using motion cloud stimuli, artificial textures which conserve some of the properties of natural images, mainly in terms of frequency bandwidths. These stimuli are characterized by a spatial frequency, a spatial frequency bandwidth (equal to 0 for regular gratings) and a temporal frequency, resulting in a broader and less binary distribution of contrast, where low contrasts are more frequent.

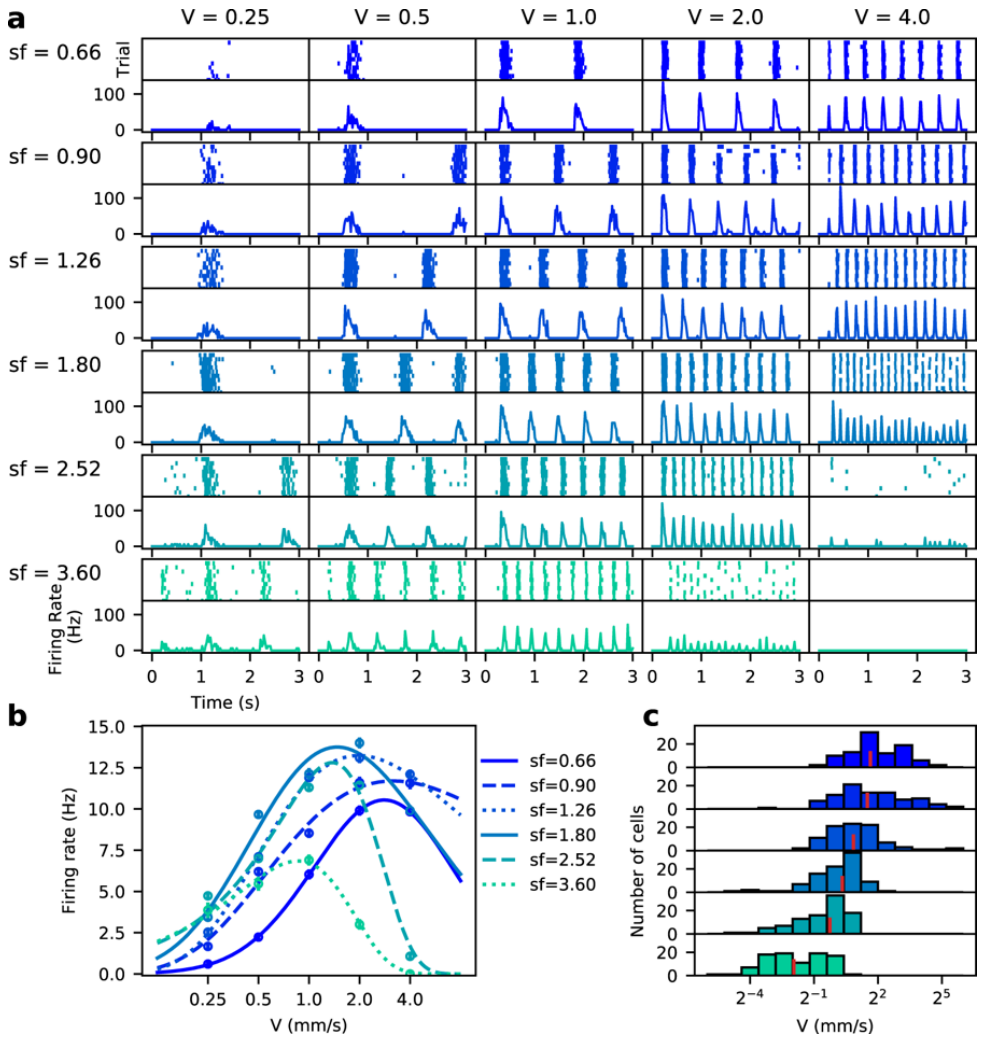

Figure 1.5: RGC response to grating stimuli with different spatial and temporal frequencies. (a) Example response (raster plot and firing rate) of a single cell at each combination of spatial frequency and speed. (b) Fitting of response curves with skewed Gaussians. (c) Distribution of speed responsiveness across cells show a preferred speed that decreases with the spatial frequency. [16] .

In their study, they studied the retinal activity of Octodon degus, rodents with a

high density of RGCs. In particular, they showed that the speed selectivity property is not inherent to a single type of RGCs, but rather shared between different classes. They first recorded the RGC response to gratings with different spatial and temporal frequencies. There is a trade-off between spatial and temporal frequencies, the higher the spatial frequency, the more the response curve shift towards lower speeds. High firing rate frequencies are reached for a combination of intermediate values of spatial frequency and speed. (See Fig. 1.5)
When presenting the rodent with motion clouds, the response curves show a narrowing effect around the preferred speed, i.e the response to low and high speeds is much weaker for motion clouds than simple gratings. The higher the complexity of the motion cloud, the larger is its spatial frequency bandwidth and the narrower is the speed response curve around the preferred speed. This shows a finer speed tuning of RGCs in naturalistic conditions.

1.1.2.3 Lag normalization

Direction selective ganglion cells (DSGCs) in the mouse retina are selective to objects moving in the cardinal directions. There exists a class of DSGCs coupled through gap junctions, eliciting spiking 106 +- 16 μm before the stimulus reaches their dendritic field. Trenhlom & al. [3] have emphasized the role of coupling in these cells response : uncoupled cells begin responding when a bar effectively enters their receptive field, i.e, their dentritic field extension, whereas coupled cells start responding *before* the bar reaches their dendritic field. The coupling considered here is towards the side from which the stimulus is approaching.
This response property accounts for lag normalization : coupled cells far from onset of the bar start responding when the bar reaches a constant distance from their soma, whatever its velocity, while uncoupled cells detect the bar at a position which is further shifted as the bar velocity increases.

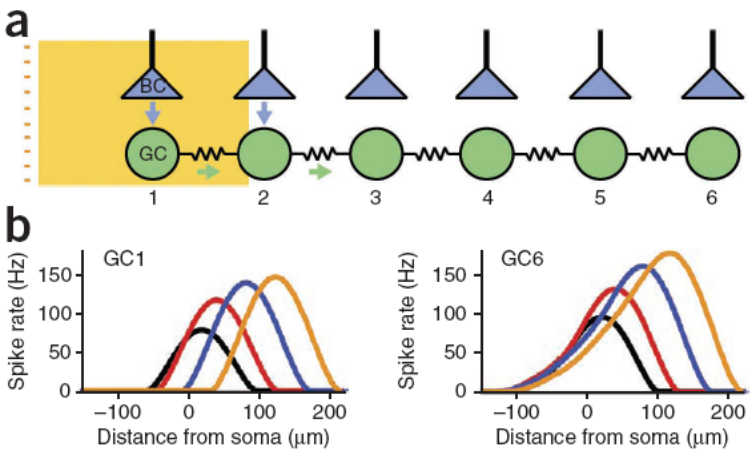

Figure 1.6: Lag normalization in an electrically coupled network of DSGCs. a) Schematic of the model : the nth ganglion cell receive a total current which is the sum of the bipolar input and the weighted pre-junctional input from the previous ganglion cell. The strength of coupling is the only free parameter in their model, and is tuned to best tune the data. b) Simulation results of the first and the sixth cell of the network, for different stimulus speeds. Lag normalization is developed by cells far from the start of motion. [3]

Partial conclusion

In this first section, we reviewed the physiological organization of the retina, and gave examples of motion processing mechanisms and pathways, showing that the retina is not a mere camera, but is rather able to perform complex computations. In particular, we reviewed the role of connectivity (amacrine cells connectivity as well as gap junction coupling) at the level of ganglion cells, in motion and speed processing.

1.2 The visual cortex

1.2.1 General organisation of the visual cortex

The visual cortex is the part of the brain specialized in the processing of visual information. It receives the sensory inputs from the Lateral Geniculate Nucleus [1] located at the level of the thalamus.

When cells in the visual cortex are stimulated within their receptive field, in a given way, they emit action potentials. This defines their neuronal tuning, i.e the stimulus properties to which they are sensitive. This tuning becomes all the more complex when going towards higher visual areas. For instance, if the receptive fields of cells in V1 correspond to simple stimulus feature such as orientation, some cells in the inferior temporal cortex will only fire if a definite object appears in their receptive field [17].

There exists two primary visual streams, receiving inputs from the primary visual cortex, the dorsal and the ventral stream. The dorsal pathway starts with V1, goes through V2, the dorsomedial area, the medial temporal area and the posterior parietal cortex. It is mainly involved in the processing of motion, and the coding of location. The ventral stream begins as well with V1, goes across V2, V4 and the temporal cortex. It is mainly associated with the shapes and objects recognition, and is also involved in long-term memory. (See Fig. 1.7)

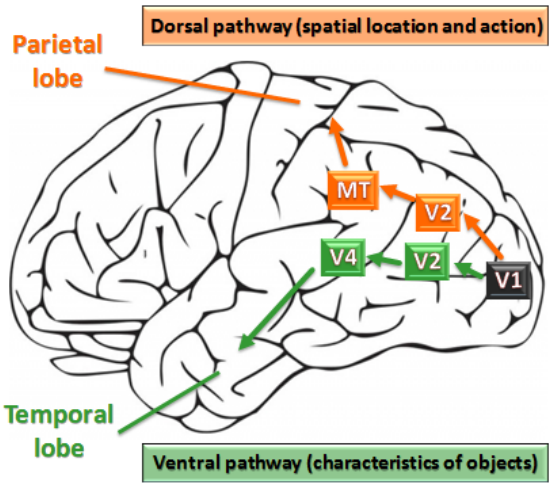

Figure 1.7: Organization of the visual cortex into two parallel streams.[18]

[1] The Lateral Geniculate Nucleus (LGN) is a central relay in the visual pathway. It transmits to the primary visual cortex the visual information received from the retina, via the optic nerve. The LGN lies in both the left and right brain hemispheres. It contains layers of parvocellular (small sized cells receiving their inputs from midget ganglion cells) and magnocellular cells (larger cells receiving their inputs from parasol ganglion cells).

1.2.1.1 The primary visual cortex

The primary visual cortex is the most commonly studied area in the visual cortex. Each brain hemisphere has a cortical area V1 receiving the visual signal from the contralateral eye. It is essentially involved in the processing of static and moving stimuli, and is specialized in pattern recognition. It is able to differentiate different features such as orientations, colors, spatial frequencies, motion ... V1 neurons can thus be viewed as a set of specialized spatio-temporal filters able to selectively respond to each of these features. Neurons with similar response properties are arranged in columns, which are in turn assembled in larger structures called modules. Each module is able to decode and analyze a small area of the visual field.
V1 is thus believed to implement a filter bank of 2D "Gabor filters" (See Fig. 1.8), which reproduces the cortical cells responses to impulse stimuli. [19] [20] [21]

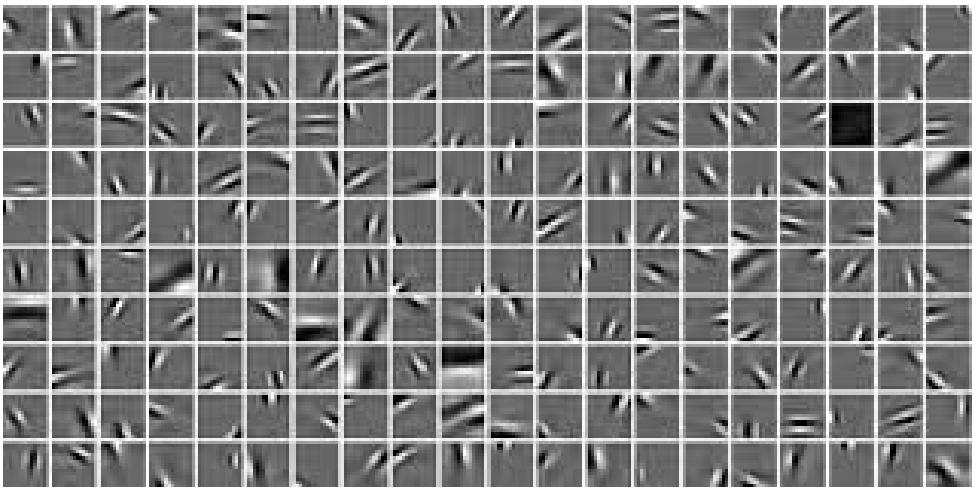

Figure 1.8: Image structures can be captured using a bank of oriented basis functions. The set of basis functions has been obtained with a sparse coding algorithm. [21]

From an anatomical point of view, the multi-level processing of the primary visual cortex is based on the feed-forward pathway, i.e the activity coming from the retina via the LGN, and extensive lateral connections between the cortical columns. The direct feed-forward activity alongside the contribution of lateral connectivity are then projected onto V2, V3, V5. V1 also receives feedback projections from V2, V3, V4 and V5.
Neurons in V1 are organized according to a retinotopic map. Indeed, the spatial positions of RGCs within the retina is conserved by their neuronal projections in the LGN, and the same topology is also preserved at the level of V1. When measuring the locations of receptive fields along V1, one can see that adjacent RF centers from posterior

to anterior correspond systematically to ganglion cells located from the fovea towards the periphery.
As stated earlier, orientation and direction selectivity are strongly present at the level of V1. The vast majority of V1 neurons are orientation selective to a certain extent, but only approximately 30% of them show strong direction selectivity.
Cells in V1 have also been shown to be either monocular, i.e solely responding more strongly to one eye, or binocular, i.e cells responding maximally to stimulation in both eyes or with a weak bias to a given eye excitation. Their proportion vary according to the area of V1 from which the cells are recorded. Binocular cells are involved in binocular disparity : the difference in the objects location between the left and right eyes, used for depth perception.
Hubel and Wiesel [22], who won the Nobel prize for their studies of the physiological and functional organization of neurons in V1 (orientation and direction selectivity, binocularity ...) , emphasized the existence of three types of neurons : simple cells, complex cells, and hypercomplex cells. Each of these different types can be discriminated based on how they respond to visual stimuli. Simple cells respond best to elongated edges. They are orientation selective, and can be monocular or binocular. Their receptive fields has distinct ON and OFF subregions. Complex cells are also orientation selective, but are mostly all binocular. Their receptive fields are homogeneous, responding to either ON or OFF stimuli. Finally, hypercomplex cells are similar to complex cells, with the difference that they have an end-stopping property : they maximally respond to a cell with a given length, and their response starts decrease for higher lengths, while complex cells response increases with the bar length before reaching a plateau. (See Fig. 1.9)

1.2.1.2 Higher order areas

Higher order areas in the visual cortex are responsible for the refinement of the visual information pre-processed by V1. V2 improves the ability to discriminate lines and edges, and enhance color interpretation. For instance, V2 is responsible for color constancy, which accounts for a constant color perception, regardless of illumination levels.
V3 is specialized in form processing but is poorly sensitive to color. Most of V3 cells are orientation selective, and the activity of some is modulated by motion and depth.

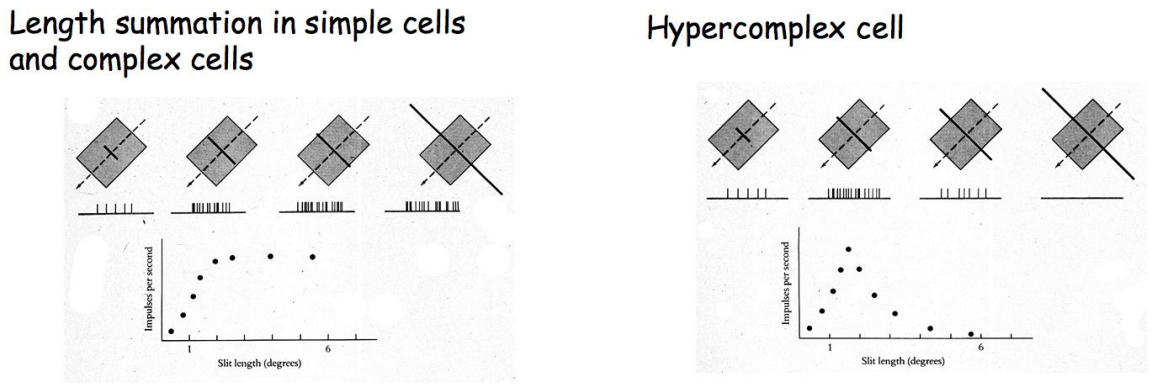

Figure 1.9: Complex cells response increases with the size of the bar before reaching a constant value, while hypercomplex cell response is maximum for an intermediate size [23].

They are also highly sensitive to contrast.
V4 is mainly responsible for color processing. Like V2, V4 is also selective to orientation and spatial frequency, but is however tuned to more complex object features such as geometric shapes. Recent studies have emphasized the existence of long-term plasticity [2]at the level of V4, sensitivity to salient stimuli, and the ability of its receptive fields to change over time, depending on attention levels.
Finally, V5, also known as the medial temporal area, is involved in motion processing. Cells in V5 are largely tuned to stimuli speed and direction. More details on the role of V5 and motion processing will be introduced in the next section.
An important feature at the level of higher order visual areas is that they are strongly influenced by past experience based expectations. Though these expectations can lead to misinterpretations or misperception of the external world, they enable the brain to process visual information very quickly [24].

1.2.1.3 The retinotopic representation

Cells in V1 form together a topographic map of the retina input, known as the retintopic representation. Each half of the visual field is displayed as a map on the contralateral hemisphere, while the fovea is mirrored on the occipital pole. The fovea refers to the center part of the visual representation, where cells have the highest reso-

[2]Synaptic plasticity is the property that connections between neurons, called synapses, have to change their strength according to their activity. It encompasses the multiple mechanisms involved in modifying synaptic transmissions over time. Long-term plasticity refers to phenomena that occur over a longer time range, lasting minutes or more.

lution, i.e the smallest receptive fields. The mapping and identification of visual areas has been achieved using magnetic resonance imaging (MRI). It has been mainly used to investigate changes in cortical activity patterns when subjects are presented with flashed checkerboard stimuli, with a changing position.
While the primary visual cortex is only split into to hemispheres, the retinotopic representation of V2 and V3 is split into 4 quadrants. Nowadays, more than 20 visual areas have been characterized, showing different levels of retinotopic representation.

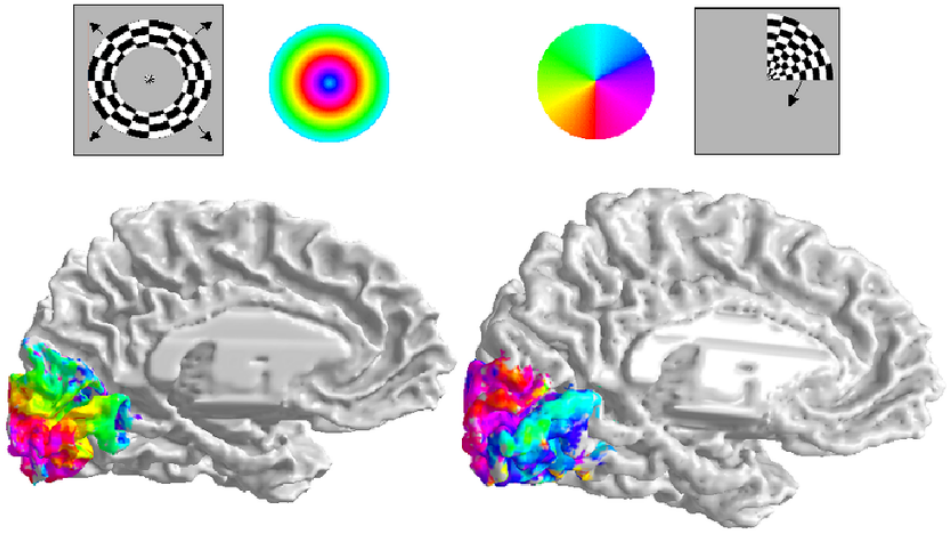

Figure 1.10: The Retinotopy paradigm. In order to measure retinotopic maps in the cortex, two stimuli are used, a ring expanding stimulus and a rotating wedge. Data has been recorded on the left hemisphere. The figure shows how the eccentricity and the polar angle are mapped into the retinotopic map of the visual cortex. [25]

1.2.2 Motion processing in the visual cortex

Motion perception is one of the most important tasks that the visual cortex attends to, analyzing and processing the visual information by a large number of interconnected neurons and areas. The complexity of cells' response increases from lower to higher cortical areas, and this is also applicable to motion processing. The latter starts at the level of V1 where there is a large proportion of direction selective cells. Motion processing is further pursued at the level of the medial temporal area (MT or V5), where cells are selective to both direction and speed. The first motion detector model has been proposed by Hassenstein and Reichardt [26](See Fig. 1.11). The model relies on changes in contrast of two spatially distant locations, inside the receptive field of a motion sensitive neuron. The neuron will only produce a response if contrast changes

are temporally delayed, and is thus not only selective to direction, but also to motion velocity. Several models have been developed based on Reichardt detectors, but they all share the common feature of integrating spatio-temporal variations of the contrast, constituting the motion sensor's receptive field. Consequently, to perceive motion as coherent and uninterrupted, an additional integration over motion detectors is hypothesized to take place. This integration usually takes the form of a pooling mechanism, over visual space and time.

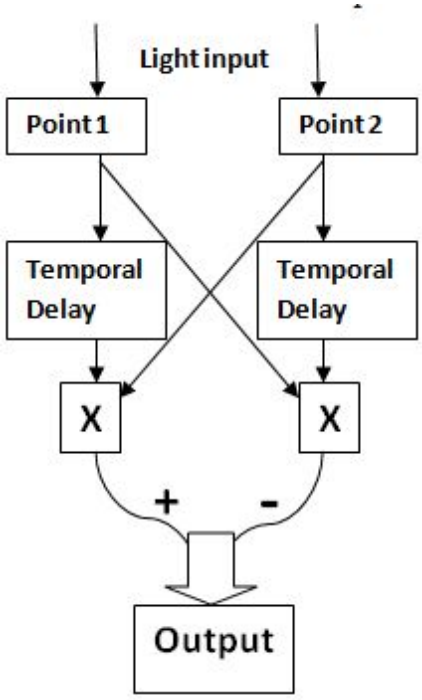

Figure 1.11: The motion detector model is composed of two subunits. The input received at the level of one unit is sent to the opposite unit, to be multiplied with the opposite unit's input with a time delay. The output of the two units are then substracted to form the output of the motion detector. Adapted from [27].

Studies [28] [29] have also shown the existence of a bias for centrifugal and centripetal motions. From a functional point of view, this could be due to the prevalence of radial motion in self-locomotion situations. When walking forward for instance, the visual scene moves centrifugally on the retina, and the opposite occurs when moving backward.

Predictive coding The brain can be seen, from a probabilistic point of view, as an engine that computes the probabilities of the most likely causes to a given neuronal activity, assuming that the computations would converge to a single optimal solution.

In order to understand how this solution is found, many studies have investigated predictive aspects of neuronal processing, directing the reconstruction of possible stimuli towards the most likely scenarios [30] [31].
The term "predictive coding" refers to the role played by predictions in the shaping of neural signals, decreasing neural activity when the stimulus does not contradict the prediction, and giving rise to a strong response when the prediction is inaccurate. There is a class of neurons, called object detectors, that respond only when the movement of an object does not correspond to the predicted trajectory. This type of neurons will have a particularly high response when an object that has not been predicted appears in the visual field. Conversely, these neurons are very strongly inhibited when the movement of the object corresponds to the prediction.

Partial conclusion

In this section, we reviewed the physiological organization of the cortex, with an emphasize on the primary visual cortex. We presented an example of motion processing at the level of the cortex, and introduced the notion of predictive coding. This notion is highly linked to anticipation. In the following, we will not focus on the probabilistic aspect of predictive coding in the retina and the cortex, but rather on its mechanistic aspects.

Chapter 2

Anticipation in the retina and the primary visual cortex

Estimation of a moving object precise position is a non trivial problem that the brain has to attend to, taking into account the time lags that are involved in neuronal computations. Let's consider a human subject, interacting with a moving object, that he has to catch for instance. How does he compensate for the delays introduced by his nervous system ? Some studies suggest that the origin of compensation is motor : the subject performs a muscular action in response to a predicted cause [32] [33] [34]. This would explain why practice, mental or physical, not only improves the timing of actions, but also the velocity at which they are realized [35] [36].
Other studies show that motion anticipation is in fact sensory : the visual system is able to extrapolate the trajectory of a moving object, delivering an anticipated representation of the object's position, when its motion is deterministic. [1] [37] [38]. It has been shown that such anticipatory mechanisms exist, first at the level of the retina, and are further carried out by the primary visual cortex.
It is likely that anticipation is ultimately due to the cooperation of both compensation mechanisms [39]. In that sense, Nijhawan et al. suggest that "compensation mechanisms [...] belong to a general principle of how the brain carries out computation efficiently in the spatio-temporal domain".

In this chapter, we will focus on motion anticipation in the retina and primary visual cortex. We will first present the psychophysical experiment known as the flash lag effect that highlights anticipation from a perceptual point of view. We will then ex-

plore the experimental findings concerning anticipation in the retina and visual cortex. Finally, we will present, in each of the sub-parts, the models that have been developed to reproduce anticipatory effects.

2.1 The flash lag effect

The flash lag effect is an optical illusion where a bar moving along a smooth trajectory and a flashed bar are presented to the subject, and are perceived with a spatial displacement, while they are actually aligned. A variation of this illusion consists of a bar moving in rotation, a bar flashed in angular alignment, giving rise to a perceived angular discrepancy. (See Fig. 2.1)
Neuroscience has explored many explanations for this illusion, including motion extrapolation. The visual system being predictive, it processes differently a bar in smooth motion, whose motion can be extrapolated, and a flashed bar which cannot be predicted by the system.
A second explanation is that the visual system, rather than extrapolating trajectories, simply processes moving objects with a smaller latency than flashed objects [40]. In the first conception, the actual position of the moving object is anticipated, while in the second, both the moving and the flashed objects elicit delayed responses, with a delay that is reduced in the case of motion.
A third explanation suggests that the flash lag effect is due to postdiction, in other words, the perception of the flash is conditioned by events happening after its appearance [41] [42]. This hypothesis is inspired by the the color phi illusion, where two dots of different colors appearing at two discrete yet close positions, with a small latency, will be perceived as a single moving dot which color has changed.

In the following, we will restrain our literature review to the first hypothesis, i.e motion anticipation and trajectory extrapolation. These two phenomena have been shown to occur at the level of the retina and the primary visual cortex for different species : small animals such as the salamander and the rabbit in the case of retinal anticipation, and bigger animals such as cats and monkeys in the case of cortical anticipation.

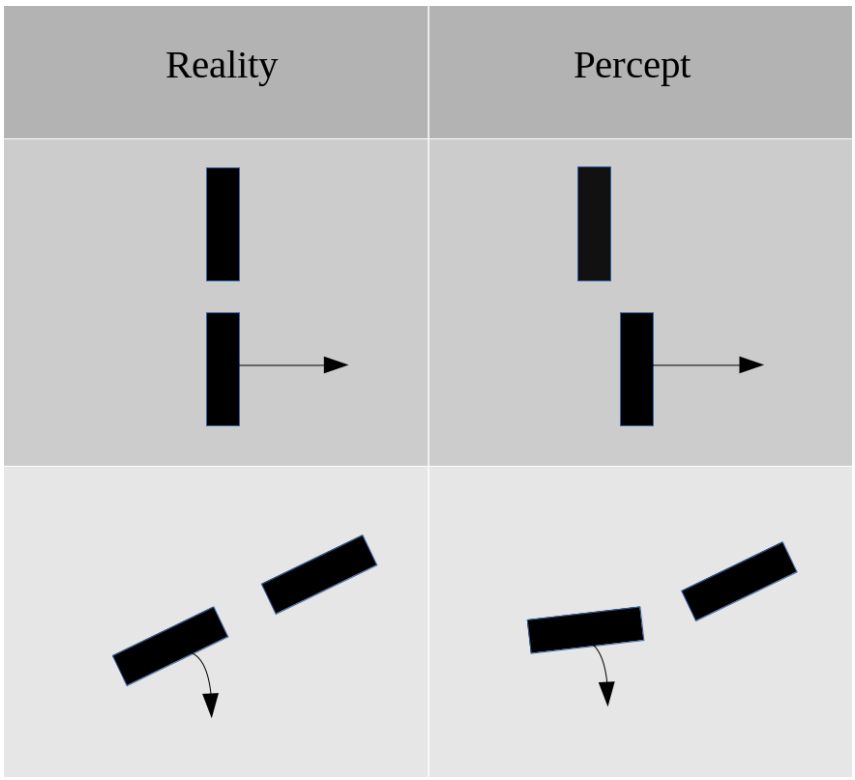

Figure 2.1: Representation of the flash lag effect. Arrows denote moving bars, versus the bar flashed in alignment. In the case of translation, the flashed bar is perceived as lagging behind the moving bar, while in the case of rotation, it is perceived with an angular displacement.

2.2 Anticipation in the retina

When an object moves across the visual field, its motion elicits a series of neuronal activities, at the level of the retina, transmitted to the LGN, that will eventually be decoded at the level of the visual cortex. All this encoding and decoding processes take time, and emphasize the necessity of having mechanisms which compensate for the generated delays.

The general consensus nowadays among retina experts, it to consider that the retina performs general features extraction, rather than just being a mere transmitter, for the visual cortex to be able to process stimuli with more efficiency. The complexity of retinal processing is achieved through a variety of cells mechanisms [6] and different connectivity pathways [43], [44], [45]. One of the most interesting features that the retina attends to is motion anticipation of moving objects. We will first present experimental evidence showing motion anticipation of a moving bar at the level of the retina, and we will then introduce the models that have been developed to account for it.

2.2.1 Experimental evidence

At the level of the retina, an object moving along a trajectory generates an activity in advance to its future position. Berry et al. [1] have first shown that local gain control mechanisms occurring at the level of bipolar and ganglion cells can explain the local anticipation of a moving bar. These mechanisms explain the change in the shape of response observed in experimental data, bringing the cells to their peak activity state earlier than when they respond to a flashed bar, without modifying the time at which the activity starts increasing, with respect to the size of the receptive field.

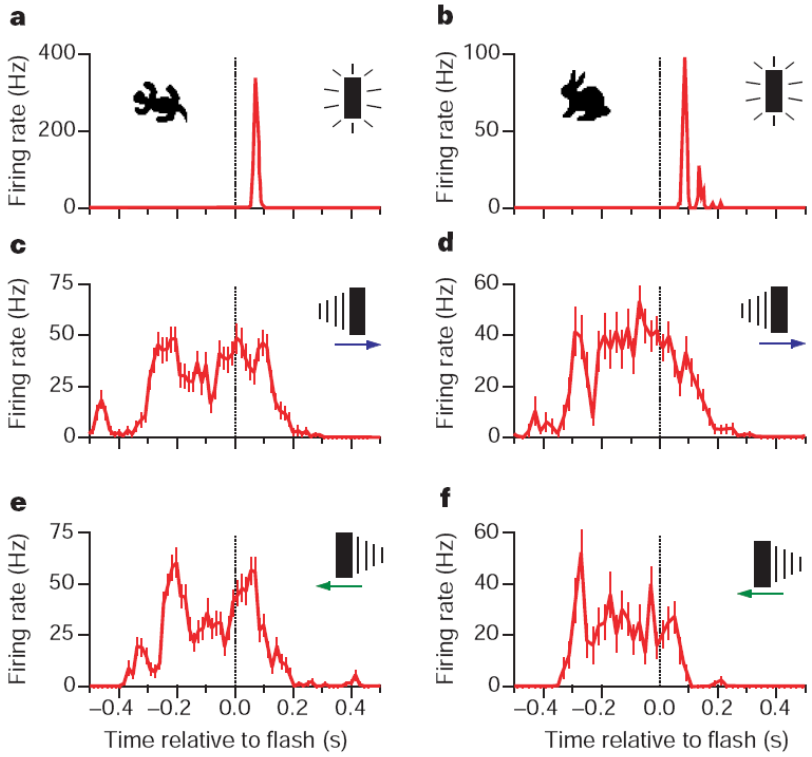

Figure 2.2: Ganglion cells firing rates in response to flashed and moving bars. a,c,e Recording of Fast OFF salamander ganglion cells. b,d,f, recordings of brisk-sustained OFF rabbit ganglion cells. The first row shows the response to a bar flashed for $15ms$. The second and third rows show the response to a bar moving at $0.44mms^{-1}$, in opposite directions. Error bars are obtained from the repeated presentations of the stimulus. The bar is the three configurations is 90% contrast, and 133 μm width. [1]

Berry et al. recorded the responses of OFF-type ganglion cells in salamander and rabbit retinas, in response to two stimuli : a bar flashed in the centre of the individual cells receptive field, and bar moving at a constant speed across the receptive field. Fig. 2.2 shows that the flashed bar generates a narrow response with a peak occurring

after the flash, while the moving bar elicits a wider response, with a peak firing rate that seemingly occurs ahead of the center of the bar, near its leading edge. This effect doesn't depend on the direction in which the bar moves, showing that this anticipatory effect is not due to direction selectivity.

Another study by Johnston et al. [46] emphasized the role of inhibition at the level of the retinal connectome in the existence of anticipatory mechanisms. Fig. 2.3 shows, using an experimental setting similar to the one used by Berry et al., the existence of anticipation, this time in the goldfish retina. Both studies show that motion anticipation is velocity dependent (Fig. 2.4). However, this velocity tuning varies across species, and according to the ganglion cell type. Similarly, the anticipation ability degrades at low contrasts.

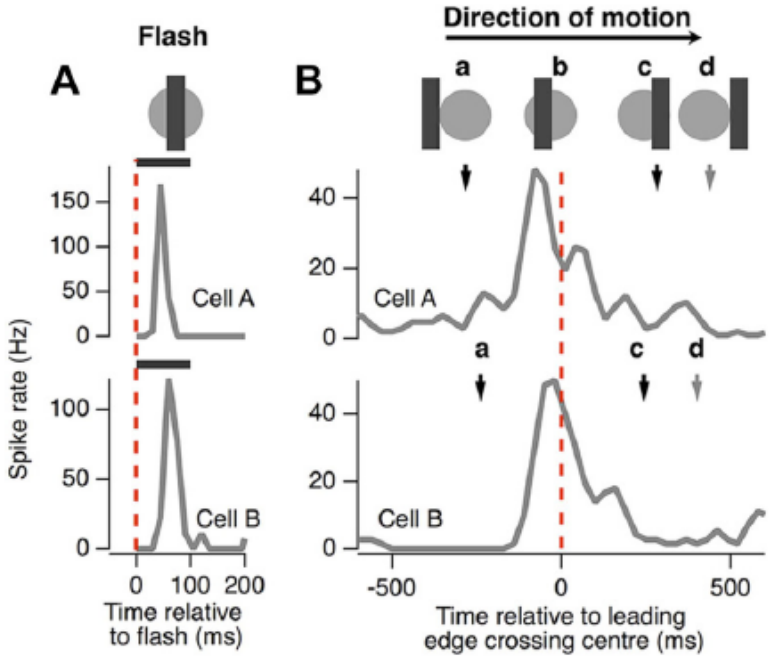

Figure 2.3: A) Goldfish ganglion cells firing rate when responding to a bar flashed for 100 ms. B) Ganglion cells firing rate when responding to a bar moving at $500\mu m/s$. The bar is 100% contrast and $160\mu m$ width. [46]

Johnston et al. have demonstrated that motion anticipation arises from the general properties of the retina connectome, namely the excess of inhibitory connections compared to excitatory ones. In particular, they show that bipolar gain control mechanisms are not responsible for motion anticipation. They emphasize instead, through pharmacological disruptive tests, the role played by feedforward inhibition, which ganglion cells receive from amacrine cells. This inhibition could be at the origin of

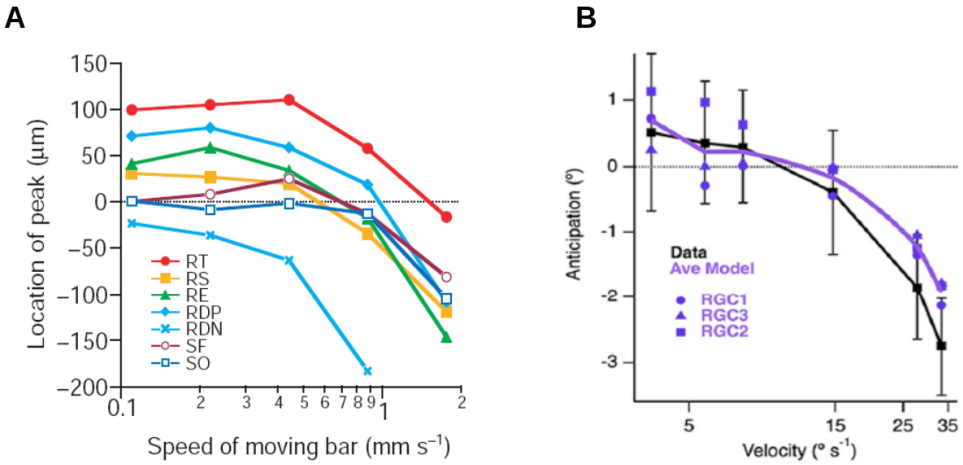

Figure 2.4: Dependence of motion anticipation on speed. A) Anticipation (the distance between the the peak response and the leading edge of the bar) plotted as a function of velocity, for salamander (SF: fast OFF, SO: other OFF) and rabbit (RT: brisk-transient OFF, RS: brisk-sustained OFF, RE: local edge detectors, RDP: ON/OFF direction-selective cells probed in preferred direction, RDN: ON/OFF direction-selective cells probed in null direction) ganglion cells [1]. B) Anticipation for goldfish ganglion cells [46].

ganglion cells gain control. Chen et al. [2], in their study of motion onset response in the salamander retina, proposed a model where they proposed the cooperation of both gain control mechanisms : while bipolar gain might not be enough to account for the anticipatory properties of ganglion cells, it may still play a role.

Another key point that has been raised by Johnston et al., is the receptive field size dependence of anticipation. They hypothesize that, given that the specialized ganglion cells of the monkey have a smaller receptive than the goldfish receptive fields they studied in their paper, monkeys and primates retina might not exhibit anticipation.

2.2.2 Anticipation models

In order to account for anticipation, Berry et al. [1] developed a cascade model implementing gain control at the level of ganglion cells, through a feedback loop. The retina receives a light stimulus function, which is convolved with a spatio-temporal kernel, denoting the receptive field of the cell. If the stimulus is strong enough for a given duration, it initiates a feedback loop which reduces the output firing rate. The retinal output being negatively modulated, its peak response is shifted, which results in motion anticipation. Fig. 2.5 summarizes the cascade model.

Johnston et al. [46] opted for a biophysical model, that takes into account the

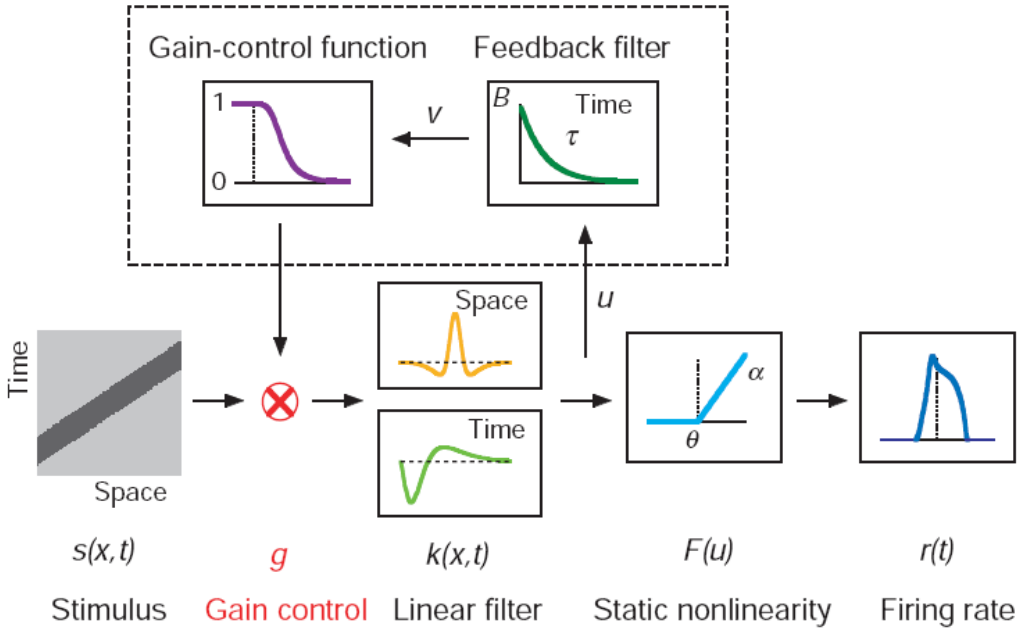

Figure 2.5: Retina model with gain control. The stimulus is multiplied by a gain factor, integrated through a spatio-temporal receptive field, and transformed into firing rate through a nonlinearity. The feedback loop computes an adaptation function which will then decrease the gain factor, consequently shifting the peak response. [1].

morphology of cells dentritic arbors. They derived the equations of synaptic excitatory and inhibitory conductances, as a function of the stimulus onset time and duration. While their model is more biologically accurate, it remains very limited because it is only adapted to the moving bar stimulus. A more phenomenological model, as the one developed by Berry et al., can on the other hand be applied to different kind of stimuli. Chen et al. [2] have further extended this model to account for the encoding of other motion features, such as the response to the appearance of the bar, motion onset and motion reversal. They added a second layer of gain control at the level of bipolar cells, as well as bipolar cells pooling (see Fig. 2.6). This model has been the foundation stone of our retina model.

Gain control based models have been often used to account for several features processing at the level of the retina. It has namely been used by Leonardo and Meister [47] to account for target tracking : when an object is moving along a 2D trajectory, and abruptly changes its direction, ganglion cells are able to quickly adapt to this direction change. Deny et al. [48] have also developed a gain control model to account for ganglion cells non-linear response to objects speed when they are moving outside their receptive field.

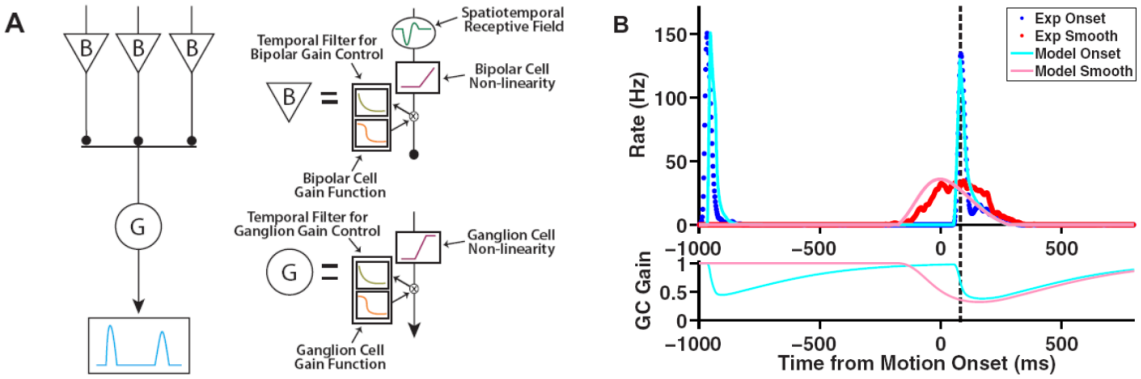

Figure 2.6: Cascade model for alert response to motion onset. A) Schematic representation of the model. The gain control layers are similar to the one described in Fig. 2.5, except for the static nonlinearity which is applied before the feedback loop. Ganglion cells pool over many bipolar cells lying in their receptive field. B) The model is able to reproduce the response to the appearance of the bar, to its motion onset, as well as the response to smooth motion [2].

Finally, an interesting work we have come across during our literature review of retina modeling is the one by Saglam and Hayashida [49], who developed a biophysical model which account for several retinal computations, including motion anticipation. The spatial structure of their model is composed of two layers of hexagonal sub-units, the first implementing photoreceptors, horizontal cells, bipolar cells and amacrine cells, and a second layer implementing other types of amacrine cells and ganglion cells. While their model is physiologically consistent and able to reproduce many features (rapid neural coding, anticipation, and motion sensitivity), its completeness and the number of parameters it involves would make it hard to only focus on mechanisms involved in anticipation, and study them thoroughly.

2.3 Anticipation in the primary visual cortex

Classical studies have been conducted to assess motion integration in the visual system of various species, but most of them share the classical feed-forward conception of both the retina and the primary visual cortex [50] [51]. However, the feed-forward framework proves to be unfitting when it comes to integrating dynamic and non-stationary stimuli. In contrast, lateral connectivity, at the level the primary visual cortex, seems to play a crucial role [52] [53] [54], namely in terms of motion anticipation.

2.3.1 Experimental evidence

Several studies have shown that the brain is not just a reactive encoder, but that it is rather able to respond in a proactive way, and can thus be considered as predictive, with regards to stimuli characteristics. In visual processing, predictions mean that the brain is able to extrapolate and estimate what the visual stimulus is most likely to be, given past information. This is of course based on the strong assumption that the stimulus is predictable to some extent. In particular, some studies have suggested that the predictability of stimuli can be learned from spatial and temporal regularities [55]. However, one can ask, where do these predictions start taking place ? Do they start at the level of the early stages of the visual system, or in late-stage processors ?
Predictions is a rather large concept. If by prediction, one refers to motion extrapolation , we have reported in the previous section that this already starts at the level of the retina. It has also been shown that this task is further carried out at the level of the primary visual cortex [56] [57] [58].
Jancke et al. [58] first demonstrated the existence of anticipatory mechanisms in the cat primary visual cortex. They recorded cells in the central visual field of area 17 of anesthetized cats, responding to small squares of light, either flashed or moving in different directions, and with different speeds. When presented with the moving stimulus, cells show a reduction of neural latencies, as compared to the flashed stimulus. Fig. 2.7 shows the population response to the two stimuli. At time 0, the response to the flash is null, due to neural delays. However, for the moving stimulus (which starts its trajectory 3.2 °outside the population receptive field), propagating activity elicited by the square motion through lateral connectivity is observed. This activity however still lags behind the real spatial cortical representation of the square. This spatial lag has been shown to increase with the speed of the moving stimulus.

Subramaniyan et al. [57] have reported the existence of similar anticipatory effects in the macaque primary visual cortex, showing that a moving bar is processed faster than a flashed bar. They give two possible explanations to this phenomenon : either a shift in the cells receptive fields induced by motion, or a faster propagation of motion signals. Consistent with the study by Jancke et al., they reported a speed dependence of the response latency (see Fig. 2.8), as well as a luminance dependence.

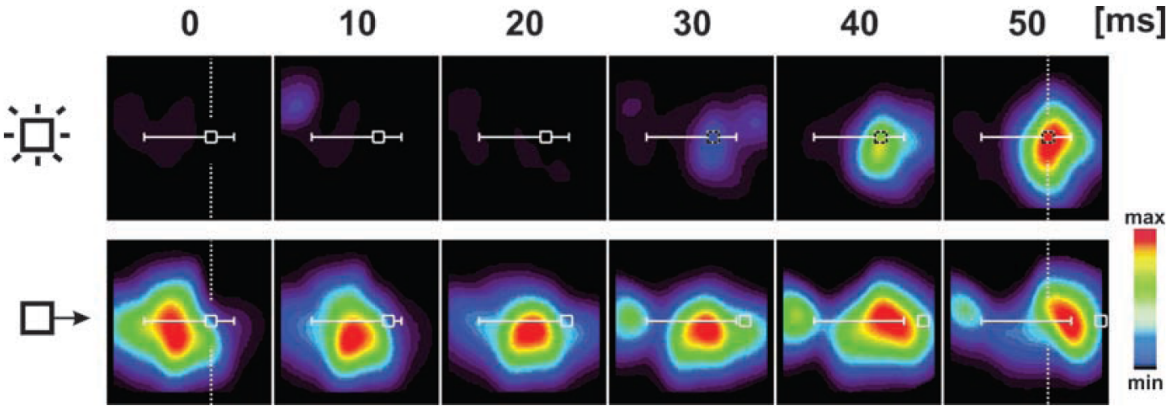

Figure 2.7: Motion induces shorter latencies than flash. Upper row : A square of 0.4 °is flashed at the population receptive field center, for 25 ms. Lower row : square at the same spatial location in smooth motion. The square is presented 3.2 °outside the population receptive field, and is moving at 38.4 °/s. Colored heat map denotes the normalized activity level. Recordings are shown with a 10 ms temporal spacing. White lines and square indicate the real spatial position of the stimulus. [58]

However, Subramaniyan et al. note that the motion representation delays are not reduced to zero, irrespective of the experimental setting of the flash lag effect. Moving objects representation in V1 will still be mislocalized, as it has been shown by Jancke et al.. This is in favor of collaborative work conducted on the one hand by the retina and V1 to help reducing the latencies, and on the other hand by other specialized brain regions which carry out predictive computations. Learning and training seem also to play important roles in calibrating the response of the nervous system to a giving moving object.

Partial conclusion

In this section, we reviewed the experimental occurrence of anticipation in the retina of the salamander, the rabbit and the goldfish, and the primary visual cortex of the cat and the monkey. While anticipation in the retina has often been modeled, the mechanisms accounting for anticipation in the cortex are not fully understood yet, and we could not find any model reproducing anticipation in V1.
In the rest of our work, we are going to make a highly speculative extrapolation, considering that there exist similar anticipation mechanisms in the monkey retina as the ones that have been shown in smaller species. This extrapolation will enable us to use our retina model as an input to a monkey cortical model.

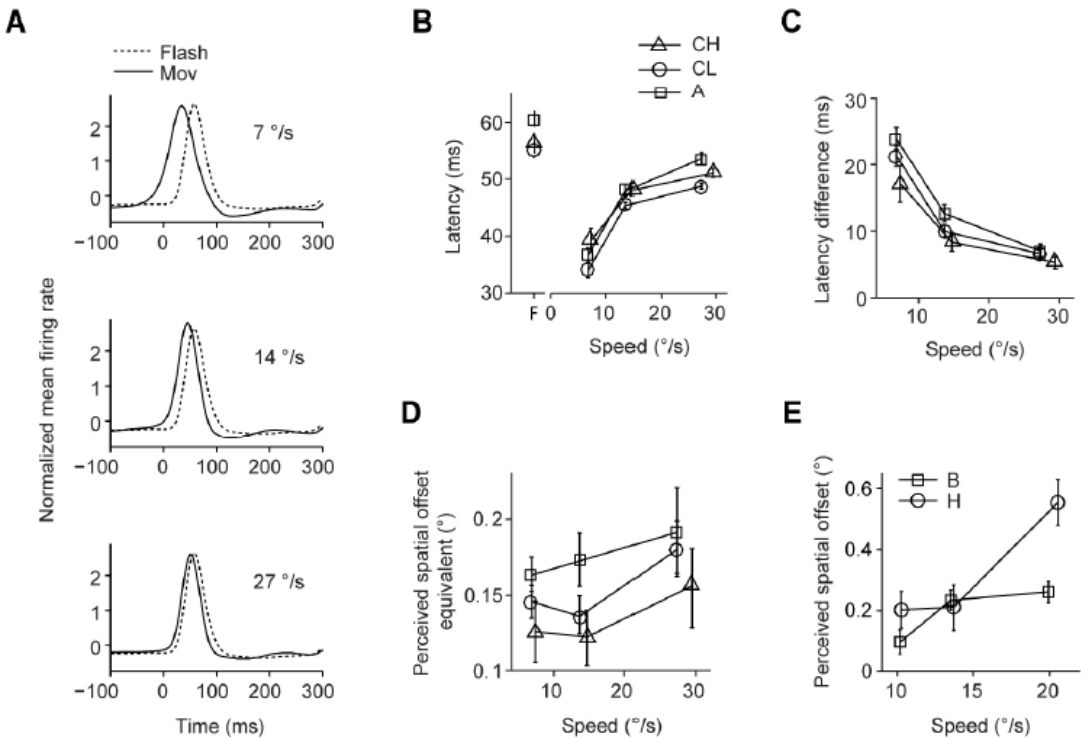

Figure 2.8: Speed dependence of the population response latencies. Figures A show the anticipatory effect in time : the response to a moving bar is shifted as compared to the response to a flashed bar. B. Response latency for the flashed bar (area F) and the moving bar. Latency increases with speed. C. Latency difference between the flashed and the moving bar. D. Spatial perceived offset computed from latencies shown in C plotted as a function of speed. E. Spatial perceived offset plotted as a function of speed. [57]

Chapter 3

Developing a 2D retina model

In this chapter, we will introduce the model that we have developed for anticipation in the retina. In particular, the model includes anisotropic spatio-temporal filtering at the level of bipolar cells, bipolar pooling at the level of ganglion cells and gain control at both levels. It also features amacrine connectivity circuit specific to differential motion sensitive ganglion cells [59] [6], and gap junction connectivity specific to direction selective ganglion cells [3].

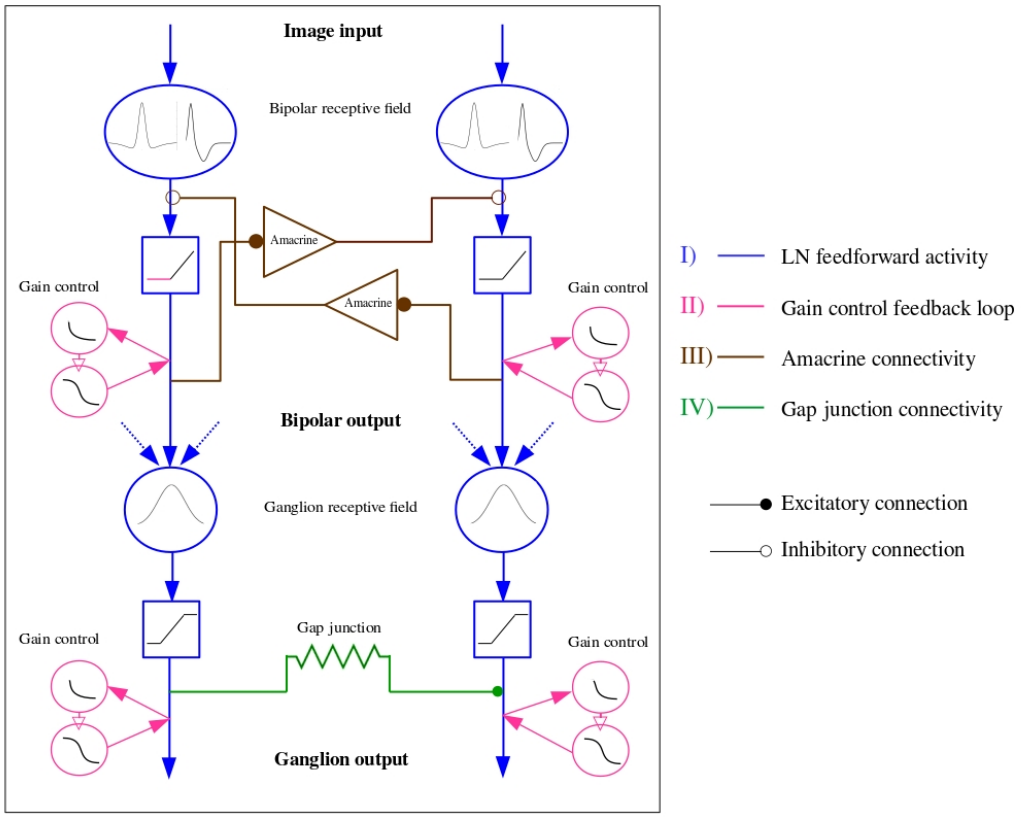

Figure 3.1: Summary of the retina model. Colors denote different processing pathways.

3.1 Retina organization

We assimilate the retina to a flat, two dimensional square of edge length L mm. Therefore, we do not integrate the 3 dimensional structure of the retina in the model, merely for mathematical convenience. Spatial coordinates are noted x, y.

Each cell population tiles the retina with a regular square lattice. The density of cells is therefore uniform for convenience but the extension to non uniform density is afforded by the model. For the population p we note δ_p the lattice spacing in mm, and N_p the total number of cells. Without loss of generality we assume that L, the retina's edge size, is a multiple of δ_p. We note $L_p = \frac{L}{\delta_p}$, the number of cells p per row or column so that $N_p = L_p^2$. Each cell in the population p has thus Cartesian coordinates $(x, y) = (i_x\delta_p, i_y\delta_p)$, $(i_x, i_y) \in \{ 1, \ldots, L_p \}^2$. To avoid multiples indices, we will often associate to each pair (i_x, i_y) a unique index $i = i_x + (i_y - 1) L_p$. The cell of population p, located at coordinates $(i_x\delta_p, i_y\delta_p)$ is then denoted by p_i. We note $d\left[p_i, {p'}_j \right]$ the Euclidean distance between p_i and ${p'}_j$.

We use the notation V_{p_i} for the membrane potential of cell p_i. Cells are coupled. The synaptic weight from cell ${p'}_j$ to cell p_i reads $W_{p_i}^{p_j}$. Thus, the pre-synaptic neuron is expressed in the upper index; the post-synaptic, in the lower index.

3.2 Bipolar cells layer

The model consists first of a set of N_B bipolar cells, regularly spaced by a distance δ_B, with spatial coordinates x_i, y_i, $i = 1 \ldots N$ coinciding with the center of their receptive field (RF).

3.2.1 Stimulus integration

The receptive field of bipolar cells is classically modeled by a difference of isotropic Gaussians. However, orientation selectivity, a mechanism first initiated at the level of the retina, is computed by different types of neurons, including bipolar cells. Antinucci et al. [60] have shown that a class of orientation selective amacrine cells, which modulate the BC output, are also able generate orientation tuning in their presynaptic terminals. A fraction of about 5% of bipolar cells is highly orientation selective. They are mainly tuned to cardinal directions and diagonal axes. As orientation selectivity is necessary to study the trajectories of objects in a two dimensional space, we consider

therefore BCs with oriented center-surround RFs. The kernel $\mathcal{K}_{B_i}(x, y, t)$, mathematically representing the RF of the bipolar cell i, is thus modeled with a difference of (non circular) Gaussians (DOG):

$$\mathcal{K}_{B_i,S}(x, y) = \frac{A_1}{2\pi\sqrt{\det C_1}}\, e^{-\frac{1}{2}\,\tilde{X}_i.C_1^{-1}.X_i} \;-\; \frac{A_2}{2\pi\sqrt{\det C_2}}\, e^{-\frac{1}{2}\,\tilde{X}_i.C_2^{-1}.X_i}, \tag{3.1}$$

where $X_i = \begin{pmatrix} x - x_i \\ y - y_i \end{pmatrix}$, $\tilde{}$ denotes the transpose, x_i and y_i are the coordinates of the receptive field center which coincide with the coordinates of the cell, C_1, C_2 are positive definite matrix whose main principal axis represent the preferred orientation.
The two Gaussians of the DOG are thus concentric and have the same principal axes. X_i has the physical dimension of a length (mm) thus the entries of $C_a, a = 1, 2$ are expressed in mm^2, as well as its eigenvalues $\lambda_{1,a}, \lambda_{2,a}$. $A_a, a = 1 \dots 2$ are dimensionless (so that the convolution (3.5) has the same dimension as $\mathcal{S}$).

We model the temporal part with a difference of non concentric Gaussians whose integral on the time domain is zero. This kernel well fits the shape of the temporal projection of the bipolar RF observed in experiments (Fig. 3.2).

$$\mathcal{K}_T(t) = \left(\frac{K_1}{\sqrt{2\pi}\sigma_1}\, e^{-\frac{(t-\mu_1)^2}{2\sigma_1^2}} \;-\; \frac{K_2}{\sqrt{2\pi}\sigma_2}\, e^{-\frac{(t-\mu_2)^2}{2\sigma_2^2}} \right) H(t) \tag{3.2}$$

where $H(t)$ is the Heaviside function. Note that μ_b, σ_b, $b = 1, 2$ have the dimension of a time (s) whereas K_b are dimensionless. These quantities must meet the following condition to ensure the continuity of $\mathcal{K}_T(t)$ at zero:

$$\frac{K_1}{\sigma_1} e^{-\frac{\mu_1^2}{2\sigma_1^2}} = \frac{K_2}{\sigma_2} e^{-\frac{\mu_2^2}{2\sigma_2^2}}. \tag{3.3}$$

Thus, $\mathcal{K}_{B_i}(x, y, 0) = 0$. In addition, we require that the integral of a constant stimulus converges to zero, so that the cell is only reactive to changes. This reads:

$$K_1\, \Pi\left(\frac{\mu_1}{\sigma_1}\right) = K_2\, \Pi\left(\frac{\mu_2}{\sigma_2}\right), \tag{3.4}$$

where Π is the repartition function of the standard Gaussian.

Note that we consider here only one family of bipolar cells. Thus, the constants $A_1, A_2, K_1, K_2, \sigma_1, \sigma_2, \mu_1, \mu_2$ and the covariance matrix C_a, $a = 1, 2$ defininig the receptive field do not depend on i. Only the center of the receptive field, with coordinates

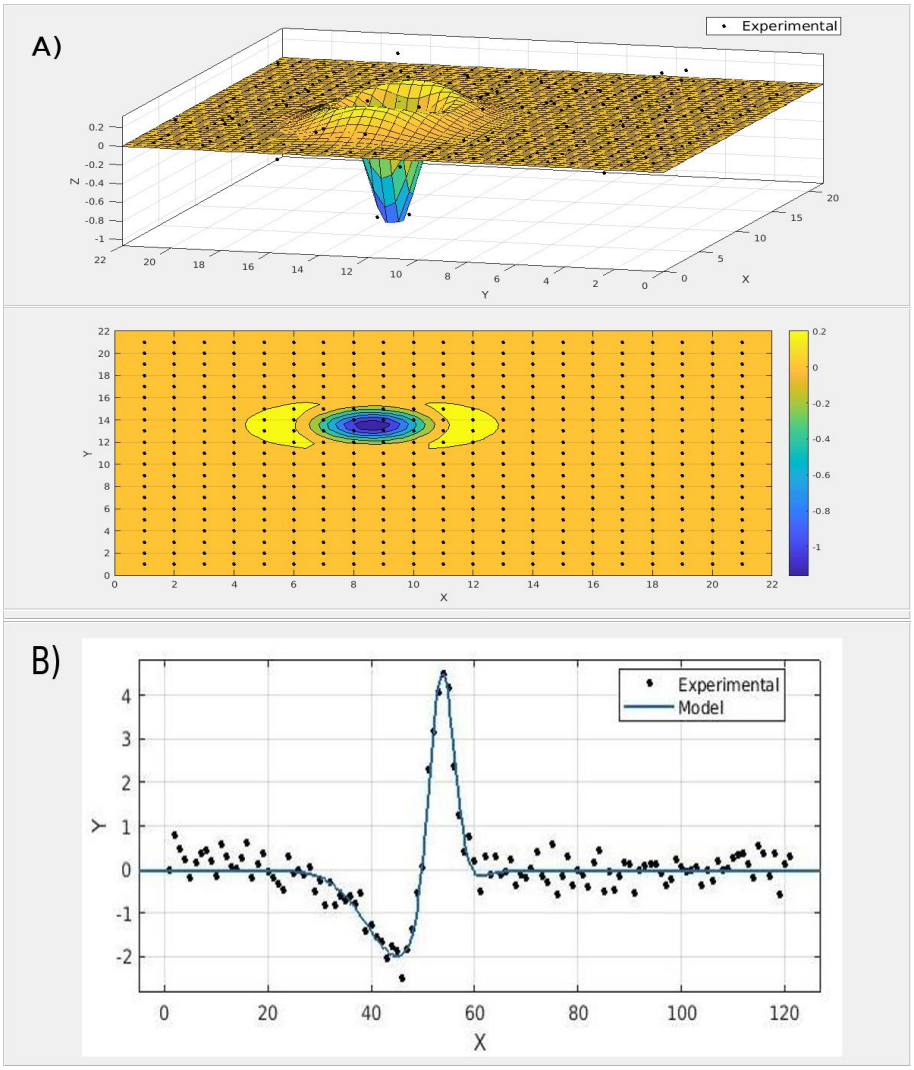

Figure 3.2: Bipolar receptive field of salamander retina obtained from Spike Triggered Average on experimental data (courtesy O. Marre). A) Spatial kernel. Up 3 dimensional view, bottom 2 dimensional projection in heat map. B) temporal kernel.

x_i, y_i, does.

Fig. 3.2 shows an example of the spatial and temporal projections of a receptive field of salamander retina, courtesy of Olivier Marre, fitted by the introduced spatial and temporal kernels.

3.2.1.1 Space-time convolution

The BCs' response is based, at first stage, on the convolution of the visual stimulus $\mathcal{S}(x, y, t)$ with the spatio-temporal receptive field:

$$\left[\mathcal{K}_{B_i} \overset{S,t}{*} \mathcal{S} \right] (t) \equiv V_{i_{drive}}(t). \tag{3.5}$$

Note that the exponential decay of the spatial and temporal part at infinity ensures the existence of the space-time integral. With choice of physical dimension for the constants defining the receptive field, the convolution has the same dimension as $\mathcal{S}$, which here is a voltage (mV).

It results from (3.3) that:

$$\frac{dV_{i_{drive}}}{dt} = \left[\mathcal{K}_{B_i} \overset{S,t}{*} \frac{d\mathcal{S}}{dt} \right](t) \tag{3.6}$$

The spatial integral $\int_{\mathbb{R}^2} \mathcal{K}_S(x,y)S(x,y,u)\,dx\,dy$ is numerically computed using error function in the case of circular RF, and a computer vision method from Geusenroek et al. [61] in the case of anisotropic RF, allowing to integrate generalized Gaussians with an efficient computational time.

3.2.1.2 Anisotropic filtering

For the sake of clarity we consider here the integration over a time interval where the stimulus is constant, and we restrict the computation to one Gaussian. The extension to a time-dependent stimulus and to difference of Gaussians is straightforward. In the following, we also consider a spatially discretized stimulus.

When dealing with a 2D stimulus, we have to integrate over two axis. In the case where the eigenvectors of the 2D of Gaussians are the axis of integration, the spatial filter is separable in the stimulus coordinate system. Considering the stimulus as a grid of pixels, we can integrate using the following discretization : let L_x be the size of the stimulus along the x axis in pixels, L_y its size along the y axis, and δ the pixel length. We set $S_{ij}(t) \equiv S(i\delta, j\delta, u)$, with $i = 0, \ldots, \frac{L_x}{\delta}$ and $j = 0, \ldots, \frac{L_y}{\delta}$. The spatial integration becomes then :

$$\begin{aligned} I(t) &= \frac{1}{2\pi\sigma_x\sigma_y} \int\int_{\mathbb{R}^2} S(x,y,u) e^{-\frac{(x-x_0)^2}{2\sigma_x^2} - \frac{(y-y_0)^2}{2\sigma_y^2}} dxdy \\ &= \sum_{i,j} S_{ij}(t) \left[erf(\frac{i+\delta-x_0}{\sqrt{2}\sigma_x}) - erf(\frac{i-x_0}{\sqrt{2}\sigma_x}) \right] \left[erf(\frac{j+\delta-y_0}{\sqrt{2}\sigma_y}) - erf(\frac{j-y_0}{\sqrt{2}\sigma_y}) \right] \end{aligned}$$

In the case where the eigenvectors of the 2D of Gaussians are the axes of integration, the spatial filter is not separable in the stimulus coordinates system.

There exists methods that perform the computation by making a linear combination

of basis filters [62], others that use Fourier based deconvolution techniques [63], and others using recursive filtering techniques [64]. However, these methods are of high computational complexity. We choose instead to use a computer vision method from Geusenroek et al. [61].

It is based on a projection in a non-orthogonal basis, where the first axis is x and the second is parametrized by a angle ϕ (see Fig. 3.3).

The new standard deviations read :

$$\sigma_{x'} = \frac{\sigma_x \sigma_y}{\sqrt{\sigma_x^2 \cos\theta^2 + \sigma_y^2 \sin\theta^2}}$$

$$\sigma_\phi = \frac{\sqrt{\sigma_y^2 \cos\theta^2 + \sigma_x^2 \sin\theta^2}}{\sin\phi}$$

with

$$\tan(\phi) = \frac{\sigma_y^2 \cos\theta^2 + \sigma_x^2 \sin\theta^2}{(\sigma_x^2 - \sigma_y^2)\cos\theta \sin\theta}$$

with $\sigma_x \neq \sigma_y$.

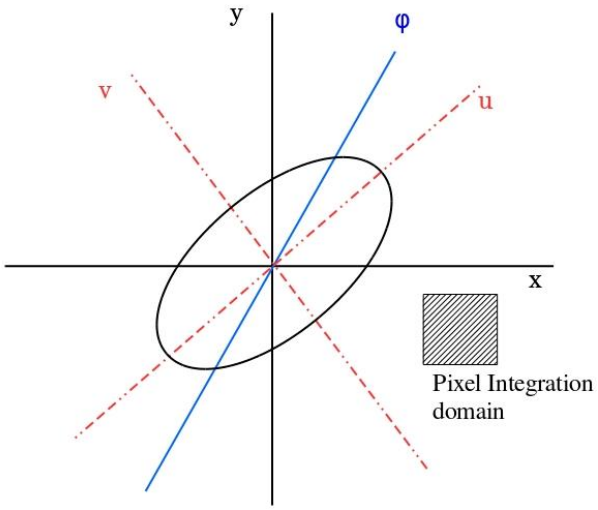

Figure 3.3: Filter transformation description. The integration domain is limited by four lines, the equations of which we can write in the new system of axes through a coordinate change..

We adapt the implementation to the spatially discretized stimulus, using an integration scheme similar to the one introduced earlier. The integral finally reads :

$$I = \sigma_{x'}\sqrt{\frac{\pi}{2}} \sum_{(i;j)\in[0,s_x]\times[0,s_y]} \int_{y\frac{\delta}{\sin(\phi)}}^{(y+1)\frac{\delta}{\sin(\phi)}} C_{ij} e^{\frac{(y'-y'_0)^2}{2\sigma_\phi^2}}$$

$$[erf(\frac{(-\cos(\phi)y' + x + 1)\delta - x'_0}{\sqrt{2}\sigma_{x'}}) - erf(\frac{(-\cos(\phi)y' + x)\delta - x'_0}{\sqrt{2}\sigma_{x'}})]dy'$$

Examples of tuning curves computed using this method are shown in fig. 3.4.

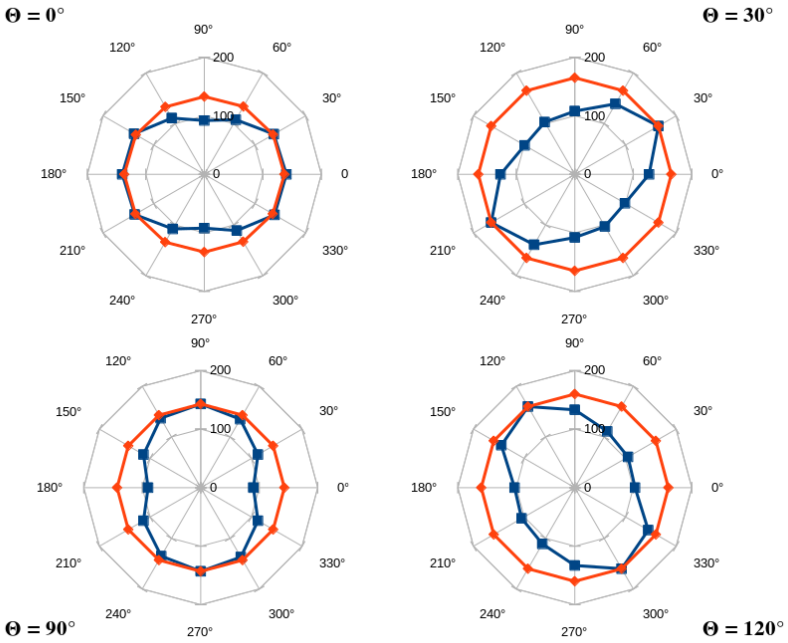

Figure 3.4: Tuning curves of simulated anisotropic bipolar cells. The stimulus consists of motionless bars with different orientations. Orange curve shows the maximum bipolar response to bars with different orientation, in the case of isotropic RF. The maximum is constant for all orientations. The blue curves show the maximum bipolar response in the case of anisotropic receptive field. Θ denotes the orientation of the receptive field. The peak of response is reached when the bar is in the preferred orientation.

3.2.2 Bipolar cells voltage

In our model, the bipolar cell voltage is the sum of the external drive (3.5) received by the bipolar cell and of a post synaptic potential P_{B_i} induced by connected amacrine cells:

$$V_{B_i}(t) = V_{i_{drive}}(t) + P_{B_i}(t). \tag{3.7}$$

The form of P_{B_i} is given by eq. (3.13) in the amacrine connectivity section.

$P_{B_i}(t) = 0$ in the gain control model where no amacrine cells are considered.

BCs have voltage thresholding:

$$\mathcal{N}_B(V_{B_i}) = \begin{cases} 0, & \text{if} \quad V_{B_i} \leq \theta_B; \\ V_{B_i} - \theta_B, & \text{else.} \end{cases} \tag{3.8}$$

Values of parameters are given in appendix.

3.2.3 Gain control

Bipolar cells have gain control, a desensitization when activated by a steady illumination. This desensitization is mediated by a rise in intracellular calcium Ca^{2+}, at the origin of a feedback inhibition preventing thus prolonged signalling of the ON bipolar cell [65] [2]. Following Chen et al., we introduce the dimensionless activity variable A_{B_i} obeying the differential equation:

$$\frac{dA_{B_i}}{dt} = -\frac{A_{B_i}}{\tau_a} + h\,\mathcal{N}(V_{B_i}(t)). \tag{3.9}$$

Assuming an initial condition $A_{B_i}(t_0) = 0$ at initial time t_0 the solution is:

$$A_{B_i}(t) = h \int_{t_0}^{t} e^{-\frac{t-s}{\tau_a}}\, \mathcal{N}(V_{B_i}(s))\, ds.$$

The bipolar output to amacrine and ganglion cells is then characterized by a non linear response to its voltage variation, given by :

$$R_{B_i} = \mathcal{N}_B\,(\,V_{B_i}\,)\;\mathcal{G}_B\,(\,A_{B_i}\,)\,. \tag{3.10}$$

where :

$$\mathcal{G}_B(A) = \begin{cases} 0, & \text{if } \; A \leq 0; \\ \frac{1}{1+A^6}, & \text{else.} \end{cases} \tag{3.11}$$

Note that R_{B_i} has the physical dimension of a voltage, whereas, from eq. 3.11, A is dimensionless. As a consequence, the parameter h in eq. 3.9 must be expressed in $ms^{-1}mV^{-1}$. The form (3.11) and its 6-th power are based on experimental fits made by Chen et al. Its form is shown in Fig. 4.1.

3.3 Amacrine cells layer

Amacrine cells play a central role in motion processing [59] [66] [67] [68]. In the model, we consider one family of amacrine cells involved in differential motion. Amacrine cells tile the retina with a lattice spacing δ_A. We index them with $j = 1 \dots N_A$.

3.3.0.1 Connections amacrines to bipolars

We consider here a simple model of amacrine cells. We assimilate them to passive cells (no active ionic channels) acting as a simple relay between bipolar cells. The amacrine cell A_j, connected to the bipolar cell B_i, induces on the latter the post synaptic potential :

$$P_{B_i}^{A_j}(t) = W_{B_i}^{A_j}(t) \int_{-\infty}^{t} \gamma_B(t-s)\, V_{A_j}(s) ds,$$

$$\gamma_B(t) = e^{-\frac{t}{\tau_B}} H(t), \tag{3.12}$$

where H is the Heaviside function that ensures causality. Thus, the post synaptic potential is the mere convolution of the presynaptic amacrine cell voltage, with an exponential α-profile [69]. In addition, we assume the propagation to be instantaneous.

Here, the synaptic weight $W_{B_i}^{A_j} < 0$ mimics the inhibitory connection from amacrine to bipolar (glycine or GABA) with the convention that $W_{B_i}^{A_j} = 0$ if there is no connection from A_j to B_i.

In general, several amacrine cells input the bipolar cell B_i giving a total PSP:

$$P_{B_i}(t) = \sum_{j=1}^{N_A} W_{B_i}^{A_j} \int_{-\infty}^{t} \gamma_B(t-s)\, V_{A_j}(s) ds. \tag{3.13}$$

3.3.1 Bipolar to amacrine cells connections

Conversely, the bipolar cell B_i connected to A_j induces on this cell a synaptic response characterized by a post-synaptic potential $P_{A_j}(t)$. We assume that amacrine cells are passive elements so that their voltage $V_{A_j}(t)$ is equal to this PSP. We have thus:

$$V_{A_j}(t) = \sum_{i=1}^{N_A} W_{A_j}^{B_i} \int_{-\infty}^{t} \gamma_A(t-s)\, R_{B_i}(s) ds, \tag{3.14}$$

with $\gamma_A(t) = e^{-\frac{t}{\tau_A}} H(t)$. Here $W_{A_j}^{B_i} > 0$ corresponding to the excitatory effect of bipolar cells on amacrine cells, through a glutamate release. Note that the voltage of the bipolar

cell is rectified and gain-controlled.

3.3.2 Dynamics

The coupled dynamics of Bipolar and Amacrine cells can be described by a dynamical system that we derive now.

Bipolar voltage. Differentiating (3.13) with respect to time gives:

$$\frac{dP_{B_i}}{dt} = -\frac{1}{\tau_B} P_{B_i} + \sum_{j=1}^{N_A} W_{B_i}^{A_j} V_{A_j},$$

while differentiating (3.7) with respect to time gives:

$$\frac{dV_{B_i}}{dt} = \frac{dV_{i_{drive}}}{dt} - \frac{1}{\tau_B} P_{B_i} + \sum_{j=1}^{N_A} W_{B_i}^{A_j} V_{A_j}$$

$$= \frac{dV_{i_{drive}}}{dt} - \frac{1}{\tau_B} \left(V_{B_i} - V_{i_{drive}} \right) + \sum_{j=1}^{N_A} W_{B_i}^{A_j} V_{A_j}.$$

Thus, introducing:

$$F_{B_i}(t) = \left[\mathcal{K}_{B_i} \overset{S,t}{*} \left(\frac{\mathcal{S}}{\tau_B} + \frac{d\mathcal{S}}{dt} \right) \right](t) = \frac{V_{i_{drive}}}{\tau_B} + \frac{dV_{i_{drive}}}{dt}, \tag{3.15}$$

we end up with the following equation for the bipolar voltage:

$$\frac{dV_{B_i}}{dt} = -\frac{1}{\tau_B} V_{B_i} + \sum_{j=1}^{N_A} W_{B_i}^{A_j} V_{A_j} + F_{B_i}(t). \tag{3.16}$$

where we have used (3.6).

This is a differential equation driven by the time dependent term F_{B_i} containing the stimulus and its time derivative. As an example let's consider an object moving with a speed $\vec{v}$ depending on time, thus with a non zero acceleration $\vec{\gamma} = \frac{d\vec{v}}{dt}$. This stimulus has the form $\mathcal{S}(t) = g\left(\vec{X} - \vec{v}(t)\, t \right)$, with $\vec{X} = \begin{pmatrix} x \\ y \end{pmatrix}$, so that $\frac{d\mathcal{S}}{dt} = -\vec{\nabla} g\left(\vec{X} - \vec{v}(t)\, t \right) . \left(\vec{v} + \vec{\gamma} t \right)$ where $\vec{\nabla}$ denotes the gradient. *Therefore, thanks to the eq.* (3.16)*, bipolar cells are sensitive to changes in directions.*

Note that this property is inherited from the simple, differential structure of the dy-

namics, the term $\frac{dV_{i_{drive}}}{dt}$ resulting from the differentiation of V_{B_i}. This term does not appear in the classical formulation (3.5) of the bipolar response, without amacrine connectivity.

Amacrine voltage Likewise, differentiating (3.14) gives:

$$\frac{dV_{A_j}}{dt} = -\frac{1}{\tau_A} V_{A_j}(t) + \sum_{i=1}^{N_A} W_{A_j}^{B_i} R_{B_i}(t). \tag{3.17}$$

Coupled dynamics. Eq. (3.9) (activity), (3.16) and (3.17) define a set of $2N_B + N_A$ differential equations, ruling the behavior of coupled bipolar and amacrine cells, under the drive of the stimulus, appearing in the term $F_{B_i}(t)$. We summarize the differential system here:

$$\begin{cases} \frac{dV_{B_i}}{dt} &= -\frac{1}{\tau_B} V_{B_i} + \sum_{j=1}^{N_A} W_{B_i}^{A_j} V_{A_j} + F_{B_i}(t), \\ \\ \frac{dV_{A_j}}{dt} &= -\frac{1}{\tau_A} V_{A_j}(t) + \sum_{i=1}^{N_A} W_{A_j}^{B_i} R_{B_i}(t), \\ \\ \frac{dA_{B_i}}{dt} &= -\frac{A_{B_i}}{\tau_a} + h\,\mathcal{N}(V_{B_i}(t)). \end{cases} \tag{3.18}$$

Note that bipolar cells act on amacrine cells via a rectified voltage (gain control and piecewise linear rectification), in agreement with fig. 3.1, pathway III.

3.3.3 Probabilistic model of amacrine connectivity

We developed a geometric connectivity model defined as follows : each cell has a given number of branches, each of which has a given length and angle. When two branches of two different cells intersect (i.e one bipolar and one amacrine cell), the two neurons are said to be connected. The lengths follow an exponential distribution:

$$f_L(l) = \frac{1}{\xi} e^{\frac{-l}{\xi}}$$

with a spatial scale ξ, favoring thus short range connections. The number of branches distribution is exponential too. The angle distribution is taken to be isotropic in the plane, i.e. uniform on $[0, 2\pi[$. We derive the condition that two neurons are connected. Let us consider two neurons each having one branch of respective length A and B, forming respectively the angle α, β with the horizontal axis. (see Fig. 3.5) The distance

$dist$ between the two cells is computed using their Cartesian coordinates. Using the sine rule, the cells are connected if and only if :

$$dist \leq A\frac{sin(\beta - \alpha)}{sin(\beta + \theta - \alpha)}$$

$$dist \leq B\frac{sin(\beta - \alpha)}{sin(\theta)}$$

Given a random variable X, we note f_X its probability distribution function and F_X its cumulative function. We note $dist$ the Euclidean distance between neurons 1 and 2.

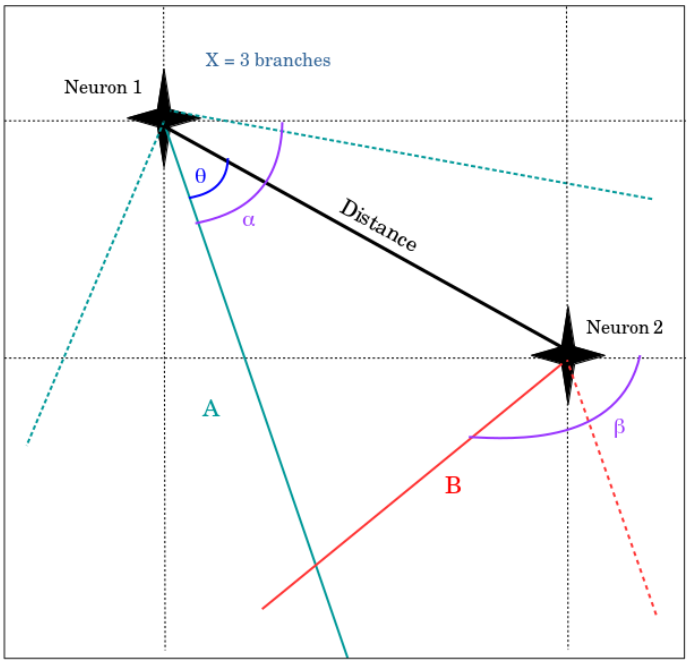

Figure 3.5: Geometrical description to compute the probability of connection between 2 neurons.

Let us first start by characterizing the probability distribution of $\beta - \alpha$. Under the assumption of convergence, the probability distribution of the sum of two random variables is given by the convolution product of their probability density functions. It follows that :

$$f_{\beta-\alpha}(x) = \int_{-\infty}^{+\infty} f_{-\alpha}(x) f_{\beta}(x-y)dy = \frac{1}{2\pi}\int_{x}^{x+2\pi} f_{\beta}(u)du$$

$$= \begin{cases} 0 & \text{if} x \in [-\infty, -2\pi] or x \in [2\pi, \infty], \\ \frac{1}{(2\pi)^2}(2\pi + x) & \text{if } x \in [-2\pi, 0], \\ \frac{1}{(2\pi)^2}(2\pi - x) & \text{if } x \in [0, 2\pi]. \end{cases} \tag{3.19}$$

We now characterize the probability distribution of $sin(\beta - \alpha)$.
The variable $X = \beta - \alpha$ evolves in the interval $[-2\pi, 2\pi]$. If $y \in [0, 1]$, the equation $sin(x) = y$ admits four solutions : $x = -2\pi + arcsin(y)$, $-\pi - arcsin(y)$, $arcsin(y)$, $\pi - arcsin(y)$, and $|dsin(x)/dx| = |cos(x)| = \frac{1}{\sqrt{1-x^2}}$, $\forall x$ in the solution set. We use variable change in the case of a non monotonous function Y = g(X). The probability density function of Y as a function of the one of X is given by :

$$f_Y(y) = \sum_{k, x_k = g^{-1}(y)} \frac{f_X(x_k)}{|dg/dx|} \tag{3.20}$$

Consequently, the probability density function of $Y = sin(\beta - \alpha)$ when $y \in [0, 1]$ reads :

$$\begin{aligned} f_Y(y) = \frac{1}{\sqrt{1-x^2}}[&f_{\beta-\alpha}(-2\pi + \arcsin y) + f_{\beta-\alpha}(-\pi - \arcsin y) + \\ &f_{\beta-\alpha}(\arcsin y) + f_{\beta-\alpha}(\pi - \arcsin y)] \\ &= \frac{1}{\pi\sqrt{1-x^2}} \end{aligned} \tag{3.21}$$

If $y \in [-1, 0]$, the equation $sin(x) = y$ admits four solutions : $x = -\pi - arcsin(y)$, $arcsin(y)$, $\pi - arcsin(y)$, $2\pi + arcsin(y)$, and similarly, $|dsin(x)/dx| = |cos(x)| = \frac{1}{\sqrt{1-x^2}}$, $\forall x$ in this solution set.

The probability density function of $Y = sin(\beta - \alpha)$, when $y \in [-1, 0]$, is then given by the same function as when $y \in [0, 1]$.

Normalization check:

$$\int_{-1}^{1} \frac{1}{\pi\sqrt{1-x^2}} dx = \left[\frac{arcsin(x)}{\pi}\right]_{-1}^{1} = 1$$

Let's now derive the probability distribution of $\beta - \alpha + \theta$, with θ a constant parameter defined by the position of neurons 1 and 2, in $[0, \pi]$. Through a simple change of variable, the density function of $\beta - \alpha + \theta$ is defined on $[-2\pi + \theta, 2\pi + \theta]$ by :

$$f_{\beta-\alpha+\theta}(x) = \begin{cases} 0 & \text{if} x \in [-\infty, -2\pi + \theta] or x \in [2\pi + \theta, \infty], \\ \frac{1}{(2\pi)^2}(2\pi + x - \theta) & \text{if } x \in [-2\pi + \theta, 0], \\ \frac{1}{(2\pi)^2}(2\pi - x + \theta) & \text{if } x \in [0, 2\pi + \theta]. \end{cases} \tag{3.22}$$

This function is non continuous in 0. However, given that its support has the same size as the support of $f_{\beta-\alpha}\ (4\pi)$, and given the periodicity of the sine function, the probability density function of $sin(\beta - \alpha + \theta)$ is identical to the one of $sin(\beta - \alpha)$.

Let $Y = sin(\beta - \alpha)$ and $Z = sin(\beta - \alpha + \theta)$. We want now to compute the density function of $\frac{Y}{Z}$. There is no straight forward way to compute the density of a ratio of two random variables. We will hence use the cumulative function in order to characterize this ratio. Let $\mathcal{D}$ the integration domain. We have then :

$$\begin{aligned} P(\frac{Y}{Z} \leq c) &= P(Y \leq cZ) \\ &= \int_{\mathcal{D}} f_X(a) f_Z(b) da db \end{aligned}$$

The evaluation of this integral depends on the value of c. When $0 \leq c \leq 1$:

$$\begin{aligned} P(\frac{Y}{Z} \leq c) &= \frac{1}{\pi^2} \int_{-1}^{1} \frac{1}{\sqrt{1-a^2}} \left(\int_{ca}^{1} \frac{1}{\sqrt{1-b^2}} db \right) da \\ &= \frac{1}{\pi^2} \int_{-1}^{1} \frac{1}{\sqrt{1-a^2}} (arcsin(ca) + \frac{\pi}{2}) da \end{aligned} \tag{3.23}$$

The function $\frac{(arcsin(ca)}{\sqrt{1-a^2}\pi}$ is odd, its integral on [-1,1] is null. It follows that :

$$P(\frac{Y}{Z} \leq c) = \int_{-1}^{1} \frac{\frac{\pi}{2}}{\sqrt{1-a^2}\pi}) da = \frac{1}{2} \tag{3.24}$$

Similarly, when $-1 \leq c \leq 0$, the probability is given by :

$$
\begin{aligned}
P(\frac{Y}{Z} \leq c) &= 1 - P(\frac{Y}{Z} \geq c) \\
&= 1 - \int_{-1}^{1} \frac{1}{\sqrt{1-a^2}\pi} \left(\int_{ca}^{1} \frac{1}{\sqrt{1-b^2}\pi} db \right) da \\
&= \frac{1}{2}
\end{aligned} \tag{3.25}
$$

When $c \geq 1$:

$$
\begin{aligned}
P(\frac{Y}{Z} \leq c) &= \int_{-1}^{1} \frac{\frac{\pi}{2}}{\sqrt{1-a^2}\pi}) da \\
&= 1 - \frac{1}{\pi^2} \int_{-1}^{1} \frac{1}{\sqrt{1-a^2}} (arcsin(ca) + \frac{\pi}{2}) da
\end{aligned} \tag{3.26}
$$

We restrict the integration domain to $[-\frac{1}{c}, \frac{1}{c}]$, where $arcsin(ca)$ is defined. Therefore :

$$
\begin{aligned}
P(\frac{Y}{Z} \leq c) &= 1 - \frac{1}{\pi^2} \int_{-\frac{1}{c}}^{\frac{1}{c}} \frac{1}{\sqrt{1-a^2}} (arcsin(ca) + \frac{\pi}{2}) da \\
&= 1 - \frac{1}{\pi} asin(\frac{1}{c})
\end{aligned} \tag{3.27}
$$

Similarly, when $c \leq -1$:

$$
\begin{aligned}
P(\frac{Y}{Z} \leq c) &= \frac{1}{\pi^2} \int_{\frac{1}{c}}^{-\frac{1}{c}} \frac{1}{\sqrt{1-a^2}} (arcsin(ca) + \frac{\pi}{2}) da \\
&= -\frac{1}{\pi} asin(\frac{1}{c})
\end{aligned} \tag{3.28}
$$

The probability density function describing $\frac{Y}{Z}$ reads :

$$
f_{\frac{Y}{Z}}(x) = \begin{cases} 0 & \text{if} x \in [-1, 1] \\ \frac{1}{\pi\sqrt{x^4 - x^2}} & \text{if } x \in [-\infty, -1] or \in [1, +\infty]. \end{cases} \tag{3.29}
$$

Normalisation check : we use the symmetry of the function, and the Gradshteyn table of integrals in order to compute the following :

$$\int_{-\infty}^{\infty} f_{\frac{Y}{Z}}(x) = 2\int_{0}^{\infty} \frac{1}{\pi\sqrt{x^4 - x^2}} = 1$$

We characterize the probability density function of $A.\frac{X}{Y}$, using the derivation of the probability distribution a product of two independent random variables. Hence, in the case of our problem, we have :

$$\begin{aligned} f_{A.\frac{X}{Y}}(z) &= \int_{-\infty}^{\infty} f_A(x) f_{\frac{X}{Y}}\left(\frac{z}{x}\right)\frac{1}{|x|}dx \\ &= \int_{-\infty}^{-1} \frac{\xi exp(-\xi x)}{|x|}\frac{1}{\pi\sqrt{\left(\frac{z}{x}\right)^4 - \left(\frac{z}{x}\right)^2}} + \int_{dx}^{\infty} \frac{\xi exp(-\xi x)}{|x|}\frac{dx}{\pi\sqrt{\left(\frac{z}{x}\right)^4 - \left(\frac{z}{x}\right)^2}} \\ &= \int_{-\infty}^{-1} -\frac{\xi exp(-\xi x)x}{\pi\sqrt{z^4 - (z.x)^2}}dx + \int_{1}^{\infty} \frac{\xi exp(-\xi x)x}{\pi\sqrt{z^4 - (z.x)^2}}dx \end{aligned} \tag{3.30}$$

If $z \geq 1$, for to integrand to be defined, we need to restrict the integration limits of the left integral to $[-z, -1]$, and to $[1, z]$ for the right integral. In this case :

$$f_{A.\frac{X}{Y}}(z) = \int_{-z}^{-1} -\frac{\xi exp(-\xi x)x}{\pi z\sqrt{z^2 - x^2}}dx + \int_{1}^{z} \frac{\xi exp(-\xi x)x}{\pi z\sqrt{z^2 - x^2}}dx \tag{3.31}$$

Similarly, if $z \leq 1$, the density function reads :

$$f_{A.\frac{X}{Y}}(z) = \int_{z}^{-1} \frac{\xi exp(-\xi x)x}{\pi z\sqrt{z^2 - x^2}}dx + \int_{1}^{-z} -\frac{\xi exp(-\xi x)x}{\pi z\sqrt{z^2 - x^2}}dx \tag{3.32}$$

It is not straightforward to compute analytically these integrals. In the case the integral has a positive support, it can be done using modified Bessel and Sturve functions (from the Gradshteyn table). The left hand integral then reads :

$$\begin{aligned} \int_{1}^{z} \frac{\xi exp(-\xi x)x}{\pi z\sqrt{z^2 - x^2}}dx &= \frac{\xi}{\pi z}\left[\int_{0}^{z} \frac{exp(-\xi x)x}{\sqrt{z^2 - x^2}}dx - \int_{0}^{1} \frac{exp(-\xi x)x}{\sqrt{z^2 - x^2}}dx\right] \\ &= \frac{\xi}{z2}(z-1)\left[L_1(\xi z) - I_1(\xi z)\right] + z - 1 \end{aligned} \tag{3.33}$$

where L_1 is the modified Sturve function of the first order, I_1 is the modified Bessel function of the first order.

We were unsuccessful in computing the integral on the right hand side.

The last probability density function we need to compute is the one of $B\sin(\beta - \alpha) = B.X$. Using the product rule we have :

$$\begin{aligned} f_{B.X}(z) &= \int_{-\infty}^{\infty} f_B(x) f_X\left(\frac{z}{x}\right) \frac{1}{|x|} dx \\ &= \int_{-1}^{-1} \frac{\xi exp(-\xi x)}{|x|} \frac{1}{\pi\sqrt{1-\left(\frac{z}{x}\right)}} \\ &= \int_{-1}^{-1} \frac{\xi exp(-\xi x)}{\pi\sqrt{x^2-1}} \end{aligned} \tag{3.34}$$

Once again, we were unsuccessful in computing the explicit form of this integral.

Conclusion

Given the two conditions required to have a connection :

$$dist \leq A\frac{sin(\beta-\alpha)}{sin(\beta+\theta-\alpha)}$$

$$distsin(\theta) \leq Bsin(\beta-\alpha)$$

we wanted to characterize the probability distribution of $A\frac{sin(\beta-\alpha)}{sin(\beta+\theta-\alpha)}$ and $Bsin(\beta-\alpha)$, to speed up the process of generating the adjacency matrix : instead of drawing 4 random variables (A, B, α and β), we would only have to draw two random variables ($A\frac{sin(\beta-\alpha)}{sin(\beta+\theta-\alpha)}$ and $Bsin(\beta-\alpha)$).

We were able to derive the integral form of these two probability distributions. However, we couldn't compute the explicit result of this integral.

In terms of implementation, in order to draw random numbers from $f_{B.X}(x)$ and $f_{A.\frac{X}{Y}}(x)$, since $F_{B.X}$ and $F_{A.\frac{X}{Y}}$ cannot be computed and neither can $F^{-1}_{B.X}$ and $F^{-1}_{A.\frac{X}{Y}}$, we cannot use the inversion sampling[1]. We have then to implement rejection sampling which is highly consuming in terms of computational time, and gives only approximate results. Consequently, we choose in the following Chapter to implement the straightforward way to compute the adjacency matrix, because it is more tractable computationally.

[1]Inversion sampling consists in drawing a random number u from the uniform distribution $\mathcal{U}[0,1]$, and get the corresponding number from the considered distribution F using $x = F^{-1}u$

3.4 Ganglion cells

There are many different types of ganglion cells in the retina, with different physiologies and functions [9] [70]. In the present computational study we focus on specific subtypes associated to the pathways I (Fast OFF cells), II (Direction selective cells), III (Differential Motion Sensitive cells) in Fig. 3.1. All these have common features: Bipolar cells pooling and Gain control.

3.4.1 Bipolar cells pooling

In the retina, ganglion cells of the same type cover with a constant density the surface, forming a mosaic. The degree of overlap between ganglion cells indicates the extent to which their dendritic arbors are intricated in one another. This overlap remains however very limited between cells of the same type [71]. We note k the index of the ganglion cells, $k = 1 \dots N_G$ and δ_G the spacing between two consecutive ganglion cells lying on the grid.

In the model, ganglion cell k pools over the output of bipolar cells in its neighbourhood. Its voltage, V_{G_k}, reads:

$$V_{G_k} = \sum_i W_{G_k}^{B_i} R_{B_i} \tag{3.35}$$

where $W_{G_k}^{B_i}$ is Gaussian with amplitude a and standard deviation c :

$$W_{G_k}^{B_i} = a\, e^{-\frac{d^2[B_i, G_k]}{2\,c^2}}. \tag{3.36}$$

where c has the dimension of a distance and a is dimensionless.

3.4.2 Ganglion cells response

The voltage V_{G_k} in eq. (3.35) is processed through a gain control loop similar to the bipolar layer. As ganglion cells are spiking cells, a non-linearity is fixed so as to impose an upper limit over the firing rate. Here, it is modeled by a piecewise linear

function :

$$\mathcal{N}_G\,(\,V\,) = \begin{cases} 0, & \text{if} \quad V \leq 0; \\ \alpha_G(V - \theta_G), & \text{if} \quad \theta_G \leq V \leq N_G^{max}/\alpha_G + \theta_G; \\ N_G^{max}, & \text{else.} \end{cases} \tag{3.37}$$

This function corresponds to a probability of firing in a time interval. Thus, it is expressed in (Hz). Consequently, α_G is expressed in ($Hzmv^{-1}$ and N_G^{max}) in (Hz). Parameters values can be found in the appendix.

Gain control is implemented with an activation function A_{G_k}, solving the following differential equation:

$$\frac{dA_{G_k}}{dt} = -\frac{A_{G_k}}{\tau_G} + h_G\,\mathcal{N}_G\,(\,V_{G_k}\,)\,, \tag{3.38}$$

and a gain function :

$$\mathcal{G}_G(A) = \begin{cases} 0, & \text{if} \quad A \leq 0; \\ \frac{1}{1+A}, & \text{else.} \end{cases} \tag{3.39}$$

Note that the origin this gain control is different from the bipolar gain control (3.11). Indeed, Chen et al. hypothesize that the biophysical mechanisms that could lie behind ganglion gain control are spike-dependent inactivation of Na^+ and K^+ channels, while the study by Jacoby et al. [72] hypothesize that ganglion cells gain control is mediated by feed-forward inhibition that they receive from amacrine cells.

Finally, the response function (firing rate) of this ganglion cell type is:

$$R_G\,(\,V_{G_k}, A_{G_k}\,) = \mathcal{N}_G(V_{G_k})\,\mathcal{G}_G(A_{G_k}). \tag{3.40}$$

3.4.3 Fast OFF cells

The model integrates a ganglion cell layer of fast OFF cells, that have been shown to account for anticipatory effects in the retina [1][2]. They correspond to the pathway I in Fig. 3.1 and they are not coupled. The firing rates of these cells show a shift in the peak response in the case of smooth motion, as compared to a flashed bar response (see Fig 3.6).

Fast OFF ganglion cells tile the retina with a mean distance of about $\delta_{G_F} = 50\,\mu m$; their receptive field extend to $\Sigma_{G_F} = 300\mu m$, thus, each RF overlaps with about $\frac{\Sigma_g^2}{\delta_{G_F}^2} = 36$

RFs of the same cell type [73].

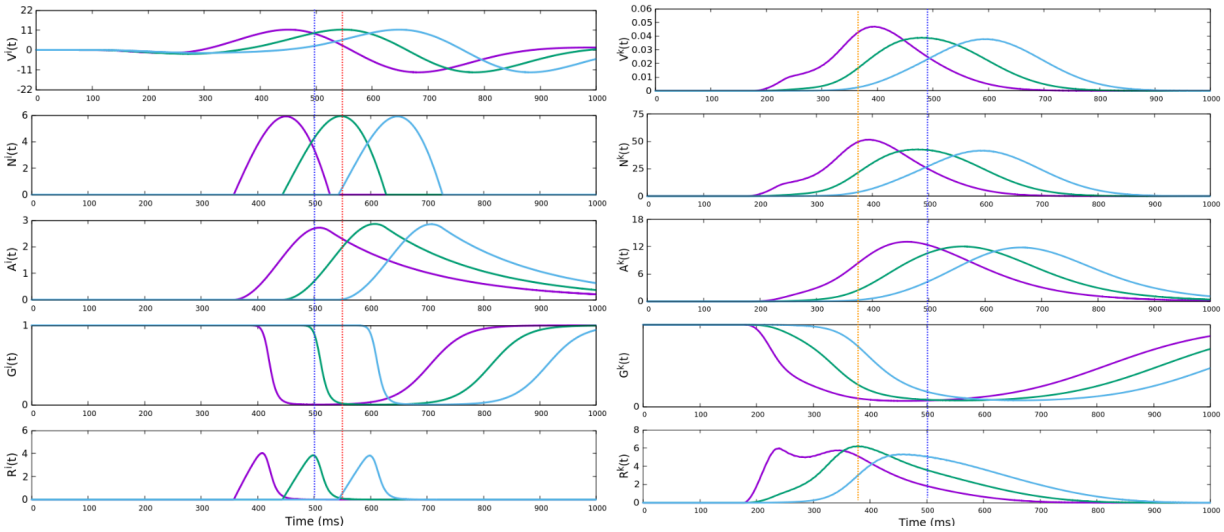

Figure 3.6: Bipolar (left) and ganglion (right) cells layers responding to a bar in smooth motion. The curves show the response of three cells lying on the trajectory, distanced by 150 μm. Colors denote cells lying on the same coordinates. The bar spans over the entire receptive fields of bipolar cells. The peak response is first shifted thanks to the bipolar gain control, and is further shifted with the ganglion gain control. Anticipation as it is defined in the text is the temporal delay between the red vertical line (peak of the linear bipolar response of the green cell) and the orange line (firing rate peak of the ganglion cell lying at the same coordinates).

3.4.3.1 Response of Fast OFF cells to motion onset

When the stimulus is a bar that appears, stays motionless and there starts translating, fast off ganglion cells demonstrate a salient activity to first the appearance and then the start of motion. The level of this activity is generally higher that the response elicited by smooth motion. The gain control model accounts for this effect, ranking the level of activity from the highest to the lowest : object appearance, motion onset, and smooth motion. This effect has an important functional purpose, denoting the detection of a possible obstacle and alerting on the danger raised by its start of motion.

3.4.3.2 Response of Fast OFF cells to motion reversal

Ganglion cells of different type have been shown to be responsive to motion reversal, firing a transient burst of firing $\tilde{2}50$ ms after reversal [74]. Chen et al. have identified and classified ganglion cell populations responsive to reversal in the salamander retina and they found that a significant proportion of cells belonged to the fast OFF cell type (45% of fast OFF are reversal responsive, wheareas only 24% of medium

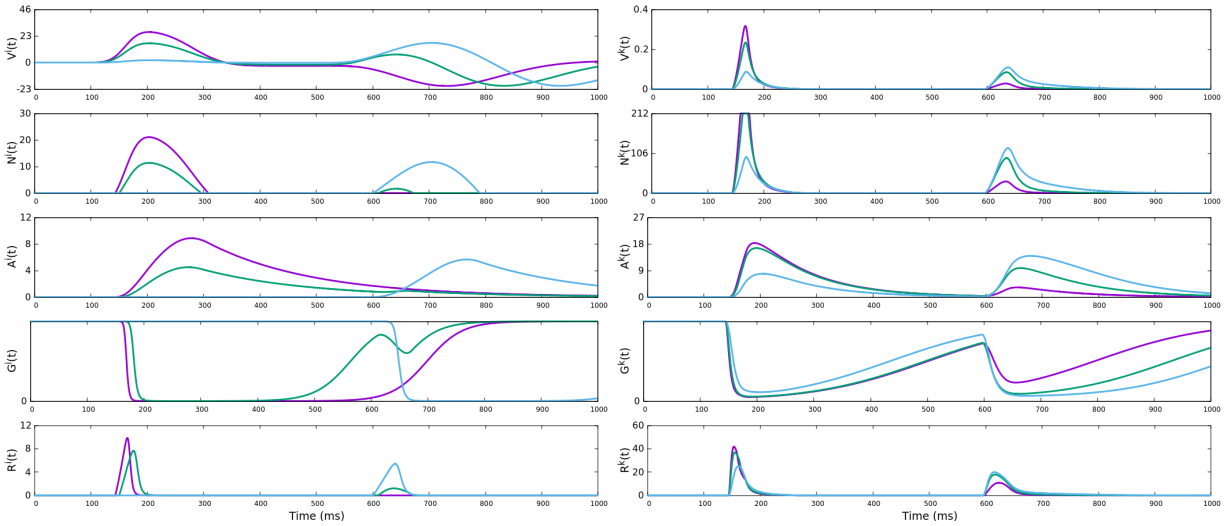

Figure 3.7: Bipolar (left) and ganglion (right) cells layers responding to the appearance of the bar and motion onset. The bar appears at t=100 ms and starts moving at t=500 ms. The curves show the response of three cells lying on the trajectory, distanced by 150 μm. Colors denote cells lying on the same coordinates. The response to the appearance of the bar is more salient than the response to the motion onset, which in turn is more salient than the response to the moving bar..

OFF and 20% of fast ON are). The stimulus type seems also to play a crucial role in the reversal responsiveness, whether it is dark or bright, a translating bar or a moving edge. Consistent with the results we showed and the structure of our model, we chose to restrict our simulation to a moving dark bar, and to fast OFF ganglion cells. It should be noted however, that in order for the gain control model to accurately reproduce motion reversal, one has also to add ON bipolar, which will generate the second peak of activity when the bar changes its motion orientation.

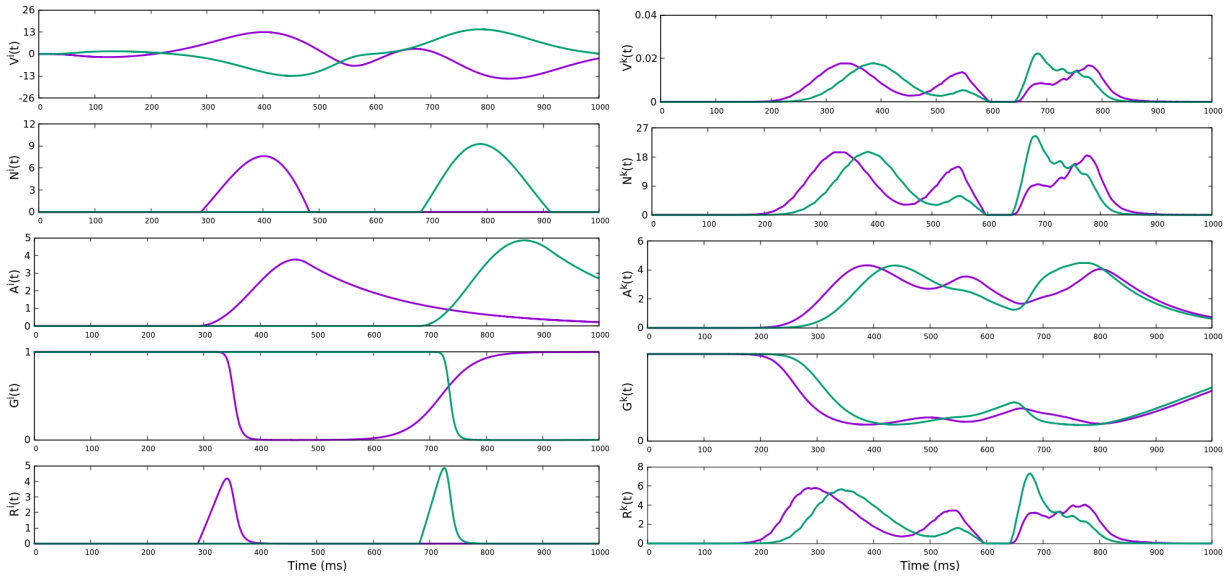

Figure 3.8: Simulation results of the bipolar (left) and the ganglion (right) cells layers responding to motion reversal. The bar changes its motion orientation at t=500 ms. In the bipolar layer, the purple curve is the response of an OFF bipolar cell, and the green curve is the response a neighbouring ON bipolar cell. In the ganglion cell layer, the curves show the response of two cells lying on the trajectory, distanced by 150 μm.

3.4.4 Direction selective ganglion cells and gap junctions connectivity

These cells correspond to the pathway II in Fig. 3.1. They are only coupled via electric synapses (gap junctions). In several animals, like the mouse, this enables the corresponding ganglion cells to be direction sensitive. Note that other mechanisms, involving lateral inhibition via Starburst Amacrine Cells have also been widely reported [15] [75] [76] [77] [67] [68] [78]. Here we focus on gap junctions direction sensitive cells, responsible of lag normalization, following Tredholm et al.

There exist four major types of these DSGCs, each responding to edges moving in one of the four cardinal directions. Trenhlom et al. [3] have emphasized the role of these cells coupling in lag normalization: uncoupled cells begin responding when a bar enters their receptive field, i.e, their dentritic field extension, whereas coupled cells start responding *before* the bar reaches their dendritic field. This anticipated response is due to the effective propagation of activity from neighboring cells through gap junctions, and is particularly interesting when comparing the responses for different velocities of the bar. Trenhlom et al. have shown that the uncoupled DSGCs detect the bar at a position which is further shifted as the velocity grows, while coupled cells respond at an almost constant position, regardless of the velocity. In our work, we show that

temporally, this spatial lag normalization induces a motion extrapolation that confers to the retina more than just the ability to compensate for processing delays. Indeed, the anticipated activity is all the more important because it has a predictive aspect to it.

Note that there is one cell type per preferred direction. We consider here only one such direction in the model description to avoid heavy notations. We note G_D this cell type (instead of G_{D_d} where $d = 1, \dots 4$ would be one of the cardinal direction). Along this direction, there is a cell ordering denoted by an index $k_D = 1 \dots N_D$. The voltage of ganglion cell $V_{G_{Dk_D}}$ is now:

$$V_{G_k}^{in}(t) = \sum_i W_{G_k}^{B_i} R_{B_i}(t) \tag{3.41}$$

Classical, symmetric bidirectional gap junctions coupling between neighbouring cells would involve a current of the form $-g(V_{G_k} - V_{G_{k-1}}) - g(V_{G_k} - V_{G_{k+1}})$ where g is the gap junction conductance. In contrast, here, the current takes the form $-g(V_{G_k} - V_{G_{k-1}})$. This is due to the specific asymmetric structure of the direction selective ganglion cell dendritic tree [3]. This induces a strong difference in the propagation of a perturbation. Indeed, consider the case $V_{G_k} - V_{G_{k-1}} = V_{G_k} - V_{G_{k+1}} = \delta$. In the symmetric form the total current vanishes whereas in the asymmetric form the current is $-g\delta$. Still, the current can have both direction depending on the sign of δ.
The main consequence in terms of propagation of a perturbation is that direction sensitive gap junctions induces a ballistic motion (displacement is proportional to t) whereas classical symmetric coupling induces a diffusive motion (displacement is proportional to $\sqrt{t}$).

In our model ganglion cells are gain-controlled. Gain control can take place before or after the effect of gap junctions. We were not able to find in the biophysical literature which option is the more plausible so we considered the two of them. In the first case the voltage of G_k obeys :

$$V_{G_k}(t) = V_{G_k}^{in} - \frac{g}{C} \int_{-\infty}^{t} (V_{G_k}(s) - V_{G_{k-1}}(s)) ds$$

Deriving the previous equation, we get the following differential equation gov-

erning the ganglion cell voltage :

$$\frac{dV_{G_k}}{dt} = \frac{dV_{G_k}^{in}}{dt} - w_{gap}\ \left[\, V_{G_k}(t) - V_{G_{k-1}}(t) \,\right] \tag{3.42}$$

where $w_{gap} = \frac{g}{C}$, and the V_k voltage is then rectified by gain control.

In the second case the voltage of G_k obeys:

$$\frac{dV_{G_k}}{dt} = \frac{dV_{G_k}^{in}}{dt} - w_{gap}\ \left[\, R_G\left(V_{G_k}, A_{G_k}\right)(t) - R_G\left(V_{G_{k-1}}, A_{G_{k-1}}\right)(t) \,\right] \tag{3.43}$$

where $R_{G_k}\left(V_{G_k}, A_{G_k}\right)$ is given by (3.40).

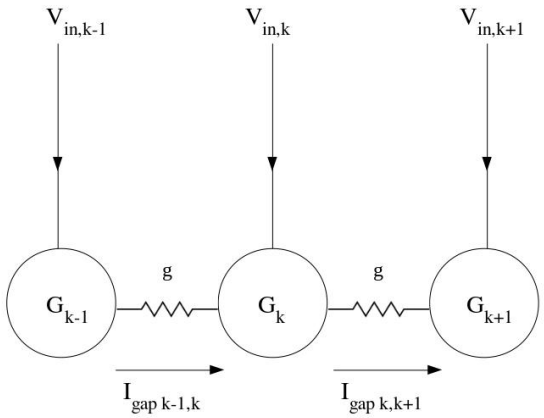

Figure 3.9: Schematic of the gap junction connectivity. A ganglion cell is coupled to its surrounding cells, in the direction of motion.

Note that these two equations takes a different from as Trendholm et. al (expressed in terms of currents), because we had to adapt it so as to match the voltage form (3.41). Still, our model reproduces the main feature of Trendholm et. al: lag normalization, as shown in Fig. 3.10 : Trendholm et. al have indeed developed a current-based model of DSGCs, able to reproduce lag normalization : coupled cells elicit an early response to a moving bar, resulting in a space normalization independent of the speed of the bar. In other words, the response of cells near the start of motion starts arising when the bar is at a given distance from their soma, which grows with the speed of the bar, while the activity of cells sufficiently far from the start of motion starts rising when the bar a quasi constant position from their soma.

We test the ability of our voltage-based approach to reproduce lag normalization re-

sults from the same ranges of speed. In our simulation setting, we don't include gain control, both at the level of bipolar and ganglion cells. The aim at this point is to find the range of coupling strength values where we are able to reproduce lag normalization results without gain control. It should be noted here that the coupling strength of our voltage based model and the α parameter of Trendholm model are not equivalent, the latter is unit-less while w_{gap} is in ms^{-1}.

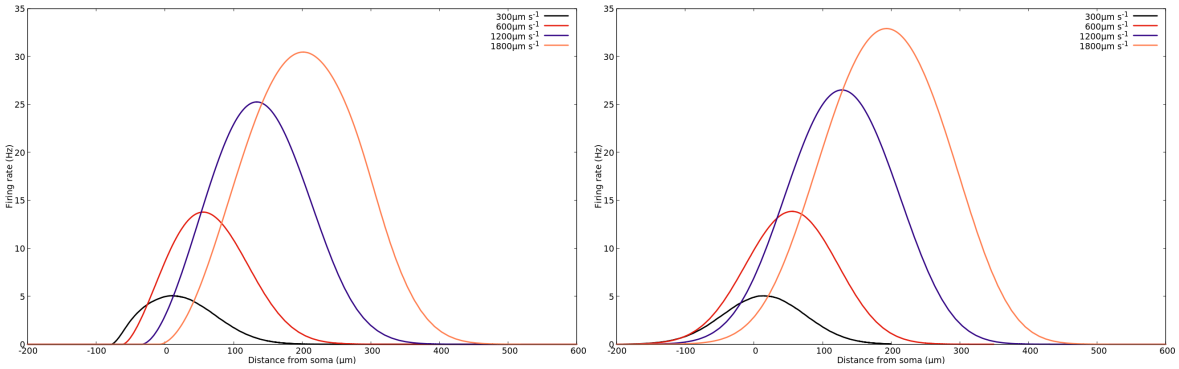

Figure 3.10: Reproducing lag normalization with our gap junction coupling model : Simulation results of the first (left) and the last (right) cell of the network, for different stimulus speeds, with $w_{gap} = 0.9\, ms^{-1}$.

Partial conclusion

In this chapter, we introduced our retina model which implements three anticipatory mechanisms : gain control, amacrine cells connectivity at the level of bipolar cells and gap junction coupling of ganglion cell. The mathematical formalism developed here enables us to conduct a mathematical study of anticipation, further emphasized through numerical simulations. While the coupling part of the model starts from biologically plausible circuits, the study conducted hereafter is purely computational.

Chapter 4

Mathematical results

In this chapter, we will present mathematical results concerning the analytical formulation of anticipation time in the case of gain control. We will then conduct a mathematical study of the gap junction coupling and show that this connectivity type induces a propagating wave of activity. Finally, we will study the amacrine cell connectivity circuit as a dynamical system, focusing on the nearest neighbor graph type. The case of the probabilistic graph being hard to handle analytically, we will study it from a numerical point of view in the next chapter.

4.1 Anticipation time in the gain control model

We define the anticipation time as :

$$\Delta = t_B - t_G, \tag{4.1}$$

where t_B is the peak in the bipolar pool response without gain control (eq. (4.7) below) and t_G is the peak in the response of the corresponding ganglion cell. In the absence of gain control and lateral connectivity $\Delta = 0$. Anticipation corresponds to a positive Δ. Note that we observe another form of anticipation, the raise of activity before the stimulus enters in the receptive field of the ganglion cell. We comment this below. Here we stick at the analysis of the anticipation time defined by (4.1).

For explanations purposes, we will often use the approximation of $V_{i_{drive}}$ by a Gaussian pulse, with width σ, propagating at constant speed v along the direction $\vec{e}_x$:

$$V_{i_{drive}}(t) = \frac{1}{\sqrt{2\,\pi}\,\sigma}\, e^{-\frac{1}{2}\,\frac{(x-vt)^2}{\sigma^2}}, \tag{4.2}$$

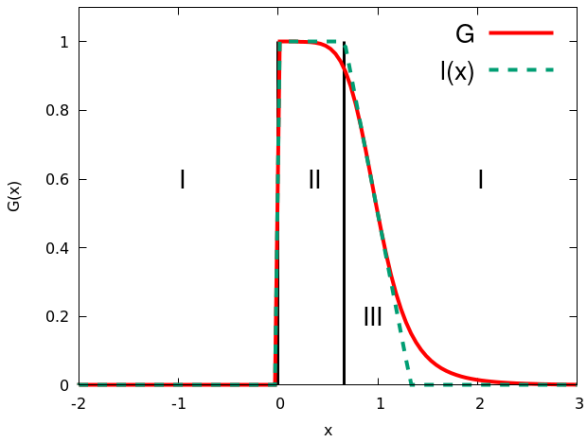

Figure 4.1: Gain function (3.11). $l(x)$, in dashed line, is a piecewise linear approximation from which region I, II and III are defined.

where $x = k\,\delta_B$ is the horizontal coordinate of Bipolar cell i.

When $V_{B_i}(s)$ has the form (4.2) this gives (for a very low threshold θ_B such that $\mathcal{N}(V_{B_i}(s)) = V_{B_i}(s)$) :

$$A_{B_i}(t) = \frac{h}{v}\, e^{\frac{1}{2}\frac{\sigma^2}{\tau_a^2\, v^2}}\, e^{\frac{1}{\tau_a v}(x - v\,t)} \left[1 - \Pi\left(\frac{x - v\,t}{\sigma} + \frac{\sigma}{\tau_a\, v}\right)\right], \tag{4.3}$$

where $\Pi(x) = \frac{1}{2}\left[1 + erf\left(\frac{x}{\sqrt{2}}\right)\right]$ is the repartition function of the Gaussian. This results holds mutantis mutandis for the activity of gain controlled ganglion cells (eq. (3.39)).

In the course of this mathematical study, we will use the following piecewise linear approximation for the bipolar gain control also represented in Fig. 4.1:

$$\mathcal{G}_B(A) = \begin{cases} 0, & \text{if } A \in]-\infty, 0[\cup [\frac{4}{3}, +\infty[, \quad \text{region I;} \\ 1, & \text{if } A \in [0, \frac{2}{3}], \quad \text{region II;} \\ -\frac{3}{2}A + 2, & \text{if } A \in [\frac{2}{3}, \frac{4}{3}], \quad \text{region III.} \end{cases} \tag{4.4}$$

Thanks to this approximation we roughly distinguish 3 regions for the gain function $\mathcal{G}_G(A)$. In region I, the gain is essentially 0; in region II it is equal to 1. Finally, in region III it decays very fast. This shape is useful to understand the mechanism of anticipation.

4.1.1 Peak times in the ganglion cell activity

In the presence of a moving stimulus the firing rate of the ganglion cell G increases up to a maximum, reached at a time t_m. Note that this maximum might not be unique so t_m is the time to reach the first maximum. In general, t_m depends on gain control, lateral connectivity, as well as characteristics of the stimulus such as speed and contrast. Finally, it also depends on the preferred orientation of the bipolar cells receptive field. We derive here a general equation for our model. We give here the main conclusions allowing to interpret the numerical results presented in the next chapter.

To avoid trivialities we will consider that the firing rate function of G is a smooth, monotonously increasing sigmoid function so that $\mathcal{N}'_G(V) > 0$. In this case the extrema in the firing rate of the ganglion cell Gk are given by $\frac{dV_{G_k}}{dt} = 0$, or, using the pooling equation (3.35) , $\sum_i W_{G_k}^{B_i} \frac{dR_{B_i}}{dt} = 0$, where from the definition (3.10) of R_{B_i}:

$$\frac{dR_{B_i}}{dt} = \mathcal{G}_B\left(A_{B_i}\right) \frac{d\mathcal{N}_B(V_{B_i})}{dt} + \mathcal{N}_B(V_{B_i})\, \mathcal{G}'_B\left(A_{B_i}\right) \frac{dA_{B_i}}{dt}.$$

There are two types of bipolar cells. The inactive ones where $V_{B_i} \leq \Theta_B$ and $\mathcal{N}_B(V_{B_i}) = 0$ and $\frac{dR_{B_i}}{dt} = 0$ so they do not contribute to the activity. The active bipolar cells, $V_{B_i} > \Theta_B$ obey $\mathcal{N}_B\left(V_{B_i}\right) = V_{B_i}$.

For those cells, the equation for the times of extrema in the firing rate of G_k is given by :

$$\sum_i W_{G_k}^{B_i} \mathcal{G}_B\left(A_{B_i}\right) \left(-\frac{1}{\tau_B} V_{B_i} + \sum_{j=1}^{N_A} W_{B_i}^{A_j} V_{A_j} + F_{B_i}(t) \right) = -\sum_i W_{G_k}^{B_i} \mathcal{G}'_B\left(A_{B_i}\right) V_{B_i}(t) \frac{dA_{B_i}}{dt}, \tag{4.5}$$

where the sum holds on active bipolar cells in the pool of Gk.

We analyse now this equation in specific cases.

4.1.2 Anticipation time in a simple example

To illustrate how gain control induces anticipation we consider first the case of a bipolar cell B connected to a ganglion cell (no pooling) where the drive has the form (4.2) so that the bipolar activity has the form (4.3). The voltage V_{B_i}, activity A_{B_i}, gain $\mathcal{G}\left(V_{B_i}\right)$ and rectified voltage R_{B_i} of the cell Bi are shown in Fig. 4.2. One can easily see the role of gain control in anticipating the peak of the rectified voltage.

In this case an explicit equation for t_G can be written. The maximum of R_{B_i} is

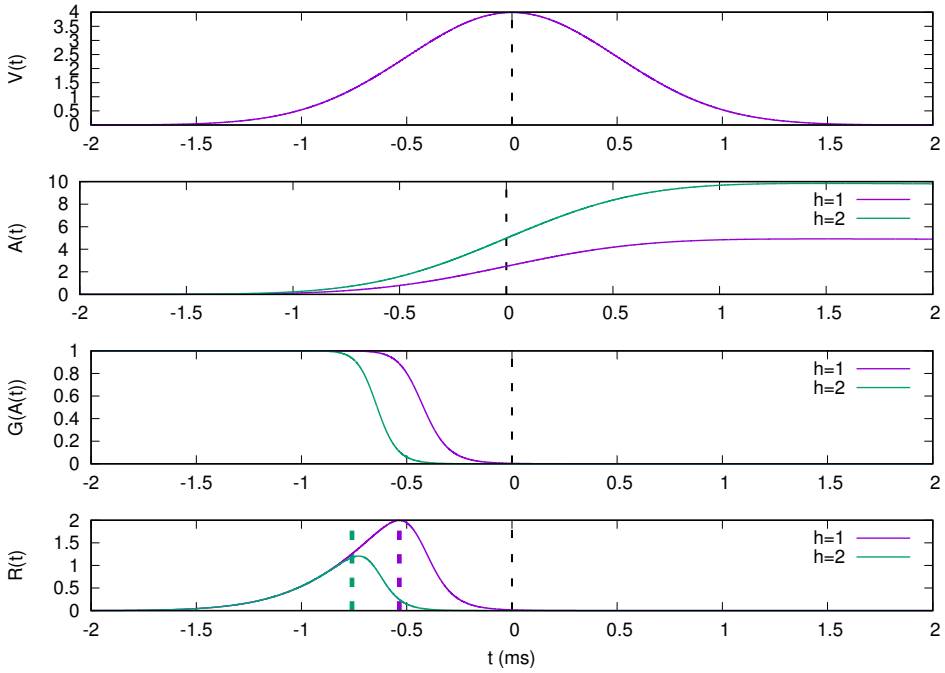

Figure 4.2: The mechanism of gain control when the drive is the Gaussian pulse (4.2) for different values of h. First line: voltage V_{B_i}; second line, activity A_{B_i}; third line, gain $\mathcal{G}\left(A_{B_i}\right)$ and fourth line, rectified voltage R_{B_i}. The black dashed line indicates the peak in $V_{i_{drive}}(t)$ (time t_B). The purple dashed line is the time t_G for $h = 1mV^{-1}ms^{-1}$. The green dashed line is the time t_G for $h = 2mV^{-1}ms^{-1}$.

reached when $\frac{1}{V_{B_i}}\frac{dV_{B_i}}{dt} = -\frac{1}{\mathcal{G}_B\left(A_{B_i}\right)}\frac{d\mathcal{G}_B\left(A_{B_i}\right)}{dt}$, with $\frac{1}{V_{B_i}}\frac{dV_{B_i}}{dt} = \frac{v}{\sigma^2}u$, $u = x - v\,t$. Using the piecewise linear form (4.4) of $\mathcal{G}_B$ and assuming that the solution if reached when A_{B_i} is in region III this gives:

$$\frac{v}{\sigma^2}u = \frac{3}{4 - 3\,A_{B_i}}\frac{dA_{B_i}}{dt} \tag{4.6}$$

It can be solved numerically using the form (4.3)
$A_{B_i}(t) = \frac{h}{v}\,e^{\frac{1}{2}\frac{\sigma^2}{\tau_a^2 v^2}}\,e^{\frac{u}{\tau_a v}}\left[1 - \Pi\left(\frac{u}{\sigma} + \frac{\sigma}{\tau_a\,v}\right)\right]$.

The fast rising in activity is mainly due to the term $1 - \Pi\left(\frac{u}{\sigma} + \frac{\sigma}{\tau_a\,v}\right)$ so we may assume that $e^{\frac{u}{\tau_a v}} \sim 1$ near the peak time.

In fig. 4.3 we show how anticipation time depends, in this case, on the stimulus size (here the mean-square deviation σ of the Gaussian peak), the bar speed, and the activity parameter h. The values of h, v has been chosen in agreement with the figures reporting the anticipation time for a moving bar (Fig 5.1).

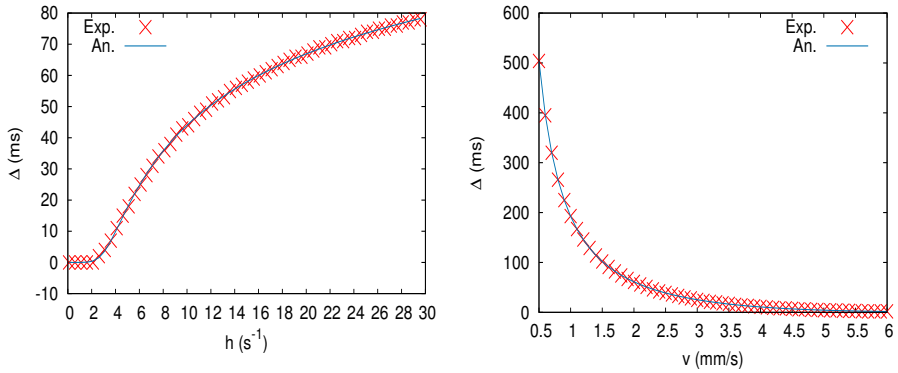

Figure 4.3: Anticipation time Δ for a Gaussian pulse. Red points correspond to the numerical simulations and blue line to the analytic approximation (4.6). Left: Δ as function of h ($v = 3$ mm/s; $\sigma = 0.162$ mm). Right: Δ as function of v ($\sigma = 0.162$ mm; $h = 6.1\ s^{-1}$).

4.1.3 Peak time without bipolar gain control and without lateral connectivity

The case without gain control corresponds to taking $\mathcal{G}_B\left(A_{B_i}\right) = 1$ so that $\mathcal{G}'_B\left(A_{B_i}\right) = 0$. The absence of connectivity implies that $W_{B_i}^{A_j} = 0$. From eq. (3.7) it also implies that $V_{B_i}(t) = V_{i_{drive}}(t)$ so that the peak in ganglion cell G_k is given by:

$$\sum_i W_{G_k}^{B_i} \frac{dV_{i_{drive}}}{dt} = 0 \tag{4.7}$$

We call t_B the solution of (4.7) giving the maximal peak. This is the time appearing in the definition (4.1) of the anticipation time. As the pooling weights $W_{G_k}^{B_i}$ are positive, we remark that (4.7) has solution only of some cells have a derivative $\frac{dV_{i_{drive}}}{dt} < 0$. More precisely, when the bar enters the receptive field of bipolar cell i, the derivative $\frac{dV_{i_{drive}}}{dt}$ is first positive, then become negative after the peak in the bipolar linear response $V_{i_{drive}}$. Thus, eq. (4.7) requires that some bipolar cells - the leftmost for a bar moving from the left to the right - in the pool are beyond their activity peak.

The general solution of this equation depends on the form of the stimulus and its time derivative. In the case of a moving bar sweeping at a constant speed one can write an explicit equation for the time peak, given in the appendix. We have not been able to find an analytic solution though, except in the case where the response is very fast. *In general, the maximum of the peak is NOT reached when the bar enters the center of the receptive field, as usually believed.*

4.1.4 Peak time with bipolar gain control and without lateral connectivity

We now explain why the time t_G solving equation 9.2 and corresponding to the maximum of the ganglion cell's peak is in advance to the time t_B defined in the previous section, so that $\Delta > 0$ in the presence of gain control. To simplify the description, but without loss of generality, we use the piecewise linear approximation of $\mathcal{G}_B$.
Inactive cells ($V_{B_i} < \theta_B$) do not contribute to the equation. For active cells we have 3 cases. Cells in region I of fig. 4.1 do not contribute as well (actually, a cell is in region I when its activity is negative, a situation which is not physically realistic). Cells in region II have $\mathcal{G}_B\,(\,A_{B_i}\,) = 1$ and $\mathcal{G}'_B\,(\,A_{B_i}\,) = 0$. Actually, the case considered in the previous section (no gain control) corresponds to having all cells in region II when the peak of GCell's activity is reached. Finally, cells in region III have a fast gain decay with $\mathcal{G}'_B\,(\,A_{B_i}\,) < 0 \sim -\frac{3}{2}$.

In this case, equation (9.2) reads:

$$\sum_{i\in II} W_{G_k}^{B_i}\,\frac{dV_{i_{drive}}}{dt} + \sum_{i\in III} W_{G_k}^{B_i}\mathcal{G}_B\,(\,A_{B_i}\,)\,\frac{dV_{i_{drive}}}{dt} = -\sum_{i\in III} W_{G_k}^{B_i}\mathcal{G}'_B\,(\,A_{B_i}\,)\,V_{i_{drive}}(t)\,\frac{dA_{B_i}}{dt}, \tag{4.8}$$

With our choice of parameters, the right-hand side is positive. Likewise, the left-hand side term corresponding to region III is positive. Finally, the left-hand side term corresponding to region II is a sum of terms than can be either positive or negative (when the corresponding bipolar cell has gone beyond its maximal response). Thus, this term is positive, increasing for short times, and starts to decrease after a sufficiently long time, until it vanishes and becomes negative. Now, in contrast to the no-gain control case, where, to have a solution, eq. (4.7) required some of the derivative $\frac{dV_{i_{drive}}}{dt}$ to be negative to achieve a zero sum, here, this condition is not necessary because the right hand side is positive. Thus, the solution of 4.9 is reached at a time $t_G < t_B$. The time t_G depends though on parameters such as the bar speed, the contrast, and the size of the object, as illustrated in section 5.1.

As the decay in gain is very fast, a possible approximation to obtain t_G is obtained by setting $\mathcal{G}_B\,(\,A_{B_i}\,) = 0$ in region III, giving:

$$\sum_{i\in II} W_{G_k}^{B_i}\,\frac{dV_{i_{drive}}}{dt} = \frac{3}{2}\sum_{i\in III} W_{G_k}^{B_i}\,V_{i_{drive}}(t)\,\frac{dA_{B_i}}{dt}, \tag{4.9}$$

4.2 The role of gap junctions

4.2.1 Propagating wave of activity

In order to better understand the role that gap junctions can have on motion anticipation we first analyse the motion of a propagating pulse of the form (4.2). We show that eq. (3.42) is associated with a transport equation of ballistic type. For this, we consider a continuous spatio-temporal field $V(x,t)$, $x \in \mathbb{R}$, such that $V_{G_k} \equiv V(k\delta_G, t)$. We assume likewise that $V^{in}_{G_k} \equiv V^{in}(k\delta_G, t)$ for some continuous function $V^{in}(x,t)$ corresponding to the GCells input. We set $\frac{\partial V^{in}(x,t)}{\partial t} \equiv f(x,t)$. Finally, we note $C(x)$ the initial profile so that $V(x,t_0) = C(x)$.

In the limit where δ_G is small eq. (3.42) becomes:

$$\frac{\partial V_G}{\partial t} = f(x,t) - v_{gap}\,\frac{\partial V_G}{\partial x} + O(\delta_G^2), \tag{4.10}$$

where $v_{gap} \equiv w_{gap}\,\delta_G$ has the dimension of a speed.

The general solution of (4.10) is:

$$V_G(x,t) = C(x - v_{gap}(t-t_0)) \; + \int_{t_0}^{t} f(x - v_{gap}(t-u), u)du.$$

Indeed :

$$\frac{\partial V_G(x,t)}{\partial t} = -v_{gap}C'\,(\,x - v_{gap}(t-t_0)\,) + f(x,t) + \int_{t_0}^{t} \frac{\partial}{\partial t} f\,(\,x - v_{gap}(t-u), u\,)\;du$$

$$= -v_{gap}C'\,(\,x - v_{gap}(t-t_0)\,) + f(x,t) - v_{gap}\int_{t_0}^{t} \frac{\partial}{\partial x} f\,(\,x - v_{gap}(t-u), u\,)\;du$$

$$\frac{\partial V_G(x,t)}{\partial x} = C'\,(\,x - v_{gap}(t-t_0)\,) + \int_{t_0}^{t} \frac{\partial}{\partial x} f\,(\,x - v_{gap}(t-u), u\,)\;du.$$

so that :

$$\frac{\partial V_G}{\partial t} = f(x,t) - v_{gap}\,\frac{\partial V_G}{\partial x}$$

We consider now a stimulation of type $V^{in}(x,t) = h(x - v\,t)$, propagating from the left to the right, with speed v. We have $f(x,t) = \frac{\partial V^{in}(x,t)}{\partial t} = -vh'(x - v\,t)$ so that:

$$V_G(x,t) = C(x - v_{gap}(t-t_0)) \; - v\int_{t_0}^{t} h'(x - v_{gap}t - (v - v_{gap})\,u)du.$$

Setting $z = x - v_{gap}t - (v - v_{gap})u$ this gives:

$$= C(x - v_{gap}(t - t_0)) + \frac{v}{v - v_{gap}} \int_{x - v_{gap}t - (v - v_{gap})t_0}^{x - vt} h'(z)dz$$

$$= C(x - v_{gap}(t - t_0)) + \frac{v}{v - v_{gap}} \left[h\left(x - vt \right) - h\left(x - v_{gap}t - (v - v_{gap})t_0 \right) \right]$$

In order to compare the cases with and without gap, we set $C(x) = V^{in}(x, t_0) = h\left(x - v\, t_0 \right)$, so that:

$$V_G(x,t) = \underbrace{\frac{v}{v - v_{gap}} h\left(x - vt \right)}_{\pi_{stim}} - \underbrace{\frac{v_{gap}}{v - v_{gap}} h\left(x - v_{gap}t - (v - v_{gap})\, t_0 \right)}_{\pi_{gap}}. \tag{4.11}$$

When $v_{gap} = 0$ the ganglion cells voltage follows the stimulation i.e. $V_G(x,t) = h\left(x - vt \right)$. In the presence of gap junctions there are two pulses: the first one, π_{stim} with amplitude $\frac{v}{v - v_{gap}}$ following the stimulation; the second one, π_{gap}, with amplitude $-\frac{v_{gap}}{v - v_{gap}}$, propagating at speed v_{gap}.

For $v_{gap} < v$ the amplitude of π_{stim} growths has v_{gap} approaches v whereas π_{gap} travels at speed v_{gap} and hyperpolarizes the neurons (Fig. 4.4 a).

At $v = v_{gap}$, $V_G(x,t) = h\left(x - v_{gap}t \right) + v_{gap}(t - t_0)h'\left(x - v_{gap}t \right)$ which diverges like t when $t \to \infty$ and $x \to +\infty$ (Fig. 4.4 b).

Finally for $v_{gap} > v$ the amplitude of π_{stim} follows the stimulation with a negative sign (hyperpolarization) whereas π_{stim} is ahead of the stimulation, with a positive sign, travelling at speed v_{gap} (Fig. 4.4 c).

We illustrate this behaviour in Fig. 4.4.

4.2.2 Effect of gain control after gap junctions

When the piecewise non linearity $\mathcal{N}_G$ (3.37) and the gain control $\mathcal{G}_G(A)$ (3.39) are applied to $V_G(x,t)$ there are two effects: (i) the hyperpolarized peak is cut by $\mathcal{N}_G$; (ii) the positive pulse induces a raise in activity, which, in turn, triggers the ganglion gain control $\mathcal{G}_G(A)$ inducing a peak in the response of the ganglion cell, similar to what happens with bipolar cells, with a different form for the gain control though. Moreover, in contrast to pathway I where only gain control generates anticipation in pathway II the wave of activity generated by gap junctions increases anticipation by two distinct

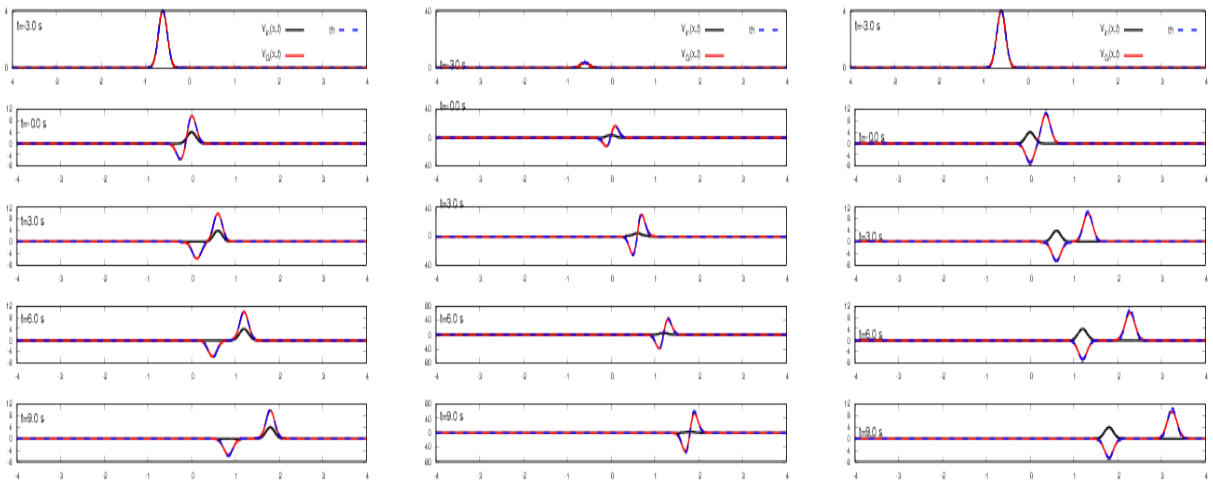

Figure 4.4: Solutions of (4.10). The stimulation $V^{in}(x,t)$ is plotted in black. Here this is a Gaussian pulse $\frac{1}{\sqrt{2\pi}\,\sigma}\,e^{-\frac{1}{2}\,\frac{(x-v\,t)}{2\,\sigma^2}}$ with $\sigma = 0.1$, $v = 0.2$. Note that the units are arbitrary here. The numerical solution of (4.10) is plotted in red. Finally, the theoretical solution (4.11) is shown in dashed blue. The agreement between numerics and theory is perfect. a) $v_{gap} < v$; b) $v_{gap} = v$; c) $v_{gap} > v$

.

effects.

If $v_{gap} < v$ the cell's response propagates at the same speed as the stimulus, but its amplitude is larger than the case with no gap junction (term π_{stim}). From eq. (4.3) this results in an increase of h with an effective $h = h\frac{v}{v-v_{gap}}$. From fig.4.3a this induces an increase in the anticipation time (with a saturation of the effect, though, as $v_{gap} \to v$).

If $v_{gap} > v$ the cell's response propagates at a larger speed than the stimulus (term π_{gap}), so that the cell responds before the time of response without gaps. From fig.4.3b this induces an increase in the anticipation time, but of a different nature than the case $v_{gap} < v$.

Finally, $v_{gap} = v$ there is a singularity in the continuous space approximation, which does not appear in a discrete lattice ($\delta_G > 0$).

As for the approximate value of v_{gap}, considering gap junction Cx36, we have the following parameters :

$$dx \sim 75\mu m$$

$$g \sim 1 - 15ns$$

$$C \sim 20pF$$

$$v_{gap} = \frac{gdx}{c} \sim [0.1175, 15]mm/s$$

4.2.3 Effect of gain control before gap junctions

We now briefly consider the solutions of (3.43) when gain control is applied before the gap junction. The corresponding continuous space equation is:

$$\frac{\partial V_G}{\partial t} = f(x,t) - v_{gap}\,\frac{\partial R_G}{\partial x} + O(\delta_G^2), \tag{4.12}$$

where R_G is now a non linear function of the activity $A(x,t)$ obeying the continuous space version of (3.38):

$$\frac{\partial A_G}{\partial t} = -\frac{A_G}{\tau_G} + h_G\,\mathcal{N}_G\,(\,V_G\,)\,, \tag{4.13}$$

This gives a coupled set of partial differential equations that we have not been able to solve analytically. We have therefore focused on numerical simulations (see the following chapter). Qualitatively, the effect of gain control is to saturate the effects of gap junctions thereby limiting the anticipation time.

Partial conclusion

In the case of gap junction connectivity, results show the emergence of a propagating wave of activity, *similar to what is happening in the cortex*. One should note here, however, that the propagation is considered instantaneous, since we assimilate ganglion cells to points and we don't take into account the axons lengths.

4.3 Differential motion sensitive ganglion cells : Amacrine connectivity

In this section we study the potential effect of amacrine cells (pathway III of Fig. 3.1) on motion anticipation. We consider the case where there are as many bipolar cells as amacrines ($N_B = N_A \equiv N$) so that the matrices W_B^A and W_A^B are square matrices.

4.3.1 General mechanisms

4.3.1.1 Vector equation

We first study mathematically the system (4.15) that we write in a more convenient form. For this study we will assume that $\mathcal{N}_B\,(\,V_{B_i}\,) = V_{B_i}$ i.e. $V_{B_i} \geq \theta_B, i = 1 \ldots N$, thus $R_{B_i} = \mathcal{G}_B\,(\,A_{B_i}\,)$.

We note $\vec{V}_{\mathfrak{A}} \equiv \left(\; V_{A_j} \;\right)_{j=1}^{N}$ the vector of voltages for amacrine cells, $\vec{V}_{\mathfrak{B}} \equiv \left(\; V_{B_i} \;\right)_{i=1}^{N}$ the vector of voltages for bipolar cells, $\vec{A} \equiv \left(\; A_{B_i} \;\right)_{i=1}^{N}$ the vector of activities for ganglion cells, and $\vec{F} \equiv \left(\; F_{B_i} \;\right)_{i=1}^{N}$. We introduce the vectors $\vec{\mathcal{X}} = \begin{pmatrix} \vec{V}_{\mathfrak{B}} \\ \vec{V}_{\mathfrak{A}} \\ \vec{A} \end{pmatrix}$, $\vec{\mathcal{F}} = \begin{pmatrix} \vec{F} \\ 0_N \\ 0_N \end{pmatrix}$ where $0_N = \left(\; 0 \;\right)_{i=1}^{N}$, and the diagonal $N \times N$ matrix $\omega\left(\vec{A}\right) = diag\,(\,\mathcal{G}_B(A_{B_i})\,)_{i=1}^{N}$.
Finally, we use the $3N \times 3N$ matrix:

$$\mathcal{L}(\vec{\mathcal{X}}) = \begin{pmatrix} -\frac{I_N}{\tau_B} & W_B^A & 0 \\ W_A^B.\omega\left(\vec{A}\right) & -\frac{I_N}{\tau_A} & 0 \\ h\,I_N & 0 & -\frac{I_N}{\tau_a} \end{pmatrix} \tag{4.14}$$

where I_N is the $N \times N$ identity matrix, so that the dynamical system (5.1) reads:

$$\frac{d\vec{\mathcal{X}}}{dt} = \mathcal{L}(\vec{\mathcal{X}}).\vec{\mathcal{X}} + \vec{\mathcal{F}}(t). \tag{4.15}$$

We introduce the Greek indices $\alpha, \beta, \gamma = 1 \dots 3N$ such that $\vec{\mathcal{X}}$ has entries:

$$\vec{\mathcal{X}}_\alpha = \begin{cases} V_{B_i}, & \alpha = i, & i = 1 \dots N; \\ V_{A_i}, & \alpha = N + i, & i = 1 \dots N; \\ A_i, & \alpha = 2N + i, & i = 1 \dots N; \end{cases}$$

Likewise $\vec{\mathcal{F}}_\alpha = F_{B_i}$, if $\alpha = i, i = 1 \dots N$ and $\vec{\mathcal{F}}_\alpha = 0$ otherwise.

4.3.1.2 No gain control

General solution. When $\mathcal{G}_B(A_{B_i}) = 1$, $i = 1 \dots N$, in a low activity state, the system (4.15) is linear. In this case, the activity variables does not play any role in the dynamics of $\vec{V}_{\mathfrak{B}}, \vec{V}_{\mathfrak{A}}$. The general solution is:

$$\vec{\mathcal{X}}(t) = e^{\mathcal{L}(t-t_0)}.\vec{\mathcal{X}}(t_0) + \int_{t_0}^{t} e^{\mathcal{L}(t-s)}.\vec{\mathcal{F}}(s)\, ds, \tag{4.16}$$

where t_0 is the initial time. The behaviour of the solution, in the long time limit, depends on the spectrum of $\mathcal{L}$. In particular, when there are unstable modes (eigenvalues with positive real part) the amplitude of $\vec{\mathcal{X}}$ projected on the unstable modes increases thereby triggering the gain control mechanisms, which, in turn stabilizes the dynamics. We illustrate this in the specific case of Laplacian connectivity 4.3.2.

We assume that a bipolar cell connects only one amacrine cell, with a weight w^+ uniform for all bipolar cells, so that $W_A^B = w^+ I_N$, $w^+ > 0$. We also assume that amacrine connect to bipolar with a connectivity matrix $\mathcal{W}$, not necessarily, symmetric, with a uniform weight $-w^-$, $w^- > 0$, so that $W_B^A = -w^- \mathcal{W}$. In the case with no gain control it is enough to consider the join dynamics of $\vec{V}_{\mathfrak{B}}, \vec{V}_{\mathfrak{A}}$ without taking into account the activity $\vec{A}$. The projection of $\mathcal{L}$ on the subspace spanned by $\vec{V}_{\mathfrak{B}}, \vec{V}_{\mathfrak{A}}$ reads:

$$\mathcal{M} = \begin{pmatrix} -\frac{I_N}{\tau_B} & -w^- \mathcal{W} \\ w^+ I_N & -\frac{I_N}{\tau_A} \end{pmatrix}. \tag{4.17}$$

Eigenvalues and eigenvectors. We note $\kappa_n, n = 1 \dots N$, the eigenvalues of $\mathcal{W}$ ordered as $|\kappa_1| \leq |\kappa_2| \leq \dots \leq |\kappa_n|$ and $\vec{\psi}_n$ is the corresponding eigenvector. We normalize $\vec{\psi}_n$ so that $\vec{\psi}_n^\dagger.\vec{\psi}_n = 1$ where $\dagger$ is the adjoint. (Note that, as $\mathcal{W}$ is not symmetric in general, eigenvectors are complex).

For each n, there is a pair of eigenvalues $\lambda_n^{\pm}$ and eigenvectors $\begin{pmatrix} \vec{\psi}_n \\ \rho_n^{\pm}\vec{\psi}_n \end{pmatrix}$ of $\mathcal{M}$ with:

$$\rho_n^{\pm} = \begin{cases} \frac{1}{2\,\tau\,w^-\,\kappa_n}\left(1 \pm \sqrt{1-4\,\mu\,\kappa_n}\right), & \kappa_n \neq 0, \frac{1}{\tau} \neq 0; \\ w^+\,\tau, & \kappa_n = 0, \frac{1}{\tau} \neq 0; \\ \pm\sqrt{-\frac{w^+}{w^-}\,\frac{1}{\kappa_n}}, & \frac{1}{\tau} = 0. \end{cases} \tag{4.18}$$

where:

$$\frac{1}{\tau} = \left(\frac{1}{\tau_A} - \frac{1}{\tau_B}\right). \tag{4.19}$$

and:

$$\frac{1}{\tau_{AB}} = \left(\frac{1}{\tau_A} + \frac{1}{\tau_B}\right). \tag{4.20}$$

When $\frac{1}{\tau} = 0$, ($\tau_A = \tau_B$) eigenvalues are given by:

$$\lambda_n^{\pm} = \begin{cases} -\frac{1}{2\,\tau_{AB}} \mp \frac{1}{2\,\tau}\sqrt{1-4\,\mu\,\kappa_n}, & \frac{1}{\tau} \neq 0; \\ -\frac{1}{\tau_A} \mp \sqrt{-w^-\,w^+\kappa_n}, & \frac{1}{\tau} = 0. \end{cases} \tag{4.21}$$

with:

$$\mu = w^-\,w^+\,\tau^2 \geq 0, \tag{4.22}$$

Thus μ summarizes the effect of bipolar cells on amacrine cells (w^+), and amacrine cells on bipolar cells (w^-), and the time scales τ_A and tau_B. It's the mean parameter of the problem, and it is dimensionless.

Proof of eigenvectors and eigenvalues Indeed, assume that $\vec{\phi}_m$ is of the form $\vec{\phi}_m = \begin{pmatrix} \vec{\psi}_n \\ \rho\vec{\psi}_n \end{pmatrix}$, then we have:

$$\mathcal{M}.\vec{\phi}_m = \begin{pmatrix} -\frac{I}{\tau_B} & -w^-\,\mathcal{W} \\ w^+\,I & -\frac{I}{\tau_A} \end{pmatrix}.\begin{pmatrix} \vec{\psi}_n \\ \rho\vec{\psi}_n \end{pmatrix} = \begin{pmatrix} \left(-\frac{1}{\tau_B} - w^-\,\rho\,\kappa_n\right).\vec{\psi}_n \\ \left(-\frac{\rho}{\tau_A} + w^+\right).\vec{\psi}_n \end{pmatrix} = \lambda_m \begin{pmatrix} \vec{\psi}_n \\ \rho\vec{\psi}_n \end{pmatrix},$$

which gives:

$$\begin{cases} \left(-\frac{1}{\tau_B} - w^-\,\rho\,\kappa_n\right) = \lambda_m \\ \left(-\frac{\rho}{\tau_A} + w^+\right) = \lambda_m\rho, \end{cases}$$

$$\rho\left(-\frac{1}{\tau_B} - w^-\,\rho\,\kappa_n\right) = -\frac{\rho}{\tau_A} + w^+$$

$$-w^- \kappa_n \rho^2 + \left(\frac{1}{\tau_A} - \frac{1}{\tau_B} \right) \rho - w^+ = 0$$

$$w^- \kappa_n \rho^2 - \frac{1}{\tau} \rho + w^+ = 0,$$

where:

$$\frac{1}{\tau} = \left(\frac{1}{\tau_A} - \frac{1}{\tau_B} \right).$$

This gives, if $\kappa_n \neq 0$ and $\frac{1}{\tau} \neq 0$:

$$\rho_n^{\pm} = \frac{1}{2\, w^- \kappa_n} \left(\frac{1}{\tau} \pm \sqrt{\frac{1}{\tau^2} - 4\, w^- w^+ \kappa_n} \right)$$

$$\rho_n^{\pm} = \frac{1}{2\, \tau\, w^- \kappa_n} \left(1 \pm \sqrt{1 - 4\, \mu\, \kappa_n} \right),$$

where:

$$\mu = w^- w^+ \tau^2 \geq 0.$$

Thus, for each n, there are two eigenvalues:

$$\lambda_n^{\pm} = -\frac{1}{2\, \tau_{AB}} \mp \frac{1}{2\, \tau} \sqrt{1 - 4\, \mu\, \kappa_n},$$

with:

$$\frac{1}{\tau_{AB}} = \left(\frac{1}{\tau_A} + \frac{1}{\tau_B} \right).$$

If $\kappa_n = 0$, $\frac{1}{\tau} \neq 0$, $\rho_n^{\pm} = w^+ \tau$. Then:

$$\lambda_m = -\frac{1}{\tau_B} - w^- \rho\, \kappa_n$$

Finally, if $\kappa_n \neq 0$, $\frac{1}{\tau} = 0$, ($\tau_A = \tau_B$), $\rho_n^{\pm} = -\frac{w^+}{w^-} \frac{1}{\kappa_n}$ and $\lambda_n^{\pm} = -\frac{1}{\tau_B} \pm \sqrt{-w^- w^+ \kappa_n}$. If $\kappa_n = 0$, $\frac{1}{\tau} = 0$ there is no solution for ρ.

Note that $\frac{1}{\tau_{AB}} \geq \frac{1}{\tau}$.

Remarks.

1. When $\mu = 0$, $\mathcal{M}$ is diagonal: the N first eigenvalues are $-\frac{1}{\tau_B}$, the N next eigenvalues are $-\frac{1}{\tau_A}$. We have, in this case: $\lambda_n^+ = -\frac{1}{\tau_B}$ and $\lambda_n^- = -\frac{1}{\tau_A}$. Therefore, in order to be coherent with this diagonal form of $\mathcal{L}$ when $\mu = 0$ we order eigenvalues and eigenvectors of $\mathcal{M}$ such that the N first eigenvalues are $\lambda_n^+, n = 1 \ldots N$, and the N next are $\lambda_n^-, n = N+1 \ldots 2N$.

2. Returning back to $\mathcal{L}$ the pairs eigenvalues, eigenvectors have the form:

$$\begin{aligned}
\lambda_\beta = \lambda_n^+, \mathcal{P}_\beta &= \begin{pmatrix} \vec{\psi}_n \\ \rho_n^+ \vec{\psi}_n \\ \sigma_n^+ \ \vec{\psi}_n \end{pmatrix}, \qquad \beta = n = 1 \dots N, \\
\lambda_\beta = \lambda_n^-, \mathcal{P}_\beta &= \begin{pmatrix} \vec{\psi}_n \\ \rho_n^- \vec{\psi}_n \\ \sigma_n^- \ \vec{\psi}_n \end{pmatrix}, \qquad \beta = N+1 \dots 2N, \quad n = 1 \dots N, \\
\lambda_\beta = -\tfrac{1}{\tau_a}, \mathcal{P}_\beta &= \vec{e}_\beta, \qquad\qquad\qquad \beta = 2N+1 \dots 3N,
\end{aligned} \tag{4.23}$$

where $\sigma_n \pm = \frac{h}{\frac{1}{\tau_a} + \lambda_n \pm}$ and $\vec{e}_\beta$ is the canonical basis vector in direction β.

3. The eigenvectors $\mathcal{P}_\beta$ are the column of the matrix $\mathcal{P}$ transforming $\mathcal{L}$ in the diagonal form $\Lambda = \mathcal{P}^{-1}\mathcal{L}\mathcal{P}$ where $\Lambda = Diag\{ \lambda_\beta, \beta = 1 \dots 3N \}$.

$$\mathcal{P}_{\alpha\beta} = \begin{cases}
\psi_{\alpha\beta}, & \alpha = 1 \dots N, \beta = 1 \dots N; \\
\rho_\alpha^+ \psi_{\alpha\beta}, & \alpha = N+1 \dots 2N, \beta = 1 \dots N; \\
\sigma_\alpha^+ \psi_{\alpha\beta}, & \alpha = 2N+1 \dots 3N, \beta = 1 \dots N; \\
\psi_{\alpha\beta}, & \alpha = 1 \dots N, \beta = N+1 \dots 2N; \\
\rho_\alpha^- \psi_{\alpha\beta}, & \alpha = N+1 \dots 2N, \beta = N+1 \dots 2N; \\
\sigma_\alpha^- \psi_{\alpha\beta}, & \alpha = 2N+1 \dots 3N, \beta = N+1 \dots 2N; \\
\delta_{\alpha\beta}, & \alpha = 1 \dots 3N, \beta = 2N+1 \dots 3N
\end{cases} \tag{4.24}$$

Stability. If $\mathcal{W}$ is symmetric, its eigenvalues κ_n are real, but λ_β, $\beta = 1 \dots 2N$ can be real or complex, depending on κ_n, as μ is positive. We have four cases:

- $\kappa_n < 0$. Then λ_β are real and there are two cases. If $\frac{1}{\tau} > 0$ the mode $\mathcal{P}_\beta$, $\beta = 1 \dots N$ can become unstable while $\mathcal{P}_\beta$, $\beta = N+1 \dots 2N$ is always stable; for $\frac{1}{\tau} < 0$ the situation is inverted. In both case, the mode is unstable for:

$$\mu > -\frac{1}{\kappa_n} \frac{\tau_A \tau_B}{(\tau_B - \tau_A)^2} \equiv \mu_{n,u}, \tag{4.25}$$

  Thus, τ_A, τ_B play a symmetric role. If $\frac{1}{\tau} = 0$ ($\tau_A = \tau_B$), all eigenvalues are real. Eigenvalues λ_n^- all stable. The eigenvalue λ_n^+ becomes unstable if:

$$w^- w^+ > \frac{1}{\tau_A^2} \frac{1}{\kappa_n^2}. \tag{4.26}$$

Proof There are two cases.

– $\frac{1}{\tau} > 0 \Leftrightarrow \tau_A < \tau_B$.

$$-\frac{1}{2\,\tau_{AB}} \pm \frac{1}{2\,\tau}\sqrt{1-4\,\mu\,\kappa_n} > 0$$

$$\pm\sqrt{1-4\,\mu\,\kappa_n} > \frac{\tau}{\tau_{AB}}$$

Only $+$ is possible.

$$1-4\,\mu\,\kappa_n > \frac{\tau^2}{\tau_{AB}^2}$$

$$1-\frac{\tau^2}{\tau_{AB}^2} = -4\,\frac{\tau_A\tau_B}{\left(\,\tau_B-\tau_A\,\right)^2} > 4\,\mu\,\kappa_n$$

which is possible because $\kappa_n < 0$. Thus, n is unstable if:

$$\mu > -\frac{1}{\kappa_n}\,\frac{\tau_A\tau_B}{\left(\,\tau_B-\tau_A\,\right)^2} \equiv \mu_{n,u}.$$

– $\frac{1}{\tau} < 0 \Leftrightarrow \tau_A > \tau_B$.

$$-\frac{1}{2\,\tau_{AB}} \pm \frac{1}{2\,\tau}\sqrt{1-4\,\mu\,\kappa_n} > 0$$

$$\pm\sqrt{1-4\,\mu\,\kappa_n} < \frac{\tau}{\tau_{AB}}$$

Only $-$ is possible.

$$1-4\,\mu\,\kappa_n > \frac{\tau^2}{\tau_{AB}^2}$$

Same as before.

– If $\frac{1}{\tau} = 0$, $\lambda_n^{\pm} = -\frac{1}{\tau_A} \mp \sqrt{-w^-\,w^+\kappa_n}$ so that eigenvalues are real. The eigenvalue λ_n^- are all stable. The eigenvalue λ_n^+ becomes unstable if:

$$w^-\,w^+ > \frac{1}{\tau_A^2}\frac{1}{\kappa_n^2}.$$

- $\kappa_n > 0$. Then λ_β, $\beta = 1\ldots 2N$ are real or complex. If $\frac{1}{\tau} \neq 0$ they are complex if:

$$\mu > \frac{1}{4\,\kappa_n} \equiv \mu_{n,c}. \tag{4.27}$$

In this case the real part is $-\frac{1}{2\,\tau_{AB}}$, the imaginary part is $\pm\frac{1}{2\,\tau}\sqrt{1-4\,\mu\,\kappa_n}$, and all the modes $\mathcal{P}_\beta$ are stable. If $\mu \leq \mu_{n,c}$ eigenvalues λ_β are real and all modes are stable as well. If $\frac{1}{\tau} = 0$, all eigenvalues are stable and complex.

– $\frac{1}{\tau} > 0 \Leftrightarrow \tau_A < \tau_B$.

$$-\frac{1}{2\,\tau_{AB}} \pm \frac{1}{2\,\tau}\sqrt{1-4\,\mu\,\kappa_n} > 0$$

$$\pm\sqrt{1-4\,\mu\,\kappa_n} > \frac{\tau}{\tau_{AB}}$$

which is not possible because $\frac{\tau}{\tau_{AB}} > 1$ whereas $\sqrt{1-4\,\mu\,\kappa_n} < 1$.

– $\frac{1}{\tau} < 0 \Leftrightarrow \tau_A > \tau_B$.

$$-\frac{1}{2\,\tau_{AB}} \pm \frac{1}{2\,\tau}\sqrt{1-4\,\mu\,\kappa_n} > 0$$

$$\pm\sqrt{1-4\,\mu\,\kappa_n} < \frac{\tau}{\tau_{AB}}$$

Only $-$ is possible.

$$1-4\,\mu\,\kappa_n > \frac{\tau^2}{\tau_{AB}^2}$$

which is not possible because $\frac{\tau}{\tau_{AB}} > 1$ whereas $\sqrt{1-4\,\mu\,\kappa_n} < 1$.

– If $\frac{1}{\tau} = 0$, $\lambda_n^{\pm} = -\frac{1}{\tau_A} \mp \sqrt{-w^-\,w^+\kappa_n}$ so that eigenvalues are stable, complex.

If $\mathcal{W}$ is asymmetric, eigenvalues κ_n are complex, $\kappa_n = \kappa_{n,r} + i\,\kappa_{n,i}$. We write $\lambda_\beta = \lambda_{\beta,r} + i\,\lambda_{\beta,i}$, $\beta = 1 \ldots 2N$ with:

$$\left\{\begin{array}{rcl} \lambda_{\beta,r} & = & -\frac{1}{2\,\tau_{AB}} \pm \frac{1}{2\,\tau}\frac{1}{\sqrt{2}}\sqrt{1+\sqrt{1+\mu^2\,\frac{\kappa_{n,i}^2}{\kappa_{n,r}^2}}}\,\sqrt{1-4\,\mu\,\kappa_{n,r}}; \\ \lambda_{\beta,i} & = & \frac{\kappa_{n,i}}{\sqrt{2}}\,\frac{1}{\sqrt{1+\sqrt{1+\mu^2\,\frac{\kappa_{n,i}^2}{\kappa_{n,r}^2}}}\,\sqrt{1-4\,\mu\,\kappa_{n,r}}}. \end{array}\right. \tag{4.28}$$

Due to the imaginary part, unstable modes can appear when μ becomes large enough (depending on n).

4.3.1.3 The role of gain control

For simplicity we use the approximate form (4.4) of $\mathcal{G}_B$. The linear form (4.17) is valid if $A_{B_i} < \frac{2}{3}, i = 1 \ldots N$ (region II). What happens if a set of bipolar cells $\mathcal{S}$ has an activity which exceeds the activity threshold ? Even with the simplified form (4.4) we have not been able to answer the question in full generality (numerical examples are given in the next chapter). However, a qualitative explanation can be done by simplifying further the form (4.4) by assuming that $\mathcal{G}_B$ is 1 in region II and is 0 in region III ($A_{B_i} \geq \frac{2}{3}$). In this case the matrix $\omega\left(\vec{A}\right)$ becomes a binary matrix $\omega\left(\vec{A}\right) = diag\,(\,\chi_{II}(A_{B_i})\,)_{i=1}^N$ where χ_{II} is the indicator function of region II. Then, the

matrix $W_A^B.\omega\left(\vec{A}\right)$ has vanishing columns at indices $i \in \mathcal{S}$. With this approximation the system (4.15) becomes piecewise linear. It is linear in each partition element $\mathcal{P}_\mathcal{S}$ of $\mathbb{R}^{3N}$ defined by $\mathcal{P}_\mathcal{S} = \left\{ \vec{\mathcal{X}} \in \mathbb{R}^{3N} \mid A_{B_i} \geq \frac{2}{3},\, i \in \mathcal{S} \right\}$. In $\mathcal{P}_\mathcal{S}$, $\mathcal{L}(\vec{\mathcal{X}}) \equiv \mathcal{L}_\mathcal{S}$ with:

$$\mathcal{L}_\mathcal{S} = \begin{pmatrix} -\frac{I}{\tau_B}\begin{pmatrix} I_{N-K} & 0_{N-K,K} \\ 0_{K,N-K} & I_K \end{pmatrix} & W_B^A & 0_{N,N} \\ w^+\begin{pmatrix} I_{N-K} & 0_{N-K,K} \\ 0_{K,N-K} & 0_K \end{pmatrix} & -\frac{I_N}{\tau_A} & 0_{N,N} \\ h\, I_N & 0_{N,N} & -\frac{I_N}{\tau_a} \end{pmatrix}$$

where K is the number of elements of $\mathcal{S}$, I_K the $K \times K$ identity matrix and $0_{N-K,K}$ the $N-K \times K$ 0 matrix. It is easy to see that $\mathcal{L}_\mathcal{S}$ has N eigenvalues $-\frac{1}{\tau_a}$, corresponding to the subspace generated by bipolar cells activities Ai. Projecting $\mathcal{L}_\mathcal{S}$ on the complementary subspace one easily sees that the K cells in $\mathcal{S}$ generate K eigenvalues. Thus, in this approximation of $\mathcal{G}_B$, the (expected) effect of gain control is to stabilize the unstable modes. Using the piecewise linear approximation one can formally extend the solution (4.16) of the linear system, by using a product of evolution operators $\mathcal{L}_{\mathcal{S}_1}, \ldots, \mathcal{L}_{\mathcal{S}_r} \ldots$ where $\mathcal{S}_r$ is the r-th domain encountered by the dynamical system along its trajectory. We shall not pursue along these lines here though, focusing on numerical simulations in two examples. Note that this analysis holds mutandis mutandis for the case where $\mathcal{N}(V)$ is a linear rectifier.

Therefore, the overall picture is the following. Without loss of generality we may assume that $\vec{X}(t_0) = 0$ in (4.16) so that dynamics are driven by $\vec{\mathcal{F}}$. In the presence of a stimulus $\vec{\mathcal{F}}$ the voltage of bipolar raises and eventually affects the behaviour of connected cells via the amacrine connectivity. Below threshold, this interaction is described by the linear operator $\mathcal{L}$. Then, some bipolar cell can cross the threshold of gain control due to two possible reasons, not exclusive: (i) The intensity of $\vec{\mathcal{F}}$, when it is large enough; (ii) The effects of amacrine lateral connectivity. This arises for example when there are a positive eigenvalues, but this is not necessary. In the next examples we show that the effect of amacrine lateral connectivity is to enlarge the width of the response wave triggered by the stimulus, thereby enhancing the anticipation.

4.3.1.4 Network response to a stimulus

We consider here the situation where eigenvalues of $\mathcal{L}$ are negative. This could correspond to the evolution of the network, under the influence of a stimulus, *before* gain control takes place, so that $\mathcal{L}$ has the form (4.14) with $\omega\left(\vec{A}\right) = I$. The goal of this section is to show that, in this situation, the lateral amacrine cells connectivity, although inhibitory, can enhance the response of bipolar cells, thereby increasing the anticipation time.

For simplicity, we will assume that taking the limit $t_0 \to -\infty$ in (4.14) is a good approximation, so that we may write:

$$\vec{\mathcal{X}}(t) = \int_{-\infty}^{t} e^{\mathcal{L}(t-s)}.\vec{\mathcal{F}}(s)\,ds,$$

where the integral is finite because eigenvalues of $\mathcal{L}$ are assumed to be negative.

We have:

$$\vec{\mathcal{X}}_\alpha(t) = \sum_{\beta=1}^{3N}\sum_{\gamma=1}^{3N} \mathcal{P}_{\alpha\beta}\mathcal{P}^{-1}_{\beta\gamma} \int_{-\infty}^{t} e^{\lambda_\beta(t-s)}.\vec{\mathcal{F}}_\gamma(s)\,ds.$$

We recall that, from (3.15), $F_{B_i}(t) = \frac{V_{i_{drive}}}{\tau_B} + \frac{dV_{\gamma_{drive}}}{dt}$, so that:

$$\int_{-\infty}^{t} e^{\lambda_\beta(t-s)}.\vec{\mathcal{F}}_\gamma(s)\,ds =$$

$$\frac{1}{\tau_B}\int_{-\infty}^{t} e^{\lambda_\beta(t-s)}.V_{i_{drive}}(s)\,ds + \int_{-\infty}^{t} e^{\lambda_\beta(t-s)}.\frac{dV_{\gamma_{drive}}}{ds}(s)\,ds.$$

$$\int_{-\infty}^{t} e^{\lambda_\beta(t-s)}.\frac{dV_{\gamma_{drive}}}{ds}(s)\,ds = \left[\, e^{\lambda_\beta(t-s)}.V_{\gamma_{drive}}(s)\,\right]_{-\infty}^{t} + \lambda_\beta \int_{-\infty}^{t} e^{\lambda_\beta(t-s)}.V_{\gamma_{drive}}(s)\,ds$$

$$= V_{\gamma_{drive}}(t) + \lambda_\beta \int_{-\infty}^{t} e^{\lambda_\beta(t-s)}.V_{\gamma_{drive}}(s)\,ds$$

and:

$$\vec{\mathcal{X}}_\alpha(t) = \sum_{\beta=1}^{3N}\sum_{\gamma=1}^{3N} \mathcal{P}_{\alpha\beta}\mathcal{P}^{-1}_{\beta\gamma}V_{\gamma_{drive}}(t) + \sum_{\beta=1}^{3N}\left(\frac{1}{\tau_B} + \lambda_\beta\right)\sum_{\gamma=1}^{3N}\mathcal{P}_{\alpha\beta}\mathcal{P}^{-1}_{\beta\gamma}\int_{-\infty}^{t} e^{\lambda_\beta(t-s)}.V_{\gamma_{drive}}(s)\,ds$$

We have:

$$\sum_{\beta=1}^{3N}\sum_{\gamma=1}^{3N} \mathcal{P}_{\alpha\beta}\mathcal{P}^{-1}_{\beta\gamma}V_{\gamma_{drive}}(t) = \sum_{\gamma=1}^{3N} V_{\gamma_{drive}}(t)\left(\sum_{\beta=1}^{3N}\mathcal{P}_{\alpha\beta}\mathcal{P}^{-1}_{\beta\gamma}\right) = \sum_{\gamma=1}^{3N} V_{\gamma_{drive}}(t)\delta_{\alpha\gamma} = V_{\alpha_{drive}}(t).$$

Thus, finally:

$$\vec{\mathcal{X}}_\alpha(t) = V_{\alpha_{drive}}(t) + \sum_{\beta=1}^{3N} \left(\frac{1}{\tau_B} + \lambda_\beta \right) \sum_{\gamma=1}^{3N} \mathcal{P}_{\alpha\beta}\mathcal{P}^{-1}_{\beta\gamma} \int_{-\infty}^{t} e^{\lambda_\beta(t-s)}.V_{\gamma_{drive}}(s)\, ds, \quad \alpha = 1 \dots 3N. \tag{4.29}$$

4.3.1.5 Interpretation

Let us interpret this result. The first term is the direct effect of the drive, while the second term contains network effects. Note that this equation gives the effect of the drive on bipolar voltages ($\alpha = 1 \dots N$), as well as amacrine voltages ($\alpha = N+1 \dots 2N$) and bipolar activities ($\alpha = 2N+1 \dots 3N$). For these two last $V_{\alpha_{drive}}(t) = 0$ so that the effect is mediated by the network. Note that $V_{\gamma_{drive}}(s) = 0$ for $\gamma = N+1 \dots 3N$. We can thus write the second term as $\mathcal{E}_B^B + \mathcal{E}_A^B + \mathcal{E}_a^B$ where:

$$\mathcal{E}_B^B = \sum_{\beta=1}^{N} \left(\frac{1}{\tau_B} + \lambda_\beta \right) \sum_{\gamma=1}^{N} \mathcal{P}_{\alpha\beta}\mathcal{P}^{-1}_{\beta\gamma} \int_{-\infty}^{t} e^{\lambda_\beta(t-s)}.V_{\gamma_{drive}}(s)\, ds$$

$$\mathcal{E}_A^B = \sum_{\beta=N+1}^{2N} \left(\frac{1}{\tau_B} + \lambda_\beta \right) \sum_{\gamma=1}^{N} \mathcal{P}_{\alpha\beta}\mathcal{P}^{-1}_{\beta\gamma} \int_{-\infty}^{t} e^{\lambda_\beta(t-s)}.V_{\gamma_{drive}}(s)\, ds$$

$$\mathcal{E}_a^B = \sum_{\beta=2N+1}^{3N} \left(\frac{1}{\tau_B} + \lambda_\beta \right) \sum_{\gamma=1}^{N} \mathcal{P}_{\alpha\beta}\mathcal{P}^{-1}_{\beta\gamma} \int_{-\infty}^{t} e^{\lambda_\beta(t-s)}.V_{\gamma_{drive}}(s)\, ds.$$

These terms cant be interpreted as follows. The drive (index $\gamma = 1 \dots N$) excites the eigenmodes $\beta = 1 \dots 3N$, with a weight proportional to $\mathcal{P}^{-1}_{\beta\gamma}$. The mode β, in turn excites the index $\alpha = 1 \dots 3N$ with a weight proportional to $\mathcal{P}_{\alpha\beta}$. Thus, $\mathcal{E}_B^B$ corresponds to the effect of bipolar drive on bipolar voltages, $\mathcal{E}_A^B$ corresponds to the effect of bipolar drive on amacrine voltages, and $\mathcal{E}_a^B$ corresponds to the effect of bipolar drive on bipolar activities.

In the absence of network ($W_B^A = W_A^B = 0$) $\mathcal{L}$ is diagonal thus $\mathcal{P}_{\alpha\beta} = \delta_{\alpha\beta}$. For $\beta = 1 \dots N$, $\lambda_\beta = -\frac{1}{\tau_B}$ so that $\mathcal{E}_B^B = 0$. For $\beta = N+1 \dots 2N$, $\lambda_\beta = -\frac{1}{\tau_A}$ thus:

$$\mathcal{E}_A^B = \left(\frac{1}{\tau_B} - \frac{1}{\tau_A} \right) \sum_{\beta=N+1}^{2N} \sum_{\gamma=1}^{N} \delta_{\alpha\beta}\delta_{\beta\gamma} \int_{-\infty}^{t} e^{-\frac{1}{\tau_A}(t-s)}.V_{\gamma_{drive}}(s)\, ds = 0$$

because of $\delta_{\beta\gamma}$. The same holds for $\mathcal{E}_a^B$. Therefore, $\vec{\mathcal{X}}_\alpha(t) = V_{\alpha_{drive}}(t)$ as expected.

4.3.1.6 Response to the simple stimulus

In order to go further in the interpretation, we consider the case when the stimulus has the Gaussian form (4.2). We consider a one dimensional motion along the x direction. Cells are spaced with a distance δ so that:

$$V_{\gamma_{drive}}(t) = \frac{1}{\sqrt{2\,\pi}\,\sigma}\, e^{-\frac{1}{2}\,\frac{(\gamma\,\delta - v t)^2}{\sigma^2}},$$

It is then easy to compute the integral:

$$\int_{-\infty}^{t} e^{\lambda_\beta (t-s)} V_{\gamma_{drive}}(s)\, ds = e^{\frac{1}{2}\,\frac{\sigma^2\,\lambda_\beta^2}{v^2}}\, e^{-\frac{\lambda_\beta}{v}\,(\gamma\,\delta - v\,t)}\, \Pi\left[\frac{\lambda_\beta \sigma}{v} - \frac{1}{\sigma}\,(\gamma\,\delta - v\,t)\right]. \tag{4.30}$$

Indeed :

$$\int_{-\infty}^{t} e^{\lambda_\beta (t-s)} V_{\gamma_{drive}}(s)\, ds =$$

$$\frac{1}{\sqrt{2\,\pi}\,\sigma} \int_{-\infty}^{t} e^{\lambda_\beta (t-s)} e^{-\frac{1}{2}\,\frac{(\gamma\,\delta - v t)^2}{\sigma^2}}\, ds$$

$$= \frac{e^{\lambda_\beta\, t}}{\sqrt{2\,\pi}\,\sigma}\, e^{-\frac{\gamma^2\,\delta^2}{2\,\sigma^2}}\, e^{\frac{1}{2}\,\frac{\sigma^2\, r_{\beta\gamma}^2}{v^2}} \int_{-\infty}^{t} e^{-\frac{1}{2}\left[\frac{vs}{\sigma} - \frac{r_{\beta\gamma}\,\sigma}{v}\right]^2} ds$$

with $r_{\beta\gamma} = -\lambda_\beta + \frac{\gamma\,\delta\,v}{\sigma^2}$

$$= e^{\frac{1}{2}\,\frac{\sigma^2\,\lambda_\beta^2}{v^2}}\, e^{-\frac{\lambda_\beta}{v}\,(\gamma\,\delta - v\,t)}\, \Pi\left[\frac{\lambda_\beta \sigma}{v} - \frac{1}{\sigma}\,(\gamma\,\delta - v\,t)\right].$$

Note that this tends to zero as $t \to \pm\infty$ (as $t \to -\infty$, $\Pi(z) \sim e^{-\frac{1}{2}\,z^2}$. The term $\Pi\left[\frac{\lambda_\beta \sigma}{v} - \frac{1}{\sigma}\,(\gamma\,\delta - v\,t)\right]$ corresponds to a front propagating at speed v with a sharp rising (controlled by the function Π and $\frac{1}{\sigma}$) and an exponential decay $e^{-\frac{\lambda_\beta}{v}\,(\gamma\,\delta - v\,t)}$, for $t > \frac{\gamma\,\delta}{v}$ with a time scale λ_β^{-1} (see Fig. 4.5).

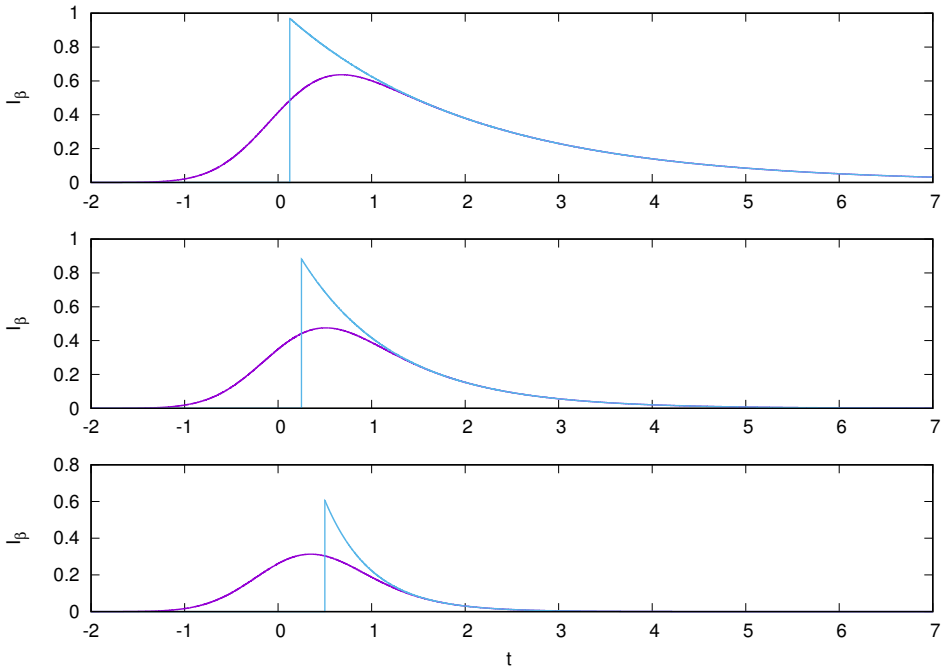

Figure 4.5: Activation mode (4.30) for different values of β (Purple). In blue is plotted the same equation when Π is a step function ($\sigma = 0$). All figures are drawn with $v = 0.2$ mm/s; $\sigma = 0.1$ mm. Up: $\lambda_\beta = 0.5\ ms^{-1}$; Middle : $\lambda_\beta = 1\ ms^{-1}$; Bottom : $\lambda_\beta = 2\ ms^{-1}$

In order to further develop the consequences of this result we consider two examples. In the next sections, for simplicity, we consider the case $w_- = w_+ = w$ and $\tau_A = \tau_B$ so that $\frac{1}{\tau} = 0$. In this case, from (4.21), $\lambda_n^\pm = -\frac{1}{\tau_A} \pm w\sqrt{-\kappa_n}$. Thus, when $\kappa_n > 0$ eigenvalues are stable, complex, whereas, when $\kappa_n < 0$ they are real and destabilize if:

$$w > \frac{1}{\tau_A}\frac{1}{\sqrt{-\kappa_n}} \equiv w_{nc}. \tag{4.31}$$

In the simulations we avoid cases when $\kappa_n = 0$.

4.3.2 Nearest neighbours interactions

We consider here the case where the matrix $\mathcal{W}$ connecting amacrines to bipolar is a matrix of nearest neighbours symmetric connections. In this case, it can be written in terms of the discrete Laplacian Δ on a d dimensional regular lattice, $d = 1, 2$ with lattice spacing $\delta_A = \delta_B$, set here equal to 1:

$$\mathcal{W} = 2d\, I + \Delta. \tag{4.32}$$

As $W_B^A = -w^- \mathcal{W}$, the coefficient $D = w^-\, \delta^2$, in mm^2/s is a diffusion coefficient. Thus, in contrast to gap junctions, we expect here a diffusive effect.

We also assume that dynamics holds on a square lattice with null boundary conditions. That is, amacrine and bipolar cells are located on d-dimensional grid with indices $i_x, i_y = 0 \dots L+1$ where, the voltage and activity of cells with indices $i_x = 0$, $i_x = L+1$, $i_y = 0$ or $i_y = L+1$, vanishe.

We note $\vec{\psi}_n$ the eigenvectors of Δ with eigenvalue s_n, $\Delta\vec{\psi}_n = s_n\vec{\psi}_n$ where $n = n_x$ in one dimension and $n = (\, n_x, n_y\,)$, in two dimensions $n_x, n_y \in \{\, 1 \dots L\,\}$. The eigenvalues of $\mathcal{W}$ are then $\kappa_n = (\, 2d + s_n\,)$. Using the Greek indices notation introduced above we define $\alpha = i_x \in \{\, 1 \dots L = N\,\}$ in one dimension and $\alpha = i_x + (i_y - 1)\, L \in \{\, 1 \dots L^2 = N\,\}$ in two dimensions. Likewise, we set $\beta = n_x \in \{\, 1 \dots L = N\,\}$ in one dimension and $\beta = n_x + (n_y - 1)\, L \in \{\, 1 \dots L^2 = N\,\}$ in two dimensions. The eigenvectors and eigenvalues of $\mathcal{W}$ have the form:

$$\begin{aligned} \psi_{\alpha\beta} &= \left(\, \tfrac{2}{L+1}\,\right)^{\frac{d}{2}} \textstyle\prod_l \sin\left(\, \tfrac{n_l \pi}{L+1}\, i_l\,\right), \\ \kappa_n &= 2 \textstyle\sum_l \left[\, \cos\left(\, \tfrac{n_l\pi}{L+1}\,\right)\,\right]; \end{aligned} \tag{4.33}$$

with $l = x$ for $d = 1$ and $l = x, y$ for $d = 2$. Especially, in one dimension:

$$\psi_{\alpha\beta} = \sqrt{\frac{2}{L+1}} \sin\left(\, \frac{\alpha\pi}{L+1}\, \beta\,\right),$$

The quantum numbers $n = (\, n_x, n_y\,)$ define a wave vector $\vec{k}_n = \left(\, \tfrac{n_x\pi}{L+1}, \tfrac{n_y\pi}{L+1}\,\right)$ corresponding to wave length $\left(\, \tfrac{L+1}{n_x}, \tfrac{L+1}{n_y}\,\right)$. Hence the first eigenmode $(1,1)$ corresponds to the largest space scale (scale of the lattice) with the smallest eigenvalue (in absolute value) $s_{(1,1)} = 2\left(\, \cos\left(\, \tfrac{\pi}{L+1}\,\right) + \cos\left(\, \tfrac{\pi}{L+1}\,\right) - 2\,\right)$. In a diffusion equation:

$$\frac{dX}{dt} = D\Delta X, \tag{4.34}$$

the projection on the eigenmode $\vec{\psi}_n$ reads $X_n(t) = X_n(0)e^{D\, s_n t} - \frac{1}{D\, s_n}\left[\, 1 - e^{D\, s_n t}\,\right]$ with $s_n < 0$. Thus $D\, s_n$ is the inverse of a characteristic time scale, the time required for the projection on eigenmode n to relax to equilibrium. In particular, the slowest time scale is $\tau_{1,1} = \frac{1}{D|\, s_{1,1}\,|}$ corresponding to the largest time scale.

Likewise, $w^-\, \kappa_n$ has the dimension of an inverse characteristic time τ_n. As n increases κ_n increases so that τ_n decreases. The slowest mode is the mode $(\, 1, 1\,)$ Note that, if L is large $\cos\left(\, \tfrac{\pi}{L+1}\,\right) \sim 1 - \left(\, \tfrac{\pi}{L+1}\,\right)^2$ so that $s_{1,1} \sim -\frac{4\pi^2}{(L+1)^2}$ and $\tau_{1,1} \sim \frac{(L+1)^2}{4\pi^2}$. Thus, the characteristic time goes like the square of the distance (diffusion).

Therefore, in contrast to gap junctions where the network effect induced by the network was a ballistic propagation, at a speed depending on the gap junction con-

ductance, here, the expected effect of the stimulus is a diffusive propagation. Thus, the only effect that could enhance anticipation here would be an enlargement of the drive response.

Eigenvalues κ_n can be positive or negative. From section 4.3.1.2 we have therefore several situations entailing the stability of the eigenmodes. For simplicity, we restrict here to 1 dimension, where $\kappa_n = 2\ \cos\left(\ \frac{n_l \pi}{L+1}\ \right)$. We choose L even to avoid having a zero eigenvalue $\kappa_{\frac{L}{2}}$.

Eigenvalues κ_n, $n = 1 \dots \frac{L}{2}$ are positive, thus the corresponding eigenvalues $\lambda_n^{\pm}$ of $\mathcal{L}$ are complex, and stable. The modes with the largest space scale $\frac{L}{n}$ are therefore stable, with oscillations. Eigenvalues κ_n, $n = \frac{L}{2} + 1 \dots L$ are negative, thus the corresponding eigenvalues $\lambda_n^{\pm}$ of $\mathcal{L}$ are real. From (4.31) the mode n becomes unstable when $w > w_{nc} = \frac{1}{\tau_A} \frac{1}{\sqrt{-2\ \cos\left(\ \frac{n\pi}{L+1}\ \right)}}$.

Therefore, the first mode to become unstable is the mode L with the smallest space scale 1 (lattice spacing) (See 4.6). For large L, this happens for $w = w_{1c} \sim \frac{1}{\sqrt{2}} \frac{1}{\tau_A}$. This instability induces spatial oscillations at the scale of the lattice spacing (). When w further increases the next modes becomes unstable. This instability results in a wave packet following the drive. The width of this wave packet is controlled by the unstable modes. The gain control prevents the unstable modes to give rise to a divergence of the response (compare Fig. 4.6 left, and Fig. 4.7).

We illustrate these effects in Fig. 4.6 and 4.7.

We now discuss the network effects on anticipation. In Fig. 4.8 we show the activity variable R_{B_i} ((3.10)) for the bipolar cell $N/2$ located in the middle of lattice, in the same conditions as fig. 4.6. Finally, figure 4.9 show the same results in time. In particular, the more the peak response of $R_{B_i}(t)$ is in advance, the lower it is.

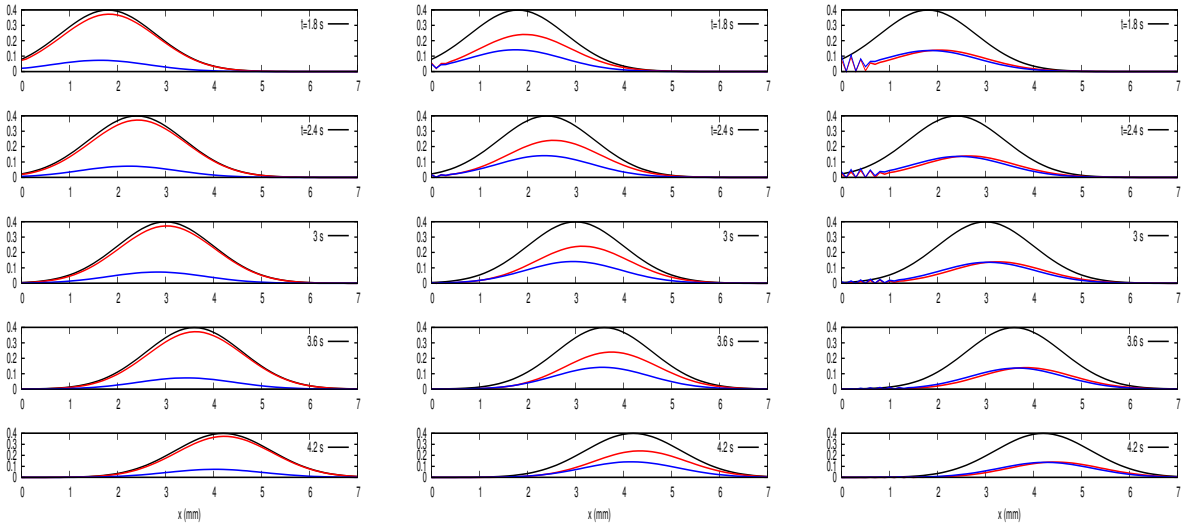

Figure 4.6: . Effect of a Gaussian drive (in black) propagating in one dimension, on the bipolar cells voltage (red) and on the amacrine cells voltage (blue). There are 100 cells, spaced by 0.1 mm. The Gaussian drive (4.2) travels at a speed $1mm/s$. Other parameters are fixed as in the Appendix. We illustrate the effects on increasing the coupling w, where $w^+ = w$, $w^- = -w$, with $\frac{1}{\tau} = 0$. Left. Weak coupling. $w = 1\ s^{-1}$. Middle. Moderate coupling where $w = 3\ s^{-1}$. Here w is smaller than the first instability threshold (here $w_{99,c} = 3.53639\ s^{-1}$) given by (4.31). Right. Strong coupling, $w = 5$, above the instability threshold $w_{67,c} = 3.53639\ s^{-1}$. That is the modes $n = 67, \dots, 99$ are linearly unstable here, but gain control and the non linearity stabilize the divergence. Compare with fig. 4.7 below.

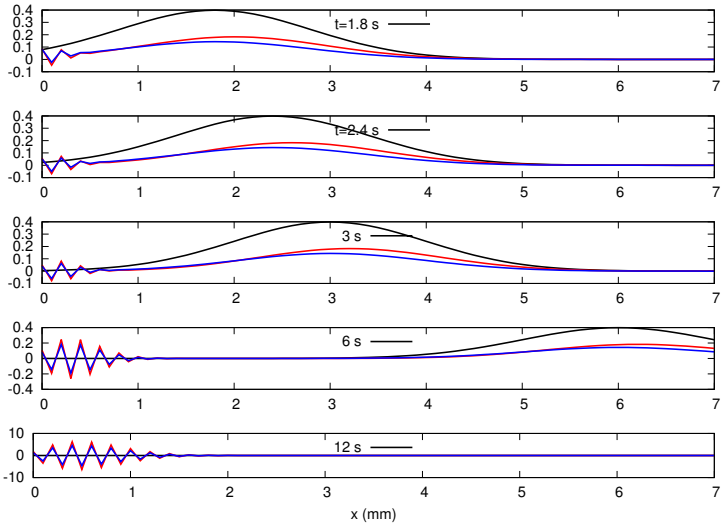

Figure 4.7: . Same as 4.6, without gain control and the non linearity, for $w = 4$, thus above the threshold $w_{79,c}$. That is, modes 79 to 99 are unstable. One sees an exponential growth and a diffusion of the wave packet induced by the initial drive (Note the change in scale on the vertical axis).

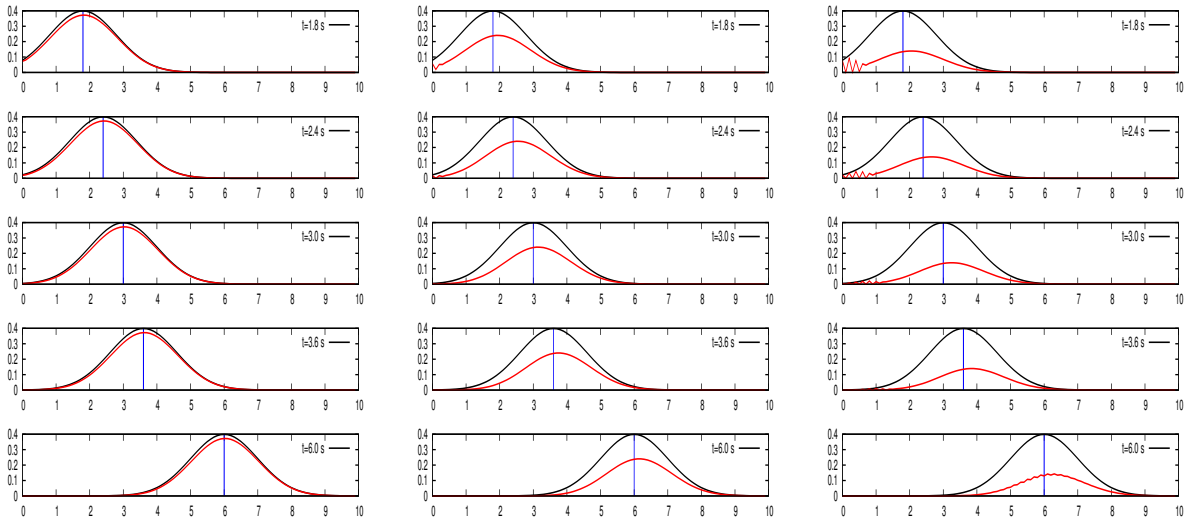

Figure 4.8: . Spatial profil of $R_{B_i}(t)$ ((3.10)) , for different times, under a Gaussian drive, in the same conditions as in Fig. 4.6. The blue vertical line gives the location of the peak in the Gaussian drive. On the left ($w = 1\ s^{-1}$) the lattice effects on anticipation are negligible. In the middle, ($w = 3\ s^{-1}$) the excitation of fast modes leads to a spatial pattern, propagating without deformation at the same speed as the drive. The peak response of $R_{B_i}(t)$ is slightly ahead of the drive peak. On the right ($w = 5\ s^{-1}$). The peak in $R_{B_i}(t)$ is more in advance than for $w = 3$, with a lower amplitude. One ca see (bottom line) small oscillations due to the unstable modes.

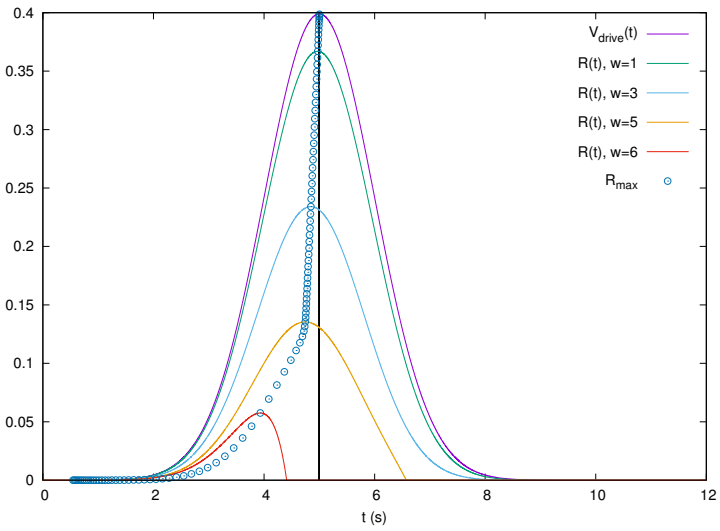

Figure 4.9: . Temporal profil of a gain control $R_{B_i}(t)$ ((3.10)) , for different values of w, under a Gaussian drive, in the same conditions as in Fig. 4.6. The peak in $R_{B_i}(t)$ is more in advance larger values of w, with a lower amplitude. R_{max} denotes the analytic peak position.

Partial conclusion

In this section, we have shown the role played by gain control and the non linearity in the stability of the system. Using a Gaussian drive, we have also been able to show, in the case of a Laplacian graph of connectivity, an anticipatory effect which increases with the coupling weight. The case of the random graph being hard to handle analytically, we shall study it through numerical simulations in the following chapter.

Chapter 5

Simulations results of the retina model

In this chapter, we will study, through numerical simulation, how anticipation time depends on the stimulus features, for the three anticipatory mechanisms we introduced earlier (gain control, amacrine connectivity and gap junction connectivity).
Then we study the amacrine connectivity (resp. gap junction connectivity) model, and assess the role of intrinsic parameters of the model (mainly the connectivity weights), in anticipation.
Finally, we present 2D responses to different kind of stimuli in order to assess qualitatively anticipatory effects for stimuli more complex than a simple moving bar.

5.1 Anticipation variability with bar's characteristics

In this section we illustrate how anticipation varies when varying stimulus characteristics: contrast, size and speed. This calibration is later used to compare to effects induced by lateral connectivity. The results are presented in Fig. 5.1.
We first observe that anticipation increases with contrast, as is has experimentally been observed. Indeed, increasing the contrast increases $V_{i_{drive}}(t)$ thereby accelerates the growth of A_i so that gain control takes place earlier. Fig 5.1 a).
We also notice that anticipation increases with the size of the object until a maximum (Fig 5.1 b).
The model shows a decrease in anticipation as a function of velocity, as it was evidenced experimentally (Fig 5.1 c). Indeed, when the velocity increases, V_{drive} varies faster, and with τ_a being constant, the adaptation peak value is lower. Consequently, gain control has a weaker effect and the peak activity is less shifted than when the bar

is slow.

Finally, the maximum firing rate increases with the velocity, the contrast and the size.

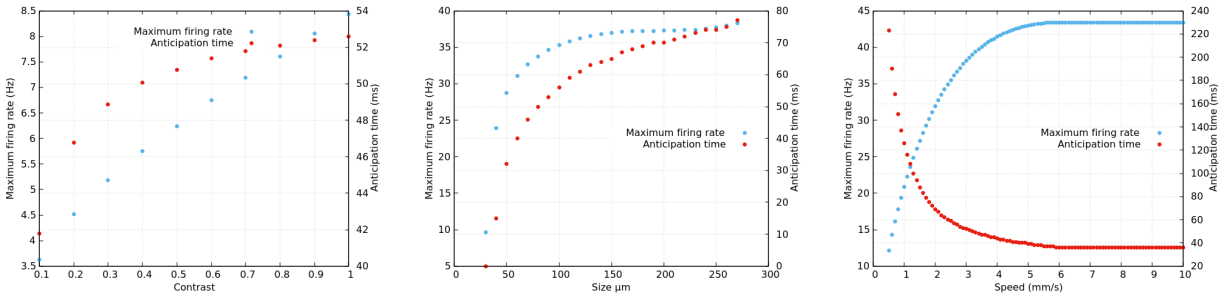

Figure 5.1: Maximum firing rate and anticipation time variability with stimulus parameters in the gain control layer of the model. a) contrast; b) size; c) speed.

5.2 Amacrine connectivity

In the following, we only study bipolar cells contribution to anticipation, via the amacrine connectivity circuit. We recall here the diffentential system governing the behavior of bipolar and amacrine cells when responding to a stimulus:

$$\begin{cases} \frac{dV_{B_i}}{dt} &= -\frac{1}{\tau_B} V_{B_i} + \sum_{j=1}^{N_A} W_{B_i}^{A_j} V_{A_j} + F_{B_i}(t), \\ \frac{dA_{B_i}}{dt} &= -\frac{A_{B_i}}{\tau_a} + h\mathcal{N}(V_{B_i}(t)), \\ \frac{dV_{A_j}}{dt} &= -\frac{1}{\tau_A} V_{A_j}(t) + \sum_{i=1}^{N_A} W_{A_j}^{B_i} R_{B_i}(t). \end{cases} \tag{5.1}$$

τ_a and h being adaptation constants that have been fitted on experimental data, our aim here is to identify the range of the remaining parameters (τ_A, τ_B, $W_{B_i}^{A_j}$ and $W_{A_j}^{B_i}$) which allow this circuit to significantly improve anticipation, as compared to gain control alone.

5.2.1 Anticipation variability : Laplacian connectivity

Under the assumption that the characteristic time of the bipolar voltage and the amacrine voltage are within the same order of magnitude as the characteristic time of adaptation, we set $\tau_B = \tau_A = 100ms$ $\tau_a = 100.5ms$, and we vary the value of weight. For the sake of simplicity, we also choose $w^+ = -w^-$.

We run several simulations to identify the range of values where the effect of

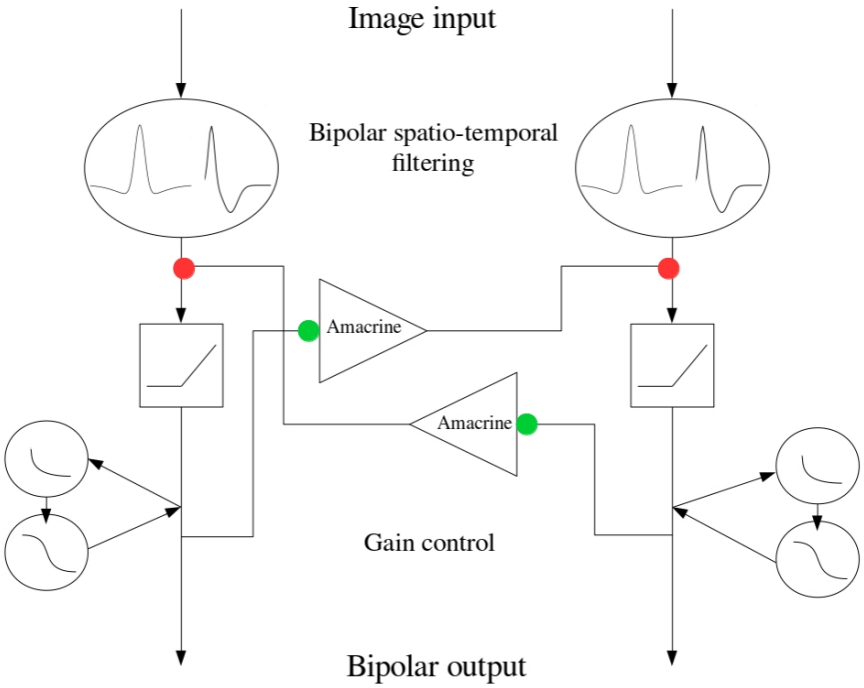

Figure 5.2: Schematic of the amacrine connectivity. Green points denote an excitatory connection while red points denote an inhibitory one. This figure shows the case of Laplacian connectivity

amacrine connectivity outperforms gain control. We show in the following the response of bipolar cells to a moving bar, with a width $= 200\mu m$, moving at $2mm/s$. The bipolar cells are placed on a 1D horizontal grid, with a spacing of $20\mu m$ between to consecutive cells. The first cell lies at $100\mu m$ from the leading edge of the moving bar. Cells are connected according to a nearest neighbor graph : one amacrine cell receives activity from the downstream bipolar cell, and is connected to the 2 surrounding bipolar cells (4 in case of a 2D grid).

Fig. 5.3 shows the reference response of bipolar cells without amacrine connectivity. The response of bipolar cells in this reference case will be reported in dashed lines on the following figures for comparison.

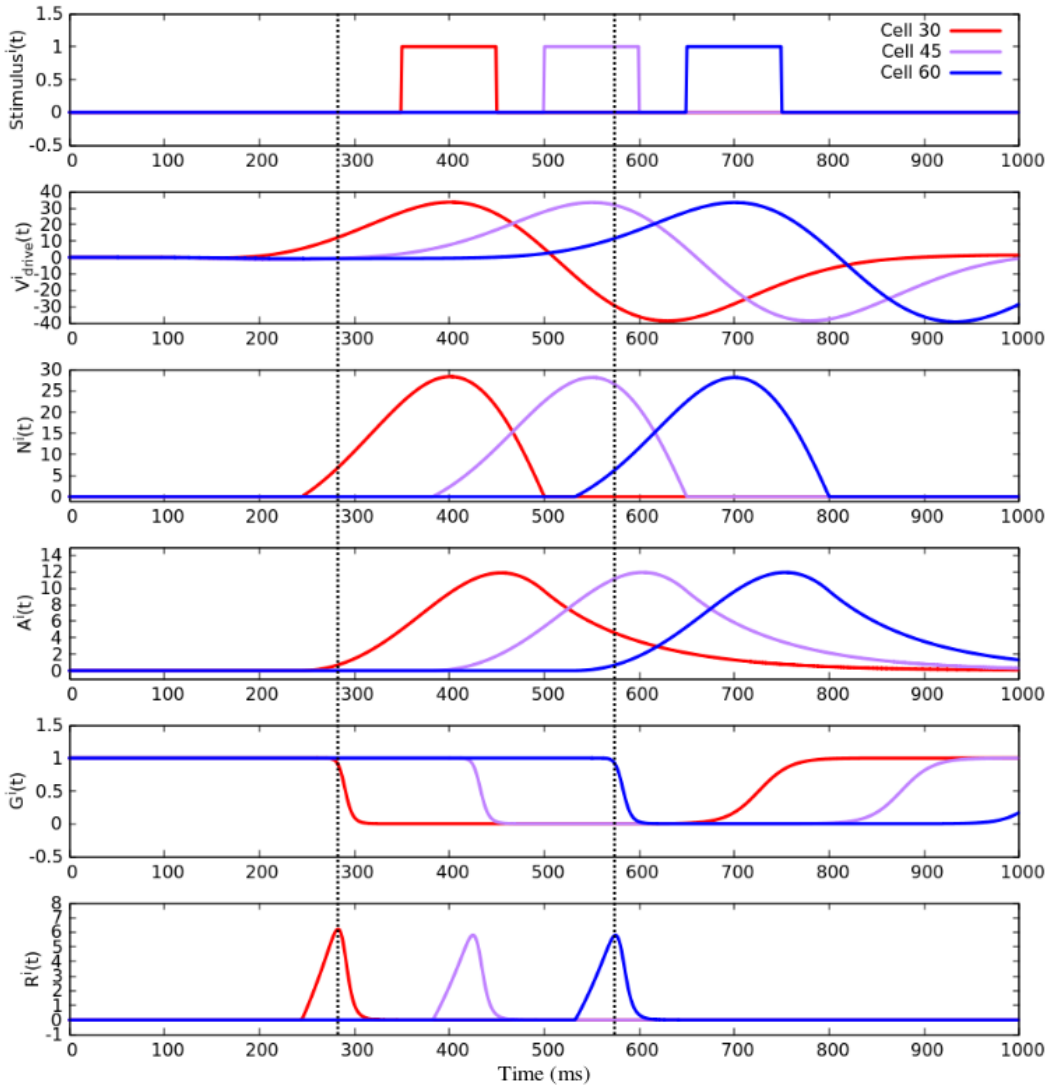

Figure 5.3: Response of bipolar cells without amacrine connectivity shows that the peak of the gain control response $R_i(t)$ occurs prior to the linear non-linear response $N_i(t)$. The curves correspond to three cells spaced by $200\mu m$.The first line shows the stimulus time course, which is equal to 1 when the location of the cell is dark and 0 otherwise. The second line shows the linear filtering of the stimulus, corresponding to a spatio-temporal convolution with a kernel. The 3^{rd} line corresponds to a thresholding non-linearity applied to the linear response, the 4^{th} to the adaptation function (see 5.1, the 5^{th} line to the gain control. Finally, the last line corresponds to the response of the cells.

Fig. 5.4 shows the response of bipolar cells when plugging the amacrine connectivity, setting $w^+ = -w^- = 0.03ms^{-1}$. For consistancy, we show in the first of this figure the spatio-temporal filtering prior to the dynamical system, which is identical to the filtering of the reference figure. In this case, the inhibitory effect of amacrines changes the shape of the the bipolar voltage curve, however not strongly enough to completely cancel out the effect of gain control. Indeed, the peak of $R^i(t)$ occurs before the peak of $N^i(t)$, while it lags behind the reference peak. In this regime, amacrine

connectivity has a negative effect on anticipation.

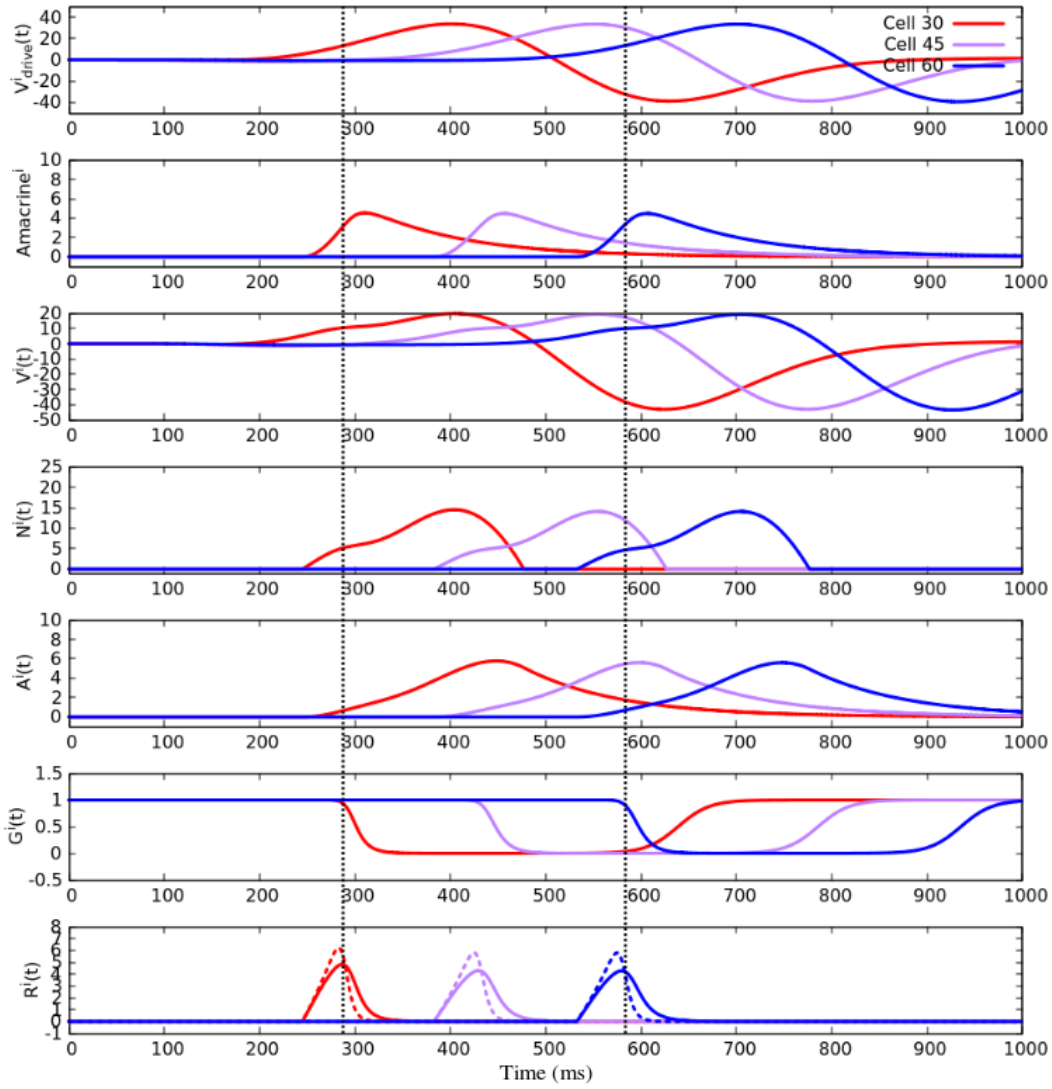

Figure 5.4: Response of bipolar cells with amacrine connectivity, with $W_{B_i}^{A_j}$ = -$W_{A_j}^{B_i}$ = $0.03ms^{-1}$. The peak of the gain control response $R_i(t)$ occurs before the linear non-linear response $N_i(t)$ reaches its maximum, indicating that in this regime, gain control still plays a role. The peak of activity with amacrine connectivity is reached slightly after the gain control peak.

Fig. 5.5 shows the response of bipolar cells when setting $w^+ = -w^- = 0.05ms^{-1}$. In this case, the inhibitory effect of amacrines strongly alters the shape of the the bipolar voltage curve, and the gain control effect becomes negligible. The peak of $R^i(t)$ occurs at the exact same time as the peak of $N^i(t)$, and before the reference peak. In this regime, amacrine connectivity has a positive effect on anticipation.

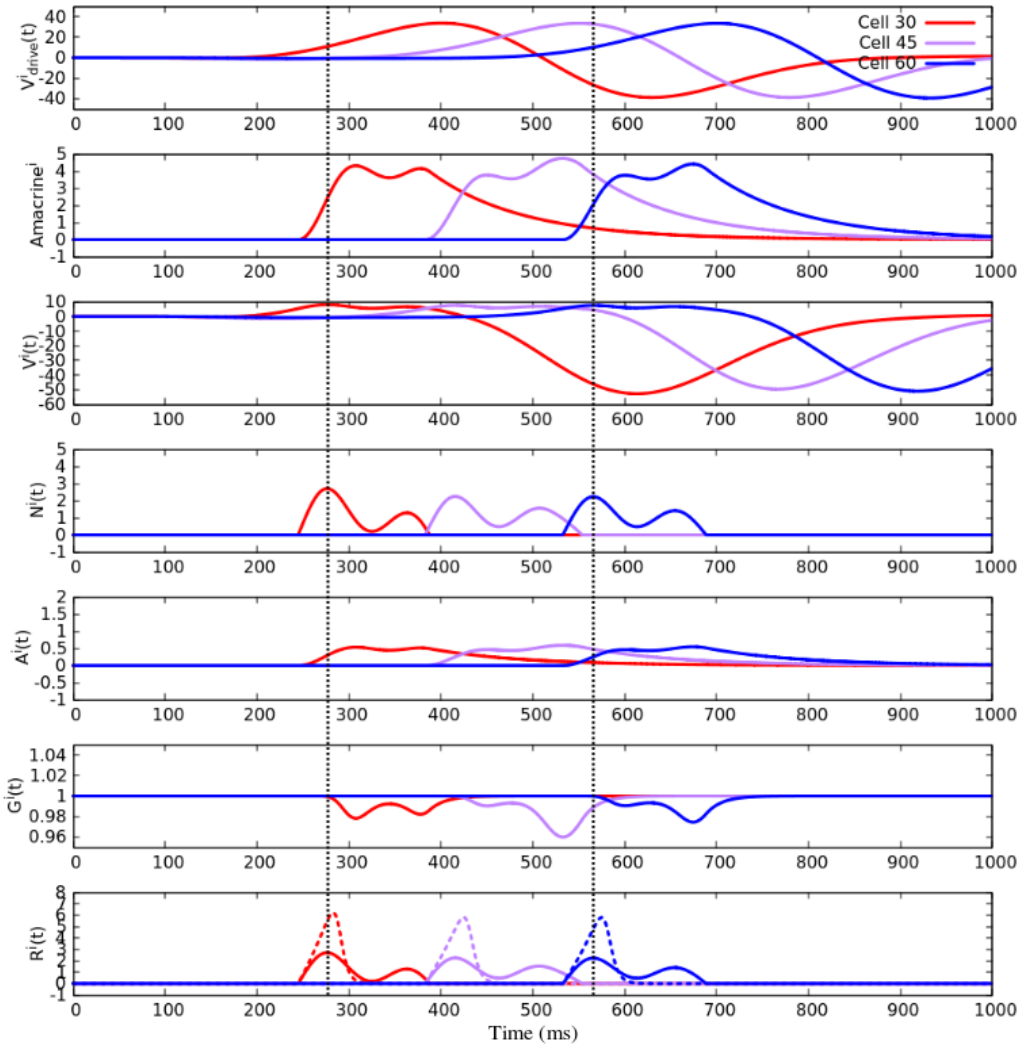

Figure 5.5: Response of bipolar cells with amacrine connectivity, with $W_{B_i}^{A_j}$ = -$W_{A_j}^{B_i}$ = $0.05ms^{-1}$. The peak of the gain control response $R_i(t)$ occurs at the same time as the linear non-linear response $N_i(t)$, indicating that bipolar gain control has a negligible effect when cells are coupled, within this intermediate regime. The peak of activity with amacrine connectivity is reached before the gain control peak, showing that amacrine connectivity improves anticipation.

Fig. 5.6 shows the response of bipolar cells when setting $w^+ = -w^- = 0.1ms^{-1}$. In this case, amacrine connectivity has a heterogeneous effect on bipolar cells : the further we move from the bar, the weaker is the effect of inhibition. However, over all positions, the peak of $R^i(t)$ occurs before the peak of $N^i(t)$, and after the reference peak, similarly to the weak coupling. In this regime, amacrine connectivity has a negative effect on anticipation. It should also be noted that within this range of parameters and given the Laplacian connectivity, the effect on cells is not homogeneous, with regards to the parity of the cell's index.

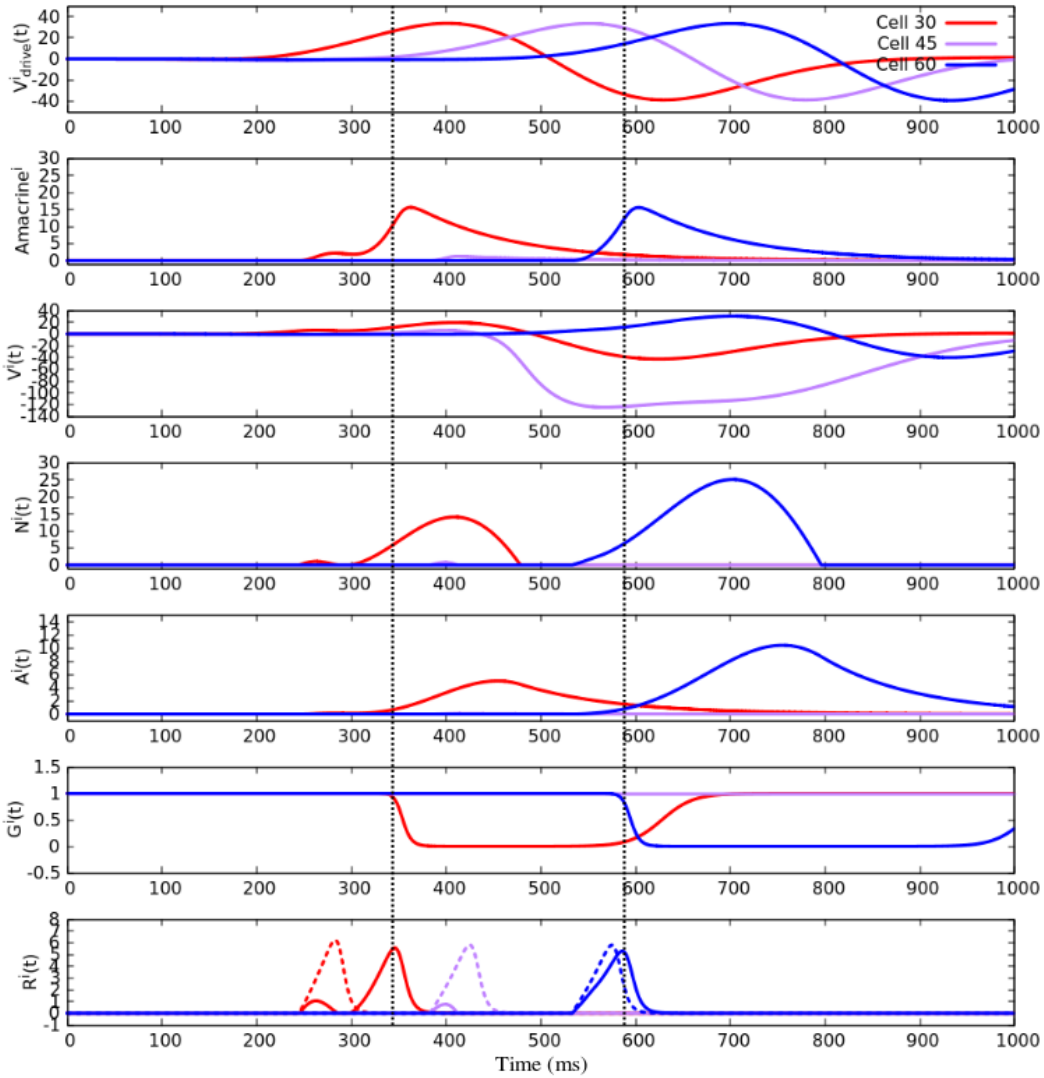

Figure 5.6: Response of bipolar cells with amacrine connectivity, with $W_{B_i}^{A_j}$ = -$W_{A_j}^{B_i}$ = $0.1ms^{-1}$. The peak of the gain control response $R_i(t)$ occurs before the linear non-linear response $N_i(t)$ reaches its maximum, indicating that in this regime, gain control plays a role again in anticipation. The peak of activity with amacrine connectivity is reached after the gain control peak for cells with even indexes and the response is negligible for cells with odd indexes.

Finally, Fig. 5.7 shows the response of bipolar cells when setting $w^+ = -w^- = 0.15ms^{-1}$. Similarly to the previous case, the effect on cells depends on the parity of their index. In this case, the response of bipolar cells is either completely suppressed or identical to the response of the reference case (with gain control alone). In this regime, amacrine connectivity doesn't have any effect on anticipation.

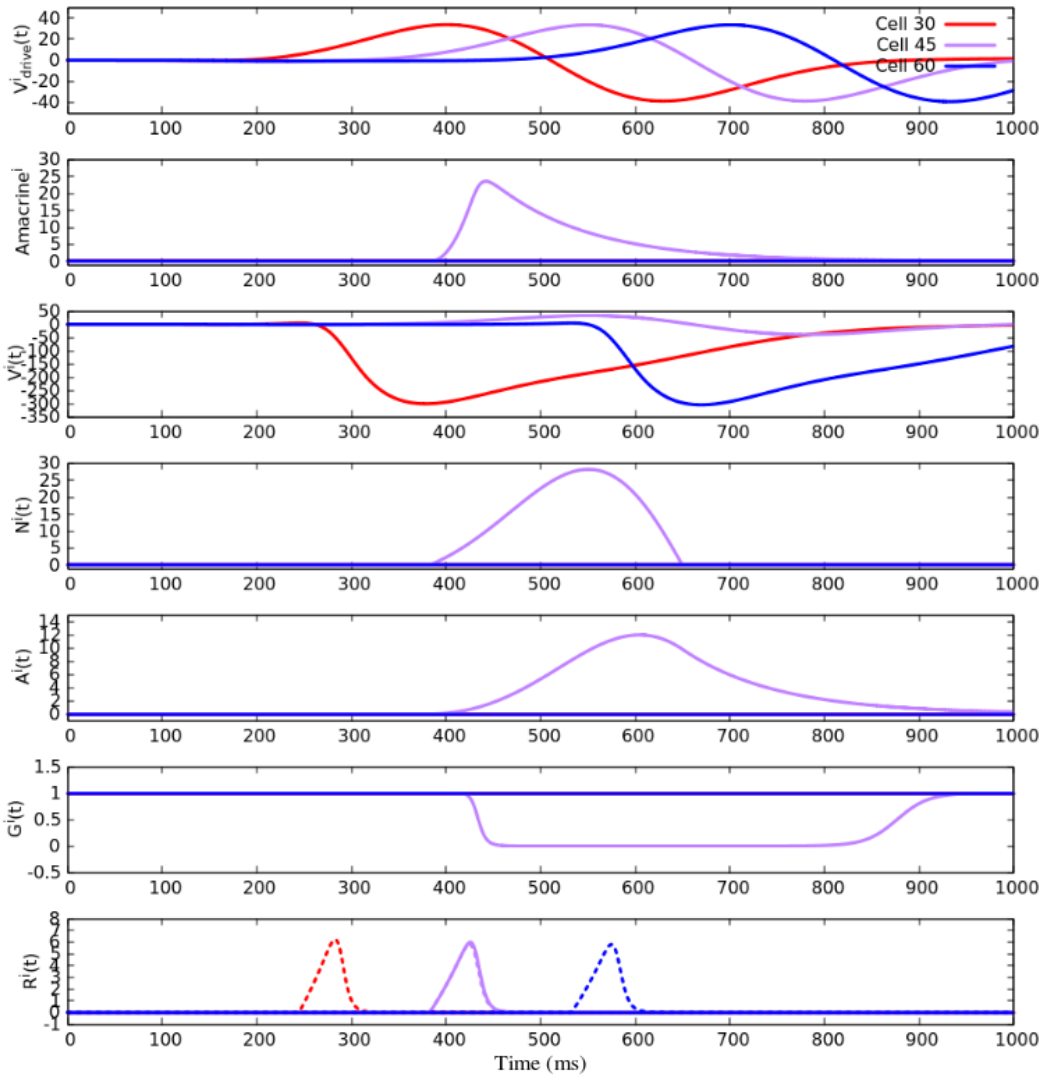

Figure 5.7: Response of bipolar cells with amacrine connectivity, with $W_{B_i}^{A_j}$ = -$W_{A_j}^{B_i}$ = $0.15ms^{-1}$. Cells with even indexes are completely suppressed while cells with odd indexes have a response which is identical to the reference case.

It would appear, through these test figures, that there is an intermediate interval in which amacrine connectivity is advantageous for anticipation, with a marginal role played by gain control. To verify this hypothesis, we plot the anticipation time and the maximum firing rate as a function of the coupling strength. Fig. 5.8 shows the existence of three areas of interest: the first corresponds to the two regimes where amacrine connectivity has a relatively negative effect on anticipation, and where gain control has a significant effect (curves with and without gain control do not match in these zones). The second zone corresponds to the interval over which the two curves coincide, which means that gain control plays there a negligible role. Furthermore, anticipation time is higher than the one of the circuit without amacrines (the point corresponding to a null weight). Finally, the third zone corresponds to the steady state

where only the presence or absence of gain control plays a role.

We then vary the value of τ_B and τ_A and plot the same curves. When $\tau_B = \tau_A = 50ms$, the intermediate zone where the curves with and without gain control coincide is inexistant, and the amacrine connectivity doesn't improve anticipation. When $\tau_B = \tau_A = 200ms$, the intermediate zone is larger than the one of when $\tau_B = \tau_A = 100ms$, with a higher maximum of the anticipation curve. This shows that the increase of τ_B and τ_A plays a positive role in anticipation. Regarding the maximum firing rate, its value decreases within the intermediate interval, showing that amacrine connectivity increases the coding efficiency.

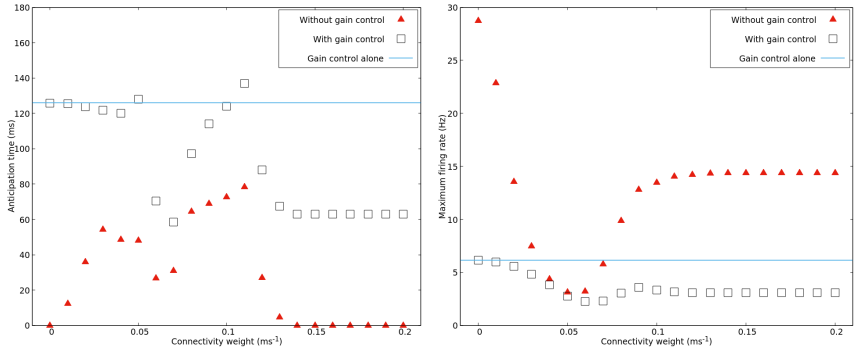

(a) τ = 50 ms

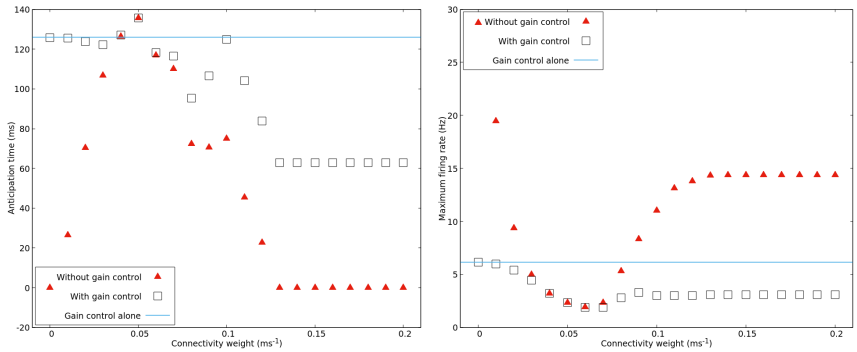

(b) τ = 100 ms

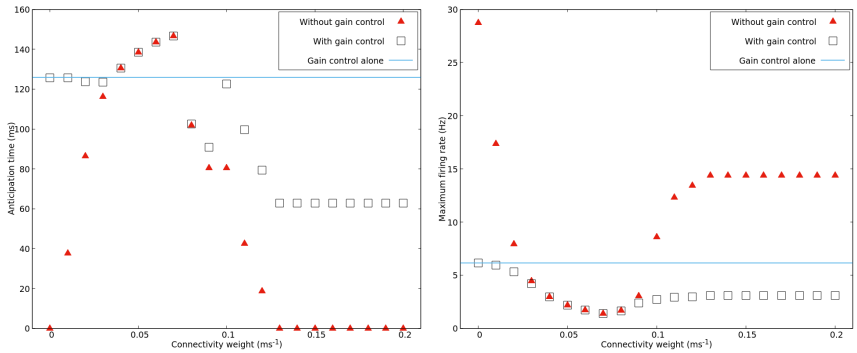

(c) τ = 200 ms

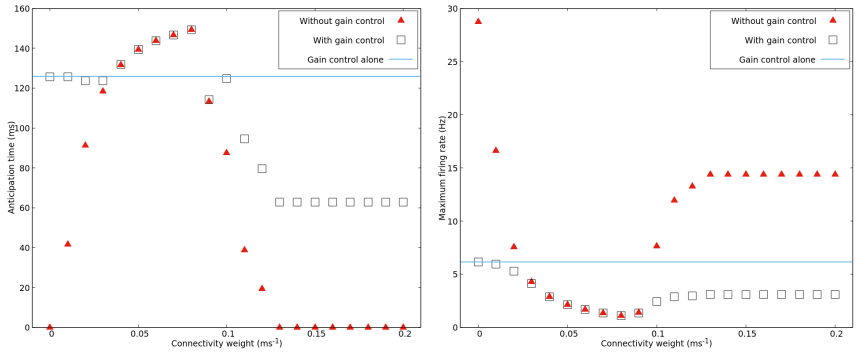

(d) τ = 300 ms

Figure 5.8: Anticipation time (left) and maximum firing rate (right) with respect to the strength of the amacrine coupling. The results correspond to the plugging and unplugging of bipolar gain control on the amacrine connected circuit.

5.2.1.1 The role of non linearity

We want now to understand the role played by the non linearity in the system. For that we compare anticipation time and maximum firing rate switching on and off the non linear function $\mathcal{N}(V)$.

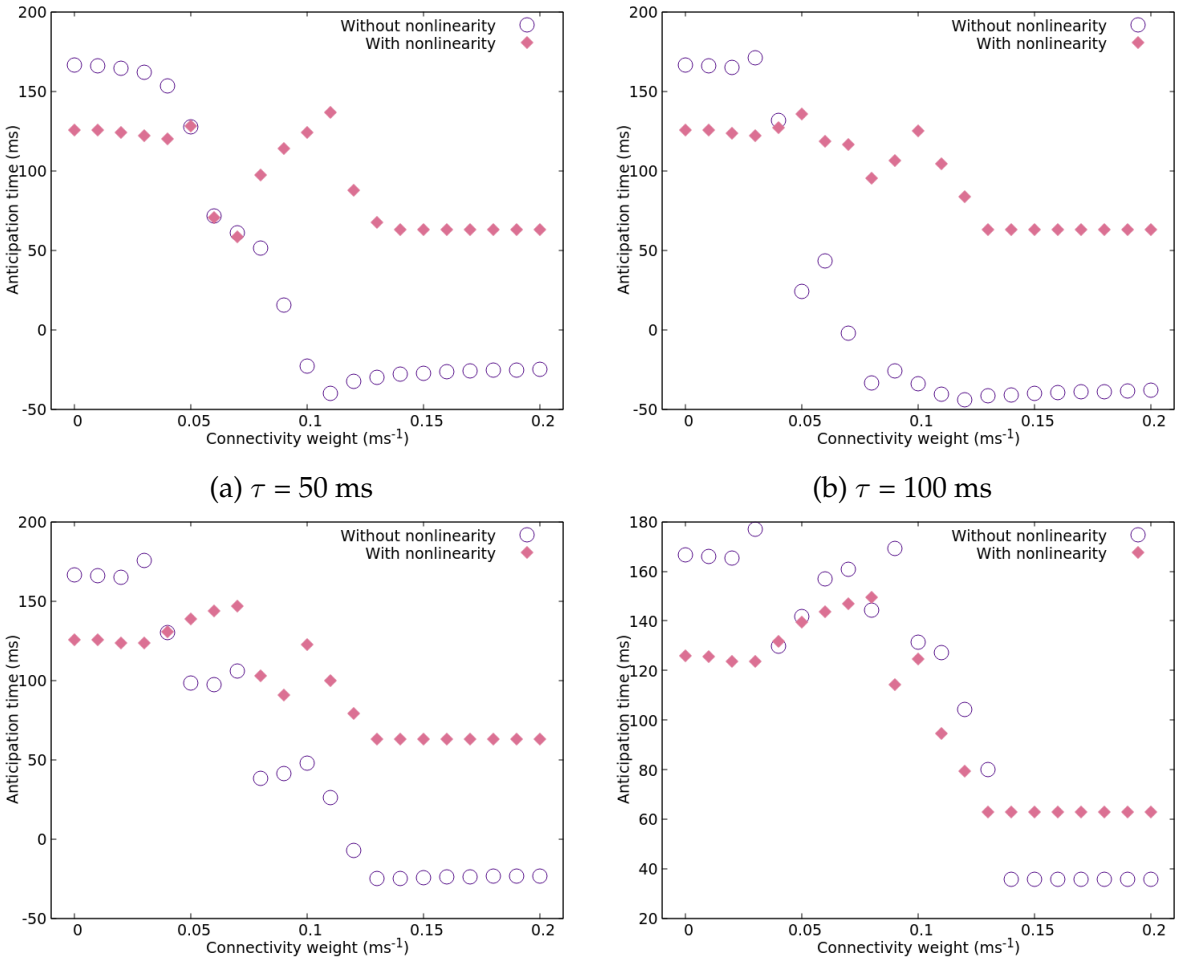

(a) τ = 50 ms (b) τ = 100 ms

(c) τ = 200 ms (d) τ = 300 ms

Figure 5.9: Anticipation time with respect to the strength of the amacrine coupling. The results correspond to the on and off switching of the bipolar non linearity on the amacrine connected circuit, while keeping gain control.

Fig. 5.9 shows the behavior of the system in terms of anticipation time when turning off the non linearity, while keeping gain control. There are three major intervals : the first where the anticipation functions (with and without non linearity) are quasi constant, and where the absence of the non linearity outperforms its presence. The last interval, where the system reaches its steady state, corresponds to the interval where amacrine connectivity doesn't play a role anymore (see Fig. 5.8). In this region, the presence of the non linearity outperforms its absence. Finally, in the intermediate interval where both the curves are varying, the non linearity generally improves the

anticipation capacity of the system, except for the case where $\tau = 300ms$. As for the maximum firing rate (Fig. 5.10) , the curves roughly coincide for week coupling (up to $W_{B_i}^{A_j}$ = -$W_{A_j}^{B_i} \approx 0.05ms^{-1}$), and the curve without non linearity branches off after this point, which shows that the non linearity has a shunting effect on the system.

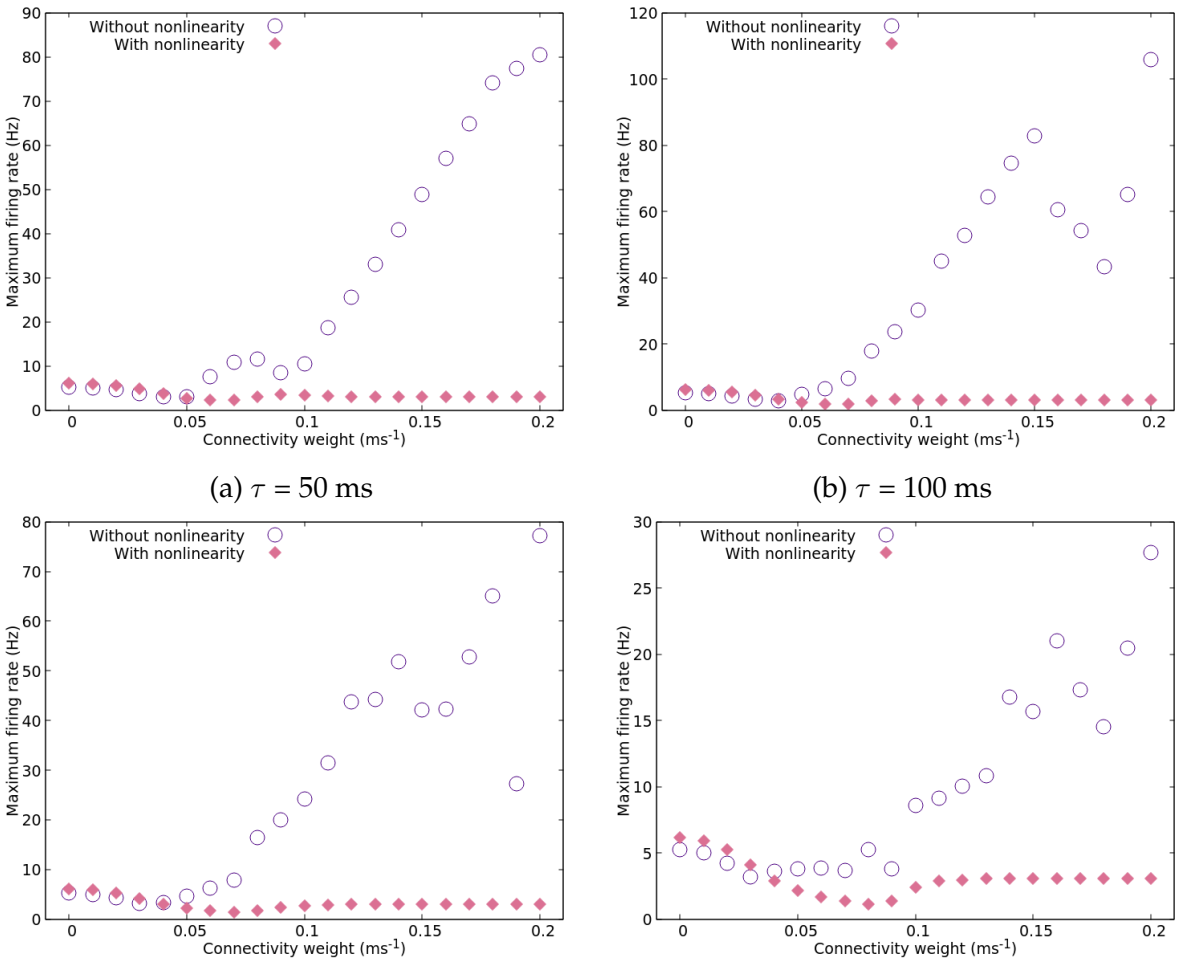

(a) τ = 50 ms

(b) τ = 100 ms

(c) τ = 200 ms

(d) τ = 300 ms

Figure 5.10: Maximum firing rate with respect to the strength of the amacrine coupling. The results correspond to the on and off switching of the bipolar non linearity on the amacrine connected circuit, while keeping gain control.

5.2.2 Probabilistic connectivity

5.2.2.1 The effect of symmetry

In this section, we will study the behavior of the system using the probabilistic model of connectivity. Within this framework, a given amacrine cell A_i receives the upstream activity from the bipolar lying at the same position, B_i, with a constant weight w. The same amacrine cell inhibits bipolar cells with which it is coupled through the random adjacency matrix, generated by the probabilistic model of connectivity. We recall that the model has two parameters : the maximum length of branches and the maximum number of branches, which are drawn according to an exponential distribution. The angle of each branch is drawn according to a uniform distribution $\mathcal{U}[0 : 2\pi]$. The weight matrix W_A^B will then consist of the adjacency matrix multiplied by a constant weight w.

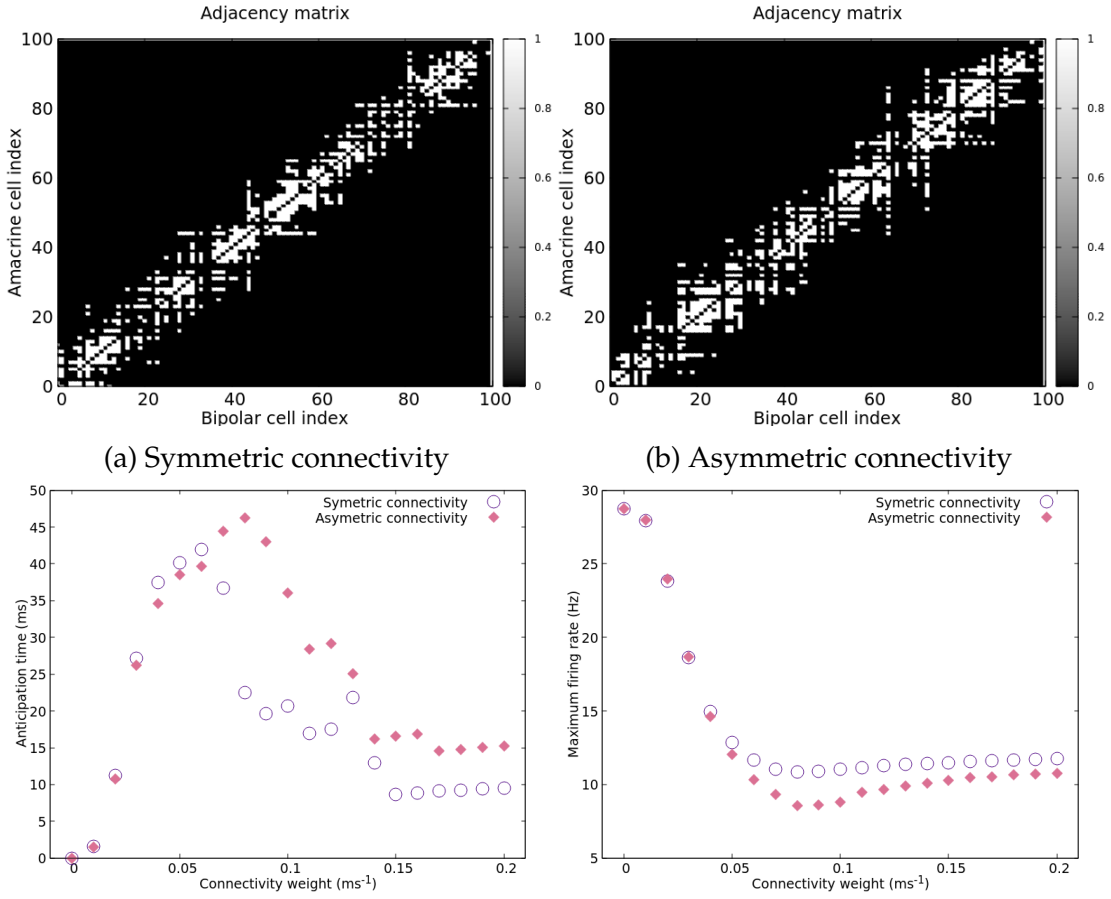

(a) Symmetric connectivity

(b) Asymmetric connectivity

(c) Anticipation time

(d) Maximum firing rate

Figure 5.11: a) and b) Symmetric and asymmetric Adjacency matrices drawn using the probabilistic model of connectivity. c) The effect of symmetry on anticipation time, d) on maximum firing rate.

We first investigate how the symmetry of this matrix affects anticipation. A sym-

metric matrix means that connectivity is position driven : if the amacrine cell A_i is connected to the bipolar cell B_j then the amacrine cell A_j is connected to the bipolar cell B_i. Using the same parameters, we draw two adjacency matrices, symmetric and asymmetric, and compute anticipation time and maximum firing rate in each case. Fig. 5.11 shows that for low values of weights, both symetric and asymetric connectivity perform similarly. Above a certain value of weight (around $0.04ms^{-1}$), the asymmetric connectivity outperforms the symmetric one : the anticipation time is higher while the maximum firing rate is lower.

5.2.2.2 Random connectivity and gain control

We study how the system anticipates when random connectivity is coupled with gain control. In contrast with the laplacian connectivity, in this framework, we were not able to identify a regime of connectivity weights where the effect of gain control can be neglected : for all values of weights, gain control improves the anticipatory effect and decreases firing rate.

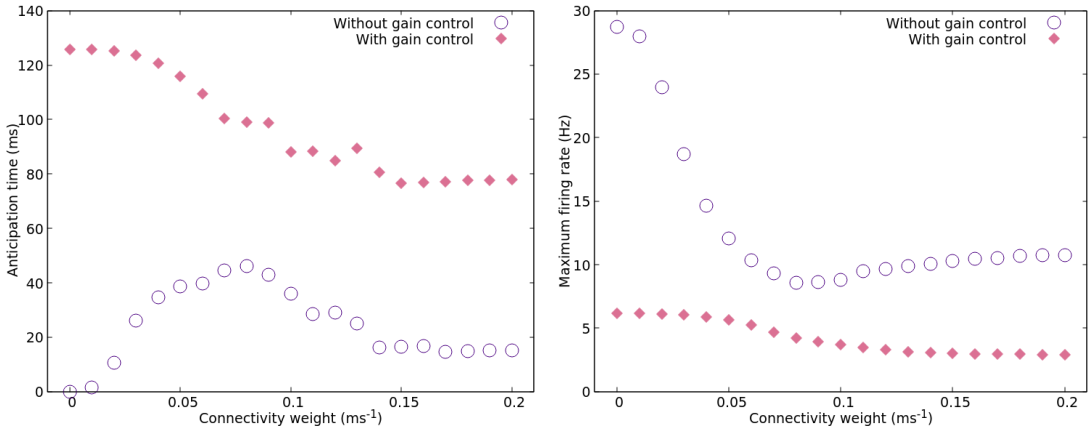

Figure 5.12: The joint effect of the random amacrine connectivity and gain control, showing

5.2.2.3 The role of the maximum number of branches

Throughout our simulation experiments, we observed a dependence of anticipatory effects on the connectivity parameters. We investigate in this subsection how anticipation and maximum firing rate evolve with the maximum number of branches. Keeping the maximum length of branches constant, we draw three adjacency matrices with different values of the maximum number of branches, giving rise to a denser

connectivity graph. For small values of weights, networks with dense connectivity perform generally better than the ones with a sparse connectivity in terms of anticipation time, whereas for large values weights, there is no clear tendency in the anticipation time ranking with respect to the maximum number of branches. As for the maximum firing rate, it decreases with the number of branches, due the fact that denser graphs increase the overall amount of inhibition in the system.

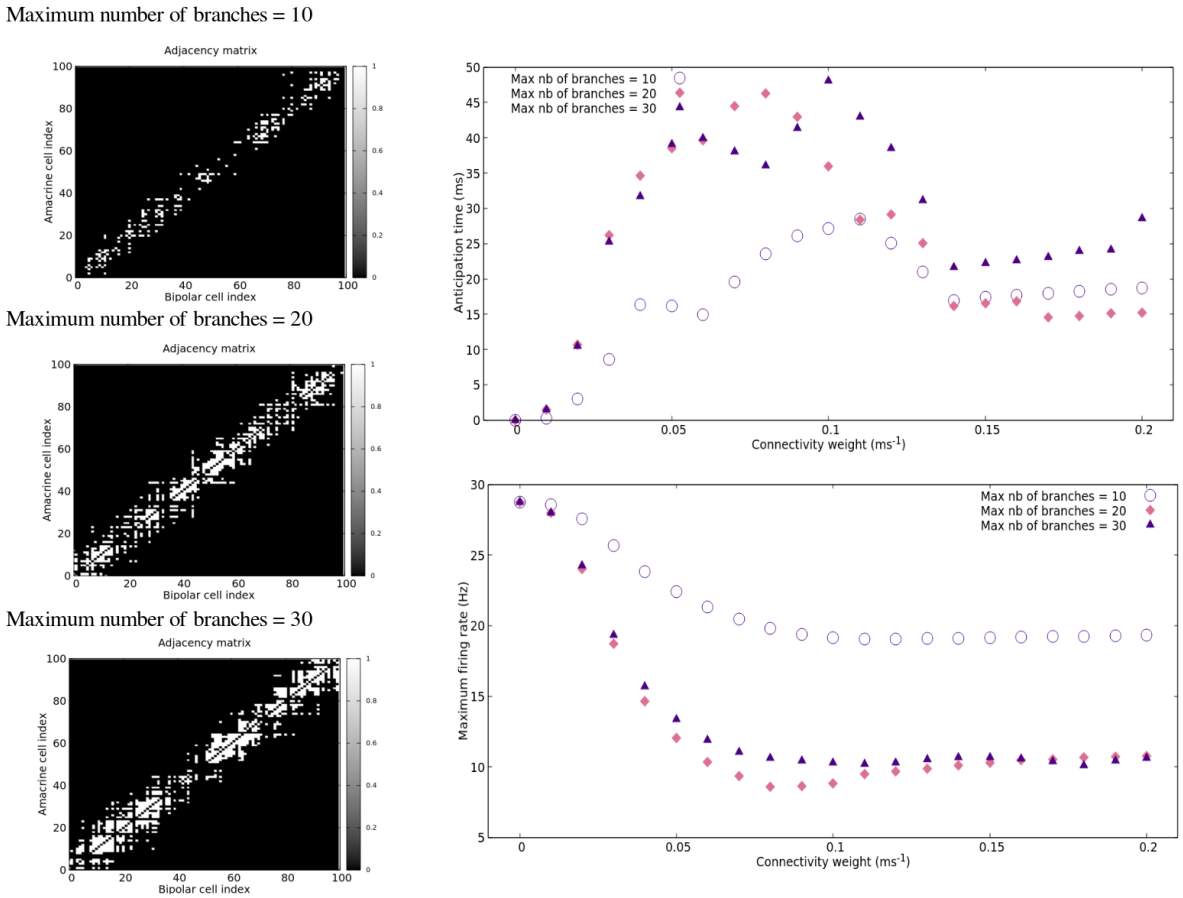

Figure 5.13: Variability of anticipation time and maximum firing rate with the maximum number of branches.

5.2.2.4 The role of the maximum length of branches

We investigate in this subsection how anticipations and maximum firing rate evolve with the maximum length of branches. Keeping the maximum number of branches constant, we draw three adjacency matrices with different values of the maximum length of branches, giving rise to adjacency matrices that are wider around the diagonal. For small values of weights, there is no significant different between the various lengths values. However, for large values of weights, graphs with small branch

lengths perform better in terms of anticipation time. The maximum firing rate decreases with the length of branches, and this can be explained using the same argument as in the previous subsection : the increase the overall amount of inhibition in the system.

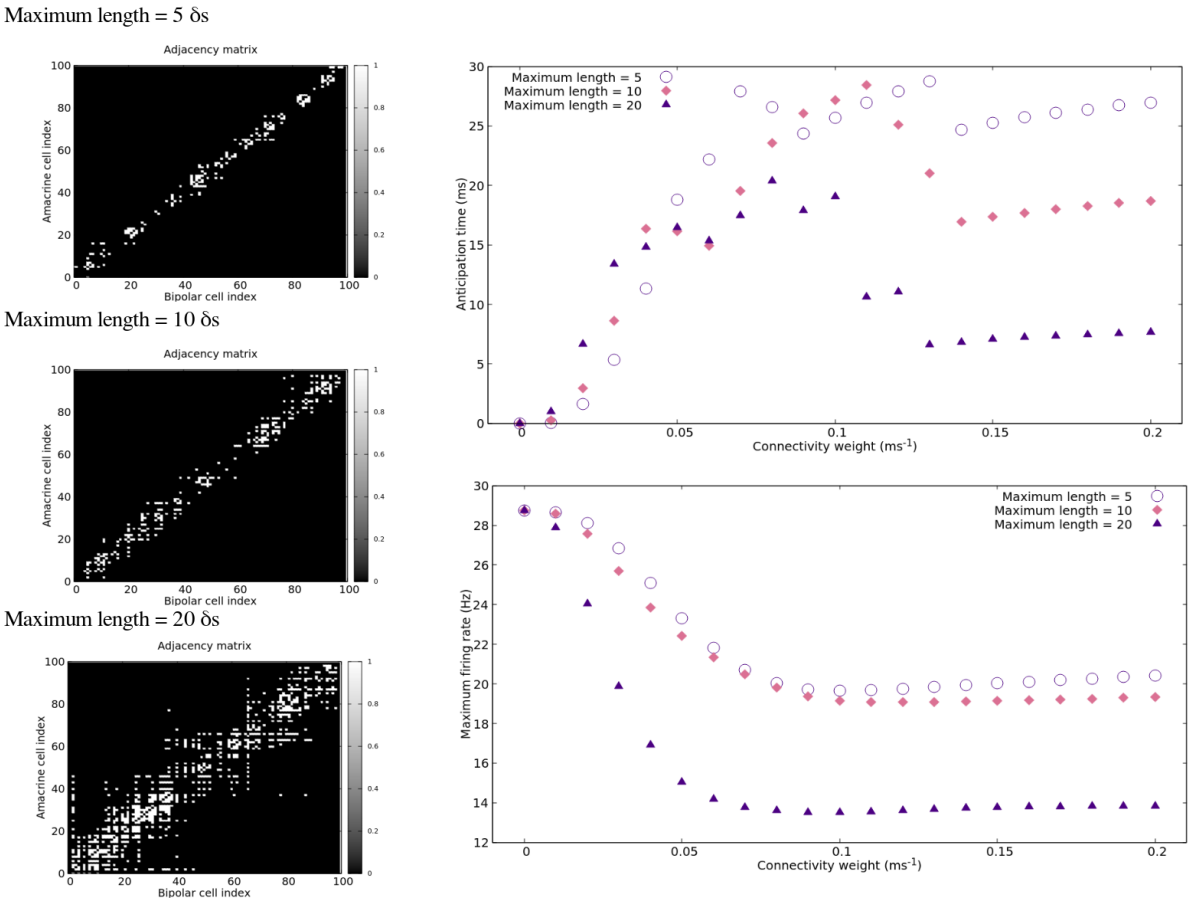

Figure 5.14: Variability of anticipation time and maximum firing rate with the maximum length of branches.

5.3 Gap junction connectivity

5.3.1 The model equations

As introduced in chapter IV, the ganglion cell voltage is governed by the following equation:

$$\frac{dV_{G_k}}{dt} = \frac{dV_{G_k}^{in}}{dt} - \frac{g}{C}(V_{G_k}(t) - V_{G_{k-1}}(t))$$

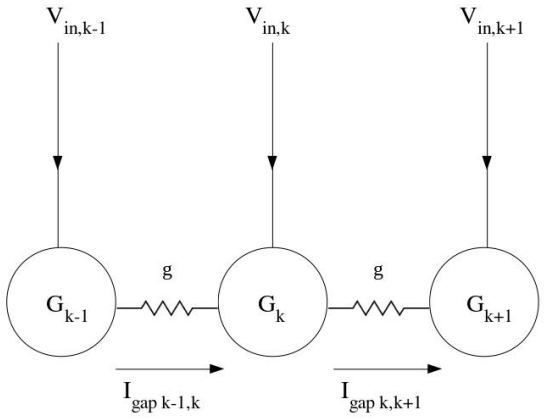

Figure 5.15: Schematic of the gap junction connectivity. A ganglion cell is coupled to its surrounding cells, in the direction of motion.

In the following, we will set $\frac{g}{C} = w_{gap}$, the strength of gap junction coupling. Taking into account the gain control mechanism occurring at the level of ganglion cells, one could speculate on the order at which the two phenomena (gain control and gap junction coupling) occur. Should gain control happen prior to gap junction coupling, gain control would appear in the computation of $V_{G_{k-1}}$, in the previous equation. Alternatively, gain control can occur after gap junction connectivity, making the coupling independent of single cell adaptation mechanisms.

5.3.2 Anticipation variability

In this section, we want to study the network ability to improve anticipation in the presence of gap junction coupling, alongside gain control at the level of ganglion cells. As in the previous section, we omit again gain control mechanisms occurring at the level of the uncoupled layer (here bipolar cells).

In Fig 5.18 we compare the anticipation time and maximum firing rate when apply-

ing gain control before and after gap junction coupling, as a function of the coupling weight. It is important here to find the right range of pooling strength (from bipolar cells to ganglion cells, defined as the amplitude of the Gaussian pooling w_{pool}^{max}) and coupling weights to avoid non linearity saturation effects, when the latter is applied before gap junction coupling. For a given range of coupling weights, the pooling strength has to be high enough for the gap junction coupling to have an effect when it occurs prior to gain control, and low enough for gain control not to rapidly saturate.

When the value of w_{pool}^{max} is such that the non linearity doesn't have a saturating effect, the system behave similarly whether the gain control precedes the gap junction coupling or not (Fig 5.16. When the value of w_{pool}^{max} is large enough, the non linearity has a strong effect and the system performs better in terms of anticipation time when gain control is applied after gap junction coupling. Fig 5.18 shows however that in both cases, the coupling improves anticipation time as compared to the non coupled case (point with $w_{gap} = 0ms^{-1}$.

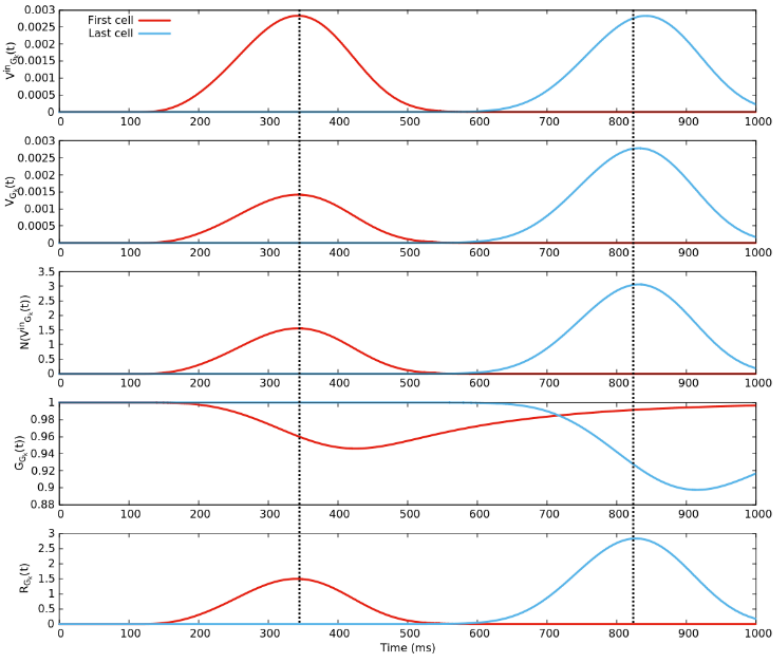

(a) Gain control is applied after gap junction coupling.

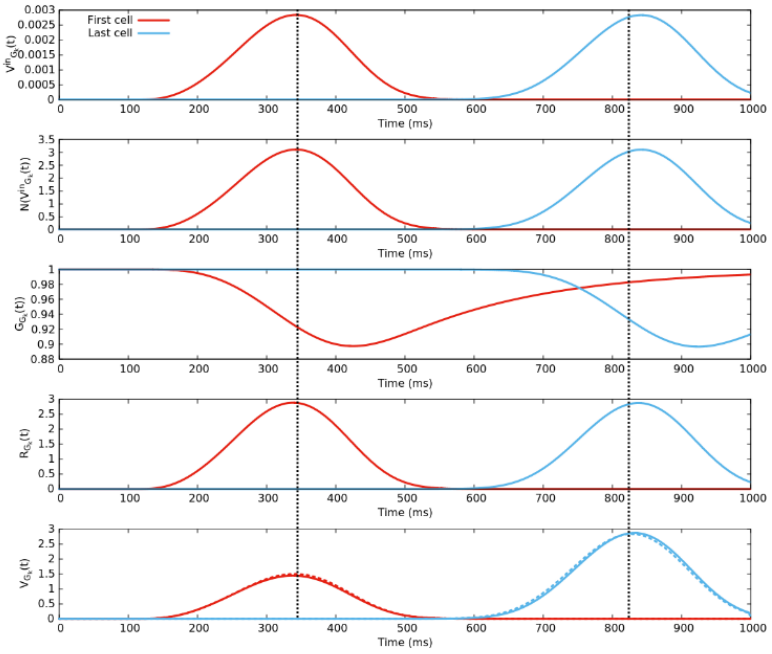

(b) Gain control is applied before gap junction coupling.

Figure 5.16: Ganglion cell response with weak pooling strength. The order of gain control and gap junction coupling doesn't play a significant role. The response of ganglion cells when gain control is applied after gap junction connectivity is reported in dashed lines.

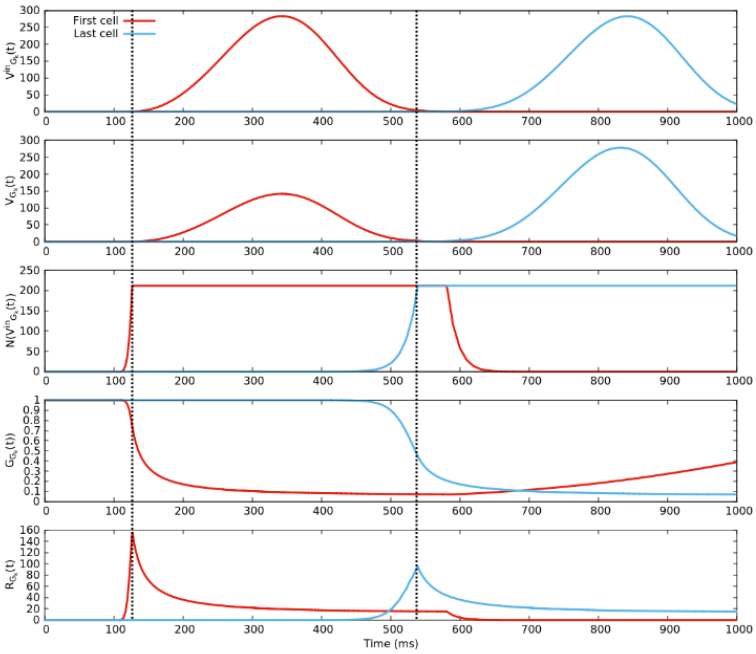

(a) Gain control is applied after gap junction coupling.

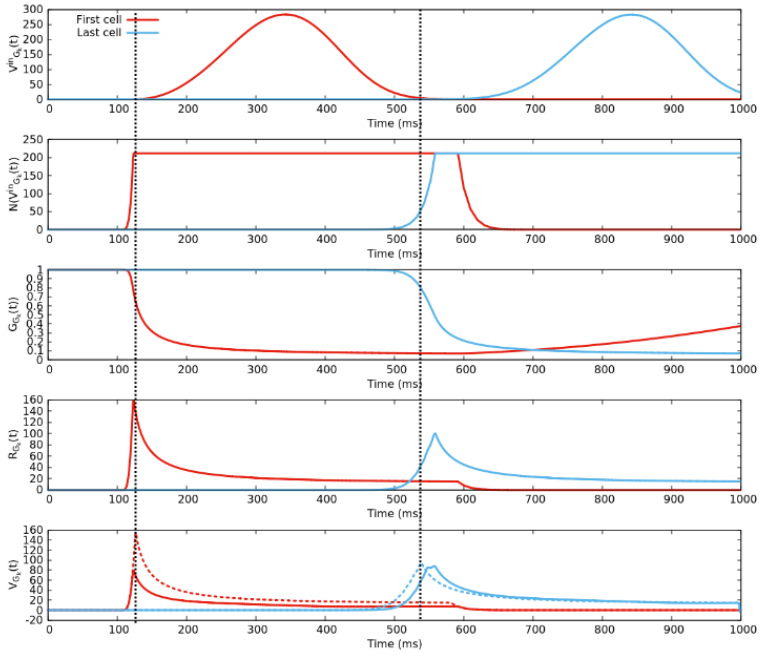

(b) Gain control is applied before gap junction coupling.

Figure 5.17: Ganglion cell response with strong pooling strength. The order of gain control and gap junction coupling plays a role for cells far from the start of motion.

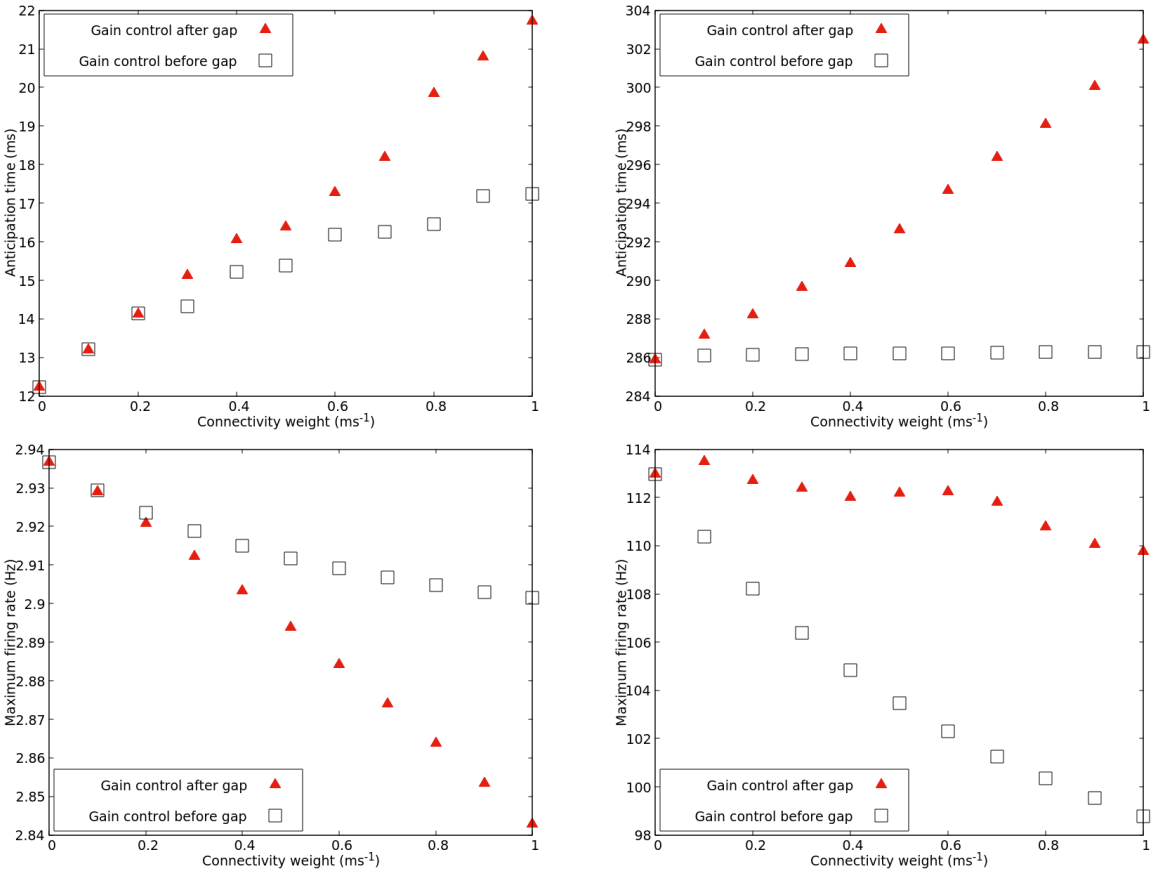

(a) Weak pooling weight ($w_{pool} = 0.05$).

(b) Strong pooling weight ($w_{pool} = 0.5$).

Figure 5.18: Ganglion cell anticipation time and maximum firing rate as a function of the coupling weight w_{gap}. (a) In this case, the non linearity doesn't play a role because $V_{G_k}^{in}$ is below its threshold. The system performs slightly better when gain control is applied after gap junction coupling. (b) In this case, $V_{G_k}^{in}$ is above threshold and the non linearity saturates. The system performs better in terms of anticipation time when gain control is applied after gap coupling, at the cost of a higher firing rate.

5.4 Response to 2D stimuli

In this section, we will present 2D reconstructions of retinal responses to 2D stimuli. The aim here is not to do an exhaustive study of anticipation in 2D but rather to assess qualitatively the anticipatory effects first in the case of the flash lag effect stimulus, and then in the case of more complex stimuli.

5.4.1 Flash lag effect

In all the following simulations, we use the CImg Library, an open-source C++ toolkit for image processing, in order to reconstruct the retina activity.

Fig. 5.19 shows the response to a bar moving in smooth motion, with a second bar flashed in alignment for one frame. In the case of the gain control response, the peak of response is shifted by the flashed bar elicits a low response.

We choose amacrine connectivity parameters which improve anticipation. In this case, the response to the flashed bar is also more salient. However given the response is strongly suppressed, the bar representation is significantly shrunk as compared to its original size.

Finally, gap junction connectivity displays a wave propagating ahead of the bar. In this case, the flashed bar only increases the central blop, which is much larger than the size of the bar in the stimulus

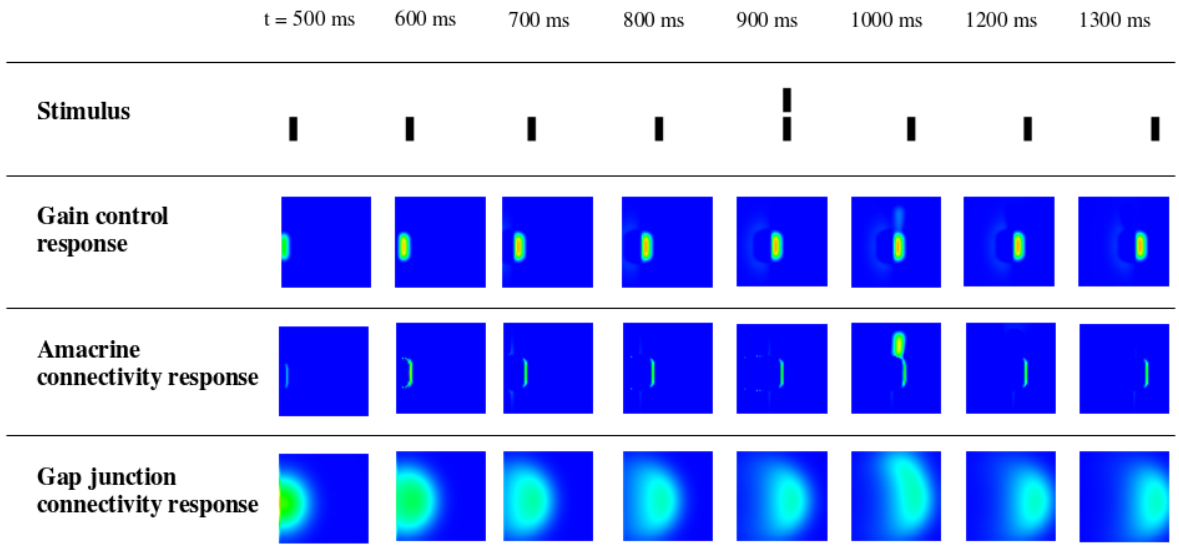

Figure 5.19: Reproducing the flash lag effect with different anticipatory mechanisms.

5.4.2 Gain control accounts for angular anticipation

Fig. 5.21, shows the gain controlled retina response to a rotating bar. The response around the center of the bar is suppressed due to the spatio-temporal filtering and gain control. We fit the response with an ellipsoid. The main axis of this ellipsoid defines the orientation of the retinal representation of the bar. Note that the fitting procedure is robust to the suppression of activity in the response center.

We plot the orientation of the bar along with the orientation of its reconstruction, at the different stages of the model. Fig. 5.21 shows an angular anticipation during the first complete rotation of the bar, which vanishes during the second rotation. This is due to a persistent effect of the activation function, both at the bipolar and the ganglion level, which in turns is due to the time scale of its dynamics.

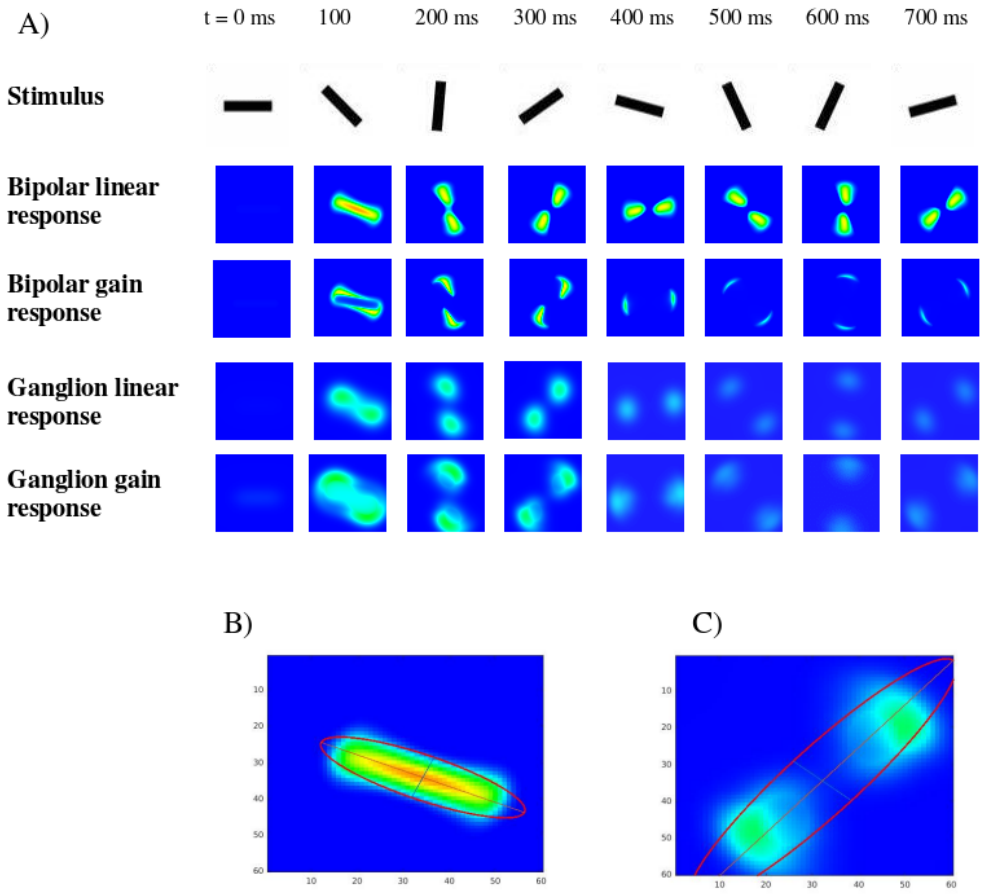

Figure 5.20: Retina response to a rotating bar. A) Stimulus and response frames are displayed every 100 ms. B) and C) Fitting the response with an ellipsoid.

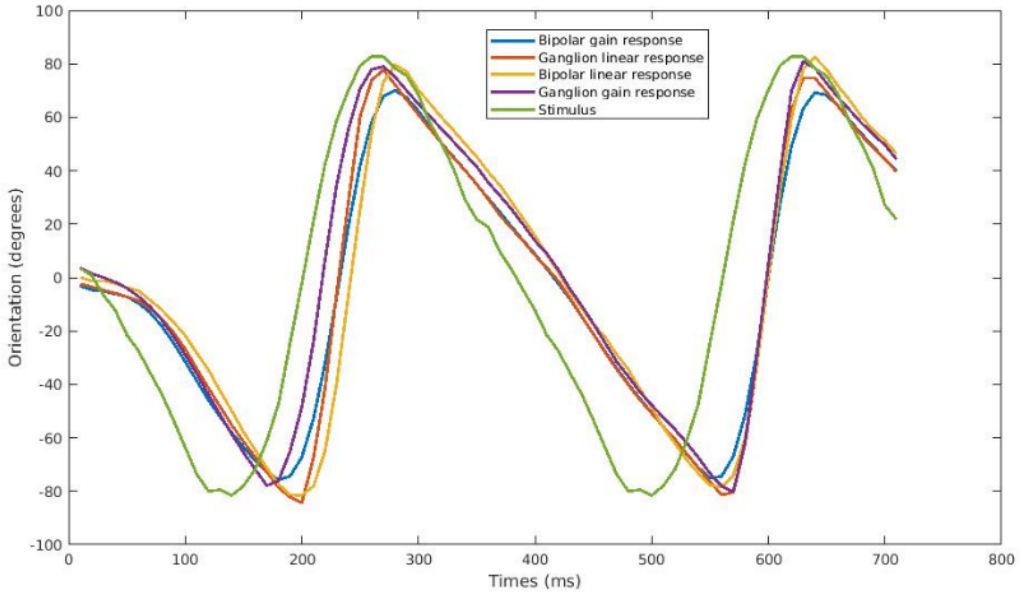

Figure 5.21: Orientation curves of the stimulus and its reconstruction show angular anticipation.

5.4.3 Retina response to a parabolic trajectory

Fig. 5.22 shows the response to a dot moving along a parabolic trajectory, using the same size of the bipolar receptive field.

The results display the sensitivity of the amacrine connectivity model to the stimulus derivative. Not only does the flow of activity follow more accurately the stimulus, but the elicited response is also more localized, as compared to the gain control response. Finally, the gap junction connectivity model performs worse in this case, since the trajectory of the bar is not parallel to the direction ganglion cells to which are sensitive. Unlike the smooth motion case, we don't have the emergence of a wave propagating ahead of the stimulus. Instead, the response is slightly delayed.

The amacrine model is also more sensitive to the appearance of the dot than the gain control, which in turn performs slightly better than the gap junction model.

The figure also shows that these effects are persistent with the size of the ganglion cell pooling.

Partial conclusion

We have been able to show in this chapter, though numerical simulations, that lateral connectivity can indeed improve anticipation. In the case of amacrine connec-

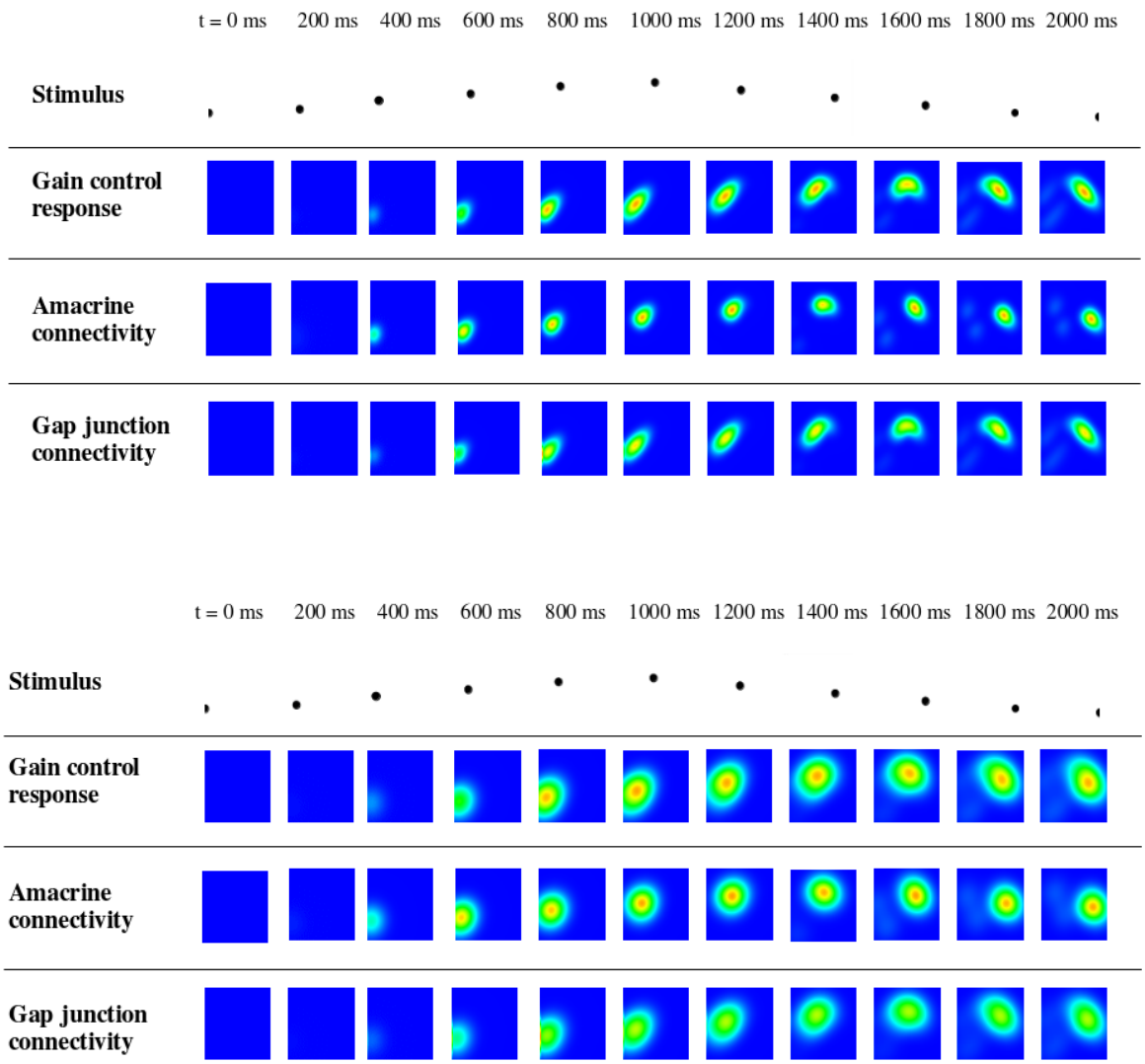

Figure 5.22: Assessing the effect of anticipatory mechanisms on a parabolic trajectory. Top : results with a small ganglion cell pooling. Bottom : results with a large ganglion cell pooling.

tivity, anticipation can be improved as compared to the gain control alone when the network effect is such that the adaptation function increases faster. We have tried to understand whether this type on connectivity can have an interesting effect on anticipation when the bar is moving on a noisy background, but this is still work in progress. In the case of gap junction connectivity, anticipation is improved only when the trajectory of the bar is parallel to the preferred direction of ganglion cells. However, in this case, the blur around the retinal representation of the bar is increased. In general, there seems to be a trade-off between anticipation and object recognition.

Chapter 6

Primary visual cortex model

In this chapter, we introduce the cortical basis of our retino-cortical model : a mean field model that has been developed by Zerlaut et. al [79] to reproduce VSDI activity as recorded in V1. This model has later been used by Chemla et al. [80] in order to account for the cortical representation of apparent motion, a visual illusion where two dots are flashed close in space and with a small time delay, giving rise to motion perception. We first introduce the mean field model equations derivation, a method that can be applied using different single cell models (Adaptive Exponential IF, Hodgkin Huxley and Morris Lecar), and show examples of response properties in the case of the Adaptive Exponential IF and Hodgkin Huxley models. We then modify the Adaptive Exponential IF implementation to link it to our retina model. In order to validate our implementation, we reproduce V1 activity in response to apparent motion. Finally, we study the ability of the cortical model to anticipate a trajectory, using synthetic external drives, and assess the role of cortical connectivity parameters in anticipation.

6.1 General introduction to the mean field model

Cortical dynamics during awake states display asynchronous spiking activity, characterized by irregular spike trains at the level of single neurons. In this context, network correlations decrease sufficiently fast in time, giving the possibility to apply a Makovian formalism to obtain mean field equations of the average activity of neurons [81]. El Boustani et al. [82] have derived differential equations describing the average rate as well as higher order moments of populations of spiking neurons. However, the function that links the input and output of these populations is generally not a simple

sigmoid, but rather a complex function that takes into account realistic properties of the neurons, such us conductance-based interactions.

Zerlaut et al. [79] have developed a general semi-analytic approach to determine the transfer function applied to Adaptive Exponential IF models, which allows a mean field description of the population dynamics. In particular, they were able to study a network of regular-spiking excitatory neurons, and fast-spiking inhibitory neurons, reproducing VSDI spatio-temporal patterns of the network spontaneous activity, as well as the network response to a time-varying external drive.

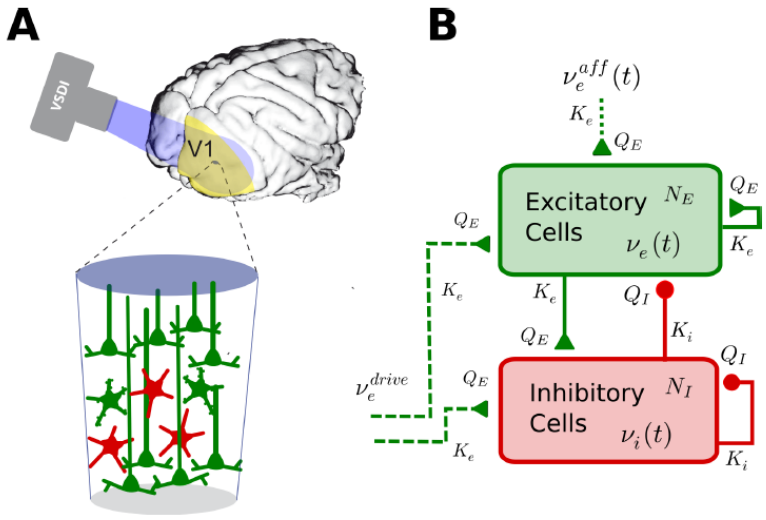

Figure 6.1: Mean Field modeling of the cortex dynamics. (A) A local network accounts for the complex assembly of cortical neurons measured in experiments (here VSDI). (B) Excitatory-inhibitory network structure. Parameters are described in the text and their values are given in the Appendix. [79]

During the spring school organized at the EITN [1] in 2018 and 2019, two groups of students have worked on the application of the transfer function approach to Hodgkin Huxley [83] and Morris Lecar [84] models, under the supervision of Matteo Di Volo. I took part in this work which was concretized in a journal paper, currently under review. Being part of the first group who worked on the Hodgkin Huxley model, we briefly present here the formalism as it has been applied to the Adaptive Exponential IF and Hodgkin Huxley models, and show the major results in terms of transfer function computation and population dynamics.

The mean field model which is later used in our simulations consists of a spatially

[1] European Institute of Theoretical Neuroscience, Paris.

extended ring where each node shows the network activity of a large population of excitatory regular spiking and inhibitory fast spiking cells, based on the Adaptive Exponential IF model.

6.1.1 Mean field equations

Under the hypothesis that the neural network is in an asynchronous irregular regime, we can describe the first and second order dynamics using the master equation formalism developed by El Boustani et al. [82]. The main argument used in this derivation is to consider the network dynamics as Markovian at a given time scale, typically 20 ms. The differential system reads :

$$T\frac{d\nu_\mu}{dt} = (F_\mu - \nu_\mu) + \frac{1}{2}c_{\lambda\eta}\frac{\partial^2 F_\mu}{\partial\nu_\lambda\partial\nu_\mu}, \tag{6.1}$$

$$T\frac{dc_{\lambda\eta}}{dt} = \delta_{\lambda\eta}\frac{F_\lambda(1/T - F_\lambda)}{N_\lambda} + (F_\lambda - \nu_\lambda)(F_\mu - \nu_\mu) + \frac{\partial F_\mu}{\partial\nu_\lambda}c_{\lambda\mu} + \frac{\partial F_\mu}{\partial\nu_\eta}c_{\mu\eta} - 2c_{\lambda\mu}, \tag{6.2}$$

where $\mu = \{E, I\}$ is the population index (excitatory or inhibitory), ν_μ the population firing rate and $c_{\lambda\eta}$ the covariance between population λ and η. The function $F_{\mu=\{E,I\}} \equiv F_{\mu=\{E,I\}}(\nu_E, \nu_I)$ is the transfer function which describes the firing rate of population μ in function of excitatory and inhibitory inputs (with rates ν_E and ν_I).

At the first order, i.e. neglecting the dynamics of the covariances $c_{\lambda\eta}$, the model reduces to :

$$\begin{cases} \frac{T\partial\nu_E(x,t)}{dt} = -\nu_E(x,t) + F_E(\nu_E^{aff}(x,t) + \nu_E^{input}(x,t), \nu_I^{input}(x,t)) \\ \frac{T\partial\nu_I(x,t)}{dt} = -\nu_I(x,t) + F_I(\nu_E^{input}(x,t), \nu_I^{input}(x,t)) \end{cases} \tag{6.3}$$

where $\nu_E^{input}(x,t)$ (resp. $\nu_I^{input}(x,t)$) is the population rate at column with spatial location x, at time t, of excitatory cells (resp. inhibitory). ν_E^{drive} denotes the constant external drive and ν_E^{aff} the retino-thalamic input. The function F_E (resp. F_I) is the transfer functions of excitatory (resp. inhibitory) neurons.

Let $N_E(x)$ (resp. N_I) denote the spatial connectivity at the level of the excitatory population (resp. inhibitory), and v_c is the speed of axonal conduction. The excitatory input $\nu_E^{input}(x,t)$ (resp. inhibitory $\nu_I^{input}(x,t)$) adds up the constant excitatory constant drive ν_E^{drive} (resp. 0) and incoming excitatory (resp. inhibitory) activity from the con-

nected columns, with a delay that depends on the distance between the columns and the axonal conduction speed. For two columns at positions x and y, the delay reads :

$$\tau = ||y - x||/v_c$$

Integrating the connectivity input over all the spatial locations, ν_E^{input} and ν_I^{input} read :

$$\begin{cases} \nu_E^{input}(x,t) = \nu_E^{drive} + \int_{\mathbb{R}} dy N_E(x-y)\nu_E(y, t - ||y-x||/v_c) \\ \nu_I^{input}(x,t) = \int_{\mathbb{R}} dy N_I(x-y)\nu_I(y, t - ||y-x||/v_c) \end{cases} \tag{6.4}$$

6.1.2 Transfer function

The transfer function links the output firing rate of a neuron to its input presynaptic excitatory and inhibitory activities, which consequently describes the dynamics of the neuronal activity. Finding the analytic formulation of the transfer function for complex models such as the Adaptive Exponential IF or Hodgkin Huxley is a non trivial problem. Zerlaut et al. [79] have developed a semi-analytic method which fits a phenomenological threshold, using numerical simulations of a given neuron model. This method assumes that the phenomenological threshold depends on mean values describing the statistics of the subthreshold membrane voltage dynamics.

The transfer function reads :

$$F = \frac{1}{\tau_V} erfc(\frac{\nu_{thr}^{eff} - \mu_V}{\sigma_V}) \tag{6.5}$$

where ν_{thr}^{eff} is a phenomenological threshold expressed as a first order expansion of μ_V, σ_V and τ_V. These mean values are calculated from shot-noise theory [85] :

$$\mu_{G_E} = \nu_E K_E \tau_E Q_E$$

$$\sigma_{G_E} = Q_E \sqrt{\frac{\nu_E K_E \tau_E}{2}}$$

$$\mu_{G_I} = \nu_I K_I \tau_I Q_I$$

$$\sigma_{G_I} = Q_I \sqrt{\frac{\nu_I K_I \tau_I}{2}}$$

where, K_E (resp. K_I) is the number of excitatory synapses (resp. inhibitory), Q_E

(resp. Q_I) the excitatory conductance (resp. inhibitory), and τ_E (resp. τ_I) the excitatory decay (resp. inhibitory). The parameter values are given in the Appendix.

The total input of the neuron μ_G and its effective membrane time constant τ_m^{eff} are controlled by the mean conductances as follows:

$$\begin{aligned} \mu_G(\nu_e, \nu_i) &= \mu_{Ge} + \mu_{Gi} + g_L, \\ \tau_m^{\text{eff}}(\nu_e, \nu_i) &= \frac{c_m}{\mu_G}. \end{aligned} \tag{6.6}$$

Therefore, we can write the equation for the mean subthreshold voltage:

$$\mu_V(\nu_e, \nu_I) = \frac{\mu_{Ge}\, E_e + \mu_{Gi}\, E_i + g_L\, E_L}{\mu_G}. \tag{6.7}$$

where E_e (resp. E_i) are the Nernt potentials of excitatory (resp. inhibitory) neurons, and E_L the leak Nernst potential.

The final formulae for σ_V and τ_V follow from calculations introduced in [79] they read:

$$\sigma_V(\nu_e, \nu_i) = \sqrt{\sum_s K_s\, \nu_s\, \frac{(U_s \cdot \tau_s)^2}{2\,(\tau_{\text{m}}^{\text{eff}} + \tau_s)}}, \tag{6.8}$$

$$\tau_V(\nu_e, \nu_i) = \Big(\frac{\sum_s \big(K_s\, \nu_s\, (U_s \cdot \tau_s)^2\big)}{\sum_s \big(K_s\, \nu_s\, (U_s \cdot \tau_s)^2/(\tau_{\text{m}}^{\text{eff}} + \tau_s)\big)}\Big), \tag{6.9}$$

where we defined $U_s = \frac{Q_s}{\mu_G}(E_s - \mu_V)$ and $s = (e, i)$.

The quantities μ_V, σ_V and τ_V can now be reported into Eq. 6.5.

Using experimental considerations, Zerlaut et al. have shown that the phenomenological threshold can be expressed as a function of $(\mu_V, \sigma_V, \tau_V)$, as a second order polynomial :

$$\begin{aligned} V_{thre}^{eff}(\mu_V, \sigma_V, \tau_V^N) = P_0 + \sum_{x \in \{\mu_V, \sigma_V, \tau_V^N\}} P_x \cdot \Big(\frac{x - x^0}{\delta x^0}\Big) + \\ \sum_{x,y \in \{\mu_V, \sigma_V, \tau_V^N\}^2} P_{xy} \cdot \Big(\frac{x - x^0}{\delta x^0}\Big)\Big(\frac{y - y^0}{\delta y^0}\Big), \end{aligned} \tag{6.10}$$

where $\tau_V^N = \tau_V G_l / c_m$ is an unitless parameter. The fitting procedure consists then of finding the values of the P parameters for each of the considered models.

6.1.3 Application to the Adaptive Exponential IF model

The Adaptive Exponential integrate and fire model is described by the following differential equations :

$$c_m \frac{dv}{dt} = g_l(E_l - v) + \Delta e^{\frac{v - v_{th}}{\Delta}} - w + I_{syn} \tag{6.11}$$

$$\frac{dw}{dt} = -\frac{w}{\tau_w} + a(v - E_L) + b \sum_k \delta(t - t_k) \tag{6.12}$$

where c_m is the membrane capacity, v the voltage of the neuron, g_L the leak conductance, and E_L the leak reversal potential. When v is above the threshold v_{th}, it is reset to its resting value v_{rest}. The second equation denotes an adaptive dynamics for excitatory neurons (a=b=0 for inhibitory cellls). Finally, the synaptic current is given by :

$$I_{syn} = Q_E(E_E - v)S_E + Q_I(E_I - v)S_I$$

where E_E and E_I are the reversal potentials of excitatory and inhibitory neurons, Q_E and Q_I the quantal conductances. S_E (resp. S_I) is the postsynaptic activity due to the spiking of presynaptic excitatory neurons (resp. inhibitory) at time t_{pre} given by :

$$S_{E/I}(t) = \sum_{pre} \Theta(t - t_{pre,E/I}) e^{\frac{t - t_{pre,E/I}}{\tau_{E/I}}}$$

with Θ the Heaviside function and $\tau_{E/I}$ the synaptic decays (resp. for excitatory and inhibitory cells).

6.1.4 Application to the Hodgkin Huxley model

The dynamics of the Hodgkin Huxley model are given by the following differential system [86] :

$$
\begin{aligned}
c_m \frac{dvi}{dt} &= g_L(E_L - v_i) + g_{Na} m^3 h(E_{Na} - v_i) + \\
&\quad + g_K n^4 (E_K - v_i) + g_M p_i (E_K - v_i) + I_{syn}, \qquad (6.13)\\
\frac{dn_i}{dt} &= \alpha_n(v_i)(1 - n_i) - \beta_m(v_i) n_i, \qquad (6.14)\\
\frac{dm_i}{dt} &= \alpha_m(v_i)(1 - m_i) - \beta_m(v_i) m_i, \qquad (6.15)\\
\frac{dh_i}{dt} &= \alpha_h(v_i)(1 - h_i) - \beta_h(v_i) h_i, \qquad (6.16)\\
\frac{dp_i}{dt} &= (p_\infty(v_i) - p_i)/\tau_p(v_i), \qquad (6.17)
\end{aligned}
$$

with the gating functions,

$$
\begin{aligned}
&\alpha_n(v_i) = \frac{-0.032(v_i - V_T - 15)}{\exp[-(v_i - V_T - 15)/5] - 1}, \quad \beta_n(v_i) = 0.5 \exp[\frac{-(v_i - V_T - 10)}{40}],\\
&\alpha_m(v_i) = \frac{-0.32(v_i - V_T - 13)}{\exp[-(v_i - V_T - 13)/4] - 1}, \quad \beta_m(v_i) = \frac{0.28(V - V_T - 40)}{\exp[(V - V_T - 40)/5] - 1},\\
&\alpha_h(v_i) = 0.128 \exp[-(V - V_T - 17)/18], \quad \beta_h(v_i) = \frac{4}{1 + \exp[-(V - V_T - 40)/5]},\\
&p_\infty(v_i) = \frac{1}{1 + \exp[-(V + 35)/10]}, \quad \tau_p(v_i) = \frac{\tau_{\max}}{3.3 \exp[(V + 35)/20] + \exp[-(V + 35)/20]},
\end{aligned} \qquad (6.18)
$$

where v_i is the membrane voltage and (n_i, m_i, h_i, p_i) are the corresponding gating variables of the i^{th} neuron. The membrane capacity $c_m = 200$pF, the maximal leak conductance (per unit of surface) $g_L = 10$mS/cm^2, the sodium conductance (per unit of surface) $g_{Na} = 20$mS/cm^2, the delayed-rectifier potassium conductance (per unit of surface) $g_K = 6$mS/cm^2, the slow non-inactivating potassium conductance of the excitatory regular spiking neurons (per unit of surface) $g_M = 0.003$mS/cm^2 and of the inhibitory fast spiking neurons $g_M = 0$mS/cm^2, with corresponding reversal potentials $E_L = -65$mV, $E_{Na} = 50$mV, $E_K = -90$mV.
The spiking voltage threshold $V_T = -53.5$mV and $\tau_{\max} = 4$s are the fixed parameter values in Eqs.(6.13)-(6.18). When $v > v_{thr} = 10$ mV a spike is emitted at time $t_{sp}(k)$.

6.1.4.1 Mean field results

When seeking an existing plausible model of the cortex accepting firing rates retino-thalamic input, the model developed by ElBoustani et al. [82] was the most adapted choice. It remained then to find the right underlying neuron model. It is in this spirit that we show here the application of the semi-analytic approach to fit the nu-

merical transfer function when applied to Adaptive Exponential as well as Hodgkin-Huxley models. The evaluated effective threshold encodes the specificities of neurons microscopic and mesoscopic activity, which present, as we show it in the following, similarities in terms of spontaneous activity and response to external stimuli. We choose therefore the Adaptive Exponential implementation in our study of cortical anticipation, the single cell model being simpler. The main problem with the Hodgkin-Huxley in this approach being it has many parameters and regimes, each requiring a new fit.

All together, by comparing the theoretical prediction with numerical simulations we observe that, for both the Adaptive Exponential model and the more complex Hodgkin Huxley model, the transfer function is correctly estimated both for inhibitory and excitatory neurons, showing the efficiency of this approach.

We now assess the mean field predictions of the dynamics that emerge from networks of Adaptive Exponential IF and Hodgkin Huxley neurons. A sparse network of RS and FS cells coupled through conductance-based interactions is simulated, using the same connectivity parameters. As the transfer functions of RS and FS cells are similar we expect the regime of population dynamics to be analogous. This comes from the assumption that the population dynamics depend on cellular details only through the transfer function.

Fig. 6.3 shows that the dynamics reach an asynchronous regime, characterized by irregular microscopic dynamics. Inhibitory FS cells fire at a higher frequency with respect to RS cells. The discrepancy we observe for the Hodgkin Huxley model, in the case of FS cells, is related to a higher mismatch of the transfer function linked to the higher complexity of the model.

Finally, we compare the mean field and network activity when the system is responding to an external stimulus. The drive is a time-varying frequency targeting both excitatory and inhibitory cells, defined by the following function :

$$\nu(t) = A\Big(\Theta(t_0 - t)e^{\frac{-(t-t_0)^2}{T_1^2}} + \Theta(t - t_0)e^{\frac{-(t-t_0)^2}{T_2^2}}\Big), \tag{6.19}$$

where Θ is the Heaviside function, and T_1 and T_2 are the rise and decay time constants, respectively.

Fig. 6.4 shows the comparison between the mean field prediction and the network dynamics.

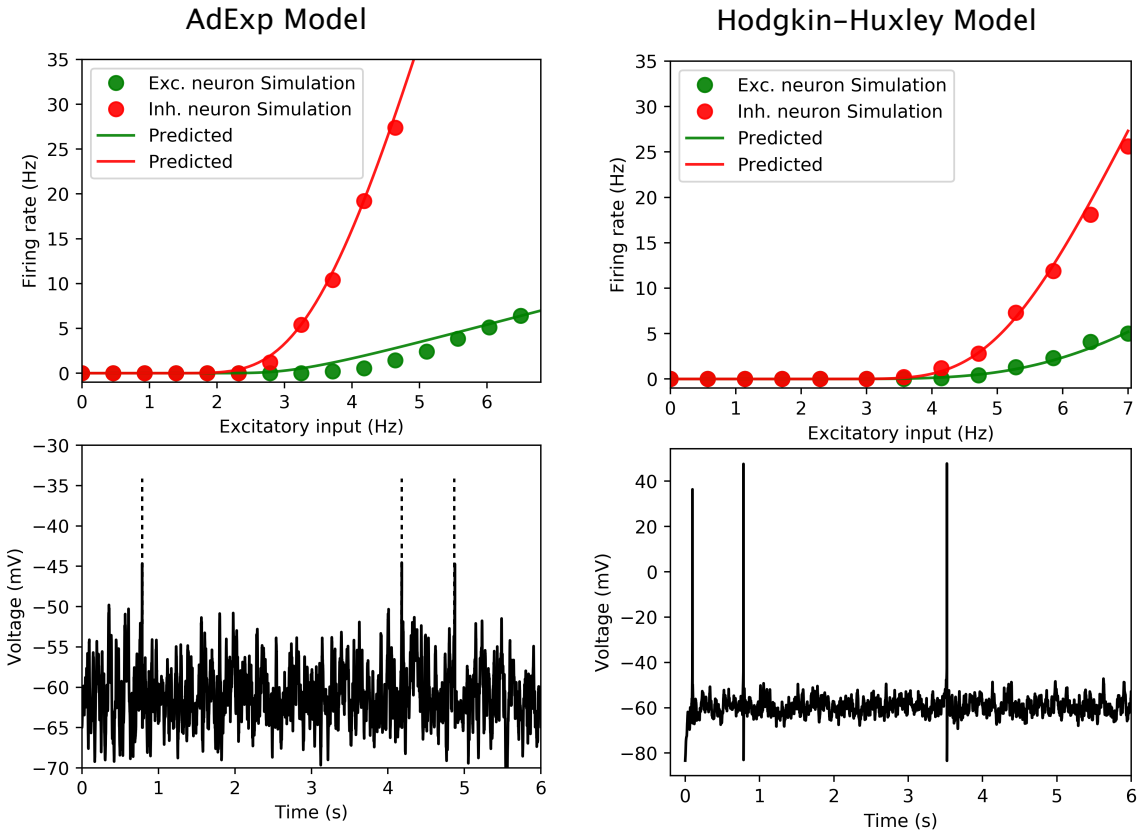

Figure 6.2: **Transfer function for Regular Spiking (RS) and Fast Spiking (FS) cells, for Adapative Exponential IF and Hodgkin Huxley** We report the output firing rate for excitatory RS (green) and inhibitory FS (red) cells obtained from numerical simulation (dots) and from the semi-analytic approach for the transfer function (continuous line). The inhibitory Poissonian spike train has a fixed rate, $r_I = 8$Hz. The bottom panel shows the trace in time of the membrane voltage of an RS cell for an excitatory input equal to 4Hz. Left columns is obtained for Adapative Exponential IF model and right column for Hodgkin Huxley.

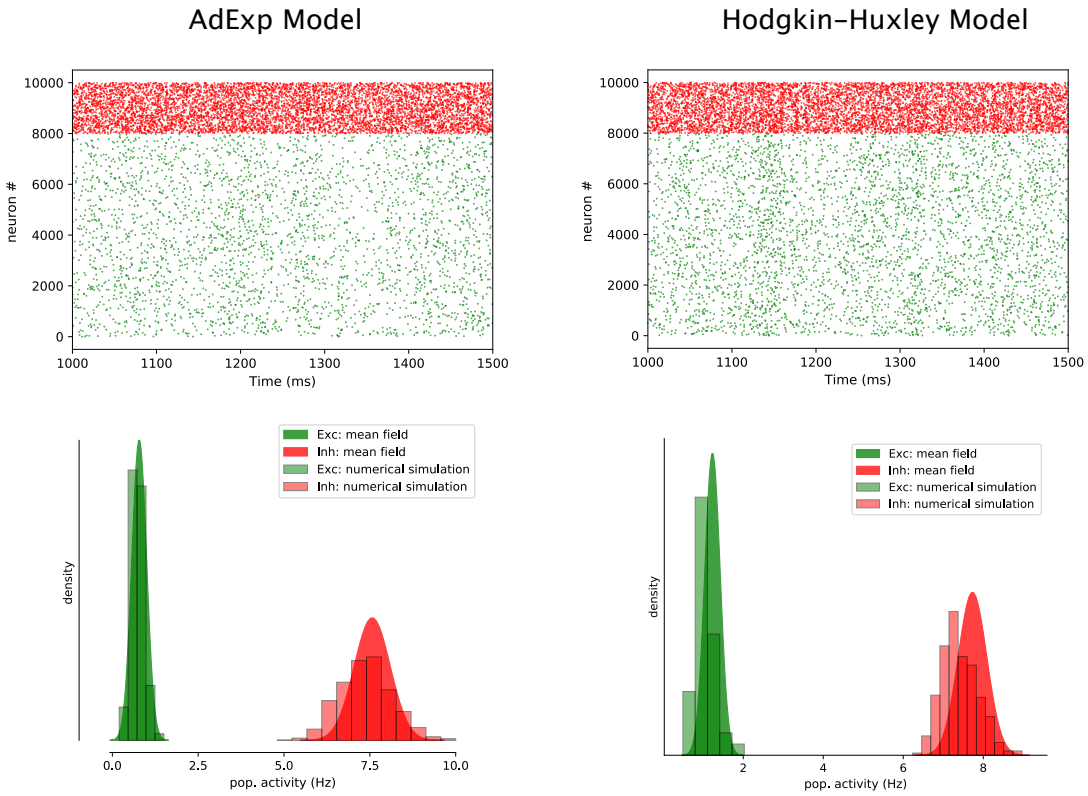

Figure 6.3: **Mean Field predictions and spontaneous activity, for Adapative Exponential IF and Hodgkin Huxley** Top subfigures show the raster plot for excitatory (green dots) and inhibitory (red dots) neurons. Similarly, the lower subfigures show the populations PSTH. The Gaussian distribution has been drawn with mean field predictions giving access to average firing rate and its variance. Left column is obtained for Adapative Exponential IF model and right column for Hodgkin Huxley.

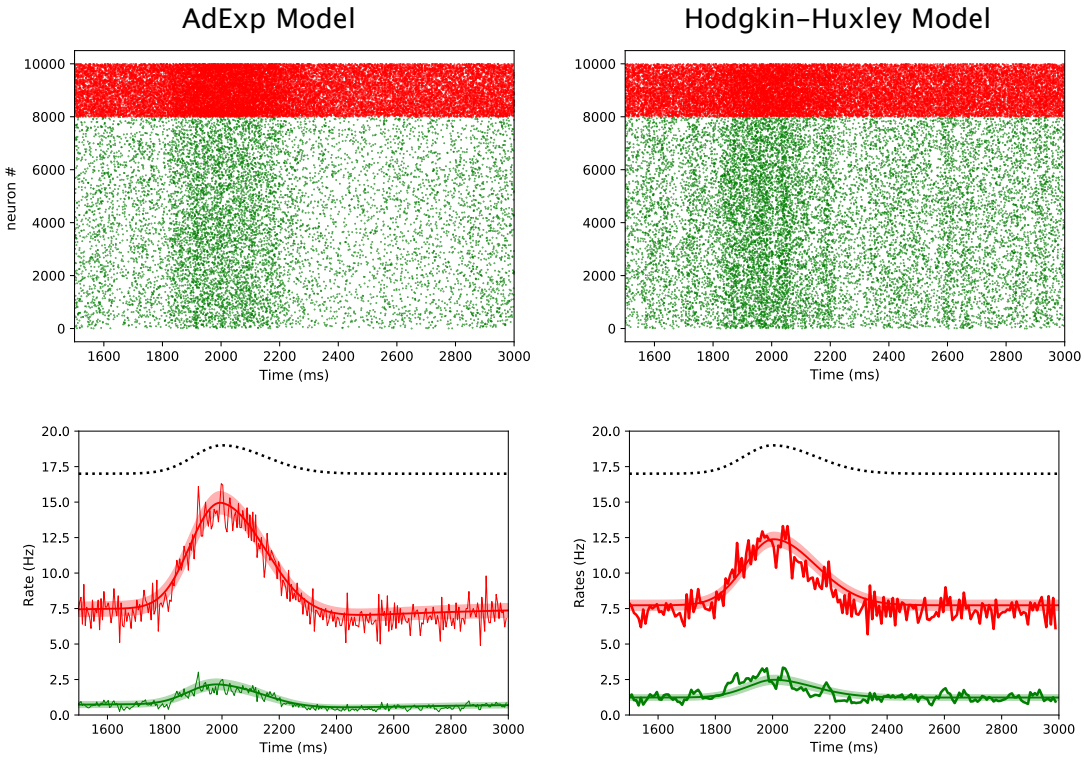

Figure 6.4: **Population response to external stimuli, for Adapative Exponential IF and Hodgkin Huxley** Same as Fig. 6.3. The system is driven by an external excitatory stimulus with $A = 2$Hz, $T_1 = 100$ms, $T_2 = 150$ms and $t_0 = 2000$ms (eq. 6.19).

6.2 Cortical representation of apparent motion

6.2.1 Experimental and modeling results

In 1912, Wertheimer introduced a visual illusion known as apparent motion : when two stationary stimuli appear at two spatially distinct yet close positions, with a given delay, it generates a motion percept. This illusion has been well studied from a psychophysics point of view [87], and has been shown to widely depend on the spatio-temporal characteristics of the stimulus. Indeed, the larger the spatio-temporal separation, the more challenging it is for the visual system to preserve the object identity along the path. Chemla et al. [80] used VSDI recordings in the primary visual cortex of the awake monkey in order to study the role played by intra-cortical connections in the cortical representation of apparent motion. In particular, they have emphasized the existence of a suppressive wave propagating in the opposite direction of the apparent motion.

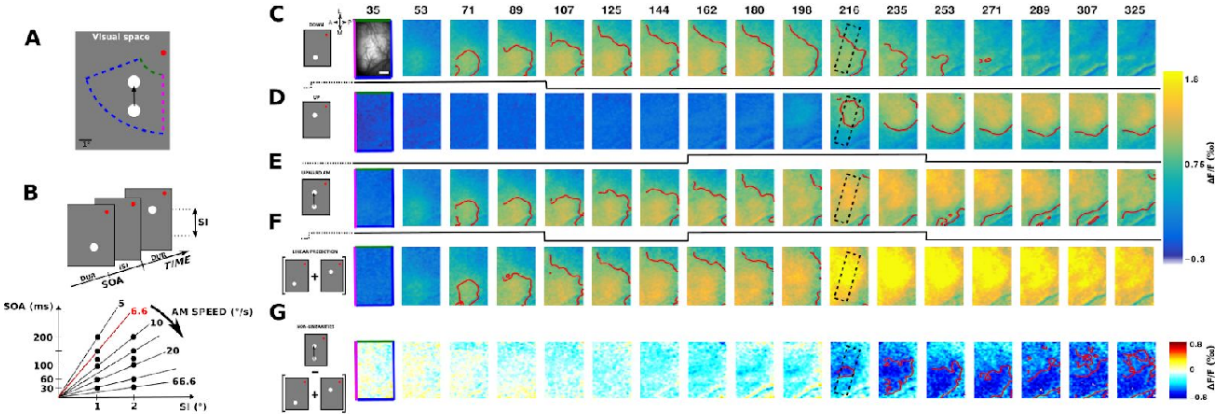

Figure 6.5: Experimental protocol and time-sequence of the cortical response to the long-range apparent motion . A: Two-step apparent motion stimuli are presented to two awake fixating monkeys in their bottom left visual field, while recording in their right visual cortex using VSDI. B: Spatio-temporal characteristics of the stimuli, i.e. duration, interstimulus interval and spatial interval, were varied to cover a [5-66.6]°/s range of speed. C-E: Cortical representation of evoked VSDI activity as a function of time, in response to respectively, a 100 ms local stimulus in the down position, another one in the up position, and the sequence of these two stimuli. F: Activity pattern predicted by the linear combination in space and time of the response to stimulus 1 (row C) and the response to stimulus 2 (row D). G: Suppression pattern obtained by subtracting the observed apparent motion response (row E) and the linear prediction (row F). From Chemla et al. [80]

Fig. 6.5 summarizes the results of the above-mentioned paper : it shows the wave of cortical activation that propagates from the first stimulus representation to the second one, as well the suppressive wave that emerges when subtracting the linear com-

bination of responses to single stimuli from the response to the apparent motion stimulus.

6.2.2 Reproducing apparent motion results

We use apparent motion to calibrate our implementation of the mean field cortical model. In particular, we want to study whether anticipation in the primary visual cortex involves a lateral propagation similar to the one involved in apparent motion. We rewrite the original implementation of the mean field model, coded in Python [80] , in C++. In addition to linking the retina model to the cortical one, this translation allows more modularity in the code, and offers the possibility to parallelize it and thus reduce computational time. The control case that has been used to test the accuracy of the new implementation is the response to the apparent motion stimulus [80].
In response to a localized stimulus with a diameter of $0.25°$, presented at two positions separated by $1°$ to $2°$, for a stimulus duration of 100 ms, and with a latency of 50 ms, we observe an increase in the activity of the retinotopic representations of the two stimuli which then spreads laterally over millimeters of cortical surface.

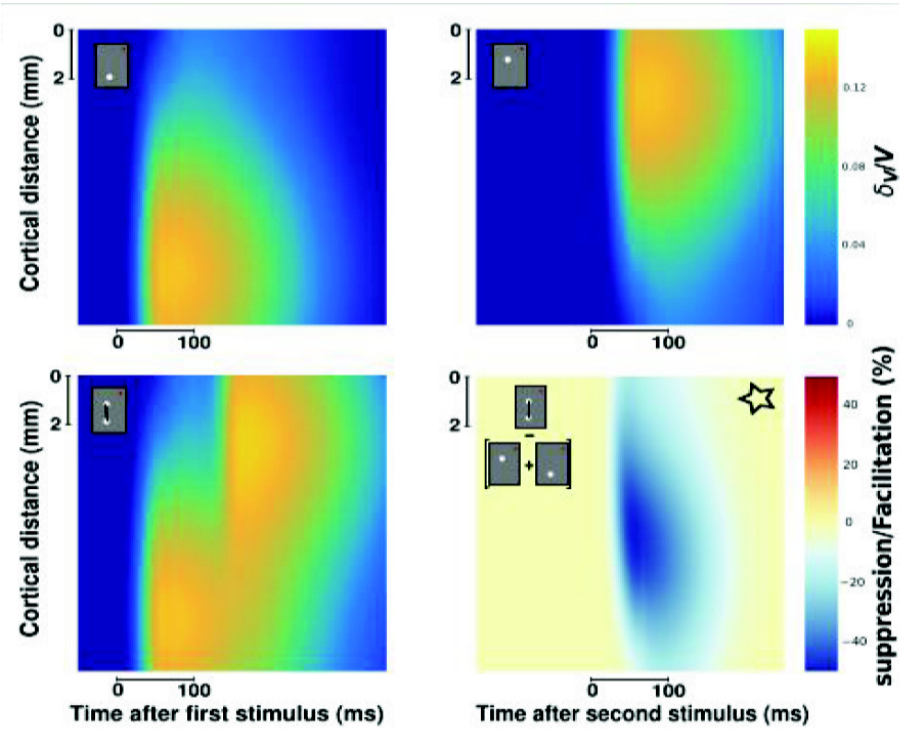

Figure 6.6: Python implementation of the model : A) Model response to the first stimulus. B) Response to the second stimulus. C) Response to the apparent motion sequence. D) Response to the apparent motion stimulus subtracted from the sum of responses to the two stimuli, showing suppression [80].

Fig. 6.6 and 6.7 show the response of the model, first with the python implementation and then with our C++ implementation, to two distant stimuli S1 and S2, and the response to the temporal succession of S1 and S2. This temporal sequence generates a propagation of activity from the cortical response to the first stimulus moving towards the cortical response of the second one, giving rise to the illusion phenomenon of apparent motion. In agreement with experimental results, when subtracting the response to the apparent motion from the linear summation of the individual responses, a suppression wave emerges, propagating from the spatial onset of the second stimulus S2 towards the onset of S1.

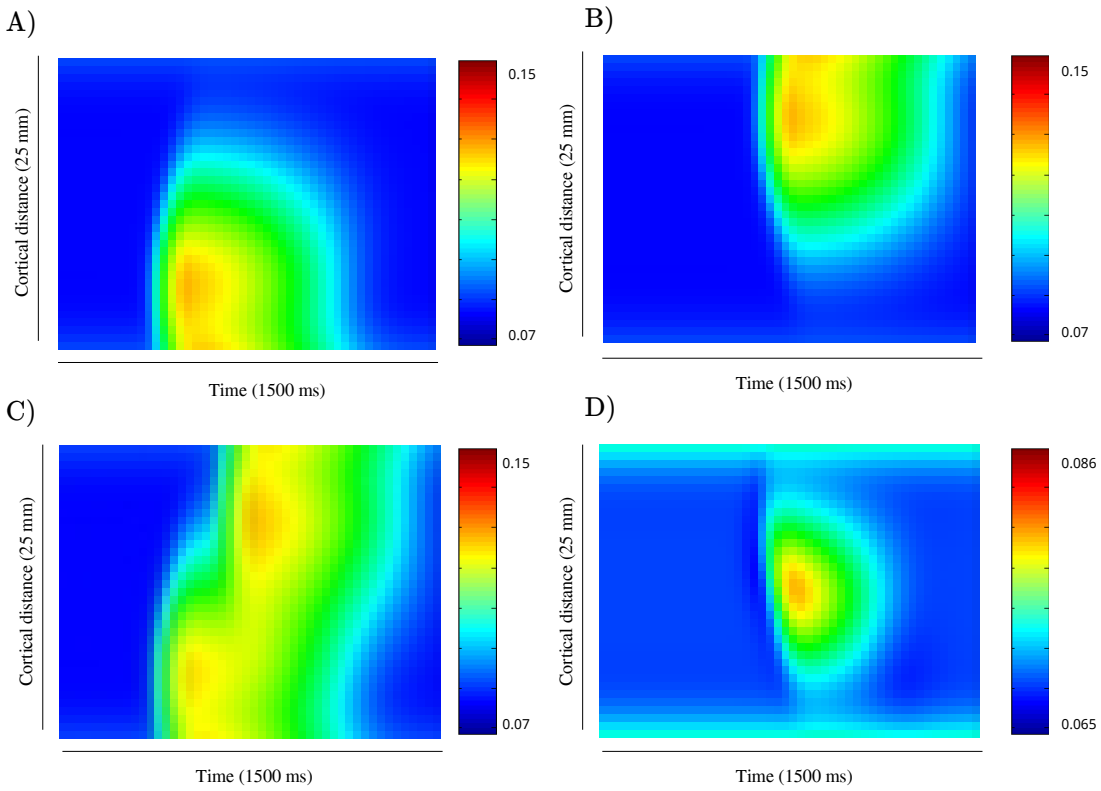

Figure 6.7: C++ implementation of the model.A), B), C) and D) are the same as Fig. 6.6. Unlike Fig. 6.6, sub-figure D) is not normalized, showing only the activity instead of the ratio of suppression and facilitation.

The obtained results and their validation enable us to use our implementation to conduct new computational experiments regarding motion anticipation in V1.

6.3 Studying anticipation in V1

6.3.1 Experimental measures (Courtesy of F. Chavane)

The experimental data provided by the lab of F. Chavane are VSDI recordings of cortical columns spanning over a cortical area of 2 to 3 degrees, responding to a bar moving at $6.6°/s$.

In order to analyze these experimental data, we form clusters of cortical columns that are spatially close and have similar responses. We use the time of the peak of response as a clustering criterion : columns whose temporal peak of activity is close up to a threshold (5ms) belong to the same cluster. We compute the mean and standard deviation of these clusters, which provide a synthetic view of the population's activity. We then determine the width at the 2/3 of the height for the different clusters. This measure decreases with distance from the start of motion, giving responses that are narrower and narrower.

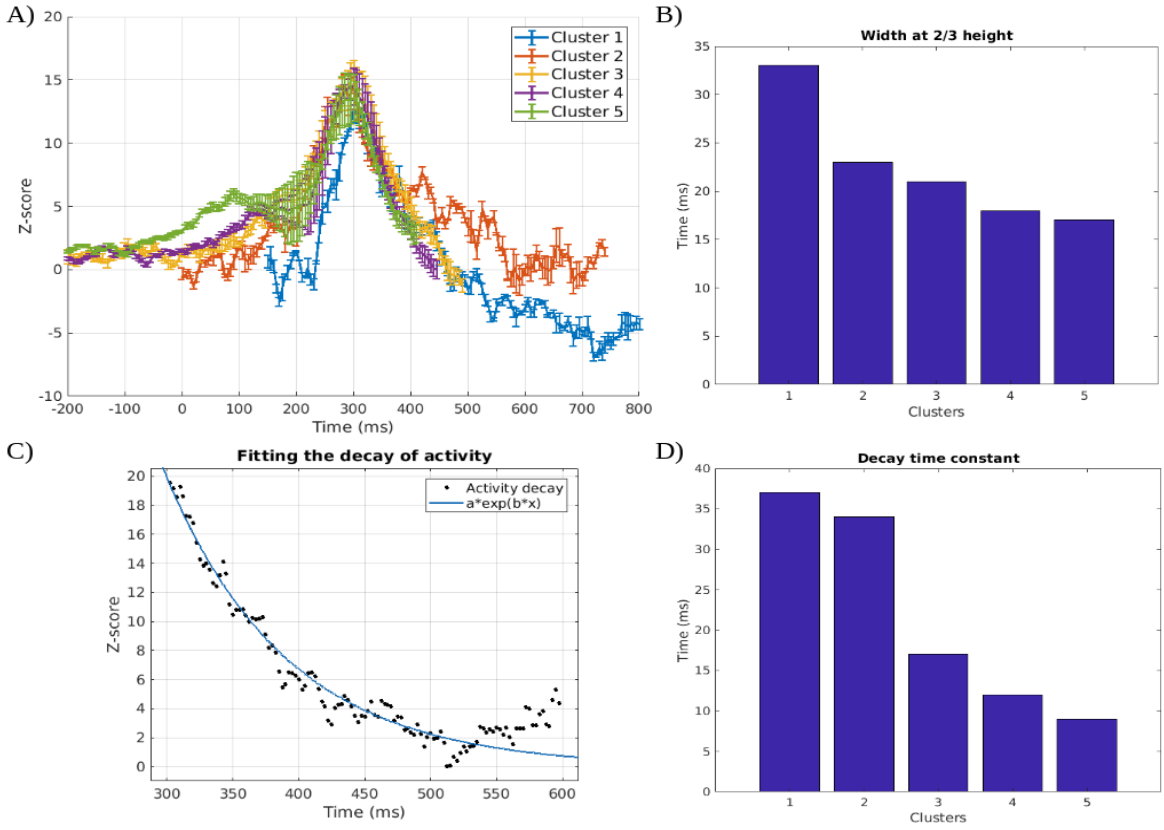

Figure 6.8: A)Cortical columns have been divided into five clusters, ranked as a function of distance from the start of motion. B) The width at 2/3 height decreases with distance. C) Fitting the decreasing part of the response with an exponential. D) The characteristic time of decay decreases with distance. *The data has been provided by F. Chavane's Lab.*

As shown in Fig. (6.8 A), the peak response is almost constant for all clusters. To estimate the time decay, we fit the curve with a decaying exponential, and then plot the characteristic times of decay for the different clusters. The characteristic time of the decay decreases with distance, which could mean that the anticipatory increase in the activity could be compensated by a faster decay.
Finally, for cells that are far enough from the onset of motion (yellow, purple, and green clusters in Fig. 6.8), there is an emergence of we will call in the following the "Shoulder" effect. This effect denotes an increase in the VSDI activity to an intermediate steady state prior to the incoming excitatory drive, due to lateral connectivity, and possibly to feedback.

6.3.2 Studying anticipation with the mean field cortical model

6.3.2.1 Gaussian external drive

As a first step, the retino-thalamic input is replaced by a moving stimulus with a Gaussian shape, to study the ability of the model to reproduce anticipation. We use for all the following simulations the same parameters as for the apparent motion stimulus:

- Number of cortical columns = 40
- Length of cortical space = 25 mm
- Extent of excitatory connections : 5 mm
- Extent of inhibitory connections : 1 mm
- Conduction velocity : 300 mm/s

The moving Gaussian has a velocity of $1.4mm/s$ (equivalent to $4.2°/s$). In this framework, anticipation depends on the width of the Gaussian, appearing for smaller values of the standard deviation. The built-up anticipatory "shoulder" effect doesn't arise in this setting though.

Fig. 6.9 shows the VSDI activity of a one dimensional cortical area of 25 mm of three cortical columns with a spacing of 6 mm, responding to a moving Gaussian with a standard deviation $\sigma = 3.5mm$. Though the increase in the activity is faster as we move further from the start of activity (the distance between the VSDI purple and green curves is smaller than the distance between their respective external drive),

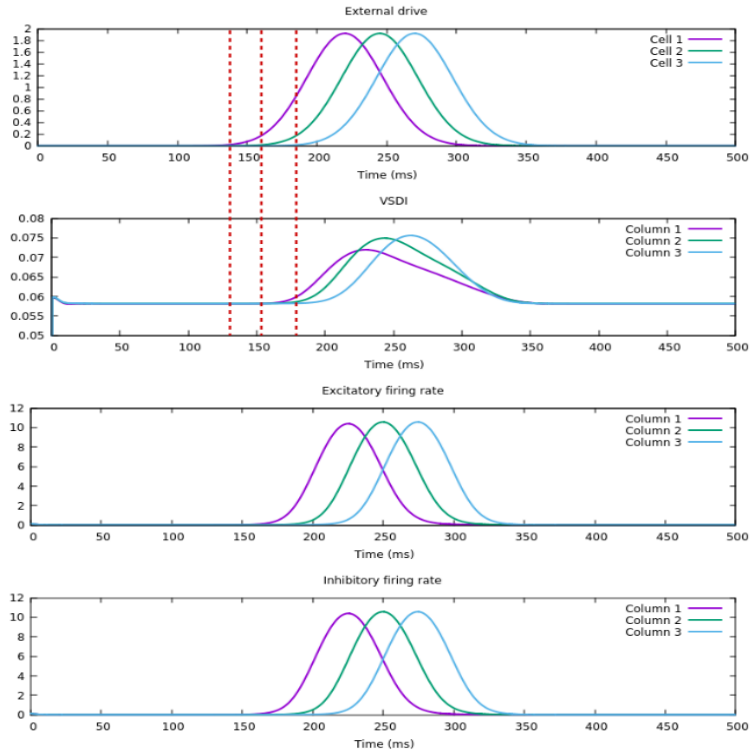

Figure 6.9: Mean field response to Gaussian with a standard deviation $\sigma = 3.5mm$ moving at $1.4mm/s$. From up to bottom : the external drive, mimicking three ganglion cells spaced by 0.1 mm, the VSDI activity, the excitatory firing rate and the inhibitory firing rate of three cortical columns spaced by 1 mm. The red dashed lines show the onset of motion in the external drive.

anticipation doesn't occur in this configuration since the response always lags behind the external drive.

Fig. 6.10 shows the VSDI response to a Gaussian with a standard deviation $\sigma = 0.7mm$. The further the cortical column from the start of motion, the earlier its activity starts increasing as compared to its external drive, showing here an anticipatory effect. However, after the curves reach their peak, a sustained activity appears which doesn't correspond to the shape of response observed in the experimental data. This might be indicating that either the speed of the bar is very low as compared to the conduction speed, giving a large accumulation of the propagating activity after the peak response, or that the Gaussian shape of the external drive is not realistic.

In the setting that allowed us to reproduce anticipation, we want to suppress the post-peak sustained activity. We test our first hypothesis by increasing the value of the velocity to $2.8mm/s$ (equivalent to $8.4°/s$). While the sustained activity doesn't die out, this velocity increase suppresses the anticipatory effect. (Fig. 6.11)

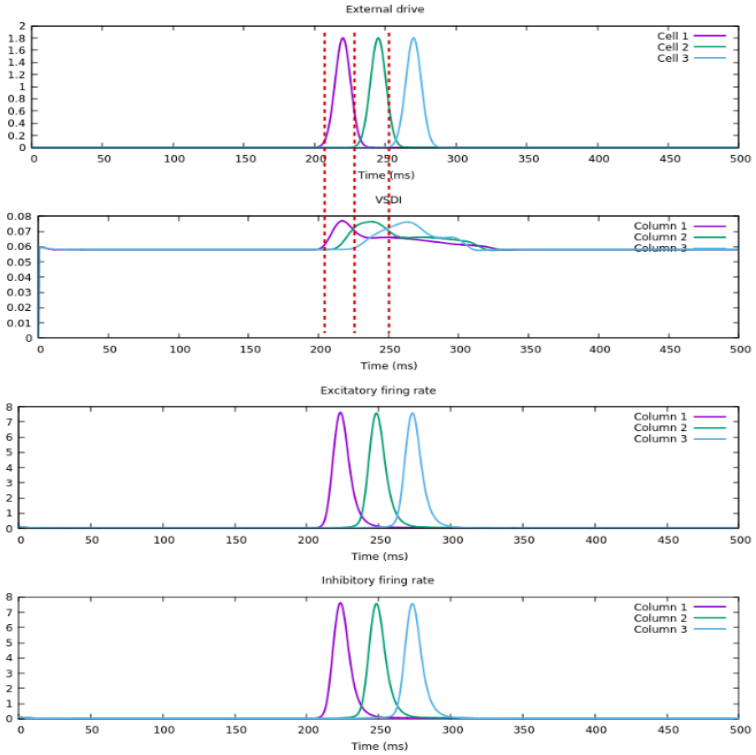

Figure 6.10: Same as Fig. 4. The Gaussian has a standard deviation $\sigma = 0.7mm$. Anticipation arises in this configuration : the onset of cortical VSDI activity occurs before the onset of the external drive, denoted by the red dashed line.

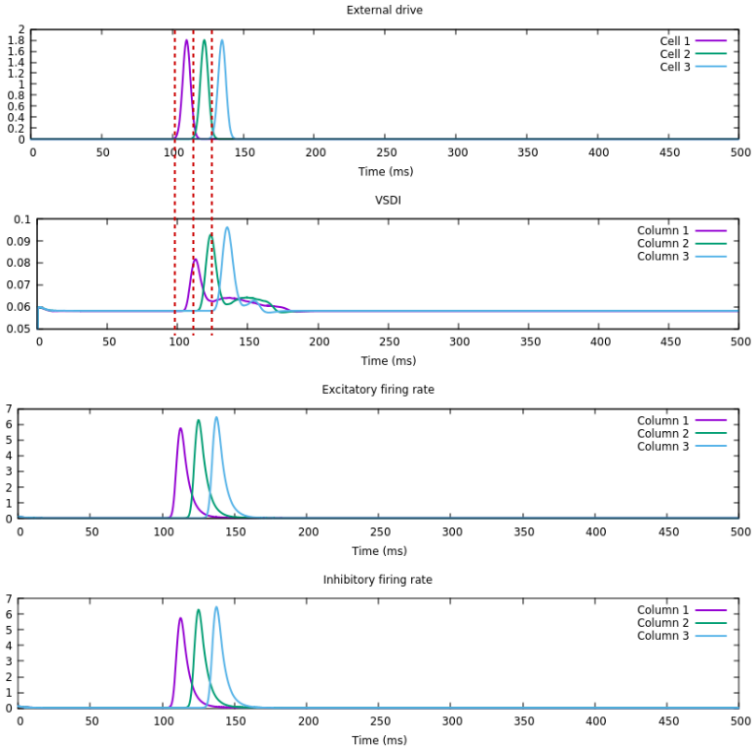

Figure 6.11: Same as Fig. 4. The Gaussian has a standard deviation $\sigma = 0.7mm$, and a velocity of $2.8mm/s$. Anticipation is suppressed by the increase in the velocity. However, the sustained post-peak activity doesn't depend on the speed. After the peak in the VSDI activity, there is an emergence of a sustained activity.

6.3.2.2 Alpha profile external drive

All in the same configuration, we now test the possibility to suppress of the sustained activity without affecting the anticipatory effect, by changing the shape of the external drive.

We set it as a moving alpha profile, with the same initial velocity of the form :

$$f(t) = exp(-\frac{t}{\tau})t\mathcal{H}(t)$$

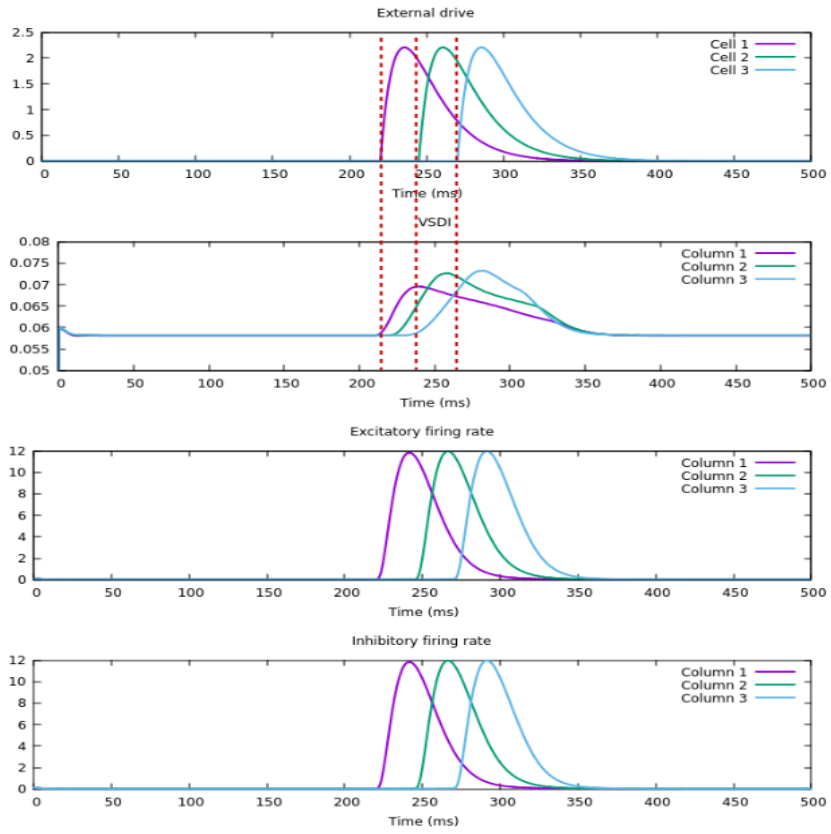

Figure 6.12: The external drive is taken here as an alpha profile in space with $\tau = 2mm$, and a velocity of $1.4mm/s$. The sustained post-peak activity fades away while the anticipatory effect is preserved, with a VSDI activity that starts increasing before the onset of the external drive.

With an alpha profile moving at $1.4mm/s$, we manage to get a VSDI response showing anticipation, while suppressing the sustained activity. *One should note here that the amplitude and speed of the alpha profile is equal to the Gaussian drive we used in the previous subsection, meaning that the mean field model is sensitive to the external drive shape.* It's all the more interesting as the different external drives that we will be using in the future chapter, coming from our retina model, generally have an asymmetric shape

close from the alpha profile, with a fast increase and a slow decay.

6.3.3 Understanding the origin of the "shoulder" effect

We now want to investigate the emergence of the "shoulder" effect (the rise of an activity plateau prior to the peak that we observe in experimental data). For that, we use, as an external drive, a moving alpha profile that stops at the middle of the cortical area. Thus, the cortical columns located in the second half of the cortical field only receive the activity coming from lateral connectivity. This propagating activity undergoes an attenuation as a function of distance. In order to have the "shoulder" effect, the propagating activity should accumulate in a way to give a plateau, meaning that the activity coming from different columns should get to the considered column with more or less the same amplitude. It is therefore unlikely to get a shoulder effect with the mean field model, unless the external drive is designed in a way to compensate this spatial attenuation.

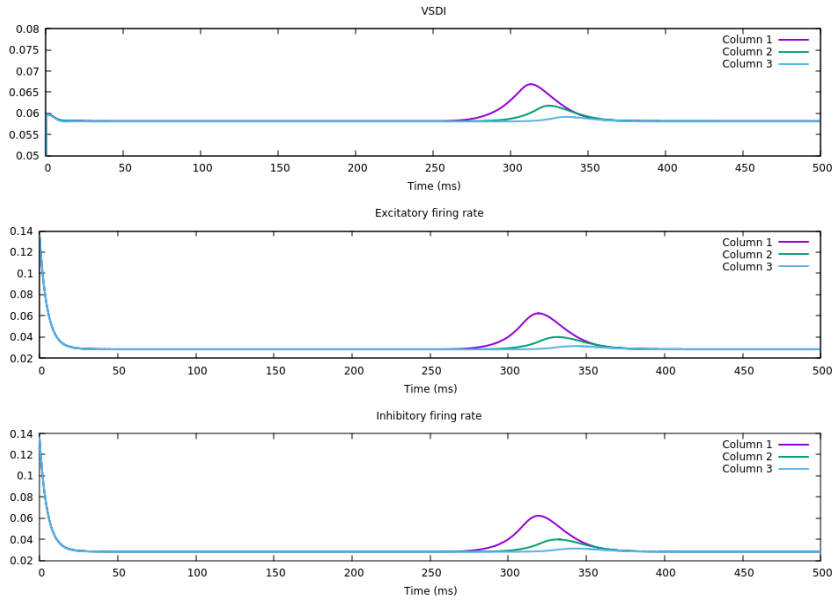

Figure 6.13: Mean field response to an external drive consisting of alpha profile moving at $1.4mm/s$. The stimulus stops when it gets to the middle of the cortical columns line. Hence, the columns shown in the figure don't receive any external drive. Their activity is only due to lateral propagation. The figure shows the attenuation of the propagating activity as a function of distance.

As stated earlier, the shape of the VSDI response highly depends on the shape of the afferent external drive, but also on its amplitude. Using an alpha profile with the same velocity but with a higher amplitude, we were able to find a regime where the

VSDI activity a steady state for time span of 50 ms before starting to decrease again. We were unfortunately not successful in finding a regime where the activity increases more saliently when the cortical column effectively receives the stimulus.

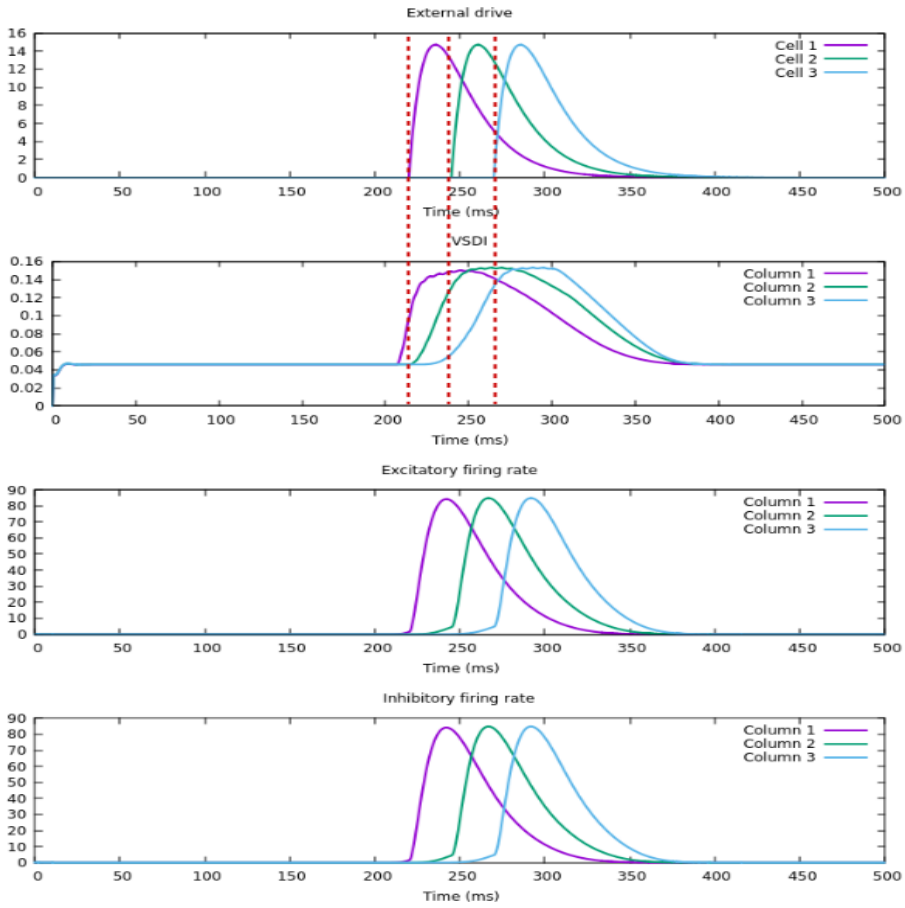

Figure 6.14: Mean field response to an external drive consisting of a translating alpha profile with a velocity of $1.4mm/s$. We set the amplitude of the stimulus to 15 mV. The VSDI shows a sustained activity prior to the the peak of the external drive. However the activity doesn't increase further, in contrast to the experimental data.

6.3.4 Studying the latency and time to peak

In this subsection, the external drive of the cortical model consists of an alpha profile moving at $6°/s$ (equivalent to 18 mm/s of the cortex). The simulated cortical space is $8°$ long and two consecutive cortical columns have a spacing of $0.225°$. We discard the last degree in the latency and time to peak figures to avoid edge effects, giving thus a cortical space of $7°$. The bar starts its motion at $2°$.
We keep the same parameters as the ones used for the apparent motion stimulus.

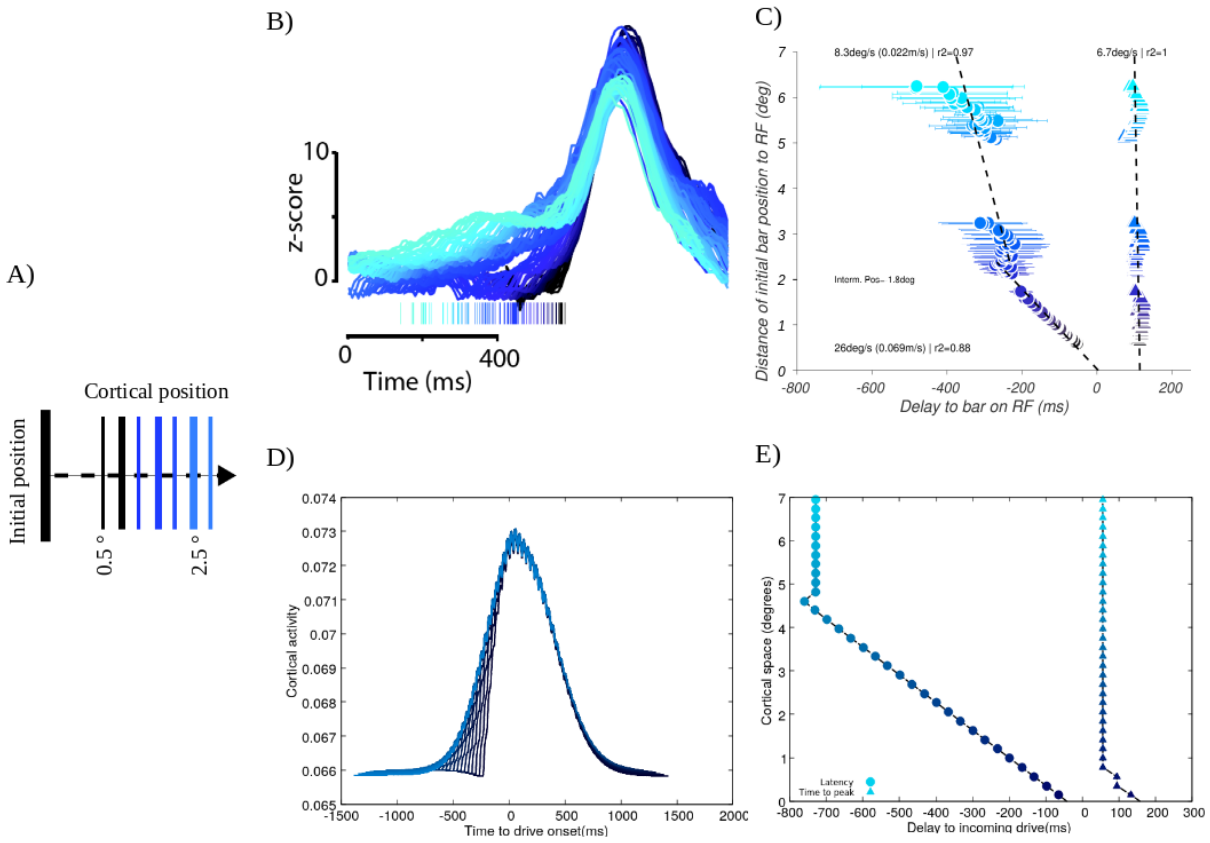

Figure 6.15: Top : Experimental setting and results (courtesy of F. Chavane lab) . Bottom : Simulation results. A) Stimulus description. B) Experimental response of cortical columns centered around their peak. C) Latency (circles) and time to peak (triangles) as a function of cortical space. The speed of the peak follows the speed of the bar (hence 6.7 deg/s) whereas the latency increases faster than the speed of the bar (hence 8.3 deg/s). D) Response of cortical columns to an alpha drive. The curves are centered around the peak response of there corresponding drive. E) Latency and time to peak as a function of cortical space. The lighter the color, the further the cell is from the onset of motion.

Fig. 6.15 shows the response of cortical columns to a bar spanning over their entire receptive field. While as in the data, the time to peak function is constant, the la-

tency function increases linearly with space, and in contrast with experimental results where the latency slope decreases, the latency function becomes constant starting from approximately 4.5 °. This is due to the fact that the cortical mean field model doesn't implement a feedback mechanism.

6.3.4.1 Assessing the role of excitatory and inhibitory connections

We first change the ratio of excitatory and inhibitory connections by taking the extent of inhibitory connections equal to 3 mm.
Fig. 6.16 shows that there is no significant change in the latency and time to peak curves, but only an increase in the min and max values of the cortical activity.

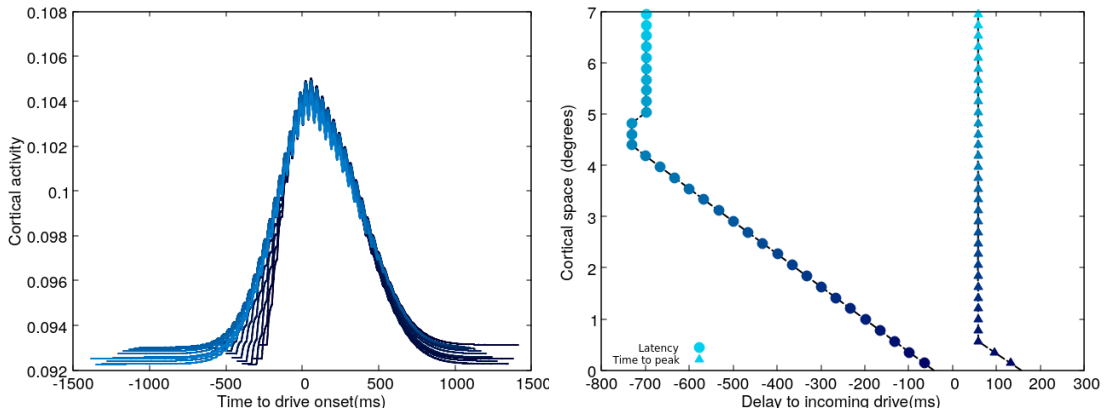

Figure 6.16: Simulation results, changing the ratio of excitatory and inhibitory connection extents (excitatory extent = 5mm and inhibitory extent = from 1mm to 3 mm). Left and right figures are the same as in figure 6.15. The ratio of connection extents doesn't change the latency and time to peak curves. .

We now change the connection extents while keeping the initial ratio :

- Extent of excitatory connections : (a) 3 mm, (b) 2 mm and (c) 1 mm
- Extent of inhibitory connections : (a) 0.6 mm, (b) 0.4 mm and (c) 0.2 mm

Fig. 6.17 shows that the lowest the connectivity extents are, the faster the latency function saturates, denoting a steady state of the network where all the cortical columns start anticipating equally. The time to peak function is always constant, irrespective of the value of the connectivity extents.

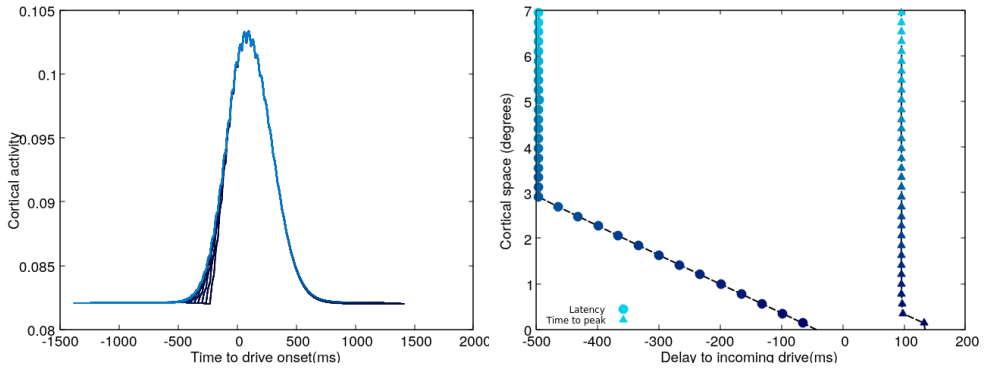

(a)

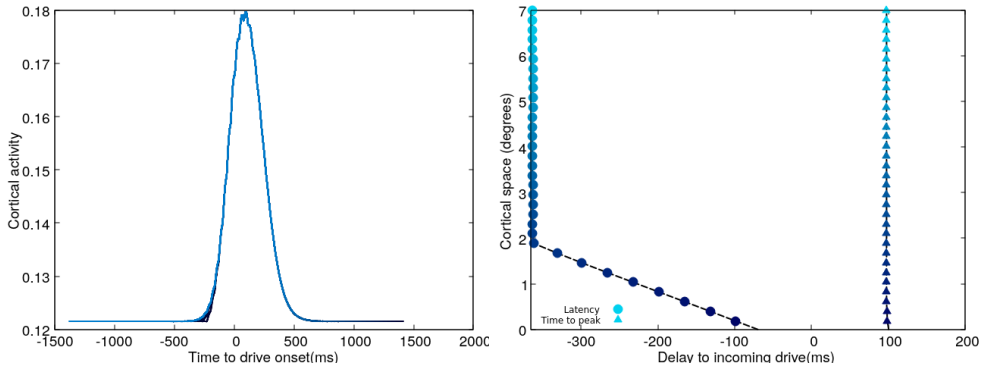

(b)

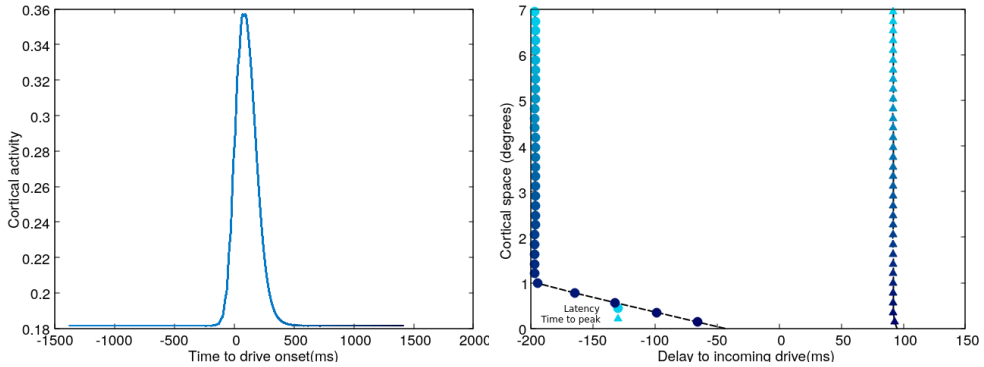

(c)

Figure 6.17: The effect of connection extents. Time course of responses and latency-time to peak curves, for an excitatory connectivity extent (resp. inhibitory) of (a) 3 mm (resp. 0.6) (b) 2 mm (resp. 0.4) and (c) 1 mm (resp. 0.2). The lower the connection extents, the faster the latency curve saturates. .

6.3.4.2 Assessing the role of conduction velocity

Keeping the connectivity extents equal to the reference parameters, we vary the conduction velocity : (a) 50 mm/s (b) 100 mm/s and (c) 400 mm/s.

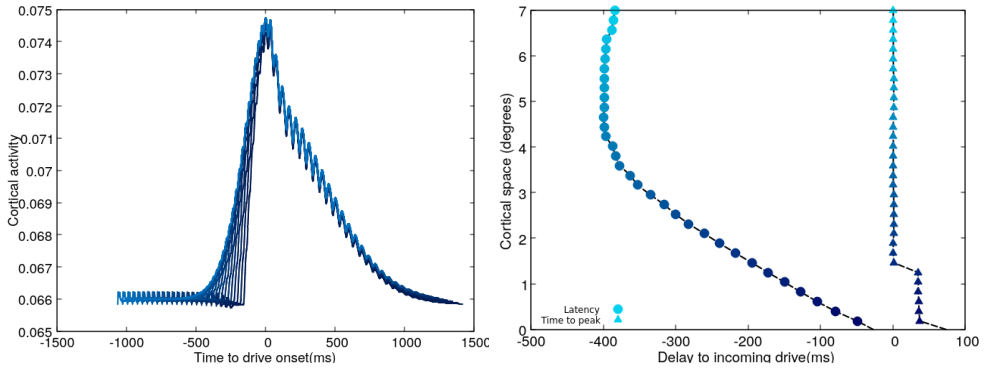

(a)

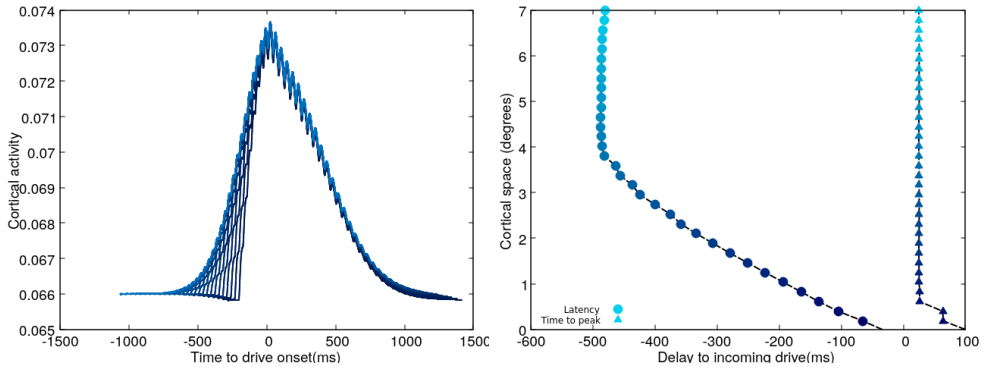

(b)

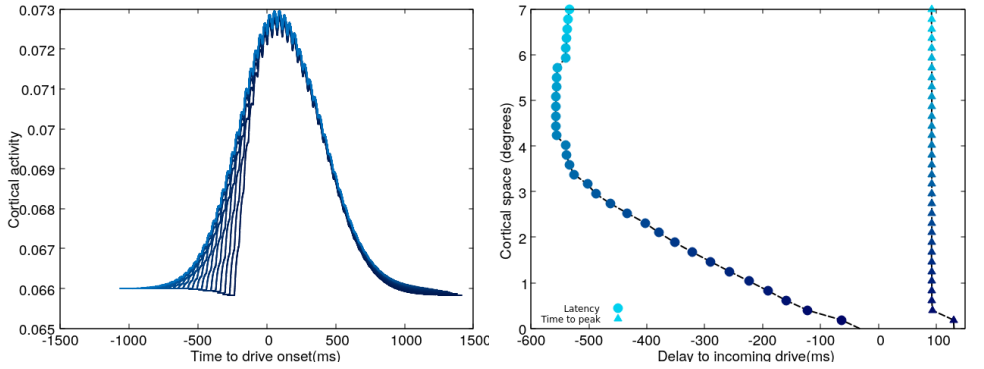

(c)

Figure 6.18: The effect of conduction velocity. Time course of responses and latency-time to peak curves, for a conduction of (a) 50 mm/s (b) 100 mm/s and (c) 400 mm/s.

Fig. 6.18 shows that, as it could be expected, the latency slope is correlated with the value of conduction. The higher the conduction, the higher the slope (in algebraic value). The function linking the latency slope to the conduction velocity can be fitted by the function $f(x) = a.e^{\frac{b}{x}}$, with $a = -18.5 \pm -0.7467$ and $b = 31.3 \pm -2.805$. The results of the fit are shown in the following figure :

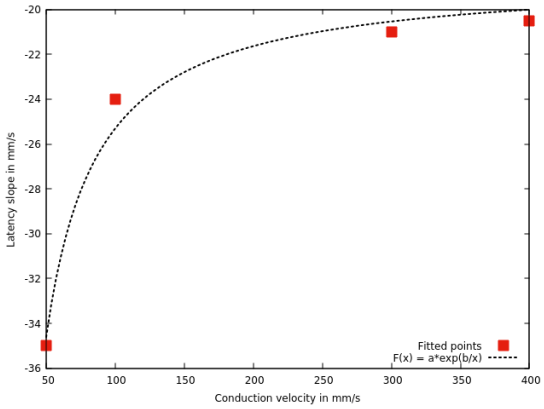

Figure 6.19: Fit of latency slope as a function of conduction velocity. .

The function suggests the existence of a limit value of the latency slope (here equal to -18.5 ms), showing the bounded nature of the network ability to anticipated.

6.3.5 Concluding remarks

In this chapter, we presented the mean field model that we use for cortical simulation of anticipation. We studied the ability of the model to anticipate, replacing the retino-thalamic input by ad-hoc Gaussian and alpha function (thus without a retinal drive). We showed that the cortical response features are highly driven by the shape of the external drive, with the alpha drive given more realistic results. We also demonstrated that the anticipatory effect decreases with speed.

We then computed the latency and time to peak function in different simulation settings. We demonstrated that the latency depends on the values of the connectivity extent, as well as the conduction velocity. In particular, the latency saturates for low values of connectivity extent. Additionally, the slope of the latency increases with the conduction velocity before also saturating. Finally, the time to peak function, except for border effects due to the start of motion, is constant throughout the cortical space.

Chapter 7

Results of the retino-cortical model

In this chapter, we report the results of the integrated retino-cortical model. We first explain how the retina and the cortex models are connected. Then, we focus on the effect of the anticipatory mechanisms occurring in the retina and studied in Chapters 3 and 4 on cortical anticipation. Our aim here is to emphasize the collaborative aspect of retinal and cortical anticipation.

7.1 Connecting the retina and the cortex models

In the monkey, 1 degree of visual angle corresponds to approximately $0.3mm$ of the retina. While the size of the cortical degree is not sharply determined in the literature, values range from $3mm$ to a maximum of $15mm$ [88]. In order to be consistent with the conversions used in [80], we will choose the value of $3mm$ for the cortical degree.

As a first approximation, we neglect the anisotropic effects involved in visual retinotopy, and we consider that retinal ganglion cells project linearly on cortical neurons with a magnifying factor (Fig. 7.1). The average distance between two neighboring ganglion cells is about 50 μm [89], which gives a retinal linear density ϱ_r of 20 $neurons/mm$. The density ϱ_c of neurons in V1 is taken equal to 10^4 $neurons/mm^2$ which boils down to 10^2 $neurons/mm$. Each ganglion cell projects then on 50 neurons in 1D, and 2500 in 2D.

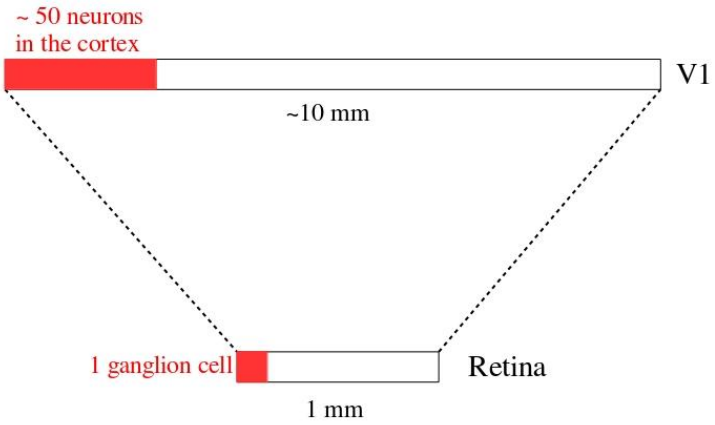

Figure 7.1: Schematic description of the retino-cortical conversion.

7.2 Latency and time to peak using a retinal drive

7.2.1 LN retina drive

We simulate a 1D grid of 120 bipolar cells spaced by 20 μm, pooled by 40 ganglion cells spaced by 62.5 μm, such that the total length of the retinal grid is 2.5 mm. The grid projects on a cortical field with a length of 25 mm. Each ganglion cell projects on a single ganglion column, with the strength of connectivity as a free parameter.
At t = 100 ms, a bar enters from the left edge of the grid, mimicking the gradual appearance of the bar in the visual field, and starts moving with a speed of 6 $^\circ$/s (equivalent to 1.8 mm/s in the retina).
We first simulate a linear non linear retina response, with a spatio-temporal filtering of the stimulus followed by a non linearity at the level of bipolar cells, and a Gaussian pooling followed by a non linearity at the level of ganglion cells.
In the figures of this subsection, we will distinguish between two definitions of latency and time to peak : the first taking as a reference time the onset of the stimulus for a given cell position, and the second taking as a reference time the onset of the retina drive. The first quantities enable us to study the compound anticipatory effect of the retina and V1, while the second show what the cortex adds to retina anticipation.
Fig. 7.2 shows the responses of 40 cortical cells receiving the LN model output. The difference in amplitudes is due to the retinal drive : cells whose receptive field center is located near the onset of the bar have a higher response since the bar doesn't span their entire receptive field, and thus doesn't activate first the inhibitory part of the receptive field.

The latency with respect to the retina input is null in the beginning of motion. This can be explained by the sharp increase in ganglion cells firing rates at the onset of motion. In this regime, the onset of cortical activity is entirely driven by the onset of retinal activity, thus resulting in a null latency. Within this same regime, the time to the peak with respect to the retina drive increases. After this initial phase, the latency starts increasing (in absolute value) linearly as a function of the cortical space, and the time to peak becomes constant. On the other hand, the latency with respect to the stimulus is uniformly increasing across cortical space, and the time to peak with respect to the stimulus becomes constant after a transient. This shows that the compound effect of the retina and the cortex in this case reproduces the behavior of the cortex alone, when fed with a translating alpha profile.

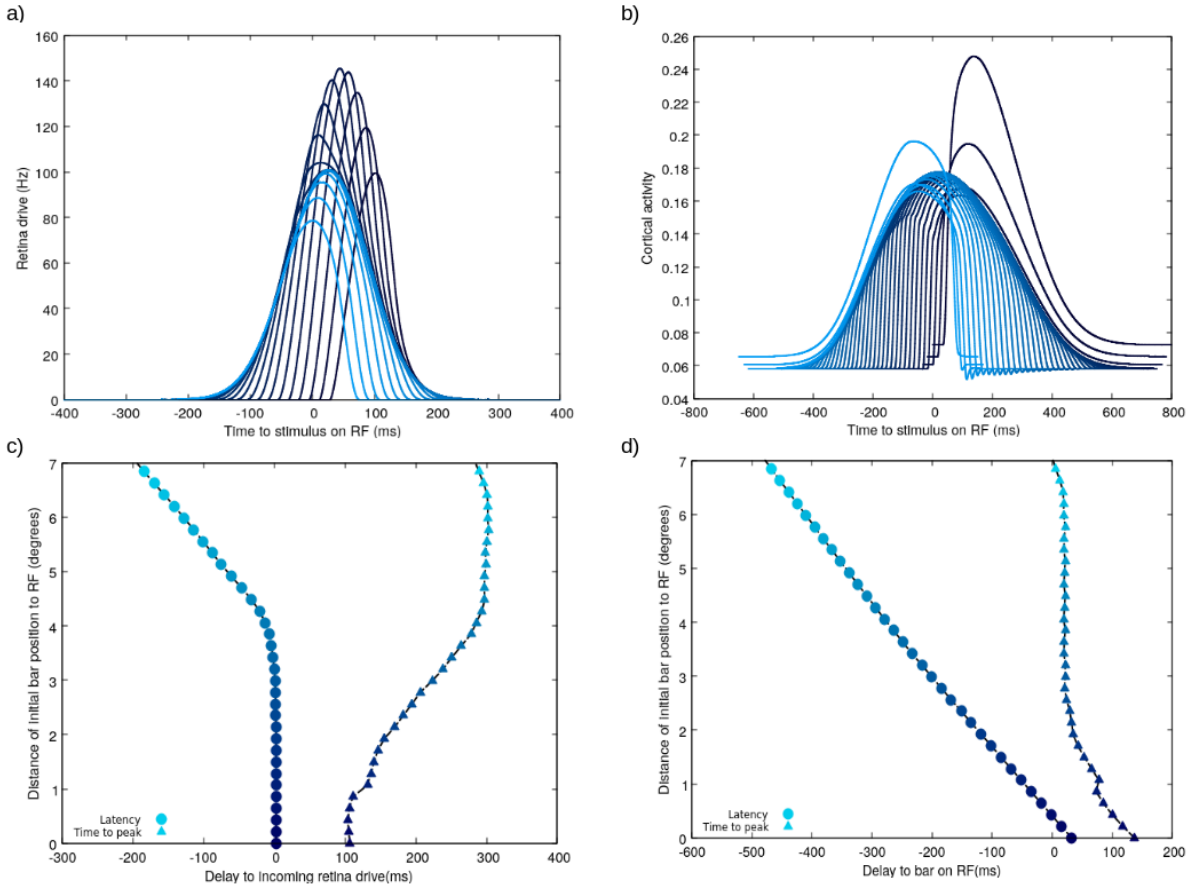

Figure 7.2: The response of the cortical model, latency and time to peak, with LN retinal drive. a) Retina responses to a moving bar, centered around the start of the stimulus. b) Cortical responses centered around their peak, driven by the retina inputs shown in a). c) Latency and time to peak taking as a reference the onset of the retina drive. d) Latency and time to peak taking as a reference the onset time of the stimulus at a given position. As in the previous chapter, the lighter the color, the further the cell is from the onset of motion.

7.2.2 Gain control retina drive

We now consider the effect of gain control in the retina on cortical anticipation. Fig. 7.3 shows the responses of 40 cortical cells receiving a retina drive with gain control. Gain control narrows the response, but doesn't affect its onset time. Consequently, compared to the response with the LN drive, only the curves of the time to peak change.

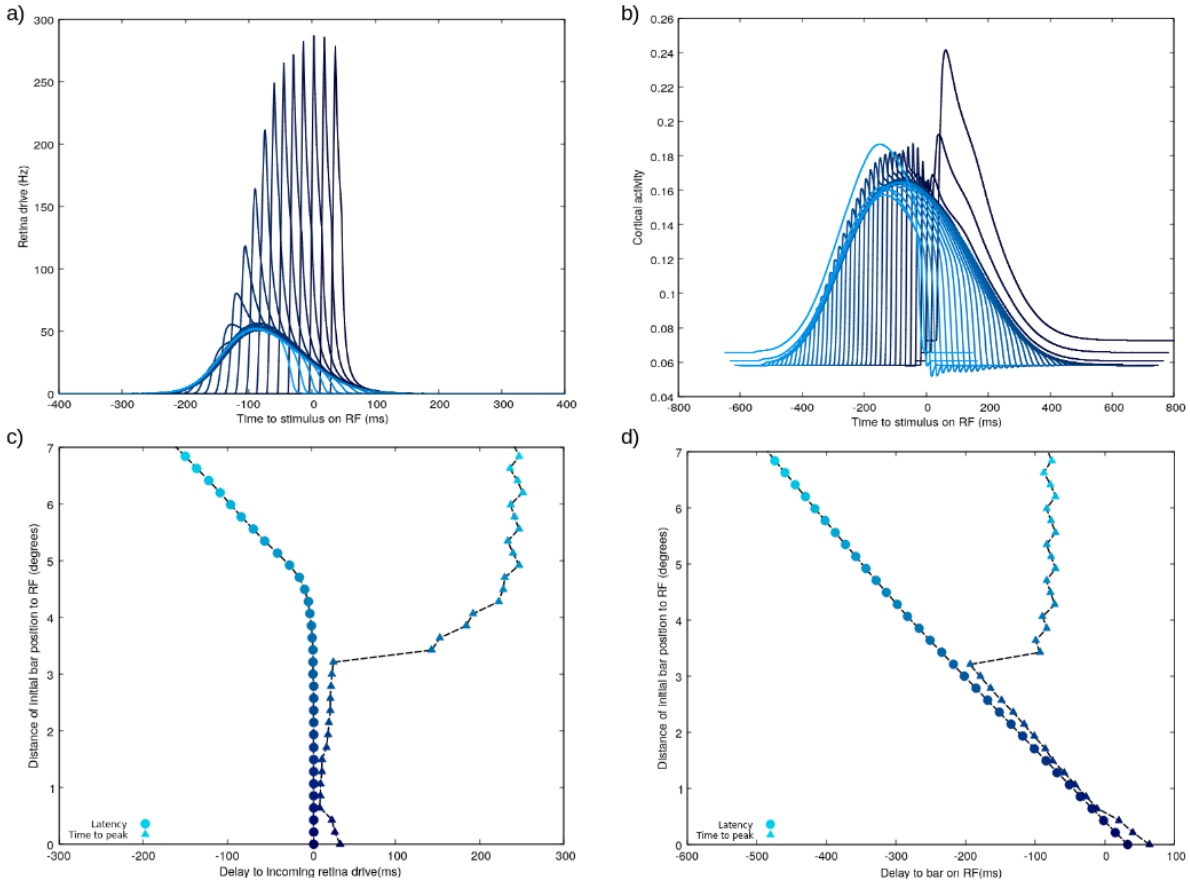

Figure 7.3: The response of the cortical model, latency and time to peak, receiving a retinal drive with gain control. a), b), c) and d) same as in the figure 7.2.

Cells near the onset of the trajectory show an increase in their firing rates which is sharper than in the previous case, due to gain control, as well as a higher peak response. Their corresponding cortical columns peaks of response are mainly driven by the retinal input peak. Consequently, in this regime, the time to peak with respect to the retinal drive is constant, while the time to peak with respect to the stimulus is decreasing, only driven by the retinal anticipation. After this transient regime, the time to peak becomes constant, but in contrast to its positive value in the LN case, the constant value of the time to peak here is negative. This is entirely due to the retina anticipation

in the case of gain control, which is characterized by a shift in the peak response, further affecting the overall retino-cortical response.

The transient spatial regime corresponds to the ganglion cells extent where the temporal response is not stationary. Fig. 7.4 show the temporal courses of ganglion cells responses and their corresponding cortical responses. Until the 15^{th} cell/column approximately, the peak of cortical activity is due to the cortical propagation of the large peaks near the stimulus onset. Afterwards, the peak of the corresponding ganglion cell takes over, giving thus a constant time to peak. The 15^{15} cell/column corresponds to $3°$, which explains the jump in the time to peak curve around this value.

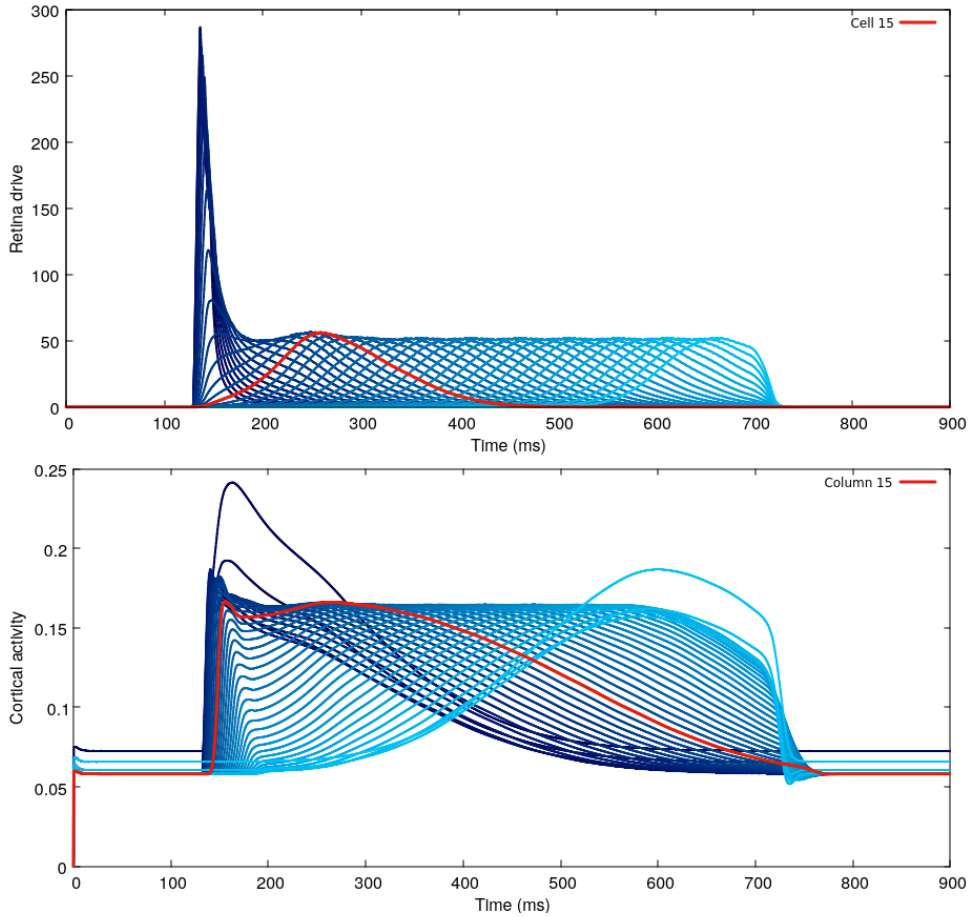

Figure 7.4: Temporal courses of ganglion cells responses and cortical activities. Columns near motion onset have two competing peaks, the first coming from activity propagation and the second from the retina input. This explains the nonlinear evolution of the time to peak curve.

7.2.3 Amacrine connectivity retina drive

In the following simulations, we add amacrine connectivity at the level of bipolar cells. In Chapter 5 a regime of parameters for the amacrine connectivity model where

it performs better than gain control in terms of retinal anticipation : the peak activity is reached earlier than with gain control alone. In this setting, we assess the effect of amacrine connectivity on the cortical anticipation. The cortical model parameters and the connectivity strength are identical to the one used in the LN model and gain control simulations.

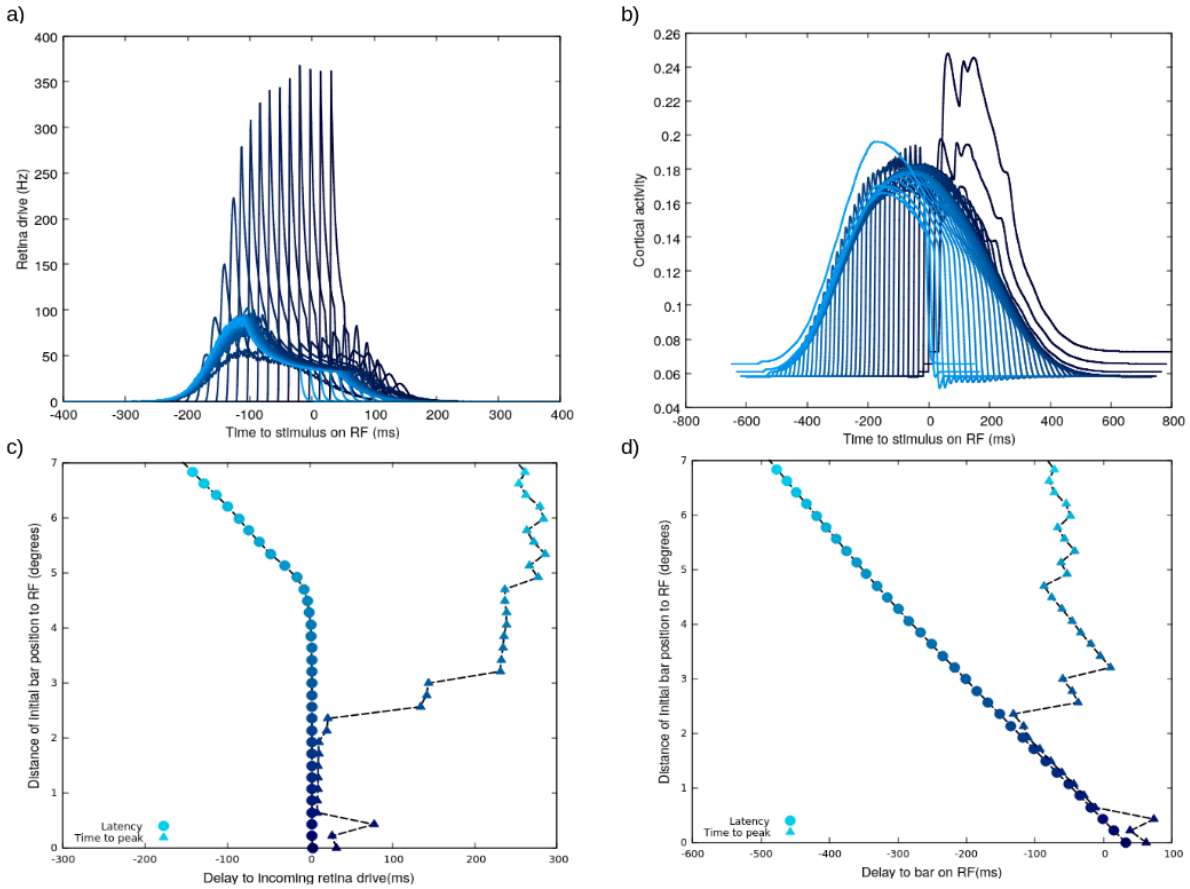

Figure 7.5: The response of the cortical model, latency and time to peak, receiving a retinal drive with gain control, and amacrine connectivity at the level of bipolar cells. a), b), c) and d) same as in the figure 7.2.

Fig. 7.5 shows that in this configuration, amacrine connectivity doesn't bring any significant change in latency and time to peak curves as compared to the gain control drive. The change appears in the level of cortical activities (see Fig. 7.6). One has to notice here that despite a significant change in the shape of the retinal drive, the cortical response shape itself doesn't substantially change, except for the amplitude, which means that more than its dependence on the external drive, the cortical model dynamics are first and foremost driven by its own network properties.

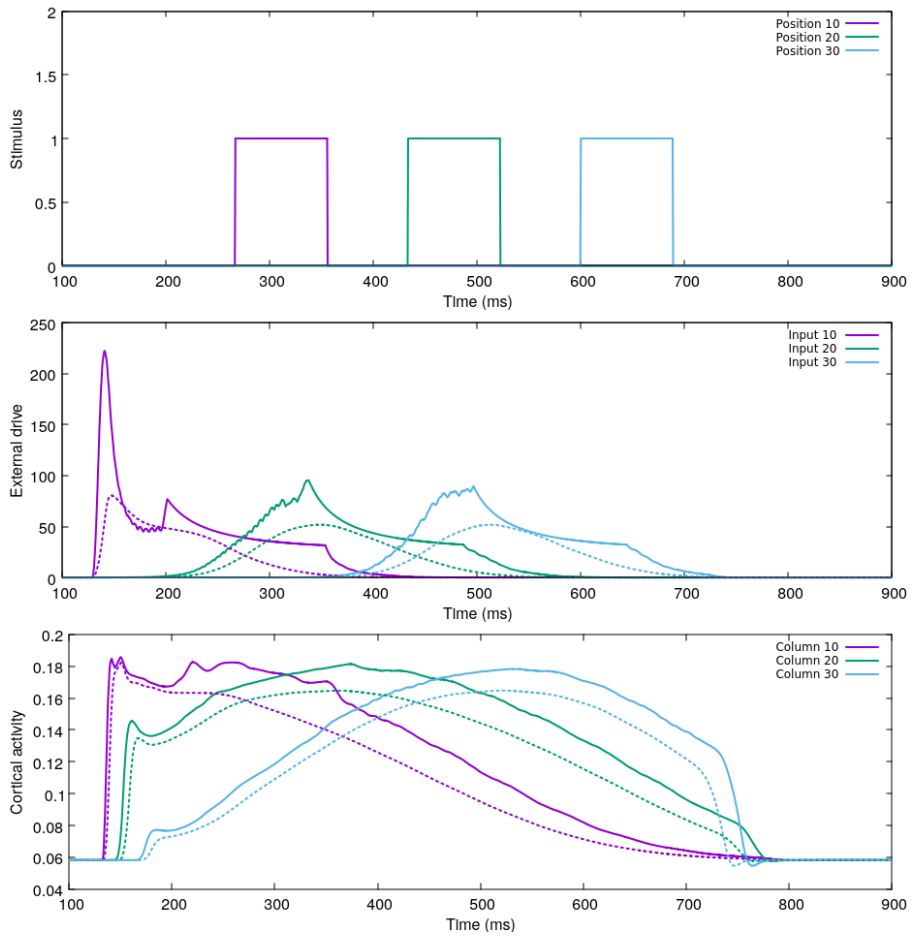

Figure 7.6: Comparison of retinal drive with amacrine connectivity and its corresponding cortical response (plain lines), and their counterparts with gain control only (dashed lines). In this regime, the ganglion cell activity with amacrine connectivity is in advanced with respect to gain control alone.

7.2.4 Gap junction connectivity retina drive

We start from the gain control model and we add gap junction connectivity at the level of ganglion cells. We have previously studied how gap junctions improve anticipation in the retina, focusing on two cases, when ganglion gain control is applied before the gap junction coupling and when it is applied after. The latter case performing better, it's the one we will use in the following simulation.

Gap junction connectivity, in contrast with gain control and amacrine connectivity, introduces an effect similar to the connectivity at the level of the cortex : the activity starts increasing before the bar reaches the receptive field.

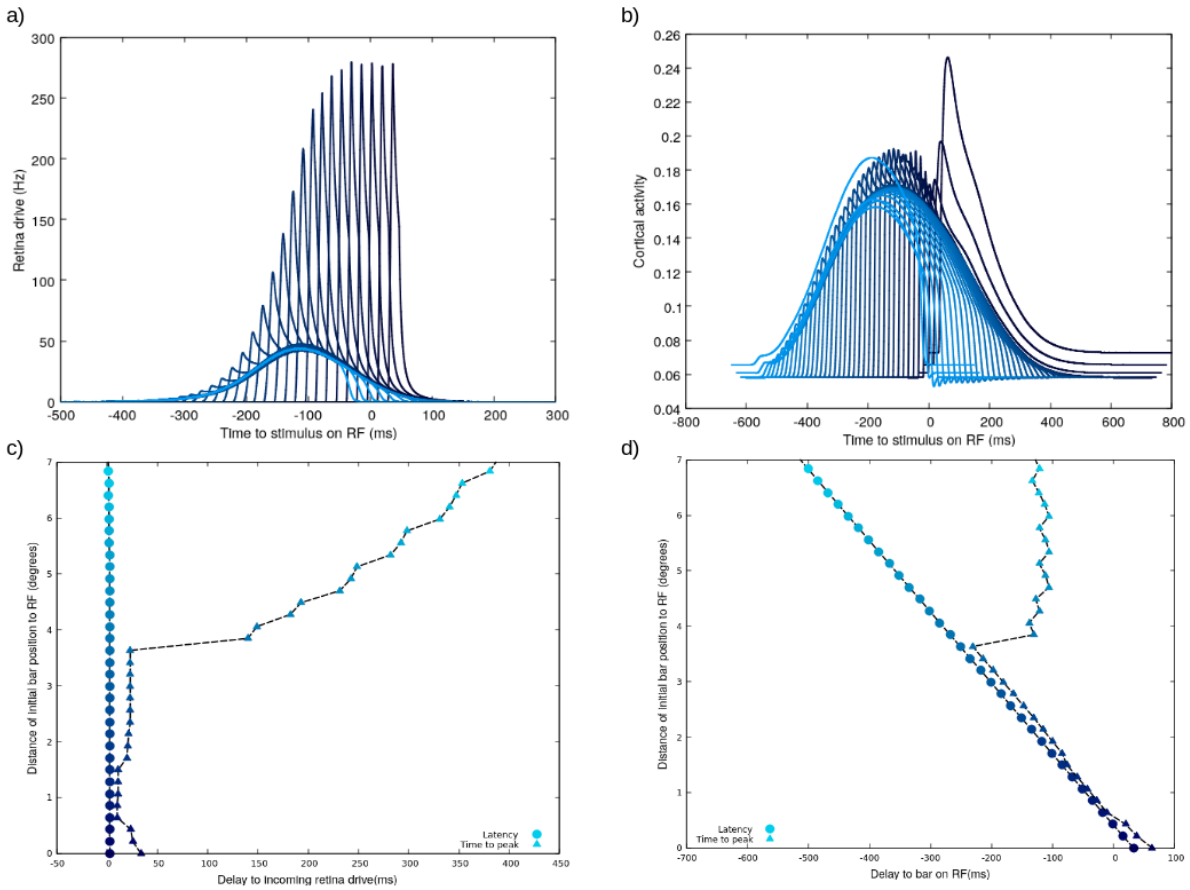

Figure 7.7: The response of the cortical model, latency and time to peak, receiving a retinal drive with gain control, and gap junction connectivity at the level of ganglion cells. a), b), c) and d) same as in the figure 7.2.

Fig. 7.7 shows that in this configuration, the cortex doesn't anticipate in terms of latency : the latency curve with respect to the retina drive is null. As for the time to peak with respect to the drive, it is first constant on the transient where the drive is not stationary, and decreases afterward, showing that the cortex delays the peak response. As for the latency and the time to peak with respect to the stimulus, the curves are similar to the gain control curves, with a slightly larger slope of latency, and a slightly more negative constant value of the time to peak.

Fig. 7.8 compares the gain control retina drive, with and without gap junctions. The figure shows in particular that the difference in the onset time at the level of the retina is much larger than in the cortex, showing that in this setting the cortex anticipated less than the retina. This result is particularly enlightening on the collaborative nature of anticipation in the retina and V1.

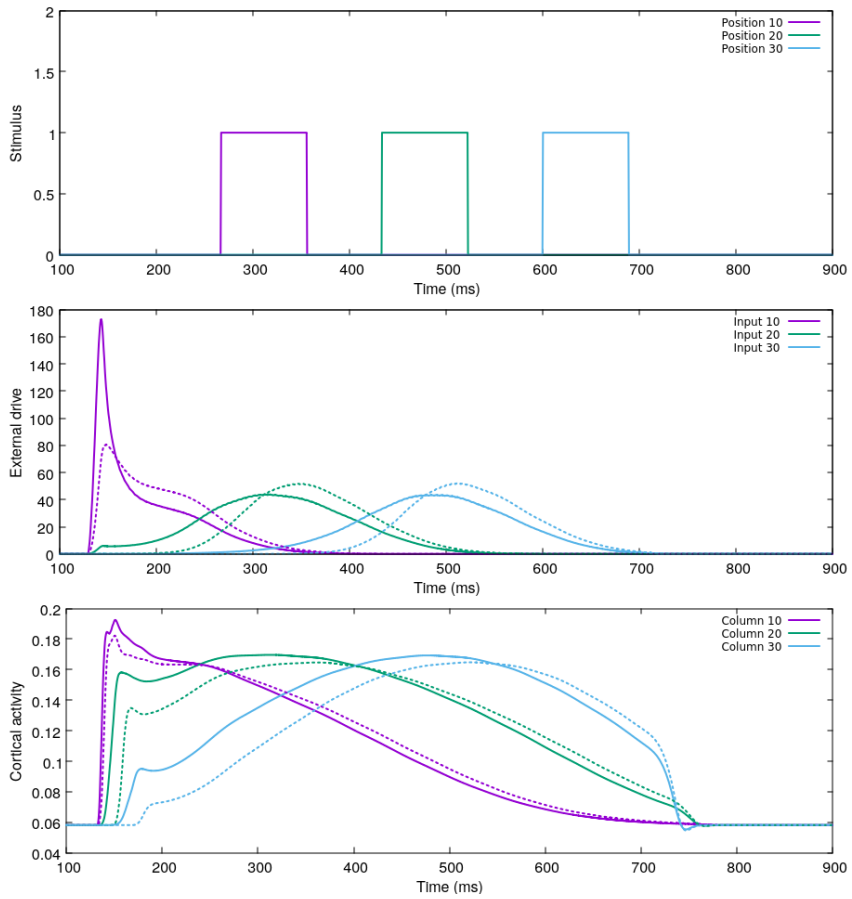

Figure 7.8: Comparison of retinal drive with gap junction connectivity and its corresponding cortical response (plain lines), and their counterparts with gain control only (dashed lines).

7.2.5 Removing edge effects

In order to be in the same conditions as in the experimental setting, we reduce the size of the ganglion cells receptive fields (the receptive fields of the monkey retina are smaller than the salamander retina). We also remove the non stationary response of the retina to the appearance of the bar, and consider only cortical columns in the center of the trajectory in order to remove cortical edge effects due to the ring connectivity. We also reduce the connectivity extent parameter to $3mm$, in order to reproduce the latency slope change that is observed in experimental data.

Fig. 7.9, 7.10, 7.11 and 7.12 show the responses of the retina and the cortex the time the stimulus reaches the RF of the cell. They also display the latency and time to peak response in the aforementioned configuration, first for the retina alone with the stimulus as a reference, then for the cortex with the same reference, and finally for the cortex with the retina as a reference, in order to emphasize the the contribution of the retina

to cortical anticipation. Note that the stimulus reference is taken when the center of the bar reaches the center of the receptive field.

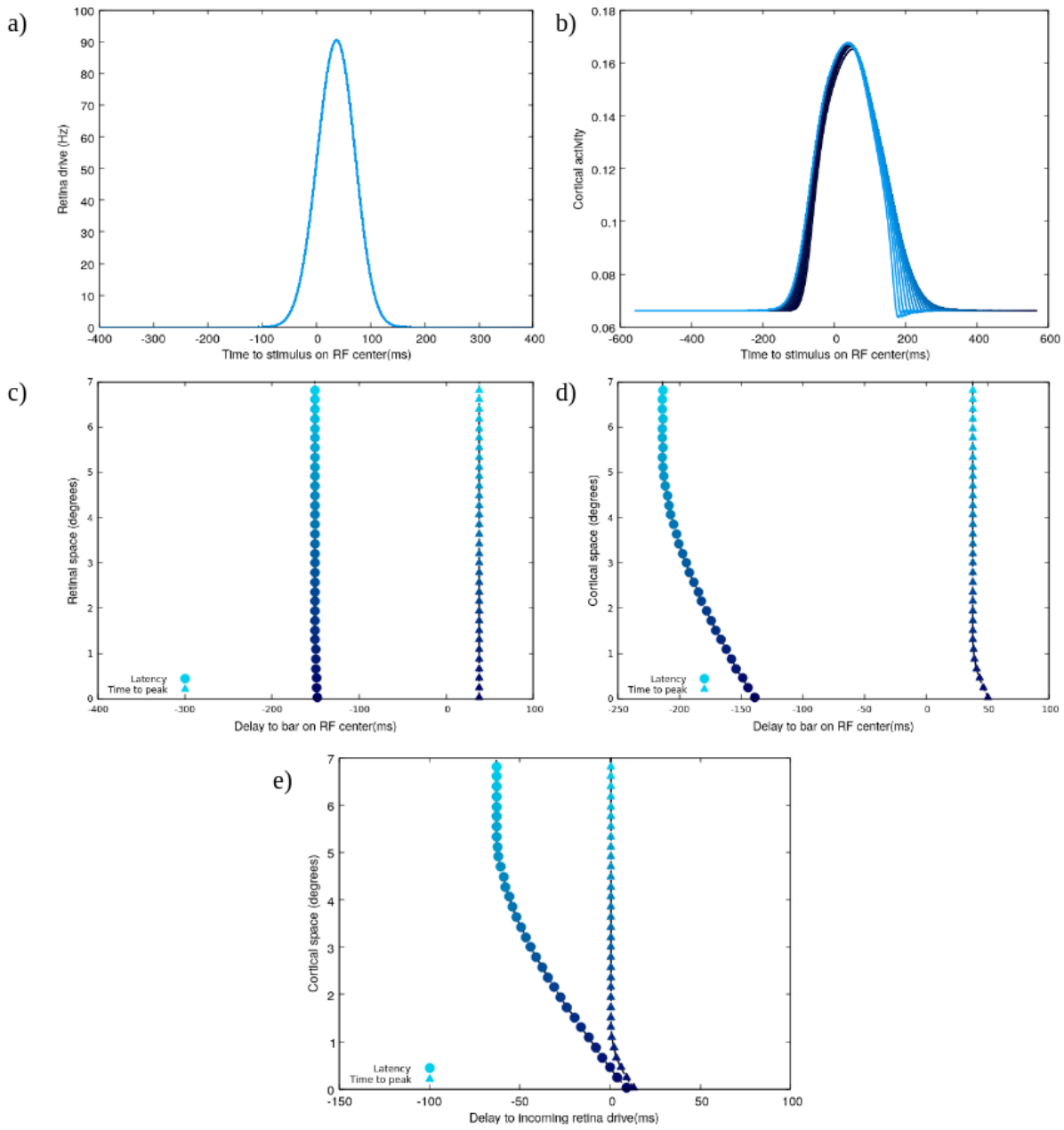

Figure 7.9: Removing edge effects for the cortical response to an LN retinal drive. a) (resp. b) Retina (Cortex) responses to a moving bar, centered around the time the stimulus reaches the RF of the cell. c) Latency and time to peak of the retina with respect to the stimulus. d) Latency and time to peak of the cortex with respect to the stimulus. e) Latency and time to peak of the cortex with respect to the retina. As before, the lighter the color, the further the cell is from the onset of motion.

When the cortex is driven by the linear non linear drive (Fig. 7.9), the latency and time to peak curves of the retina are constant, given the stationary response to the

moving bar stimulus for ganglion cells which have the bar spanning over their entire receptive field. In this case, the latency of the cortex is driven only by its own dynamics, and saturates for a given cortical length, because of the reduced connectivity. The peak response is not further displaced by the cortex.

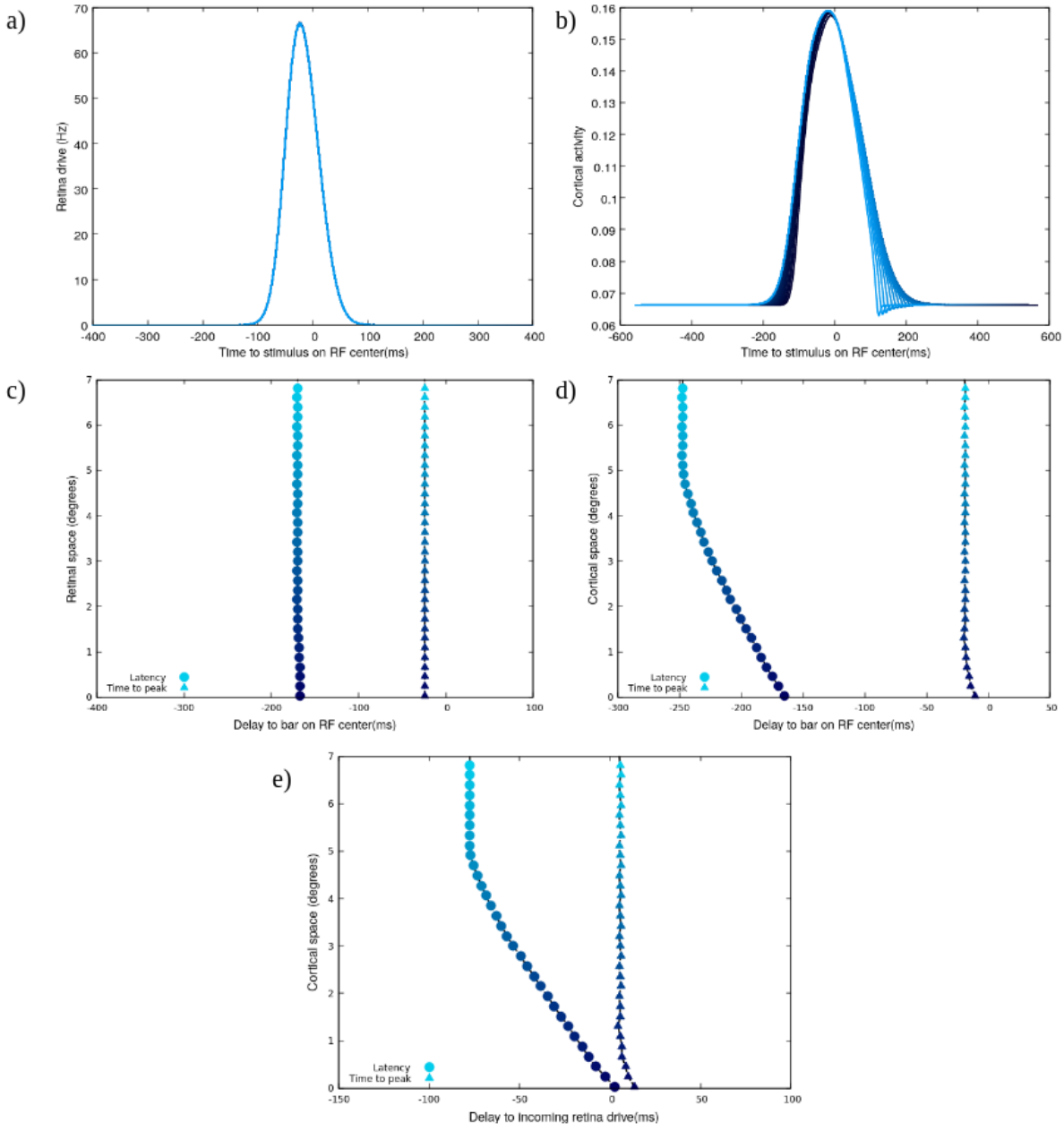

Figure 7.10: Removing edge effects for the cortical response to a retinal drive with gain control. a), b), c), d) and e) same as in the figure 7.9.

When the cortex responds to the gain control drive (Fig. 7.10), the latency and the time to peak curves of the retina are again constant, with a latency that has the same value as the LN case (the gain control mechanism doesn't change the onset of activity), and a time to peak curve which is shifted to a negative value. In this case again, the

latency curve of the cortex is entirely driven by its own dynamics. Again, the peak response is not further shifted by the cortex.

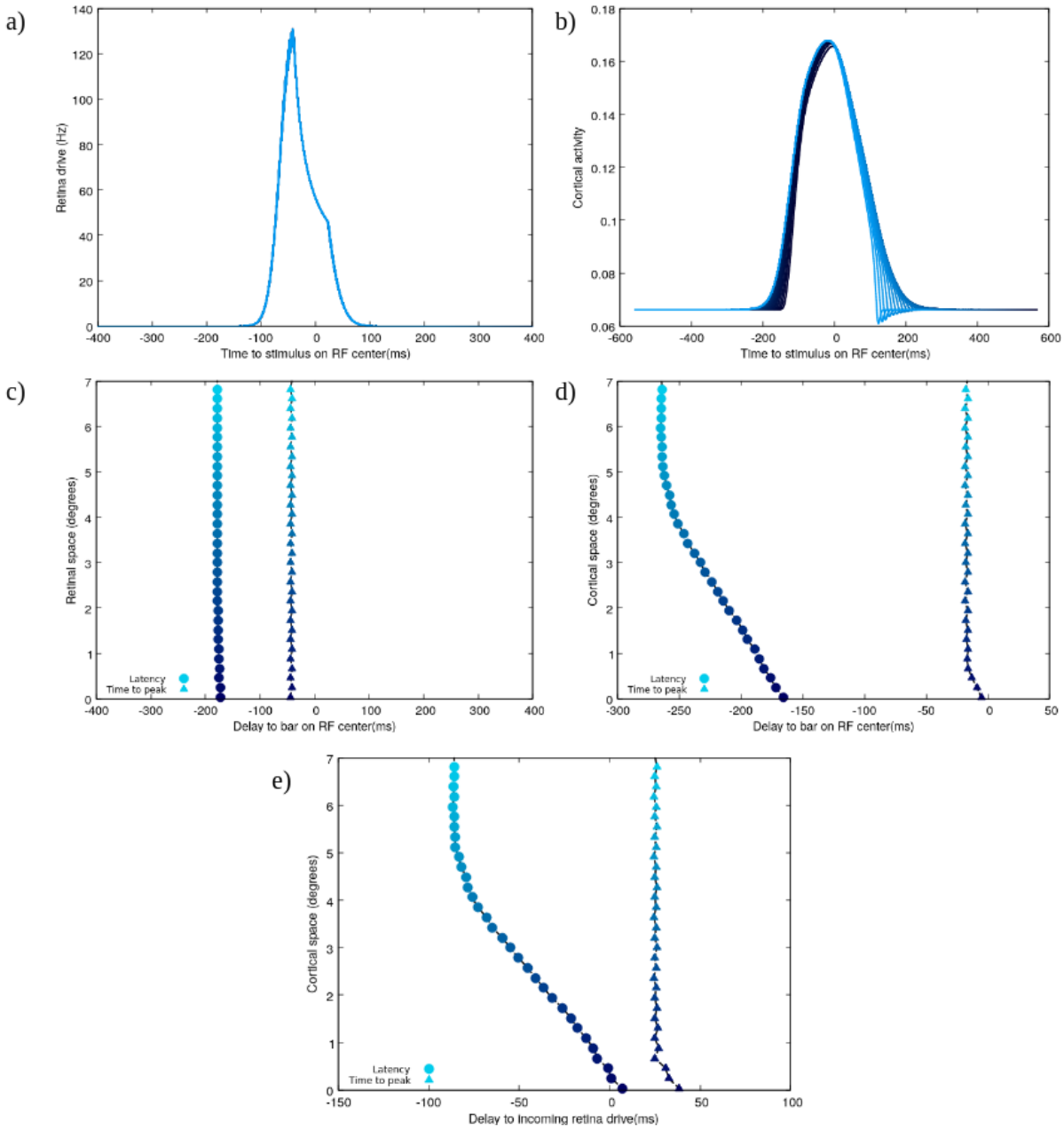

Figure 7.11: Removing edge effects for the cortical response to a retinal drive with gain control and amacrine connectivity. a), b), c), d) and e) same as in the figure 7.9.

When the cortex is responding to a retina drive with an amacrine connectivity (Fig. 7.11), the behavior of the retino-cortical model is similar to gain control case, with the following difference : the time to peak of the retina increases (in absolute value) since in this case the retina anticipates more, and the cortex delays the peak as compared to the retina.

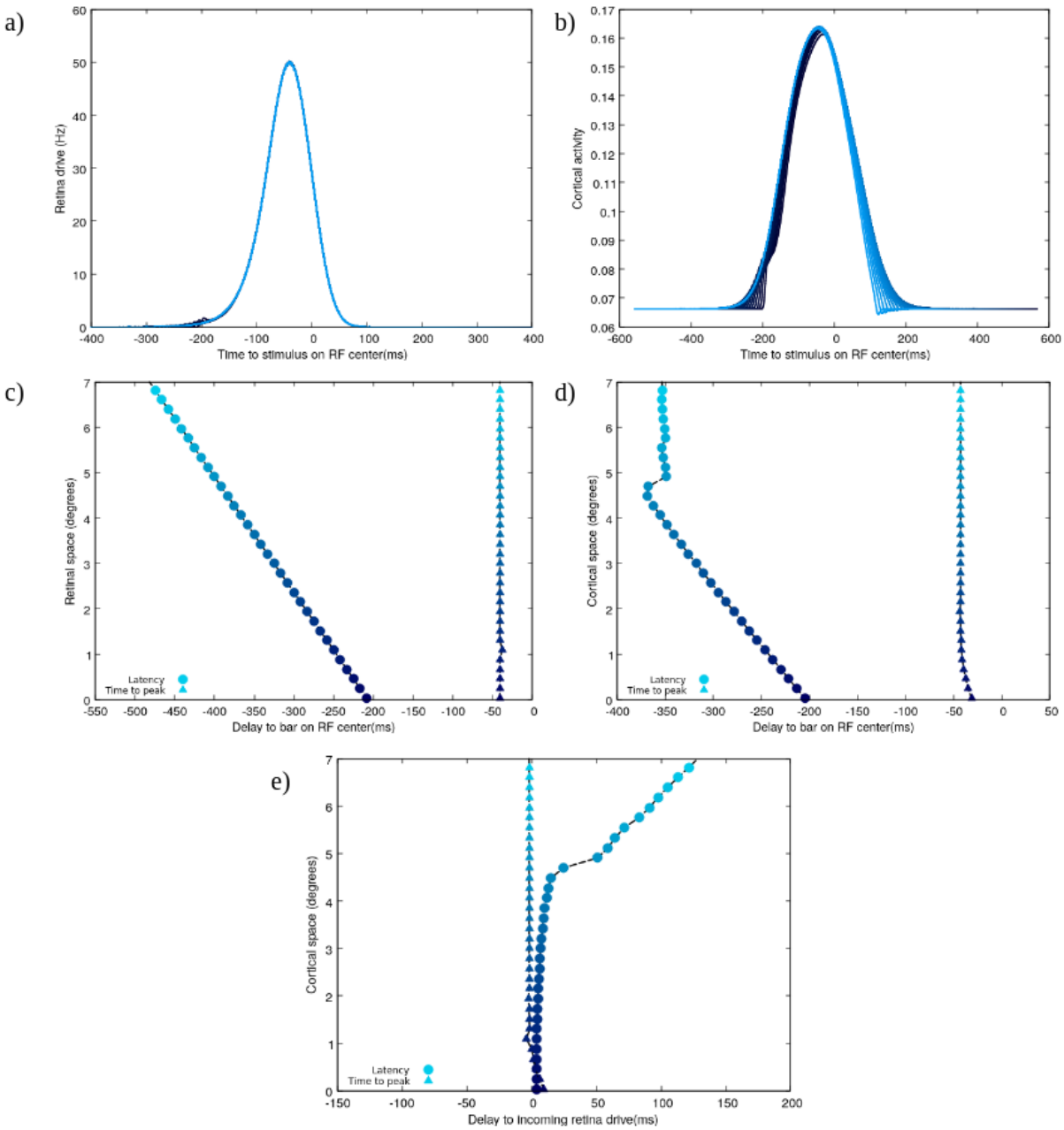

Figure 7.12: Removing edge effects for the cortical response to a retinal drive with gain control and gap junction connectivity connectivity. a), b), c), d) and e) same as in the figure 7.9.

Finally, when the cortex is driven by a retina drive with gap junction connectivity (Fig. 7.12), the latency of the retina increases linearly, given the lateral propagation occurring at its level. The cortex in the case delays the retina response in terms of latency, over the cortical area where the cortical latency saturates while the retina latency is still increasing.

7.2.6 Synthetic view of the spatio-temporal

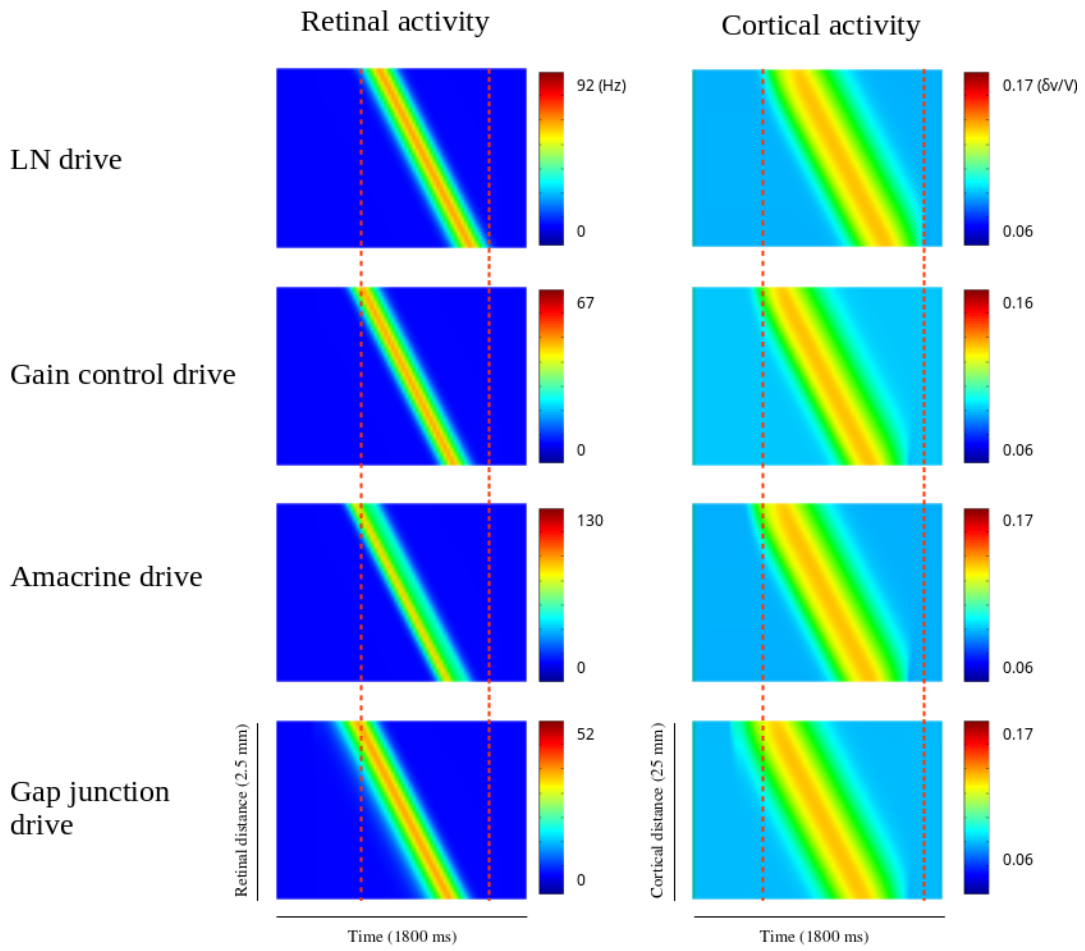

Figure 7.13: Comparing the spatio-temporal activity with the different drives. Left column figures display the spatio-temporal retinal activity with different anticipatory mechanisms, and the right column displays the corresponding spatio-temporal cortical activity. The red dashed lines denote the start and the end times of the LN retinal and cortical activities, as a reference base.

Figure Fig. 7.13 shows a spatio-temporal representation of the retinal and cortical activities, in different retinal settings. We first observe that the variation in the firing rate amplitude at the level of the retina model doesn't have any impact whatsoever on the amplitude of the VSDI activity.

The figure shows a clear shift in the wave of activation at the level of the retina and V1 first from the LN model to the gain control model, and then from the amacrine model to the gap junction model, without however any change in the wave velocity.

In these settings, the peak activity of the amacrine drive is more shifted as compared to the gain control drive, without any effect on the cortical activity peak.

Finally the wave of activation in the case of the gap junction drive is wider at the level of the retina giving rise to a wider wave of activation at the level of the cortex.

7.2.7 The effect of velocity

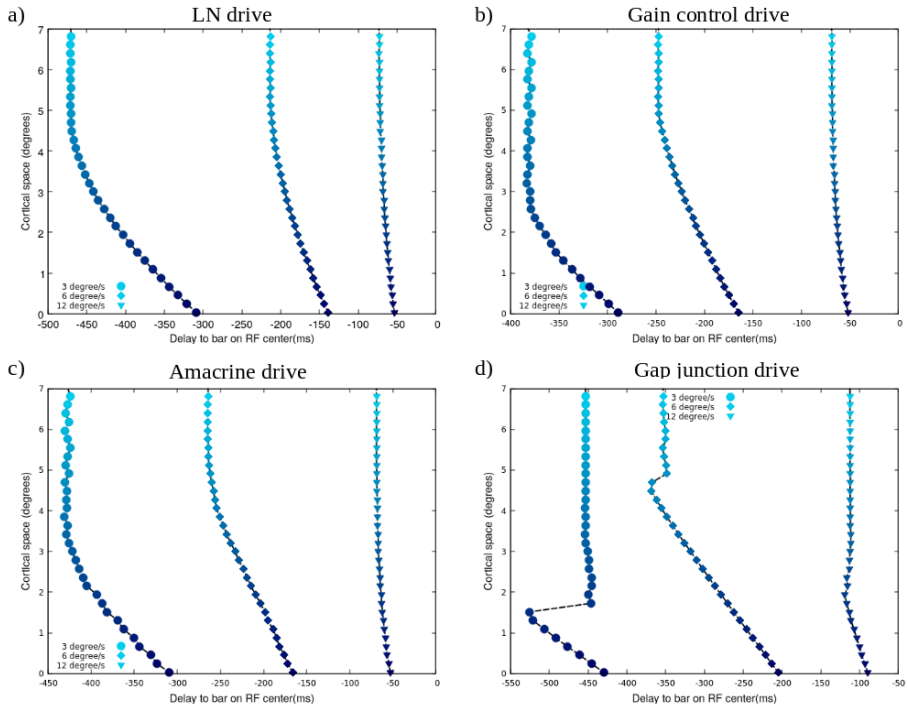

Figure 7.14: Latency of the cortex with respect to the stimulus for different values of velocity. a) Using LN retina drive. b) Using gain control retina drive. c) Using amacrine connectivity retina drive. d) Using gap junction connectivity retina drive.

Figure Fig. 7.14 displays the cortical latency, taking the stimulus as a reference for different values of velocity. The results show a decrease in both the latency onset value and slope, with the increase of velocity. This result is persistent across the different retinal anticipatory mechanisms.

The three retinal anticipatory mechanisms have a stronger effect for the intermediate value of speed, where the latency curve is more shifted and has a steeper slope as compared to the LN model.

For a low value of speed, the latency in the gap junction driven simulation saturates faster than the gain control and amacrine connectivity driven simulations, which in turn saturate faster than the LN driven simulation.

For a high value of speed, only the gap junction connectivity has a significant effect on the latency.

One can observe a jump in the latency of the gap junction driven simulation, which increases for lower values of speed. Numerically, this can be explained by the appearance of a small peak at the onset of activity, for small velocities, which decreases with cortical distance. Since the latency is computed over the derivative of the activity, the decrease of this small peak has a non linear effect on the latency curve.

Figure Fig. 7.15 shows the onset activity of 12 cortical columns, where we can see the vanishing of the small peak that emerges in the gap junction driven simulation.

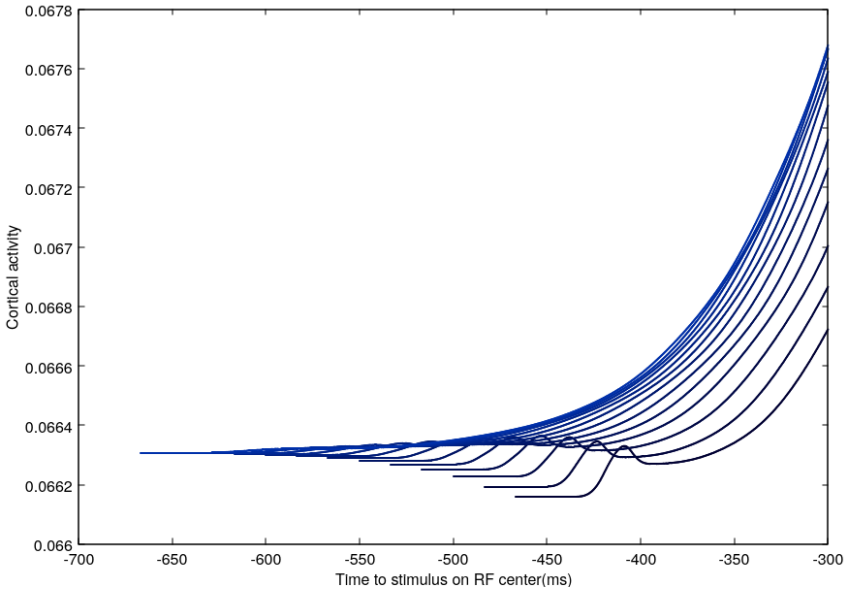

Figure 7.15: Onset activity of 12 cortical columns shows the evolution of the small peak of activity that emerges in the gap junction driven simulation. The speed here is 3 degrees/s.

Partial conclusion

In this chapter, we presented the results obtained after connecting our retinal model to the cortical model. One has to note that in the two chapters describing anticipation results after cortical processing, there has been a major paradigm shift. In our study of anticipation in the retina, our main focus was on the shift of the peak response, while in our study of anticipation in the cortex, our main focus was of the increase in the latency of the response. We also remind the reader here that our retino-cortical model is a bit of a "Frankenstein" model, linking a mouse (or salamander) retina model to a monkey cortical model, and neglecting the processing done by the thalamus. The aim being, ultimately, to understand computationally the effect of retinal anticipation on the cortical one.

As for the role of velocity, the cortical latency onset value and slope decreases with speed, irrespective of the retinal anticipatory mechanism, denoting a decrease in the ability to extrapolate motion at the cortical level.

To conclude, retina anticipation effects on the cortical one are two-fold : the shift in the peak response doesn't have a significant effect on the role played by the cortex in the latency increase, but changes the constant value of the time to peak curve. The propagating wave of activity in the retina (due to gap junctions), on the other hand, reduces the role played by the cortex in the latency increase. This may lead us to ask whether anticipation in the retina, beyond its role in compensating phototransduction delays, also allows to anticipate trajectories in the same way and at the same temporal scales as the cortex.

Chapter 8

Perspectives

In the first part of this chapter, we will introduce an algorithm for pairwise correlations measurement. We will first test it on synthetic data, and then we will apply it to recorded data from salamander retina (courtesy of O. Marre). Our aim is to understand if pairwise correlations can give us hints on the role played by connectivity in motion anticipation.
In the second part of this chapter, we will present Macular, a software that is currently being developed in the Biovision team. This software can, in the future, implement our work on retino-cortical anticipation.

8.1 On spike train correlations

It has been hypothesized that connectivity in the retina enables accurate responses to complex motion features such as brownian motion [48]. This connectivity could be assessed a posteriori through pairwise correlations computation, showing to which extent the activity of one neuron affects the other.

8.1.1 Pairwise correlations algorithm

When the retina is presented with motion stimuli, transient and non stationary changes in the firing rates can occur, measuring Pearson correlations becomes then irrelevant. We develop a method to measure time varying correlations in the case of non stationary point processes, and apply our method to spike trains to unravel the possible role played by connectivity in anticipation of a moving bar.

Given two spike trains, either two trials of the same neuron or two neuron recordings within the same trial, we compute noise correlation in the first case and pairwise correlation in the second. The central assumption in our approach is to consider spike trains as non homogeneous Poisson processes. We first compute the probability that a neuron spikes within a 5 ms time bin (average time for an action potential) using a moving window algorithm. Let $r(t)$ be the firing rate of the neuron, then, given that the rate varies slowly enough, the mean and the variance of the Poisson process are given by :

$$\mu(t) = r(t)\delta t \quad and \quad \sigma^2(t) = r(t)\delta t$$

Let $\phi(t)$ the probability of coincidence over the same δt between two spike trains, which is equivalent to the join probability of the two Poisson processes. This probability is computed either :

- without delay

- with a constant delay

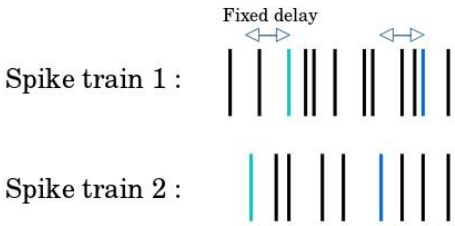

- or with a window delay

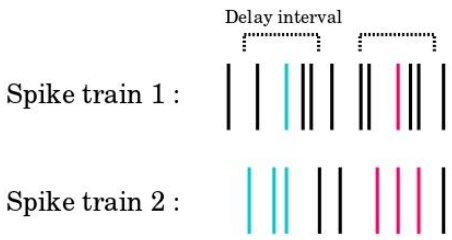

The correlation is then given by :

$$Corr(t) = \frac{\phi(t) - \mu_1(t)\mu_2(t)}{\sigma_1(t)\sigma_2(t)}$$

Testing In order to test our correlation algorithm, we generate two correlated Poisson processes using the following method :

- X, Y and Z are three independent Poisson variables of rates λ_1, λ_2 and λ_{12}.
- Π_1 Π_2 are then correlated Poisson processes with rates λ and λ' such as :

$$\Pi_1 = X \cup Z \text{ and } \Pi_2 = Z \cup Z$$

- The rates of Π_1 and Π_2 are then given by:

$$\lambda = \lambda_1 + \lambda_{12} - \lambda_1\lambda_{12}$$

$$\lambda' = \lambda_2 + \lambda_{12} - \lambda_2\lambda_{12}$$

- We compute the joint probability of Π_1 and Π_2 :

$$P = \lambda_1\lambda_2 + \lambda_{12} - \lambda_1\lambda_2\lambda_{12}$$

- And finally get the normalized correlation as follows :

$$\rho = \frac{P - \lambda\lambda'}{\sqrt{\lambda\lambda'}}$$

We generate two rasters of spike from Π_1 and Π_2 and we compute their empirical means and the empirical correlation over 100 trials. The empirical measures perfectly follows the theoretical ones. (See Fig. 8.1)

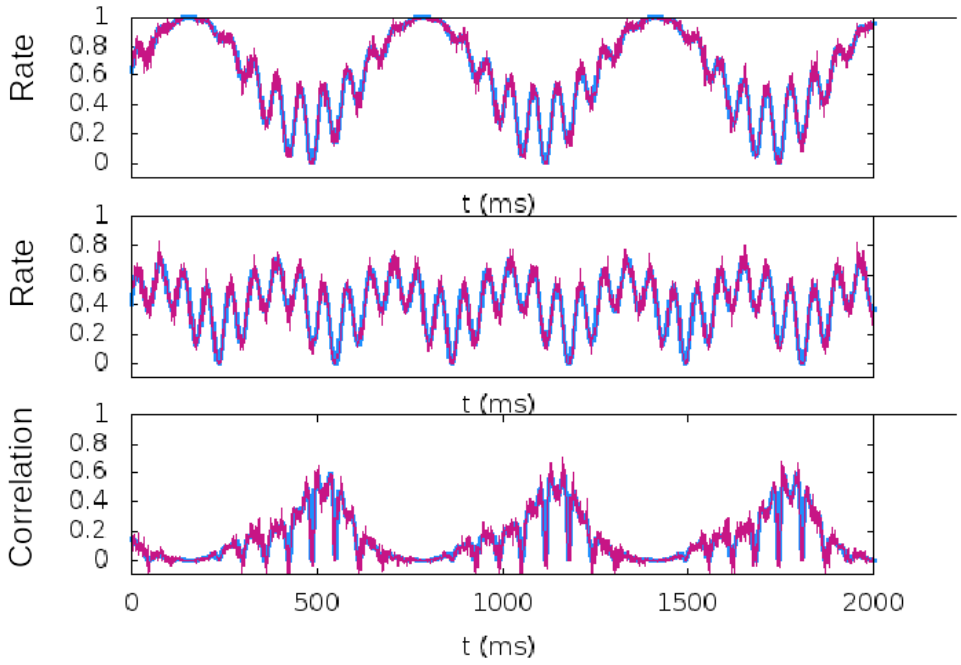

Figure 8.1: Theoretical and empirical moments of two correlated Poisson processes : the blue curves are the theoretical values of the parameters λ, λ' and ρ, and the red curves are their empirical estimation over 100 trials. Poisson processes X, Y and Z are generated using sinusoidal functions, giving non trivial rates for Π_1, Π_2 and the correlation function (See text).

We then reconstruct the firing rates and the correlation using our moving algorithm and find that they follow quite well the variation of the empirical measures.(See Fig. 8.2) The coincidence probability is computed without delay. The width of the moving window for both computations is taken equal to 30 ms, it should indeed not be too small nor too big in order to get significant statistics.

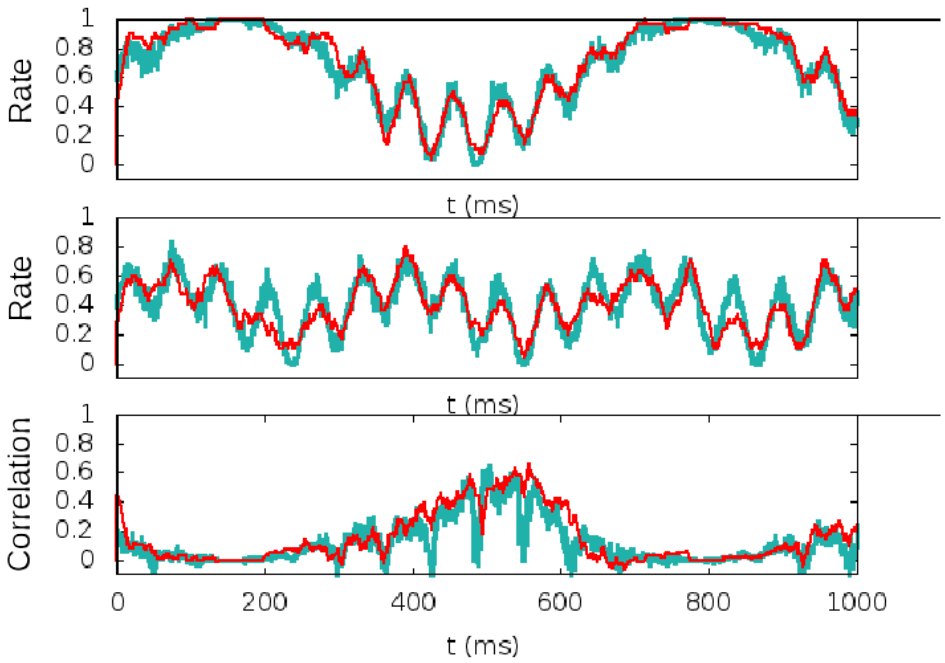

Figure 8.2: Reconstructing the firing rates and the correlation between two correlated Poisson processes : the green curves are the empirical firing rates and correlation, and the red curves are their computation through the moving window algorithm. The probability of coincidence is computed without delay.

8.1.1.1 Choosing the firing rate and correlation window size

We tried using different window widths for firing rate computation and coincidence computation, and found out that the error between the empirical correlation and the reconstructed correlation is minimum when the two widths are equal. (See Fig. 8.3)

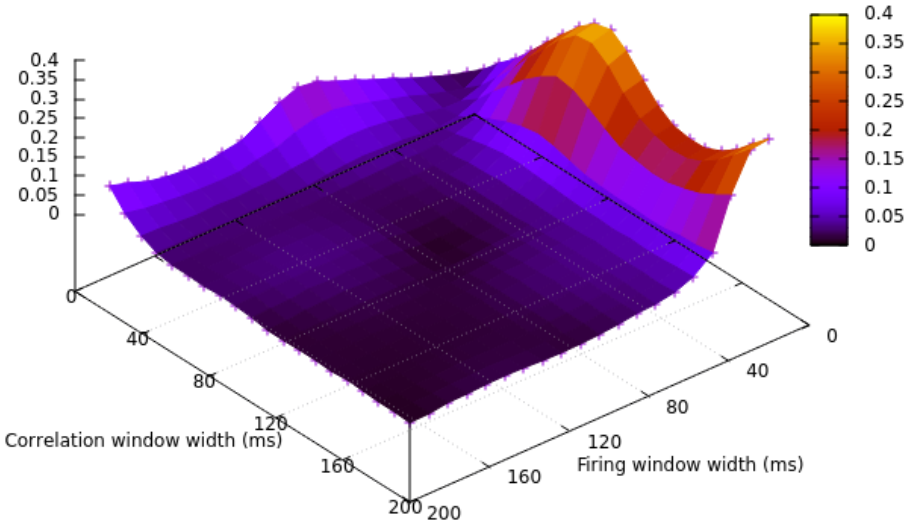

Figure 8.3: Mean square error of the correlation as a function of the firing rate and the correlation windows size.

8.1.1.2 The role of firing rates amplitudes

We assess the role of the firing rate amplitude in the moving window algorithm performance, when computing the probability of coincidence without delay. We compute the mean square error between the empirical correlation and the reconstructed correlation. One should note here here that there are two ways to compute the mean correlation for a given number of samples, either by computing the correlation for each sample and averaging over the total number of samples N, or computing a final correlation using the average rates. We call the first quantity the mean correlation c_N and the second quantity the correlation of means C_N. Let $r_i^A(t)$ (resp. $r_i^B(t)$) be the probability of spiking of neuron A (resp. B) in the sample i at time t, r_i^{AB} the joint probability of spiking of neurons A and B in the sample i at time t. c_N and C_N are then given by :

$$c_N(t) = \sum_{i=1}^{N} \frac{r_i^{AB}(t) - r_i^A(t).r_i^B(t)}{\sqrt{r_i^A(t).r_i^B(t)}}$$

$$C_N(t) = \frac{(\sum_{i=1}^{N} r_i^{AB}(t)) - (\sum_{i=1}^{N} r_i^A(t)).(\sum_{i=1}^{N} r_i^B(t))}{\sqrt{(\sum_{i=1}^{N} r_i^A(t)).(\sum_{i=1}^{N} r_i^B(t))}}$$

Fig. 8.4 shows how the firing amplitude biases the correlation results for small values. Fig. 8.4 (c) shows that the correlations of means C_N performs generally better than the mean correlation c_N.

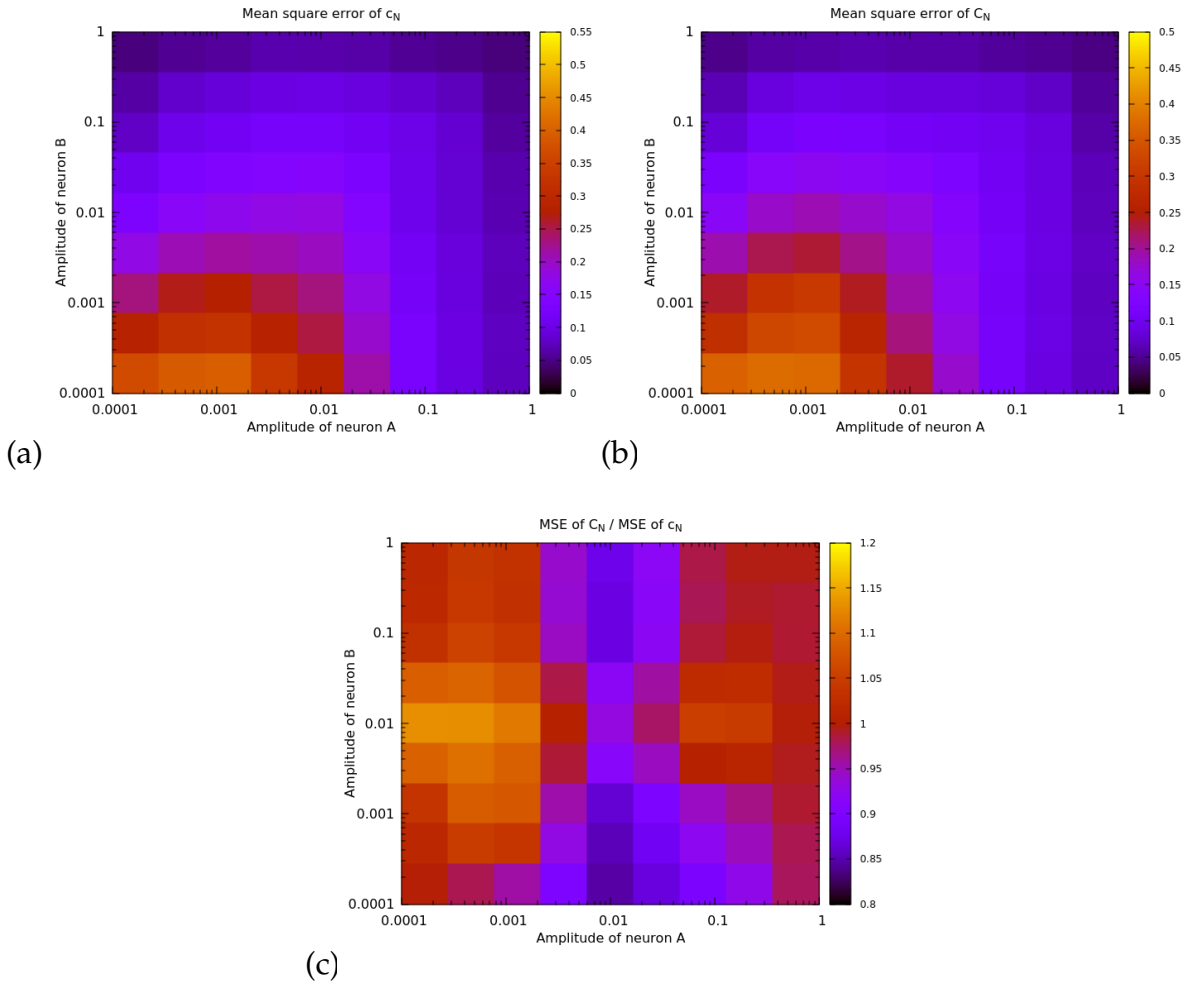

Figure 8.4: Mean square error of the correlation between two correlated Poisson processes X and Y, for different rate values. The error decreases as a function of the amplitude. Amplitudes are in logscale.(a) MSE of the mean correlation c_N. (b) MSE of the correlation of means C_N. (c) Relative error between C_N and c_N.

8.1.1.3 Does using an interval delay for joint probability computations improve the results ?

The low rate of neurons and consequently their limited number of spikes causes a discrepancy in the evaluation of their spiking probability as well as their joint probability, which could drive an underestimation of the correlation function. As introduced in 8.1.1, the probability of coincidence can be computed using an interval delay, with a width τ. In this case, the joint probability is overestimated, and we wanted to investigate whether this can help to increase the accuracy of the correlation function, in the case of low firing rates. One should note here that the value of τ should remain small enough not to bias the computation. Indeed, for large values of τ, the correlation can become larger than 1, due to the overestimation of the joint probability (See Fig.

8.5). Unfortunately, we instead that the increase of τ plays a negative role in the correlation estimation. Fig. 8.6 also show the existence of an optimal value of the moving window (around 200 ms) for which the error is minimal. Finally, as shown before, the correlations of means C_N performs generally better than the mean correlation c_N.

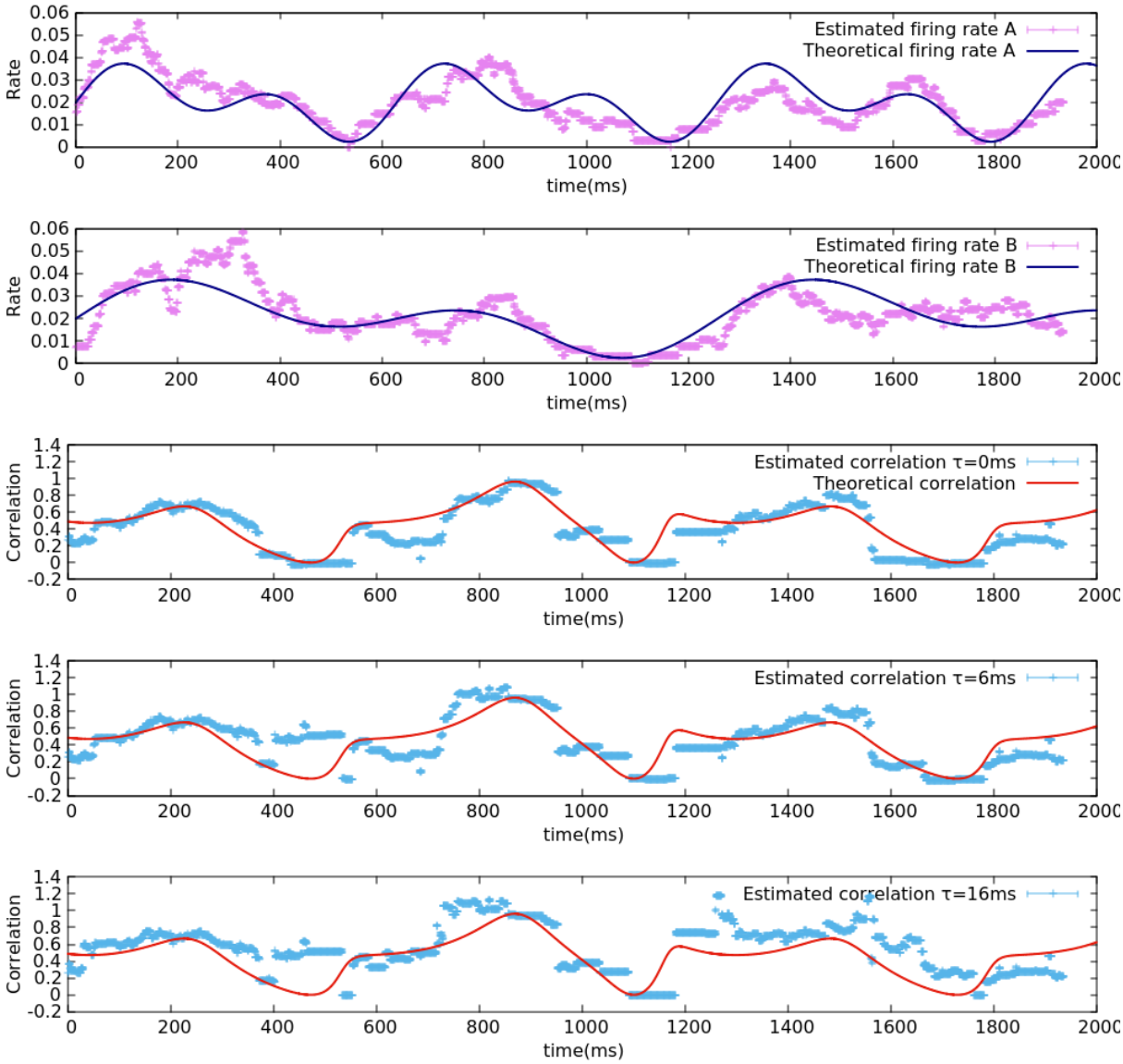

Figure 8.5: Theoretical and reconstructed firing rates and correlation for low activity levels for different values of τ. Increasing τ causes an overestimation of correlation.

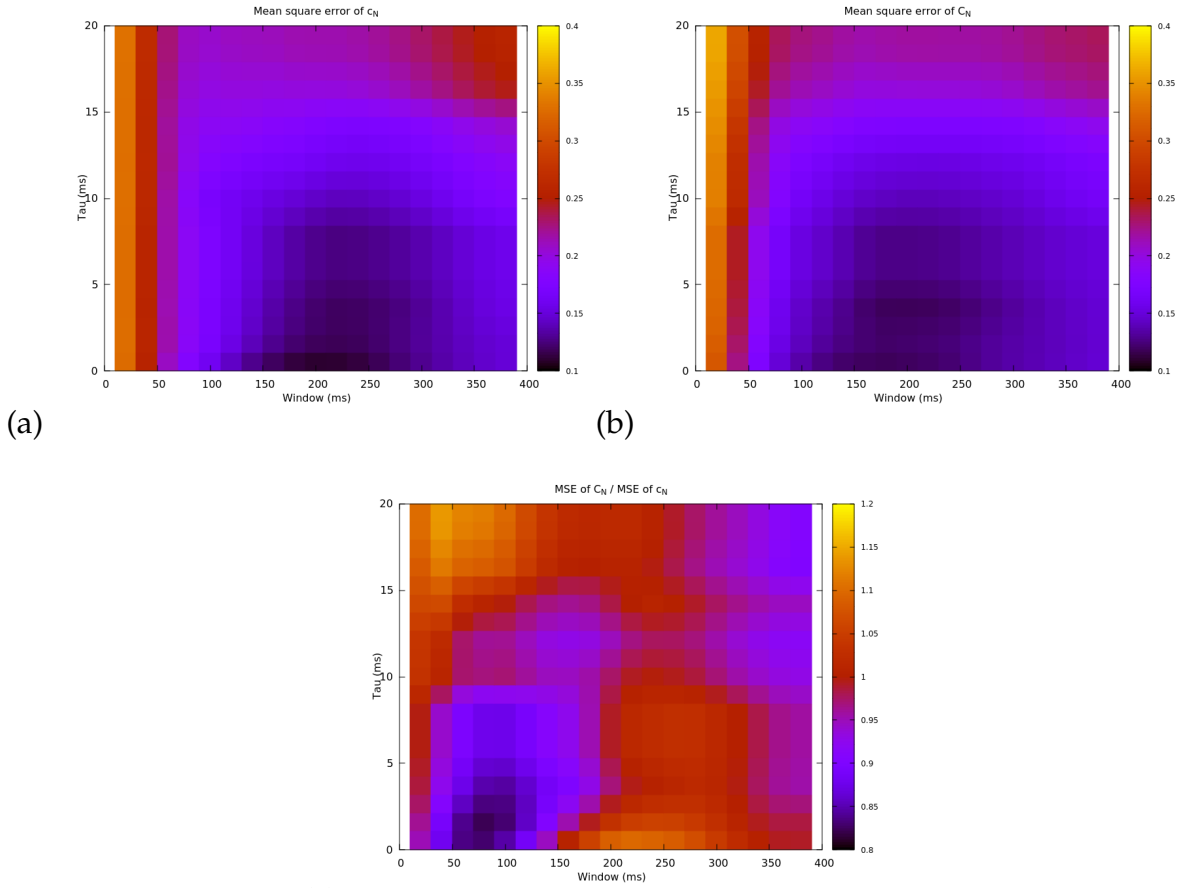

Figure 8.6: Mean square error of the correlation for different values of τ and different window sizes. (a), (b) and (c) are the same as in Fig. 8.4.

8.1.2 Correlations results on experimental recordings

8.1.2.1 Single cell correlations

The retinal recordings contain 280 cells (courtesy of O. Marre). In order to have a good estimate of correlation we needed to sort out neurons with a high number of spikes. This brought us to analyse only 5 neurons out of the 280. We don't have access to the distance between the recorded cells, hence from the their firing rate we classify them into two classes of neighbouring cells : cell 1 has a similar response to the response of cell 5, and cells 2, 3 and 4 have also a similar response. Note that the response shape of cell 2 is however different from the response of the two other cells. (See Fig. 8.7)

We first compute the correlation between several trials of the same cell, as a reference for comparison with pairwise correlations between different cells. Indeed, we

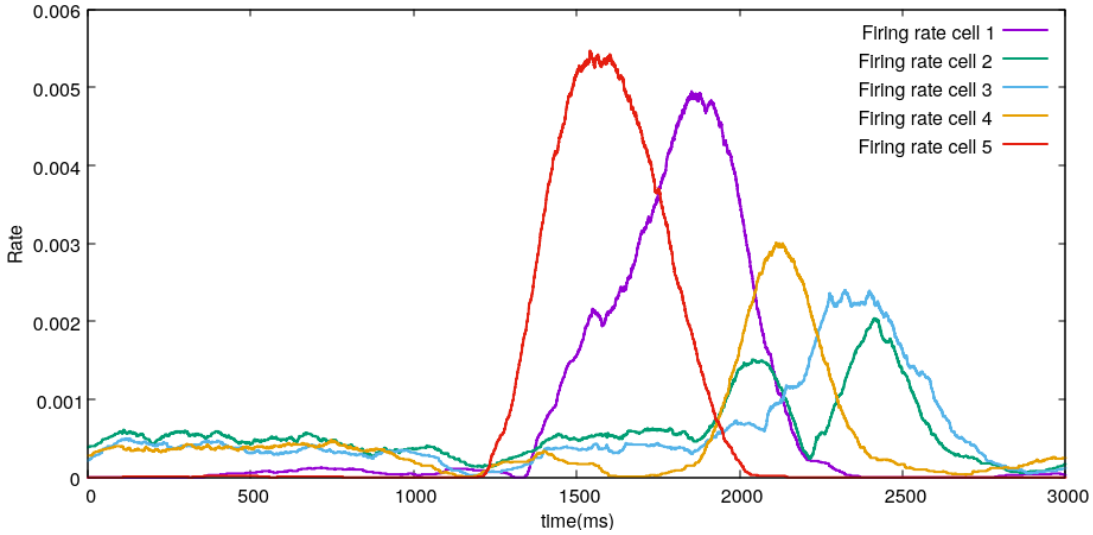

Figure 8.7: Firing rate of 5 recorded ganglion cells responding to a moving bar, with a window of 200 ms.

want to understand whether correlations are mainly driven by firing rates, or if there exist hidden synchronisation mechanisms occurring during the moving bar stimulus. In the previous section, we have shown the role played by the window size in the correlation estimate accuracy, namely the existence of an intermediate value for which the result is optimal. This optimal value of course depends on the firing rates levels and fluctuations, and is very hard to evaluate precisely. We try here to make a qualitative assessment of this optimal value, computing the firing rates and correlations estimate of the 5 cells using window sizes ranging from 50 ms to 400 ms, given a raster length of 3000 ms.

Fig. 8.8 shows the spiking probability of cells as well as their correlation, for different values of window size. When the size increases, the firing rate is flatten up, to a point where the variations of firing rate that seem to be intrinsic to the neuron is cancelled out, as it is the case for Cell 2 with widths higher than 200 ms. For small values of width however, there are big fluctuations in the firing rate estimate, which could introduce artefacts in the evaluation of the correlation (cell 1 and cell 5). It is therefore important to choose a value low enough to keep the response specifities of the cells, and high enough to reduce irrelevant fluctuations in the correlation. For the next of the study, we choose a window width of 200 ms.

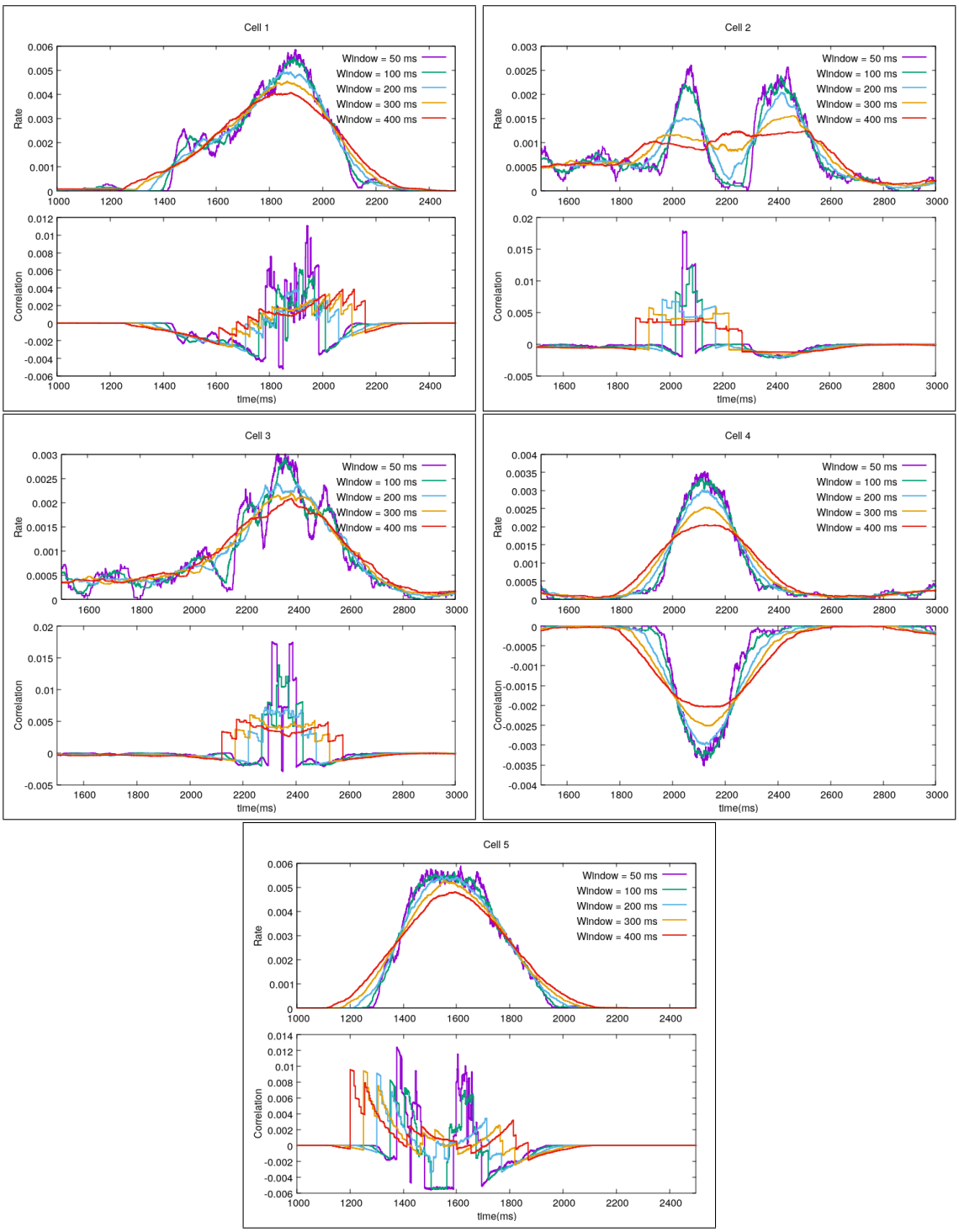

Figure 8.8: Reconstructed firing rates and correlation for single cells. Different colours denote different sizes of the sliding window.

8.1.2.2 Pairwise correlations

In this last part, we study pairwise correlations between the studied cells, averaged over 200 trials, with a window width of 200 ms.

Fig. 8.9 shows the evolution of pairwise correlation as compared to the cells firing rate. When cells have similar response shapes (Cells 1 and 5, Cells 3 and 4), and according

to the simplified classification are neighbours, their pairwise correlation increases very saliently near the onset of their firing rate curve, *and peaks to a value higher than the peak of the spiking probability of the cells*. The correlation then drops fast. This could suggest that the onset activity of the second responding cell is driven by the cell responding first to the bar, thus synchronicity, while the statistics of the cell response afterwards are driven by the cell's intrinsic dynamics. Conversely, cells with different response shapes are either anti-correlated (Cells 1 and 4) or correlated with a correlation coefficient that is at most equal to the peak spiking probability (Cells 3 and 5). In this case again, cells seem to start to be correlated when the activity of the second responding cell starts increasing.

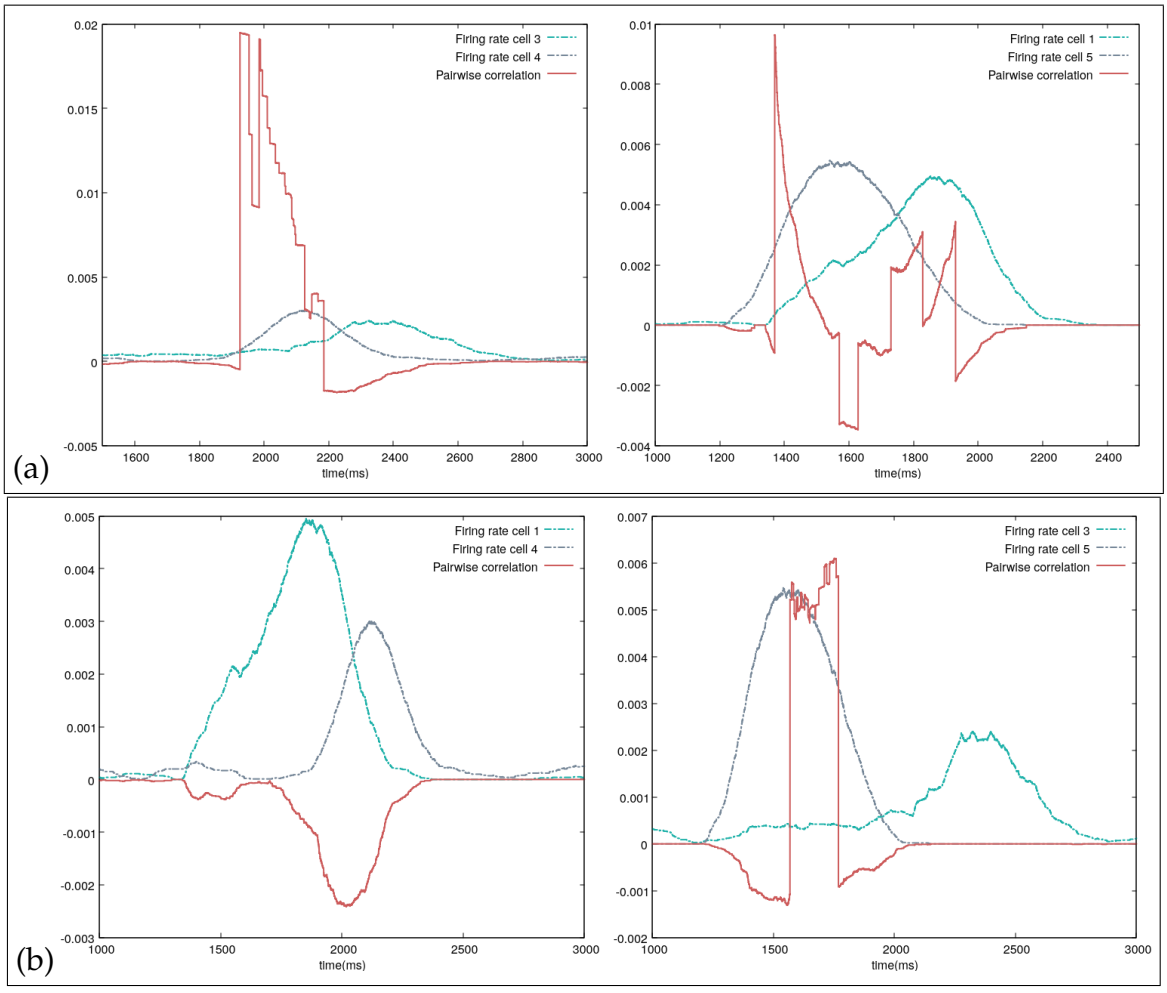

Figure 8.9: Theoretical and reconstructed firing rates and correlation for low activity levels.

Partial conclusion

The correlation study we conducted here aimed at assessing the correlation level between cells responding to a moving bar. Starting from the observation that the stimulus of a moving bar contains correlations, we wanted to investigate whether these correlations are transposed into the spiking activity of cells, through lateral connectivity, and whether these correlations have an effect on anticipation. We reported an increase in the correlation level between neighbouring cells near the onset of their activity, which shows a synchronicity enhancement that could be due to lateral connectivity.

While this work remains quite preliminary, it paves the way for a more in-depth study on the effect of stimulus correlations on the neural code, and outlines the possibility of understanding anticipatory phenomena from a correlation point of view.

8.2 Macular : a simulation platform of the retina and V1

8.2.1 General presentation

Macular is platform for retina and primary visual cortex simulations that is currently being developed within the Inria team Biovision. It aims at reproducing the retina response to visual input as well as electric stimulation, is normal and pathological settings. The objective is to develop a tool that can be used by neuroscientists to reproduce experimental findings, or, more importantly, to guide their experiments through hypotheses that can be tested with the simulator. This can save a considerable amount of resources that are required to conduct in vivo experiments.
Macular is build around the central idea that its utilization and visual interface evolve with the the user's purpose. It can be used for several scenarios, such us simulating retinal waves, simulating the retinal an cortical responses to prostheses electric stimulation, investigating how specific classes of retinal neurons contribute to the encoding of visual scenes ...
Macular is not the first simulation tool that the Biovision team has developed. A. Wohrer and P. Kornprobst have developed VirtualRetina [90], a large scale simulator of the retina, implementing gain control. B. Cessac et al. [91] have developed Enas, a platform for statistical analysis of simulated and experimental spike trains. Finally, both these software have been merged into Pranas [92]. The Macular project has then been started to extend Pranas, and overcome its technological limitations. Mainly, Macular will allow a modular architecture, which makes it more flexible to fit different simulation scenarios. It will also feature a scripting option, where the user can design his own model, with a given set of equations, variables and parameters. Finally, through a highly parallelized architecture, Macular will afford mimicking a large number of cells, of different classes. (See Fig. 8.10)

8.2.2 Development process

Inria provides technological support to research teams with the help of a team of engineers, which is subject to a call for applications. The Macular project was accepted in this context. The work with engineers from INRIA's development and experimentation center is organized in coding sprints, that are regularly held to allow the Biovision team to work in collaboration with the engineers on the development of the platform. I

had the opportunity to participate to two coding sprints at the beginning of the project, during which we laid the cornerstones of the software. These coding sprints were very formative in the sense that the engineers taught us the best coding practices, as well as the agile method. During these two sprints, we laid the groundwork for the development of the software, in terms of architecture, user experience and GUI.

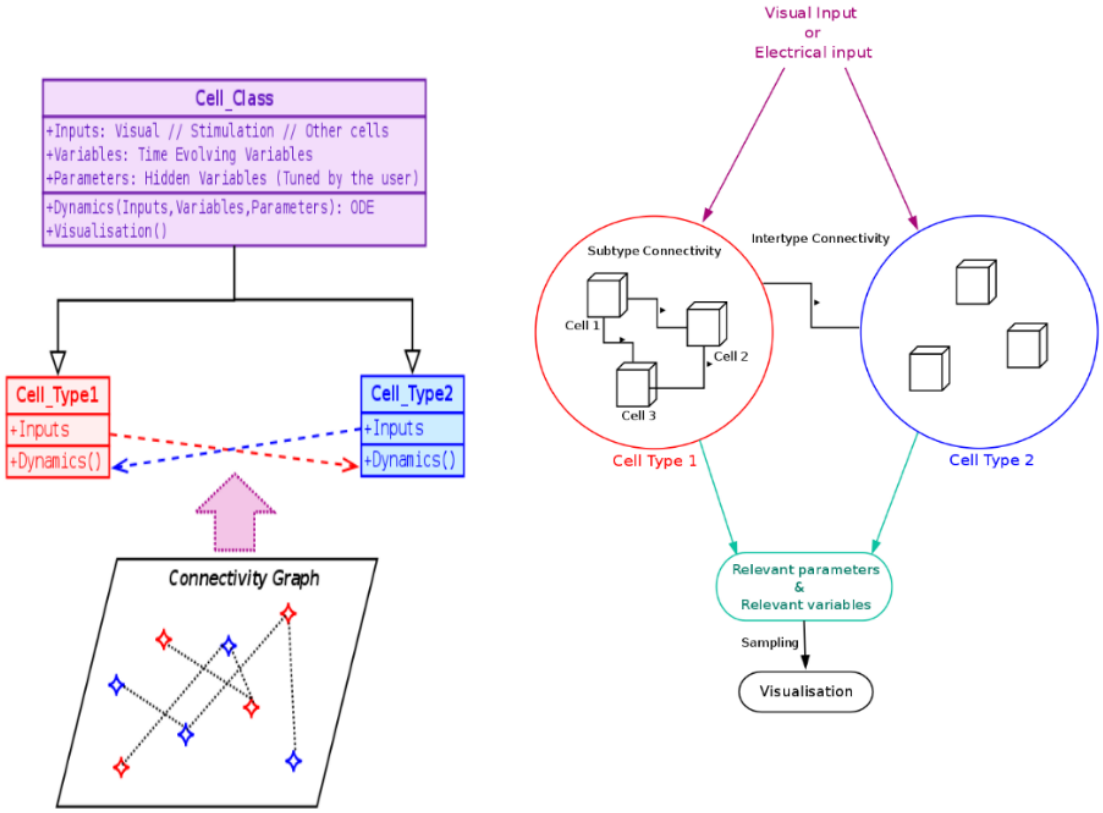

Figure 8.10: Architecture of the retina simulator embedded in Macular. Left : Different cells are represented by C++ classes, featuring their inputs, position, dynamics, variables and parameters. These cells are connected within a 2 dimensional graph. Right : Simulation setting. Different cell types arranged in layers receive a visual or an electrical input. These cells interact through inter-type connectivity. Through an adequate tuning of parameters, and a sampling of relevant variables, the user can study the response of the retina to its input.

The software has made however a long way since then, implementing a more extensive GUI, several use cases (retinal waves, simulating cortical responses to prosthetic stimulations),and improving the 3D display of the connectivity graph that shows the different retina layers, as well as synaptic connections.

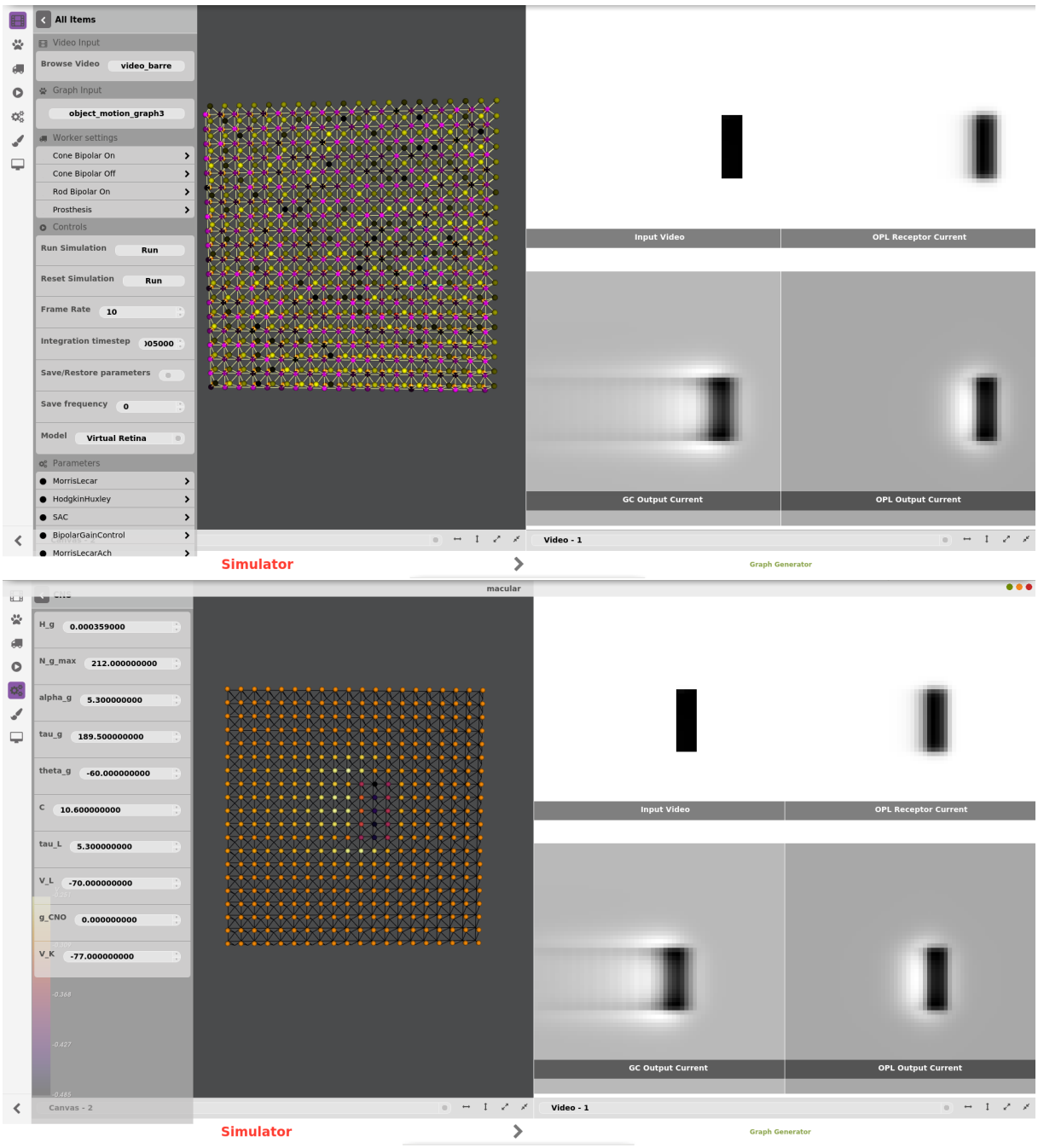

Figure 8.11: Macular : response to a moving bar. Left : 3D layered graph of retina with bipolar amacrine and ganglion cells. Right : four panels displaying the stimulus and the response it elicits at earlier stages of retinal processing. Bottom view : The 3D view only displays the activity of ganglion cells. (Version of the software at the sprints I took part in)

Partial conclusion

Future work will consist of integrating our retino-cortical model for motion anticipation in Macular, to emulate its response to different moving stimuli, and possibly

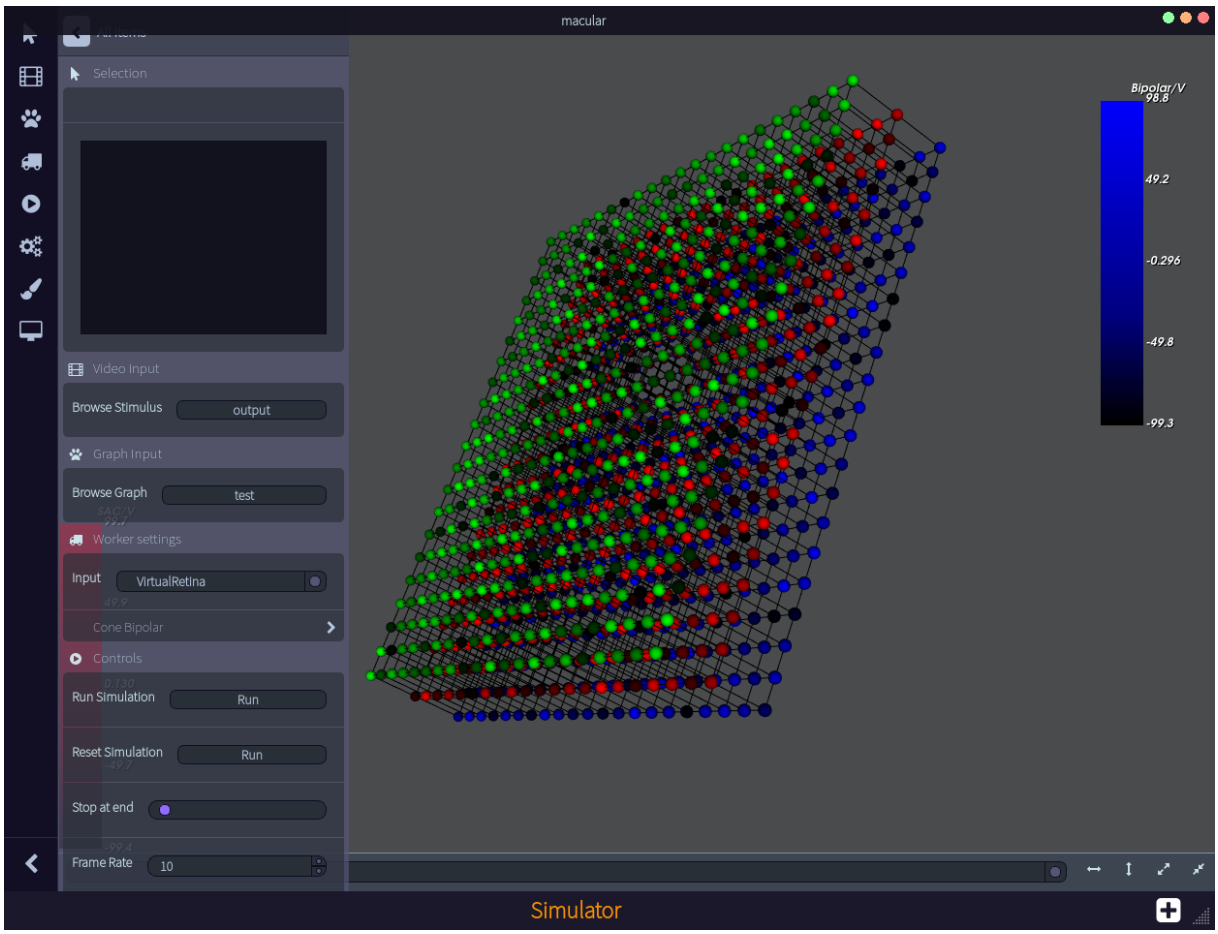

Figure 8.12: 3D layered graph of retina with bipolar cells (blue) amacrine cells (red) and ganglion cells (green). Synaptic connections are displayed in black. (Current version of the software)

suggest new experiments. Thanks to the modularity of Macular and its scripting feature, we expect it to become an essential tool in retina and cortex simulation.

English conclusion

This thesis allowed us to carry out a neuroscience modeling study, based on mathematical analysis and numerical simulation. Beyond understanding the mechanisms involved in retinal and cortical anticipation, we have tried to understand the division of labor between these two processing units. More specifically, this work was guided by a central hypothesis, that lateral connectivity plays a major role in both retinal and cotical anticipation.

At the retina level, we were able to test the anticipatory effect of two retinal circuits implementing lateral connectivity. In particular, we were able to highlight the existence of regimes of connectivity parameters that can improve anticipation at the retina level. We tested our retina model on stimuli with trajectories more complex than a simple translation (rotation and parabolic motion).

We then linked our retina model to a cortical mean field model with lateral connectivity. Through two anticipation metrics (latency and time to peak), we assessed the effect of each of the retinal mechanisms on cortical anticipation. Our results suggest that the retina could possibly be doing more than just compensating for its own processing delays, further assisting the cortex in the motion extrapolation task.

Applications of our work

The current implementation of our retino-cortical model takes as an input a set of images, processes them through the layered retina model in order to produce firing rates, which are then fed to the cortical model. It is hence possible to study the response of the model to different kind of 2D stimuli, and assess whether the mechanisms we have implemented for motion anticipation can also account for other visual effects.

Future work

Extending the retina model

The retina model could be extended through an implementation of other ganglion cell types. It could also implement other neural pathways and connectivity schemes, and assess their role in motion processing and anticipation. In particular, we studied the connectivity pathways we implemented in the retina model (gap junctions and amacrine connectivity) independently. It would be interesting to study the combined effect of both, and assess whether their collaboration can improve anticipation.
Our model only accounts for gray scale inputs. It would be very interesting to implement color-coded cells, by adding a photoreceptor layer, in order to study perceptual illusions combining motion and color vision, such us the color phi phenomenon.

Improving the retino-cortical transformation

Our model connects the retina to the cortex in a linear fashion, ignoring the visual processing occurring at the level of the thalamus. A crucial improvement of our model would be to add a thalamic transformation between the retina and the cortex. A second improvement would be to account for the retionotopic mapping of the visual space at the level of V1.

Spike trains correlations

The moving window algorithm proves to be efficient to account for correlations fluctuations in non stationary Poisson processes. However, the size of the window plays a fundamental role in the correlation estimate accuracy. The choice of this parameter has thus to be made more systematically, through a given criterion that has still to be determined.
Finally, it would be interesting to implement a plausible spike train generator at the level of the retina, and compare the correlations in artificial retinal output to correlations in real data.

Personal conclusion

On a personal level, this thesis has allowed me to expand my knowledge in computational neuroscience, and also to develop my skills in programming, dynamical systems analysis, and probability. It also allowed me to improve my scientific communication skills, both written and oral. Finally, during these three years, I was able to learn the research methodology, and a more systematic approach to problem solving.

French conclusion

Cette thèse nous a permis de réaliser une étude en neurosciences computationnelles, basée sur l'analyse mathématique et la simulation numérique. Au-delà de la compréhension des mécanismes impliqués dans l'anticipation rétinienne et corticale, nous avons essayé de comprendre la répartition des tâches entre ces deux unités de traitement. Plus particulièrement, ce travail a été guidé par une hypothèse centrale, à savoir que la connectivité latérale joue un rôle à la fois dans l'anticipation rétinienne et l'anticipation coticale.

Au niveau de la rétine, nous avons pu tester les effets d'anticipation de deux circuits rétiniens implémentant la connectivité latérale. En particulier, nous avons pu mettre en évidence l'existence de régimes de paramètres de connectivité qui peuvent améliorer l'anticipation au niveau de la rétine. Nous avons testé notre modèle rétinien sur des stimuli en 2D avec des trajectoires plus complexes qu'un simple mouvement rectiligne (rotation et mouvement parabolique).

Nous avons ensuite relié notre modèle de rétine à un modèle champ moyen du cortex, avec de la connectivité latérale. A travers deux métriques d'anticipation (latence et temps de pic), nous avons évalué l'effet de chacun des mécanismes d'anticipation rétinienne sur l'anticipation corticale. Nos résultats suggèrent que la rétine ne compense peut-être pas seulement ses propres délais de traitement, mais qu'elle aide également le cortex dans l'extrapolation du mouvement.

Applications de notre travail

L'implémentation actuelle de notre modèle rétino-cortical prend en entrée un ensemble d'images, les traite à travers le modèle stratifié de la rétine, afin de produire des fréquences de décharge, qui sont ensuite transmises au modèle cortical. Il est donc possible d'étudier la réponse du modèle à différents types de stimuli 2D et d'évaluer si les mécanismes que nous avons implémentés pour l'anticipation du mouvement peuvent également reproduire d'autres effets visuels.

Travaux futurs

Extension du modèle de la rétine

Le modèle de la rétine pourrait être étendu par la prise en compte d'autres types de cellules ganglionnaires. Il pourrait également implémenter d'autres schémas neuraux et d'autres types de connectivité, afin d'évaluer leur rôle potential dans le traitement et l'anticipation du mouvement. En particulier, nous avons étudié les deux types de connectivité que nous avons implémentées dans le modèle de la rétine de façon indépendante. Il serait intéressant d'étudier l'effet combiné des deux et si leur collaboration peut améliorer l'anticipation.
Notre modèle ne tient compte que des niveaux de gris. Il serait très intéressant de développer des cellules sensibles à couleur, en ajoutant une couche de photorécepteurs, afin d'étudier des illusions optiques combinant le mouvement et la vision des couleurs, comme le phénomène "Color Phi".

Améliorer la transformation rétino-corticale

Notre modèle connecte la rétine au cortex de façon linéaire, ignorant le traitement visuel qui se produit au niveau du thalamus. Une amélioration essentielle de notre modèle serait de tenir compte des transformations thalamiques entre la rétine et le cortex. Une deuxième amélioration consisterait à considérer la cartographie retionotopique de l'espace visuel au niveau de V1.

Corrélations des trains de spikes

L'algorithme de la fenêtre glissante se révèle efficace pour tenir compte des fluctuations des corrélations dans les processus de Poisson non stationnaires. Cependant, la taille de la fenêtre joue un rôle fondamental dans la précision de l'estimation de cette corrélation. Le choix de ce paramètre devrait donc être fait de manière plus systématique, à travers un critère qui reste à déterminer.
Enfin, il serait intéressant de mettre en place un générateur de train de spikes plausible au niveau de la rétine, et de comparer les corrélations de la sortie du modèle rétinien avec les corrélations des données réelles.

Conclusion personnelle

D'un point de vue personnel, cette thèse m'a permis d'étendre mes connaissances en neurosciences computationnelles, mais également de développer mes aptitudes en programmation, en analyse des systèmes dynamiques, et en probabilités. Elle m'a également permis de m'améliorer en communication scientifique, à l'oral et à l'écrit. Enfin, au cours de ces trois années, j'ai pu assimiler la méthodologique de recherche et adopter une approche plus systématique dans la résolution des problèmes.

Chapter 9

Appendix

9.1 Parameters of the retina model

In the following, BSK denotes the spatial kernel of the bipolar receptive field and BTK the temporal kernel. A stands for the BSK amplitude and K for the BTK amplitude.

BL denotes the bipolar cell layer, including amacrine cells connectivity. GL denotes the ganglion cell layer, including gap junction connectivity.

Parameter	**Value**	**Unit**
BSK σ_{center}	90	μm
BSK $\sigma_{surround}$	290	μm
BSK A_{center}	1.2	unitless
BSK $A_{surround}$	0.2	unitless
BTK μ_1	60	ms
BTK μ_2	180	ms
BTK σ_1	20	ms
BTK σ_2	44	ms
BSK K_1	0.22	unitless
BSK K_2	0.1	unitless
BL τ_a	100	ms
BL h	$6.11e^{-3}$	$ms^{-1}mv^{-1}$
BL θ_B	5.32	mV
BL τ_A	200	ms
BL τ_B	200	ms

GL $\sigma_{pooling}$	90	μm
GL τ_G	189.5	ms
GL h	$3.59e^{-4}$	$dimensionless$
GL α	1110	Hz/mV
GL θ_G	0	mV

9.2 Parameters of the cortical model

The transfer function fit parameters are given in the following table :

Table 9.1: Fit Parameters AdEx Neurons (in mV)

Cell Type	P_0	$P_{\mu V}$	$P_{\sigma V}$	$P_{\tau V}$	$P_{\mu V}^2$	$P_{\sigma V}^2$	$P_{\tau V}^2$	$P_{\mu_V \sigma_V}$	$P_{\mu_V \tau_V}$	$P_{\sigma_V \tau_V}$
RS-Cell	-49.8	5.06	-23.4	2.3	-0.41	10.5	-36.6	7.4	1.2	-40.7
FS-Cell	-51.5	4.0	-8.35	0.24	-0.50	1.43	-14.7	4.5	2.8	-15.3

Table 9.2: Fit Parameters Hodgkins-Huxley Neurons (in mV)

Cell Type	P_0	$P_{\mu V}$	$P_{\sigma V}$	$P_{\tau V}$	$P_{\mu V}^2$	$P_{\sigma V}^2$	$P_{\tau V}^2$	$P_{\mu_V \sigma_V}$	$P_{\mu_V \tau_V}$	$P_{\sigma_V \tau_V}$
RS-Cell	-48.1	3.2	10.9	-0.32	0.98	1.1	-1.2e-3	-1.4	3.9	-0.11
FS-Cell	-51.2	1.8	-6.1	-0.86	1.6	-0.70	-11	-0.18	1.2	-1.2

Parameter	**Value**	**Unit**
Excitatory reversal potential E_e	0	mV
Inhibitory reversal potential E_i	-80	mV
Excitatory quantal conductance Q_e	290	nS
Inhibitory quantal conductance Q_i	1.2	nS
Excitatory decay τ_e	0.2	ms
Inhibitory decay τ_i	60	ms
Number of cells	10000	unitless
Connectivity probability	0.05	unitless
Fraction of inhibitory cells	0.2	$unitless$
External drive	4	Hz

9.3 Anticipation time

We compute here analytically the anticipation time Δ in the absence of lateral connectivity. The goal is to have an analytic expression showing, in particular, that the peak of response does not correspond to the time where the bar reaches the center of the RF. The general computation in the presence of gap junctions or amacrine cells deserves longer developments that will be the subject of further work.
We therefore consider only one GGell, noted G without index.

9.3.1 Kernel form

The kernel $\mathcal{K}_{B_i}$ reads:

$$\mathcal{K}_{B_i}(x,y,t) = \sum_{a,b=1}^{2} (-1)^{a+b} \mathcal{K}_{i,a,b}(x,y,t) \tag{9.1}$$

with:

$$\mathcal{K}_{i,a,b}(x,y,t) = \frac{A_a K_b}{(2\pi)^{\frac{3}{2}} \sqrt{\det C_a}\, \sigma_b} e^{-\frac{1}{2} \tilde{X}_i . C_a^{-1} . X_i} e^{-\frac{(t-\mu_b)^2}{2\sigma_b^2}} H(t),$$

with $X_i = \begin{pmatrix} x - x_i \\ y - y_i \end{pmatrix}$ where x_i, y_i are the coordinates of the BCs RF center.

$$\mathcal{K}_{B_i}(x,y,t) = \left(\frac{A_1}{2\pi\sqrt{\det C_1}} e^{-\frac{1}{2} \tilde{X}_i . C_1^{-1} . X_i} - \frac{A_2}{2\pi\sqrt{\det C_2}} e^{-\frac{1}{2} \tilde{X}_i . C_2^{-1} . X_i} \right)$$

$$\left(\frac{K_1}{\sqrt{2\pi}\sigma_1} e^{-\frac{(t-\mu_1)^2}{2\sigma_1^2}} - \frac{K_2}{\sqrt{2\pi}\sigma_2} e^{-\frac{(t-\mu_2)^2}{2\sigma_2^2}} \right) H(t)$$

$$= \left\{ \begin{array}{l} \frac{A_1 K_1}{(2\pi)^{\frac{3}{2}} \sqrt{\det C_1}\, \sigma_1} e^{-\frac{1}{2} \tilde{X}_i . C_1^{-1} . X_i} e^{-\frac{(t-\mu_1)^2}{2\sigma_1^2}} - \frac{A_1 K_2}{(2\pi)^{\frac{3}{2}} \sqrt{\det C_1}\, \sigma_2} e^{-\frac{1}{2} \tilde{X}_i . C_1^{-1} . X_i} e^{-\frac{(t-\mu_2)^2}{2\sigma_2^2}} \\ -\frac{A_2 K_1}{(2\pi)^{\frac{3}{2}} \sqrt{\det C_2}\, \sigma_1} e^{-\frac{1}{2} \tilde{X}_i . C_2^{-1} . X_i} e^{-\frac{(t-\mu_1)^2}{2\sigma_1^2}} + \frac{A_2 K_2}{(2\pi)^{\frac{3}{2}} \sqrt{\det C_2}\, \sigma_2} e^{-\frac{1}{2} \tilde{X}_i . C_2^{-1} . X_i} e^{-\frac{(t-\mu_2)^2}{2\sigma_2^2}} \end{array} \right\} H(t)$$

9.3.2 General equation for the anticipation time

In the presence of a moving stimulus, the firing rate of the ganglion cell G increases up to a maximum, reached at a time t_m. Note that this maximum might not be unique so t_m is the time to reach the first maximum. We want to compute how t_m depends on the gain control, speed and contrast as well as other parameters such as

orientation of the receptive field. As the firing rate of G is a monotonously increasing sigmoid function, the extrema in the firing rate are given by $\frac{dV_G}{dt} = 0$.

Following what has been introduced in Chapter 4, the general equation for the times of extrema in the firing rate of G are given by :

$$\sum_i W_G^{B_i} \mathcal{G}_B\left(A_{B_i}\right) \frac{dV_{B_i}}{dt} = \sum_i W_G^{B_i} \mathcal{G}'_B\left(A_{B_i}\right) V_{B_i}(t) \left(\frac{1}{\tau_a} A_{B_i} - h\, V_{B_i}(t)\right). \tag{9.2}$$

We were not able to solve (9.2) in full generality, so that we consider specific cases.

- **No gain control.** In this case $\mathcal{G}_B\left(A_{B_i}\right) = 1$, $\mathcal{G}'_B\left(A_{B_i}\right) = 0$ so that, eq. (9.2) reduces to:

$$\left[\mathcal{K}_G \overset{S,t}{*} \frac{d\mathcal{S}}{dt}\right](t = t_m) = 0 \tag{9.3}$$

where:

$$\mathcal{K}_G = \sum_i W_G^{B_i} \mathcal{K}_{B_i}, \tag{9.4}$$

is the pooled kernel.

- **Fast gain control.** We make the approximation that, in the region of A_i values where (9.2) is satisfied, $\frac{\mathcal{G}'_B\left(A_{B_i}\right)}{\mathcal{G}_B\left(A_{B_i}\right)} \gg 1$ so that we may neglect the left hand side in eq. (9.2) and look for the solutions of:

$$\sum_i W_G^{B_i} \mathcal{G}'_B\left(A_{B_i}\right) V_{B_i}(t) \left(\frac{1}{\tau_a} A_{B_i} - h\, V_{B_i}(t)\right) = 0. \tag{9.5}$$

We are going to consider these two cases, for a moving bar.

9.3.3 Moving bar

9.3.3.1 Definition

We consider a bar, of width $2d$ and infinite height, propagating with a constant speed v_x from the left to the right in the direction x, i.e.

$$S(x, y, t) = \frac{L}{2\,d}\left[H(x - d - v_x\, t) - H(x + d - v_x\, t)\right] \tag{9.6}$$

where H is the Heaviside function. L, the stimulus intensity induced by the photoreceptors response can be here positive (white bar) or negative (dark bar). We have

normalized so that the integral of the stimulus over space is equal to L. As $\mathcal{S}$ is expressed in mV, L is expressed in $mV\,mm$. The motion in the x direction is not a loss of generality as we consider orientation selective cells where the preferred orientation is arbitrary.

9.3.3.2 Spatial integration

It is useful to compute the spatial integral of the bar, for an orientation sensitive kernel (3.1). We note $\lambda_{a,1} \geq \lambda_{a,2}$ the eigenvalues of C_a, $a = 1 \ldots 2$. As the two parts of the DOG have the same orientation, the external part of the receptive field (index 2) satisfies $\lambda_{1,2} = \rho\lambda_{1,1}; \lambda_{2,2} = \rho\lambda_{2,1}$ with $\rho > 1$, the aspect ratio between the center and the surround.

We introduce the function $\Pi(x) = \frac{1}{\sqrt{2\pi}} \int_{-\infty}^{x} e^{-\frac{1}{2}u^2}\, du$, the repartition function of the standard Gaussian, and:

$$r_a(\theta) = \sqrt{\lambda_{1,a}\cos^2\theta + \lambda_{2,a}\sin^2\theta}, \tag{9.7}$$

$a = 1, 2$. In the rest of this section, we will omit θ to alleviate the notations. r_a is a pure characteristic of the receptive field. This is the entry C_{11a} of the correlation matrix C_a. It is thus the variance of Gaussian projection on the first eigenmode. Note that $C_{11a} \geq C_{22a}$. Thus, r_a which has the dimension of a length somewhat characterize the extension of the Gaussian $a = 1, 2$ on the preferred orientation direction. We have $r_2(\theta) = \rho\, r_1(\theta)$, $\rho > 1$.

We show that this spatial integration takes the form:

$$\left[\mathcal{K}_{B_i,S} \overset{S}{*} S\right](s) = \frac{L}{2\,d}\left[\begin{array}{rl} & A_1\left(\Pi\left(\frac{x_i-d-v_x\,s}{r_1}\right) - \Pi\left(\frac{x_i+d-v_x\,s}{r_1}\right)\right) \\ - & A_2\left(\Pi\left(\frac{x_i-d-v_x\,s}{\rho\,r_1}\right) - \Pi\left(\frac{x_i+d-v_x\,s}{\rho\,r_1}\right),\right) \end{array}\right]. \tag{9.8}$$

The shape of this response depends on the parameters of the model and the characteristics of the bar. In general, this is a pulse propagating at speed v_x, with a maximum at $s = \frac{x_i}{v_x}$. There can be several extrema in the shape though.

Proof. We write:

$$\mathcal{N}_{i,a}(x,y) = \frac{1}{2\pi\sqrt{\det C_a}}\, e^{-\frac{1}{2}\,\tilde{X}_i.C_a^{-1}.X_i}, \tag{9.9}$$

with $a = 1, 2$, so that the spatial receptive field (3.1) reads:

$$\mathcal{K}_{i,S}(x,y) = A_1\,\mathcal{N}_{i,1}(x,y) - A_2\,\mathcal{N}_{i,2}(x,y).$$

We have:

$$\left[\mathcal{K}_{i,S} \overset{S}{*} S\right](s) =$$

$$\frac{L}{2\,d}\left(\left[\mathcal{K}_{i,S} \overset{S}{*} H(x-d-v_x\,s)\right](s) - \left[\mathcal{K}_{i,S} \overset{S}{*} H(x+d-v_x\,s)\right](s)\right)$$

$$= \frac{L}{2\,d}\begin{pmatrix} A_1\left[\mathcal{N}_{i,1} \overset{S}{*} H(x-d-v_x\,s)\right](t) \\ -A_2\left[\mathcal{N}_{i,2} \overset{S}{*} H(x-d-v_x\,s)\right](t) \\ -A_1\left[\mathcal{N}_{i,1} \overset{S}{*} H(x+d-v_x\,s)\right](t) \\ +A_2\left[\mathcal{N}_{i,2} \overset{S}{*} H(x+d-v_x\,s)\right](t) \end{pmatrix}$$

$$= \frac{L}{2\,d}\sum_{a,b=1}^{2}(-1)^{a+b}\,A_a\,I_{a,b}(s),$$

where:

$$I_{a,b}(s) \equiv \frac{1}{2\pi\,\sqrt{\det C_a}}\int_{x,y\in\mathbb{R}^2} e^{-\frac{1}{2}\,\tilde{X}_i.C_a^{-1}.X_i}\; H(x+d_b-v_x\,s)\,dx\,dy, \tag{9.10}$$

$a = 1, 2$, $d_1 = -d, d_2 = d$.

The matrices C_1, C_2 have the same eigenvectors $\vec{v}_1, \vec{v}_2$. We note θ the angle $(\vec{e}_x, \vec{v}_1)$. This is the preferred orientation of the cell. The rotation $R = \begin{pmatrix} \cos\theta & -\sin\theta \\ \sin\theta & \cos\theta \end{pmatrix}$ maps the initial orthonormal basis $(\vec{e}_x, \vec{e}_y)$ to the orthonormal basis $(\vec{v}_1, \vec{v}_2)$ where C_a becomes diagonal, $\tilde{R}.C_a.R = \Lambda_a$. We set $U_i' \equiv \begin{pmatrix} u' \\ v' \end{pmatrix} = \tilde{R}X_i$, $X_i = RU_i'$ so that $\tilde{X}_i.C_a^{-1}.X_i = \tilde{U}_i'.\tilde{R}.C_a^{-1}.R.U_i' = \tilde{U}_i'.\Lambda_a^{-1}.U_i'$. We have $\begin{pmatrix} x \\ y \end{pmatrix} = RU_i' + \begin{pmatrix} x_i \\ y_i \end{pmatrix}$

$$= \begin{pmatrix} \cos\theta & -\sin\theta \\ \sin\theta & \cos\theta \end{pmatrix} . \begin{pmatrix} u' \\ v' \end{pmatrix} + \begin{pmatrix} x_i \\ y_i \end{pmatrix} = \begin{pmatrix} u'\cos\theta - v'\sin\theta + x_i \\ u'\sin\theta + v'\cos\theta + y_i \end{pmatrix}.$$

Thus,

$$I_{a,b}(s) \equiv \frac{1}{2\pi\sqrt{\det C_a}} \int_{x,y\in\mathbb{R}^2} e^{-\frac{1}{2}\tilde{X}_i.C_a^{-1}.X_i} \; H(x + d_b - v_x\, s)\, dx\, dy$$

$$= \frac{1}{2\pi\sqrt{\det C_a}} \int_{u',v'\in\mathbb{R}^2} e^{-\frac{1}{2}\left(\frac{u'^2}{\lambda_{1,a}}+\frac{v'^2}{\lambda_{2,a}}\right)} H(u'\cos\theta - v'\sin\theta + x_i + d_b - v_x\, s)\, du'\, dv'$$

Then, a new variable change $u = \frac{u'}{\sqrt{\lambda_{1,a}}}, v = \frac{v'}{\sqrt{\lambda_{2,a}}}$ with $du'dv' = \sqrt{\lambda_{1,a}\,\lambda_{2,a}} du\, dv = \sqrt{\det C_a}\, du\, dv$ gives:

$$I_{a,b}(s) = \frac{1}{2\pi} \int_{u,v\in\mathbb{R}^2} e^{-\frac{1}{2}\left(u^2+v^2\right)} H(u\sqrt{\lambda_{1,a}}\cos\theta - v\sqrt{\lambda_{2,a}}\sin\theta + x_i + d_b - v_x\, s)\, du\, dv. \quad (9.11)$$

We first consider the case $\theta \in]0, \frac{\pi}{2}[$ so that $\sin\theta > 0, \cos\theta > 0$. The Heaviside function imposes that $u\sqrt{\lambda_{1,a}}\cos\theta - v\sqrt{\lambda_{2,a}}\sin\theta + x_i + d_b - v_x\, s \geq 0 \Leftrightarrow$

$$v \leq \frac{\sqrt{\lambda_{1,a}}\cos\theta}{\sqrt{\lambda_{2,a}}\sin\theta} u + \frac{x_i + d_b - v_x s}{\sqrt{\lambda_{2,a}}\sin\theta}$$

$\Leftrightarrow$

$$v \leq \frac{1}{a(\theta)} \left(\sqrt{V(\theta)}\, u + U(s)) \right)$$

with $a(\theta) = \sqrt{\lambda_{2,a}}\sin\theta$, $V(\theta) = \lambda_{1,a}\cos^2\theta$, $U(s) = x_i + d_b - v_x\, s$. Therefore:

$$I_{a,b}(s) = \frac{1}{2\pi} \int_{u=-\infty}^{+\infty} e^{-\frac{1}{2}u^2} \left[\int_{v=-\infty}^{\frac{1}{a(\theta)}\left(\sqrt{V(\theta)}\, u + U(s)\right)} e^{-\frac{1}{2}v^2} dv \right] du$$

$$= \frac{1}{\sqrt{2\pi}} \int_{u=-\infty}^{+\infty} e^{-\frac{1}{2}u^2}\, \Pi\left(\frac{1}{a(\theta)} \left(\sqrt{V(\theta)}\, u + U(s) \right) \right).$$

We use (eq. (21) of [93]):

$$\frac{1}{\sqrt{2\pi}} \int_{-\infty}^{+\infty} \Pi\left(\frac{1}{a} \left(\sqrt{V}x + U \right) \right) e^{-\frac{x^2}{2}}\, dx = \Pi\left(\frac{U}{\sqrt{a^2+V}} \right), \quad (9.12)$$

to obtain:

$$I = \Pi\left(\frac{x_i + d_b - v_x\, s}{r_a} \right). \quad (9.13)$$

Now, when $\theta = 0$, (9.11) reads:

$$I_{a,b}(s) = \frac{1}{2\pi} \int_{u,v\in\mathbb{R}^2} e^{-\frac{1}{2}\left(u^2+v^2\right)} H(u\sqrt{\lambda_{1,a}} + x_i + d_b - v_x\, s)\, du\, dv$$

$$= \frac{1}{2\pi} \int_{v=-\infty}^{+\infty} e^{-\frac{v^2}{2}}\, dv \int_{u=-\infty}^{\frac{x_i+d_b-v_x\, s}{\sqrt{\lambda_{1,a}}}} e^{-\frac{u^2}{2}}\, du = \Pi\left(\frac{x_i + d_b - v_x\, s}{\sqrt{\lambda_{1,a}}}\right),$$

which matches (9.13).

Therefore, $\left[K_S \overset{S}{*} S \right](s) = \frac{L}{2\,d} \sum_{a,b=1}^{2} \left(-1\right)^{a+b} A_a\, \Pi\left(\frac{x_i+d_b-v_x\, s}{r_a}\right)$ which is (9.8).

9.3.4 Time of the response peak without gain control

We solve eq. (9.3). We first show that:

$$\left[\mathcal{K}_{B_i} \overset{S,t}{*} \frac{d\mathcal{S}}{dt} \right](t) = \frac{L}{2\,d} \sum_{a,b,c=1}^{2} (-1)^{a+b} I_{a,b,c}(t) \tag{9.14}$$

where:

$$I_{i,a,b,c}(t) = -\frac{A_a K_b v_x}{\sqrt{2\pi\left(\, v_x^2\sigma_b^2 + r_a^2\,\right)}}\, e^{-\frac{1}{2}\frac{\left(\, x_i+d_c-v_x\left(\, t-\mu_b\,\right)\right)^2}{v_x^2\sigma_b^2+r_a^2}}\, \Pi\left(\frac{\mu_b\, r_a^2 - \sigma_b^2\, v_x\left(\, x_i + d_c - v_x t\,\right)}{r_a\, \sigma_b\, \sqrt{r_a^2 + \sigma_b^2\, v_x^2}}\right). \tag{9.15}$$

Proof. We start from (9.1) to obtain the sum decomposition (9.14). It remains then to compute the integrals $I_{a,b,c}(t)$. This can be done in two ways. Either we start from:

$$\frac{dS}{dt} = -\, v_x\, \frac{L}{2\,d} \left[\, \delta(x - d_c - v_x\, t) - \delta(x + d_c - v_x\, t)\,\right],$$

$c = 1, 2$ where $d_1 = d, d_2 = -d$, so that:

$$I_{a,b,c}(t) = -v_x \left[\mathcal{K}_{i,a,b} \overset{S,t}{*} \delta(x + d_c - v_x\, t) \right].$$

This way is a bit long, in fact. Another faster, method consists, instead, of computing

$$\frac{d}{dt}\left[\mathcal{K}_{B_i} \overset{S,t}{*} \mathcal{S} \right] = \sum_{a,b=1}^{2} (-1)^{a+b} \frac{d}{dt}\left[\mathcal{K}_{i,a,b} \overset{S,t}{*} \mathcal{S} \right] = \frac{L}{2d} \sum_{a,b=1}^{2} (-1)^{a+b} \frac{d}{dt} J_{i,a,b,c}.$$

where, using (9.8)

$$J_{i,a,b,c} = A_a \left[\mathcal{K}_T \overset{T}{*} \Pi \left(\frac{x_i + d_b - v_x\, s}{r_a} \right) \right](t)$$

$$= \frac{A_a K_b}{\sqrt{2\pi}\,\sigma_b} \int_{s=-\infty}^{t} e^{-\frac{(t-s-\mu_b)^2}{2\sigma_b^2}} \Pi \left(\frac{x_i + d_c - v_x\, s}{r_a} \right) ds.$$

Thus:

$$I_{i,a,b,c} = \frac{d}{dt} J_{i,a,b,c} = \frac{A_a K_b}{\sqrt{2\pi}\,\sigma_b} \frac{d}{dt} \int_{s=-\infty}^{t} e^{-\frac{(t-s-\mu_b)^2}{2\sigma_b^2}} \Pi \left(\frac{x_i + d_c - v_x\, s}{r_a} \right) ds$$

$$= \frac{A_a K_b}{\sqrt{2\pi}\,\sigma_b} \left[\Pi \left(\frac{x_i + d_c - v_x\, t}{r_a} \right) e^{-\frac{\mu_b^2}{2\sigma_b^2}} - \frac{1}{\sigma_b^2} \int_{s=-\infty}^{t} (\, t - s - \mu_b \,)\, e^{-\frac{(t-s-\mu_b)^2}{2\sigma_b^2}} \Pi \left(\frac{x_i + d_c - v_x\, s}{r_a} \right) ds \right]$$

$$= \frac{A_a K_b}{\sqrt{2\pi}\,\sigma_b} \left[\Pi \left(\frac{x_i + d_c - v_x\, t}{r_a} \right) e^{-\frac{\mu_b^2}{2\sigma_b^2}} - \int_{s=-\infty}^{t} \Pi \left(\frac{x_i + d_c - v_x\, s}{r_a} \right) \frac{d}{ds} e^{-\frac{(t-s-\mu_b)^2}{2\sigma_b^2}} ds \right]$$

$$= \frac{A_a K_b}{\sqrt{2\pi}\,\sigma_b} \left[\begin{array}{r} \Pi \left(\frac{x_i + d_c - v_x\, t}{r_a} \right) e^{-\frac{\mu_b^2}{2\sigma_b^2}} - \left[\Pi \left(\frac{x_i + d_c - v_x\, s}{r_a} \right) e^{-\frac{(t-s-\mu_b)^2}{2\sigma_b^2}} \right]_{-\infty}^{t} \\ + \int_{s=-\infty}^{t} \frac{d}{ds} \left(\Pi \left(\frac{x_i + d_c - v_x\, s}{r_a} \right) \right) e^{-\frac{(t-s-\mu_b)^2}{2\sigma_b^2}} ds \end{array} \right]$$

$$= -v_x \frac{A_a K_b}{\sqrt{2\pi}\, r_a} \frac{1}{\sqrt{2\pi}\,\sigma_b} \int_{s=-\infty}^{t} e^{-\frac{1}{2}\left(\frac{x_i + d_c - v_x\, s}{r_a} \right)^2} e^{-\frac{(t-s-\mu_b)^2}{2\sigma_b^2}} ds.$$

$$= -A_a K_b \int_{s=-\infty}^{t} \frac{1}{\sqrt{2\pi}\,\frac{r_a}{v_x}} e^{-\frac{1}{2}\left(\frac{\frac{x_i + d_c}{v_x} - s}{\frac{r_a}{v_x}} \right)^2} \frac{1}{\sqrt{2\pi}\,\sigma_b} e^{-\frac{(t-s-\mu_b)^2}{2\sigma_b^2}} ds$$

Setting:

$$\mu_f = \frac{x_i + d_c}{v_x}; \sigma_f = \frac{r_a}{v_x}; \mu_g = t - \mu_b; \sigma_g = \sigma_b,$$

we simplify the product of the two Gaussians $\mathcal{N}(\,\mu_f, \sigma_f\,)\,\mathcal{N}(\,\mu_g, \sigma_g\,)$ by using the following result [94]:

$$\mathcal{N}(\,\mu_f, \sigma_f\,)\,\mathcal{N}(\,\mu_g, \sigma_g\,) = \frac{S_{fg}}{\sqrt{2\pi\sigma_{fg}}} e^{-\frac{\left(s - \mu_{fg}\right)^2}{2\sigma_{fg}^2}}, \tag{9.16}$$

with:

$$\begin{aligned}
&\frac{1}{\sigma_{fg}^2} = \frac{1}{\sigma_f^2} + \frac{1}{\sigma_g^2} = \frac{v_x^2\sigma_b^2 + r_a^2}{r_a^2\,\sigma_b^2};\\
&\sigma_{fg} = \frac{r_a\,\sigma_b}{\sqrt{r_a^2 + \sigma_b^2\,v_x^2}}\\
&\mu_{fg} = \left(\frac{\mu_f}{\sigma_f^2} + \frac{\mu_g}{\sigma_g^2}\right)\sigma_{fg}^2 = \frac{\sigma_b^2\,v_x\,(\,x_i + d_c\,) + r_a^2\,(\,t - \mu_b\,)}{v_x^2\sigma_b^2 + r_a^2};\\
&S_{fg} = \frac{1}{\sqrt{2\pi\frac{\sigma_f^2\,\sigma_g^2}{\sigma_{fg}^2}}}\,e^{-\frac{1}{2}\frac{\left(\mu_f-\mu_g\right)^2}{\sigma_f^2\,\sigma_g^2}\sigma_{fg}^2} = \frac{v_x}{\sqrt{2\pi\,(\,v_x^2\sigma_b^2 + r_a^2\,)}}\,e^{-\frac{1}{2}\frac{(\,x_i+d_c-v_x(\,t-\mu_b\,)\,)^2}{v_x^2\sigma_b^2+r_a^2}}
\end{aligned} \tag{9.17}$$

Thus:

$$I_{i,a,b,c} = -A_a K_b\,\frac{S_{fg}}{\sqrt{2\pi}\sigma_{fg}}\int_{s=-\infty}^{t} e^{-\frac{\left(s-\mu_{fg}\right)^2}{2\sigma_{fg}^2}}\,ds = -A_a K_b\,\frac{S_{fg}}{\sqrt{2\pi}}\int_{s=-\infty}^{\frac{t-\mu_{fg}}{\sigma_{fg}}} e^{-\frac{v^2}{2}}\,dv$$

$$= -A_a K_b\,S_{fg}\,\Pi\left(\frac{t-\mu_{fg}}{\sigma_{fg}}\right)$$

We finally make explicit the dependence of this function in all its arguments, giving:

$$I_{i,a,b,c} = -\frac{A_a K_b v_x}{\sqrt{2\pi\,(\,v_x^2\sigma_b^2 + r_a^2\,)}}\,e^{-\frac{1}{2}\frac{(\,x_i+d_c-v_x(\,t-\mu_b\,)\,)^2}{v_x^2\sigma_b^2+r_a^2}}\,\Pi\left(\frac{\mu_b\,r_a^2 - \sigma_b^2\,v_x\,(\,x_i + d_c - v_x t\,)}{r_a\,\sigma_b\,\sqrt{r_a^2 + \sigma_b^2\,v_x^2}}\right),$$

which is (9.15).

End of proof.

The shape of this function is interesting. This is the product of a Gaussian wave, propagating at a speed v_x, maximum at $x_i + d_c$, at time $\mu_b + \frac{x_i+d_c}{v_x}$, with a variance $v_x^2\sigma_b^2 + r_a^2$, multiplied by a front (Π), moving at speed v_x, with the inflexion point, reached at $t = \frac{x_i+d_c}{v_x} - \frac{\mu_b^2 r_a^2}{\sigma_b^2\,v_x^2}$ with slope $\frac{\sigma_b\,v_x^2}{r_a\,\sqrt{r_a^2+\sigma_b^2\,v_x^2}}$. This slope is always positive so the front is growing as time goes on, up to saturation. The multiplication by the Gaussian gives a spatial extenstion of order $\sqrt{r_a^2 + \sigma_b^2\,v_x^2}$. In first approximation the Π function can be neglected.

Eq. (9.3) for the extremal time of the peak in the ganglion cell's response reads

now:

$$\sum_i W_{G_k}^{B_i} \sum_{a,b,c} (-1)^{a+b} \, I_{i,a,b,c}(t = t_m) = 0.$$

Here, we can exploit the symmetry of the Gaussian pooling (3.36). The center of the pool corresponds to a bipolar cell Bi_0 with x index l_0. As we are considering a one dimensional problem where the integration over the y axis is constant (infinite bar) one can replace the two dimensional Gaussian weight $W_{G_k}^{B_i}$ given by (3.36) by a one dimensional Gaussian pooling $W_{G_k}^{B_i} = a \, e^{-\frac{l^2 \, \delta_B^2}{2 \, c^2}}$, where the bipolar cell i is such that $x_i = (l_0 + l) \, \delta_B$. Without loss of generality we take $l_0 = 0$. Thus, the time of peak is given by:

$$\sum_{l \in \mathbb{Z}} e^{-\frac{l^2 \, \delta_B^2}{2 \, c^2}} \sum_{a,b,c} (-1)^{a+b} \frac{A_a K_b}{\sqrt{2\pi \, (\, v_x^2 \sigma_b^2 + r_a^2 \,)}} \, e^{-\frac{1}{2} \frac{(\, l \, \delta_B + d_c - v_x (\, t - \mu_b \,) \,)^2}{v_x^2 \sigma_b^2 + r_a^2}}$$

$$\Pi \left(\frac{\mu_b \, r_a^2 - \sigma_b^2 \, v_x \, (\, l \, \delta_B + d_c - v_x t \,)}{r_a \, \sigma_b \, \sqrt{r_a^2 + \sigma_b^2 \, v_x^2}} \right) = 0.$$

$$
\begin{aligned}
&\frac{A_1 K_1}{\sqrt{2\pi\left(v_x^2\sigma_1^2+r_1^2\right)}}\left[\begin{array}{l} e^{-\frac{1}{2}\frac{(-d-v_x(t-\mu_1))^2}{v_x^2\sigma_1^2+r_1^2}}\,\Pi\left(\frac{\mu_1 r_1^2-\sigma_1^2 v_x(-d-v_x t)}{r_1\sigma_1\sqrt{r_1^2+\sigma_1^2 v_x^2}}\right)\\ +e^{-\frac{1}{2}\frac{(d-v_x(t-\mu_1))^2}{v_x^2\sigma_1^2+r_1^2}}\,\Pi\left(\frac{\mu_1 r_1^2-\sigma_1^2 v_x(d-v_x t)}{r_1\sigma_1\sqrt{r_1^2+\sigma_1^2 v_x^2}}\right)\end{array}\right]\\
&-\frac{A_1 K_2}{\sqrt{2\pi\left(v_x^2\sigma_2^2+r_1^2\right)}}\left[\begin{array}{l} e^{-\frac{1}{2}\frac{(-d-v_x(t-\mu_2))^2}{v_x^2\sigma_2^2+r_1^2}}\,\Pi\left(\frac{\mu_2 r_1^2-\sigma_2^2 v_x(-d-v_x t)}{r_1\sigma_2\sqrt{r_1^2+\sigma_2^2 v_x^2}}\right)\\ +e^{-\frac{1}{2}\frac{(d-v_x(t-\mu_2))^2}{v_x^2\sigma_2^2+r_1^2}}\,\Pi\left(\frac{\mu_2 r_1^2-\sigma_2^2 v_x(d-v_x t)}{r_1\sigma_2\sqrt{r_1^2+\sigma_2^2 v_x^2}}\right)\end{array}\right]\\
&+\\
&\cdots\\
&+\sum_{l=1}^{+\infty} e^{-\frac{l^2\delta_B^2}{2c^2}}\left(\begin{array}{l}
\frac{A_1 K_1}{\sqrt{2\pi\left(v_x^2\sigma_1^2+r_1^2\right)}}\left[\begin{array}{l} e^{-\frac{1}{2}\frac{(l\delta_B-d-v_x(t-\mu_1))^2}{v_x^2\sigma_1^2+r_1^2}}\,\Pi\left(\frac{\mu_1 r_1^2-\sigma_1^2 v_x(l\delta_B-d-v_x t)}{r_1\sigma_1\sqrt{r_1^2+\sigma_1^2 v_x^2}}\right)\\ +e^{-\frac{1}{2}\frac{(l\delta_B+d-v_x(t-\mu_1))^2}{v_x^2\sigma_1^2+r_1^2}}\,\Pi\left(\frac{\mu_1 r_1^2-\sigma_1^2 v_x(l\delta_B+d-v_x t)}{r_1\sigma_1\sqrt{r_1^2+\sigma_1^2 v_x^2}}\right)\\ +e^{-\frac{1}{2}\frac{(-l\delta_B-d-v_x(t-\mu_1))^2}{v_x^2\sigma_1^2+r_1^2}}\,\Pi\left(\frac{\mu_1 r_1^2-\sigma_1^2 v_x(-l\delta_B-d-v_x t)}{r_1\sigma_1\sqrt{r_1^2+\sigma_1^2 v_x^2}}\right)\\ +e^{-\frac{1}{2}\frac{(-l\delta_B+d-v_x(t-\mu_1))^2}{v_x^2\sigma_1^2+r_1^2}}\,\Pi\left(\frac{\mu_1 r_1^2-\sigma_1^2 v_x(-l\delta_B+d-v_x t)}{r_1\sigma_1\sqrt{r_1^2+\sigma_1^2 v_x^2}}\right)\end{array}\right]\\
-\frac{A_1 K_2}{\sqrt{2\pi\left(v_x^2\sigma_2^2+r_1^2\right)}}\left[\begin{array}{l} e^{-\frac{1}{2}\frac{(l\delta_B-d-v_x(t-\mu_2))^2}{v_x^2\sigma_2^2+r_1^2}}\,\Pi\left(\frac{\mu_2 r_1^2-\sigma_2^2 v_x(l\delta_B-d-v_x t)}{r_1\sigma_2\sqrt{r_1^2+\sigma_2^2 v_x^2}}\right)\\ +e^{-\frac{1}{2}\frac{(l\delta_B+d-v_x(t-\mu_2))^2}{v_x^2\sigma_2^2+r_1^2}}\,\Pi\left(\frac{\mu_2 r_1^2-\sigma_2^2 v_x(l\delta_B+d-v_x t)}{r_1\sigma_2\sqrt{r_1^2+\sigma_2^2 v_x^2}}\right)\\ +e^{-\frac{1}{2}\frac{(-l\delta_B-d-v_x(t-\mu_2))^2}{v_x^2\sigma_2^2+r_1^2}}\,\Pi\left(\frac{\mu_2 r_1^2-\sigma_2^2 v_x(-l\delta_B-d-v_x t)}{r_1\sigma_2\sqrt{r_1^2+\sigma_2^2 v_x^2}}\right)\\ +e^{-\frac{1}{2}\frac{(-l\delta_B+d-v_x(t-\mu_2))^2}{v_x^2\sigma_2^2+r_1^2}}\,\Pi\left(\frac{\mu_2 r_1^2-\sigma_2^2 v_x(-l\delta_B+d-v_x t)}{r_1\sigma_2\sqrt{r_1^2+\sigma_2^2 v_x^2}}\right)\end{array}\right]\\
+\\
\cdots
\end{array}\right)\\
&=0
\end{aligned}
$$

There is no evident solution to this equation. In particular the time $t=0$ where the bar reaches the center of the ganglion cell receptive field ($x=0$) is NOT a solution.

A specific case holds when the time integration is instantaneous ($\sigma_1, \sigma_2 \to 0$). In this case, $\frac{1}{\sqrt{2\pi}\sigma_1} e^{-\frac{(t-\mu_1)^2}{2\sigma_1^2}} \to \delta(t-\mu_1)$ (weak convergence). In this limit we lose the continuity at 0 (condition (3.3) is not fulfilled). In addition, as $\mu_1, \mu_2 > 0$ $\Pi\left(\frac{\mu_1}{\sigma_1}\right) = \Pi\left(\frac{\mu_2}{\sigma_2}\right) = 1$ so that condition (3.4) gives $K_1 = K_2$. More generally, the contribution of

the term $\Pi(\dots) = 1$ is equal to 1 and this equation reduces to:

$$\sum_{l\in\mathbb{Z}} e^{-\frac{l^2\,\delta_B^2}{2\,c^2}} \sum_{a,b,c} (-1)^{a+b} \frac{A_a K_b}{\sqrt{2\pi} r_a}\, e^{-\frac{1}{2}\,\frac{\left(l\,\delta_B + d_c - v_x\left(t-\mu_b\right)\right)^2}{r_a^2}} = 0$$

$$\sum_{l\in\mathbb{Z}} e^{-\frac{l^2\,\delta_B^2}{2\,c^2}} \sum_{c} \left[\begin{array}{l} \frac{A_1 K_1}{\sqrt{2\pi} r_1}\, e^{-\frac{1}{2}\,\frac{\left(l\,\delta_B + d_c - v_x\left(t-\mu_1\right)\right)^2}{r_1^2}} \\ -\frac{A_1 K_2}{\sqrt{2\pi} r_1}\, e^{-\frac{1}{2}\,\frac{\left(l\,\delta_B + d_c - v_x\left(t-\mu_2\right)\right)^2}{r_1^2}} \\ -\frac{A_2 K_1}{\sqrt{2\pi} r_2}\, e^{-\frac{1}{2}\,\frac{\left(l\,\delta_B + d_c - v_x\left(t-\mu_1\right)\right)^2}{r_2^2}} \\ +\frac{A_2 K_2}{\sqrt{2\pi} r_2}\, e^{-\frac{1}{2}\,\frac{\left(l\,\delta_B + d_c - v_x\left(t-\mu_2\right)\right)^2}{r_2^2}} \end{array} \right] = 0$$

Then, for $t = \frac{\mu_1+\mu_2}{2}$ such that $t - \mu_1 = -(t - \mu_2)$ we have, for the left hand side:

$$\sum_{l\in\mathbb{Z}} e^{-\frac{l^2\,\delta_B^2}{2\,c^2}} \sum_{c} \left[\begin{array}{l} \frac{A_1 K_1}{\sqrt{2\pi} r_1}\, e^{-\frac{1}{2}\,\frac{\left(l\,\delta_B + d_c - v_x\left(t-\mu_1\right)\right)^2}{r_1^2}} \\ -\frac{A_1 K_2}{\sqrt{2\pi} r_1}\, e^{-\frac{1}{2}\,\frac{\left(l\,\delta_B + d_c + v_x\left(t-\mu_1\right)\right)^2}{r_1^2}} \\ -\frac{A_2 K_1}{\sqrt{2\pi} r_2}\, e^{-\frac{1}{2}\,\frac{\left(l\,\delta_B + d_c - v_x\left(t-\mu_1\right)\right)^2}{r_2^2}} \\ +\frac{A_2 K_2}{\sqrt{2\pi} r_2}\, e^{-\frac{1}{2}\,\frac{\left(l\,\delta_B + d_c + v_x\left(t-\mu_1\right)\right)^2}{r_2^2}} \end{array} \right]$$

$$= \sum_{l\in\mathbb{Z}} e^{-\frac{l^2\,\delta_B^2}{2\,c^2}} \left[\begin{array}{l} \frac{A_1 K_1}{\sqrt{2\pi} r_1}\, e^{-\frac{1}{2}\,\frac{\left(l\,\delta_B - d - v_x\left(t-\mu_1\right)\right)^2}{r_1^2}} \\ -\frac{A_1 K_2}{\sqrt{2\pi} r_1}\, e^{-\frac{1}{2}\,\frac{\left(l\,\delta_B - d + v_x\left(t-\mu_1\right)\right)^2}{r_1^2}} \\ -\frac{A_2 K_1}{\sqrt{2\pi} r_2}\, e^{-\frac{1}{2}\,\frac{\left(l\,\delta_B - d - v_x\left(t-\mu_1\right)\right)^2}{r_2^2}} \\ +\frac{A_2 K_2}{\sqrt{2\pi} r_2}\, e^{-\frac{1}{2}\,\frac{\left(l\,\delta_B - d + v_x\left(t-\mu_1\right)\right)^2}{r_2^2}} \\ +\frac{A_1 K_1}{\sqrt{2\pi} r_1}\, e^{-\frac{1}{2}\,\frac{\left(l\,\delta_B + d - v_x\left(t-\mu_1\right)\right)^2}{r_1^2}} \\ -\frac{A_1 K_2}{\sqrt{2\pi} r_1}\, e^{-\frac{1}{2}\,\frac{\left(l\,\delta_B + d + v_x\left(t-\mu_1\right)\right)^2}{r_1^2}} \\ -\frac{A_2 K_1}{\sqrt{2\pi} r_2}\, e^{-\frac{1}{2}\,\frac{\left(l\,\delta_B + d - v_x\left(t-\mu_1\right)\right)^2}{r_2^2}} \\ +\frac{A_2 K_2}{\sqrt{2\pi} r_2}\, e^{-\frac{1}{2}\,\frac{\left(l\,\delta_B + d + v_x\left(t-\mu_1\right)\right)^2}{r_2^2}} \end{array} \right]$$

$$
\begin{aligned}
&\left(
\begin{array}{l}
\frac{A_1 K_1}{\sqrt{2\pi} r_1}\, e^{-\frac{1}{2}\frac{(-d-v_x(t-\mu_1))^2}{r_1^2}} \\
-\frac{A_1 K_2}{\sqrt{2\pi} r_1}\, e^{-\frac{1}{2}\frac{(-d+v_x(t-\mu_1))^2}{r_1^2}} \\
-\frac{A_2 K_1}{\sqrt{2\pi} r_2}\, e^{-\frac{1}{2}\frac{(-d-v_x(t-\mu_1))^2}{r_2^2}} \\
+\frac{A_2 K_2}{\sqrt{2\pi} r_2}\, e^{-\frac{1}{2}\frac{(-d+v_x(t-\mu_1))^2}{r_2^2}} \\
+\frac{A_1 K_1}{\sqrt{2\pi} r_1}\, e^{-\frac{1}{2}\frac{(d-v_x(t-\mu_1))^2}{r_1^2}} \\
-\frac{A_1 K_2}{\sqrt{2\pi} r_1}\, e^{-\frac{1}{2}\frac{(d+v_x(t-\mu_1))^2}{r_1^2}} \\
-\frac{A_2 K_1}{\sqrt{2\pi} r_2}\, e^{-\frac{1}{2}\frac{(d-v_x(t-\mu_1))^2}{r_2^2}} \\
+\frac{A_2 K_2}{\sqrt{2\pi} r_2}\, e^{-\frac{1}{2}\frac{(d+v_x(t-\mu_1))^2}{r_2^2}} \\
\\
+\sum_{l=1}^{+\infty} e^{-\frac{l^2 \delta_B^2}{2c^2}}
\end{array}
\right. \\
&= \left[
\begin{array}{l}
\frac{A_1 K_1}{\sqrt{2\pi} r_1}\left(e^{-\frac{1}{2}\frac{(-l\,\delta_B-d-v_x(t-\mu_1))^2}{r_1^2}} + e^{-\frac{1}{2}\frac{(l\,\delta_B-d-v_x(t-\mu_1))^2}{r_1^2}} \right) \\
-\frac{A_1 K_2}{\sqrt{2\pi} r_1}\left(e^{-\frac{1}{2}\frac{(-l\,\delta_B-d+v_x(t-\mu_1))^2}{r_1^2}} + e^{-\frac{1}{2}\frac{(l\,\delta_B-d+v_x(t-\mu_1))^2}{r_1^2}} \right) \\
-\frac{A_2 K_1}{\sqrt{2\pi} r_2}\left(e^{-\frac{1}{2}\frac{(-l\,\delta_B-d-v_x(t-\mu_1))^2}{r_2^2}} + e^{-\frac{1}{2}\frac{(l\,\delta_B-d-v_x(t-\mu_1))^2}{r_2^2}} \right) \\
+\frac{A_2 K_2}{\sqrt{2\pi} r_2}\left(e^{-\frac{1}{2}\frac{(-l\,\delta_B-d+v_x(t-\mu_1))^2}{r_2^2}} + e^{-\frac{1}{2}\frac{(l\,\delta_B-d+v_x(t-\mu_1))^2}{r_2^2}} \right) \\
+\frac{A_1 K_1}{\sqrt{2\pi} r_1}\left(e^{-\frac{1}{2}\frac{(-l\,\delta_B+d-v_x(t-\mu_1))^2}{r_1^2}} + e^{-\frac{1}{2}\frac{(l\,\delta_B+d-v_x(t-\mu_1))^2}{r_1^2}} \right) \\
-\frac{A_1 K_2}{\sqrt{2\pi} r_1}\left(e^{-\frac{1}{2}\frac{(-l\,\delta_B+d+v_x(t-\mu_1))^2}{r_1^2}} + e^{-\frac{1}{2}\frac{(l\,\delta_B+d+v_x(t-\mu_1))^2}{r_1^2}} \right) \\
-\frac{A_2 K_1}{\sqrt{2\pi} r_2}\left(e^{-\frac{1}{2}\frac{(-l\,\delta_B+d-v_x(t-\mu_1))^2}{r_2^2}} + e^{-\frac{1}{2}\frac{(l\,\delta_B+d-v_x(t-\mu_1))^2}{r_2^2}} \right) \\
+\frac{A_2 K_2}{\sqrt{2\pi} r_2}\left(e^{-\frac{1}{2}\frac{(-l\,\delta_B+d+v_x(t-\mu_1))^2}{r_2^2}} + e^{-\frac{1}{2}\frac{(l\,\delta_B+d+v_x(t-\mu_1))^2}{r_2^2}} \right)
\end{array}
\right]
\end{aligned}
$$

As $K_1 = K_2$ this gives:

$$
= \left(\begin{array}{l}
\frac{A_1 K_1}{\sqrt{2\pi} r_1} \left(e^{-\frac{1}{2}\frac{(-d-v_x(t-\mu_1))^2}{r_1^2}} - e^{-\frac{1}{2}\frac{(-d+v_x(t-\mu_1))^2}{r_1^2}} - e^{-\frac{1}{2}\frac{(d+v_x(t-\mu_1))^2}{r_1^2}} + e^{-\frac{1}{2}\frac{(d-v_x(t-\mu_1))^2}{r_1^2}} \right) \\
-\frac{A_2 K_1}{\sqrt{2\pi} r_2} \left(e^{-\frac{1}{2}\frac{(-d-v_x(t-\mu_1))^2}{r_2^2}} - e^{-\frac{1}{2}\frac{(-d+v_x(t-\mu_1))^2}{r_2^2}} + e^{-\frac{1}{2}\frac{(d-v_x(t-\mu_1))^2}{r_2^2}} - e^{-\frac{1}{2}\frac{(d+v_x(t-\mu_1))^2}{r_2^2}} \right) \\
+ \sum_{l=1}^{+\infty} e^{-\frac{l^2 \delta_B^2}{2c^2}} \left[\begin{array}{l}
\frac{A_1 K_1}{\sqrt{2\pi} r_1} \left(\begin{array}{l}
e^{-\frac{1}{2}\frac{(-l\delta_B-d-v_x(t-\mu_1))^2}{r_1^2}} + e^{-\frac{1}{2}\frac{(l\delta_B-d-v_x(t-\mu_1))^2}{r_1^2}} \\
- \left(e^{-\frac{1}{2}\frac{(-l\delta_B-d+v_x(t-\mu_1))^2}{r_1^2}} + e^{-\frac{1}{2}\frac{(l\delta_B-d+v_x(t-\mu_1))^2}{r_1^2}} \right) \\
+ \left(e^{-\frac{1}{2}\frac{(-l\delta_B+d-v_x(t-\mu_1))^2}{r_1^2}} + e^{-\frac{1}{2}\frac{(l\delta_B+d-v_x(t-\mu_1))^2}{r_1^2}} \right) \\
- \left(e^{-\frac{1}{2}\frac{(-l\delta_B+d+v_x(t-\mu_1))^2}{r_1^2}} + e^{-\frac{1}{2}\frac{(l\delta_B+d+v_x(t-\mu_1))^2}{r_1^2}} \right)
\end{array} \right) \\
-\frac{A_2 K_1}{\sqrt{2\pi} r_2} \left(\begin{array}{l}
\left(e^{-\frac{1}{2}\frac{(-l\delta_B-d-v_x(t-\mu_1))^2}{r_2^2}} + e^{-\frac{1}{2}\frac{(l\delta_B-d-v_x(t-\mu_1))^2}{r_2^2}} \right) \\
- \left(e^{-\frac{1}{2}\frac{(-l\delta_B-d+v_x(t-\mu_1))^2}{r_2^2}} + e^{-\frac{1}{2}\frac{(l\delta_B-d+v_x(t-\mu_1))^2}{r_2^2}} \right) \\
+ \left(e^{-\frac{1}{2}\frac{(-l\delta_B+d-v_x(t-\mu_1))^2}{r_2^2}} + e^{-\frac{1}{2}\frac{(l\delta_B+d-v_x(t-\mu_1))^2}{r_2^2}} \right) \\
- \left(e^{-\frac{1}{2}\frac{(-l\delta_B+d+v_x(t-\mu_1))^2}{r_2^2}} + e^{-\frac{1}{2}\frac{(l\delta_B+d+v_x(t-\mu_1))^2}{r_2^2}} \right)
\end{array} \right)
\end{array} \right]
\end{array} \right) = 0.
$$

Thus, in this specific case the extremum time is $t_m = \frac{\mu_1+\mu_2}{2}$. This is a reliable approximation if σ_1, σ_2 are small.

Publications

- A mean-field approach to the dynamics of networks of complex neurons, from nonlinear Integrate-and-Fire to Hodgkin-Huxley models. M. Carlu, O. Chehab, L. Dalla Porta, D. Depannemaecker, C. Héricé, M. Jedynak, E. Köksal Ersöz, P. Muratore, S. Souihel, C. Capone, Y. Zerlaut, A. Destexhe M. di Volo (submitted).

- An integrated retino-cortical model for motion anticipation. S. Souihel, M. di Volo,S. Chemla, F. Chavane, A. Destexhe and B. Cessac (paper under preparation):

  - September 2019, European retina meeting, Helsinki, Finland (poster)
  - July 2019, Neuromod conference, Fréjus, France (talk)
  - June 2019, ICMNS conference, Copenhagen, Denmark (talk)
  - June 2019, Workshop on Visuo-motor Integration, Paris, France (talk)
  - June 2019, Waves Cote d'Azur conference, Nice, France (talk)

- A computational model of anticipation in the retina. S. Souihel and B. Cessac (paper under preparation):

  - December 2018, GDR Neural Net, Paris, France (poster prize)
  - September 2018, Bernstein conference, Berlin, Germany (poster)

- A generalized model of the retina for motion processing. S. Souihel and B. Cessac. June 2018, Cauca conference, Fréjus France

- Processing various motion features and measuring RGC pairwise correlations with a 2D retinal model. Selma Souihel, Frédéric Chavane, Olivier Marre and Bruno Cessac :

  - June 2018, AREADNE conference, Santorini, Greece (poster)

  - June 2018, ICMNS conference, Juan les Pins, France (poster)

- Motion processing in the retina. S. Souihel and B. Cessac. November 2017, GDR Neural Net, Strasbourg, France

- How does the retina anticipate the motion of complex shapes ? S. Souihel and B. Cessac. September 2017, Bernstein conference, Goettingen, Allemagne

- Modifying a biologically inspired retina simulator to reconstruct realistic responses to moving stimuli. S. Souihel, B. Cessac. June 2017, Cauca conference , Fréjus, France

Bibliography

[1] M. Berry, I. Brivanlou, T. Jordan, and M. Meister, "Anticipation of moving stimuli by the retina," Nature, vol. 398, no. 6725, pp. 334—338, 1999.

[2] E. Y. Chen, O. Marre, C. Fisher, G. Schwartz, J. Levy, R. A. da Silviera, and M. J. I. Berry, "Alert response to motion onset in the retina," Journal of Neuroscience, vol. 33, no. 1, pp. 120–132, 2013.

[3] S. Trenholm, D. Schwab, V. Balasubramanian, and G. Awatramani, "Lag normalization in an electrically coupled neural network.," Nature Neuroscience, vol. 16, pp. 154–6, Feb. 2013.

[4] H. Kolb, R. Nelson, E. Fernandez, and B. Jones, The organization of the retina and visual system. Webvision, 2013.

[5] H. Shreyer, Nonlinearities in bipolar cells and their role for encoding visual signals. PhD thesis, University of Goettingen, 2018.

[6] T. Gollisch and M. Meister, "Eye smarter than scientists believed: neural computations in circuits of the retina," Neuron, vol. 65, pp. 150–164, Jan. 2010.

[7] T. Gollisch and M. Meister, "Modeling convergent ON and OFF pathways in the early visual system," Biological Cybernetics, vol. 99, pp. 263–278, Nov. 2008.

[8] A. Borst and T. Euler, "Seeing things in motion: Models, circuits, and mechanisms," Neuron, vol. 71, no. 6, pp. 974 – 994, 2011.

[9] T. Baden, P. Berens, K. Franke, M. R. Rosón, M. Bethge, and T. Euler, "The functional diversity of retinal ganglion cells in the mouse," Nature, 2016.

[10] H. Barlow, R. Hill, and W. Levick, "Retinal ganglion cells responding selectively to direction and speed of image motion in the rabbit," The Journal of Physiology, vol. 173, no. 3, p. 377, 1964.

[11] L. Borg-Graham, "The computation of directional selectivity in the retina occurs presynaptic to the ganglion cell," Nature Neuroscience, vol. 4, pp. 176–183, 2001.

[12] S. Fried, T. Muench, and F. Werblin, "Mechanisms and circuitry underlying directional selectivity in the retina," Nature, vol. 420, no. 6914, pp. 411–414, 2002.

[13] W. Wei, A. Hamby, K. Zhou, and M. Feller, "Development of asymmetric inhibition underlying direction selectivity in the retina," Nature, vol. 469, no. 7330, pp. 402–406, 2010.

[14] H. Wassle, "Parallel processing in the mammalian retina.," Nat Rev Neurosci, vol. 5, no. 10, pp. 747–57, 2004.

[15] S. Lee, K. Kim, and Z. J. Zhou, "Role of ach-gaba cotransmission in detecting image motion and motion direction," Neuron, vol. 68, pp. 1159–1172, Dec. 2010.

[16] C. Ravello, L. Perrinet, M. Escobar, and P. AG, "Speed-selectivity in retinal ganglion cells is sharpened by broad spatial frequency, naturalistic stimuli," Scientific reports, 2019.

[17] N. K. Logothetis and D. L. Sheinberg, "Visual object recognition," Annual Review of Neuroscience, vol. 19, no. 1, pp. 577–621, 1996. PMID: 8833455.

[18] V. de Ladurantaye, J. Rouat, and J. Vanden-Abeele, Visual Cortex - Current Status and Perspectives. IntechOpen, 2012.

[19] J. Daugman, "Two-dimensional spectral analysis of cortical receptive field profiles," Vis. Res., vol. 20, pp. 847–856, 1980.

[20] D. Field, "Relations between the statistics of natural images and the response properties of cortical cells," J. Opt. Soc. Am. A, vol. 4, no. 12, pp. 2379–2394, 1987.

[21] B. Olshausen and D. Field, "Sparse coding with an overcomplete basis set: A strategy employed by V1?," Vision Research, vol. 37, pp. 3311–3325, 1998.

[22] D. Hubel and T. Wiesel, "Receptive fields, binocular interaction and functional architecture in the cat visual cortex.," J Physiol, vol. 160, pp. 106–154, 1962.

[23] D. Hubel and T. Wiesel, "Receptive fields and functional architecture of monkey striate cortex," The Journal of Physiology, vol. 195, no. 1, p. 215, 1968.

[24] S. Zeki, "Thirty years of a very special visual area, area V5," The Journal of Physiology, vol. 557, pp. 1–2, May 2004.

[25] R. Dougherty, V. Koch, A. Brewer, B. Fischer, J. Modersitzki, and B. Wandell, "Visual field representations and locations of visual areas v1/2/3 in human visual cortex," Journal of Vision, vol. 3, pp. 586–598, Oct. 2003.

[26] B. Hassenstein and R. W., "Systemtheoretische analyse der zeit, reihenfolgen und vorzeichenauswertung," In The Bewegungsperzeption Des weevil Chlorophanus. Z. Naturforsch., 1956.

[27] J. Van Santen and G. Sperling, "Elaborated reichardt detectors," Journal of the Optical Society of America A, vol. 2, no. 2, pp. 300–320, 1985.

[28] K. Ball and R. Sekuler, "Human vision favors centrifugal motion," Perception, vol. 3, pp. 317–325, 1980.

[29] T. Albright, "Centrifugal directional bias in the middle temporal visual area (mt) of the macaque.," Visual Neuroscience, vol. 2, pp. 177–88, 1989.

[30] A. M. Bastos, W. M. Usrey, R. A. Adams, G. R. Mangun, P. Fries, and K. J. Friston, "Canonical microcircuits for predictive coding," Neuron, vol. 76, no. 4, pp. 695 – 711, 2012.

[31] R. Rao and D. Ballard, "Predictive coding in the visual cortex: a functional interpretation of some extra-classical receptive-field effects," Nat Neurosci, vol. 2, no. 1, pp. 79–87, 1999.

[32] F. Lacquaniti and C. Maioli, "Adaptation to suppression of visual information during catching," Journal of Neuroscience, 1989.

[33] Y. Wang and B. J. Frost, "Time to collision is signalled by neurons in the nucleus rotundus of pigeons," Nature, 1992.

[34] J. Krakauer, Z. Pine, M. Ghilardi, and C. Ghez, "Learning of visuomotor transformations for vectorial planning of reaching trajectories.," Journal of Neuroscience, 2000.

[35] N. F. Bernardi, M. D. Buglio, P. D. Trimarchi, A. Chielli, , and E. Bricolo1, "Mental practice promotes motor anticipation: evidence from skilled music performance," Frontiers in human neuroscience, 2013.

[36] O. V. Sysoeva, M. Wittmann, A. Mierau, I. Polikanova, H. K. Strüder, and A. Tonevitsky, "Physical exercise speeds up motor timing," Frontiers in Psychology, 2013.

[37] R. Nijhawan, "Visual decomposition of colour through motion extrapolation," Nature, vol. 386, pp. 66–69, 1997.

[38] G. Benvenuti, S. Chemla, A. Boonman, G. Masson, and C. F, "Anticipatory responses along motion trajectories in awake monkey v1.," submitted, 2018.

[39] W. S. Nijhawan R, "Compensating time delays with neural predictions: are predictions sensory or motor?," Philos Trans A Math Phys Eng Sci, 2009.

[40] D. Whitney and I. Murakami, "Latency difference, not spatial extrapolation," Nature neuroscience, vol. 1, pp. 656–7, Dec. 1998.

[41] D. M. Eagleman and T. J. Sejnowski., "Motion signals bias localization judgments: a unified explanation for the flash-lag, flash-drag, flash-jump, and frohlich illusions.," Journal of vision, vol. 7, 2007.

[42] D. M. Eagleman, "Visual illusions and neurobiology," Nature Reviews Neuroscience, vol. 2, pp. 920–926, 2001.

[43] Lee, B. B., Martin, P. R., & Grünert, U., "Retinal connectivity and primate vision.," Progress in retinal and eye research, vol. 29, no. 6, pp. 622–639, 2010.

[44] Y. Tsukamoto and N. Omi, "Classification of mouse retinal bipolar cells: Type-specific connectivity with special reference to rod-driven aii amacrine pathways," Frontiers in neuroanatomy, 2017.

[45] Y. Tsukamoto and N. Omi, "On bipolar cells in macaque retina: Type-specific synaptic connectivity with special reference to off counterparts," Frontiers in neuroanatomy, 2016.

[46] J. Johnston and L. Lagnado, "General features of the retinal connectome determine the computation of motion anticipation," Elife, 2015.

[47] A. Leonardo and M. Meister, "Nonlinear dynamics support a linear population code in a retinal target-tracking circuit," Journal of Neuroscience, 2013.

[48] S. Deny, U. Ferrari, E. Macé, P. Yger, R. Caplette, S. Picaud, G. Tkačik, and O. Marre, "Multiplexed computations in retinal ganglion cells of a single type," Nature Communications, 2017.

[49] M. Salam and Y. Hayashida, "A single retinal circuit model for multiple computations," Biological cybernetics, 2018.

[50] N. C. Rust, V. Mante, E. P. Simoncelli, and J. A. Movshon, "How mt cells analyze the motion of visual patterns," Nature neuroscience, vol. 9, pp. 1421–31, Nov. 2006.

[51] E. P. Simoncelli, Dristributed Representation and Analysis of Visual Motion. PhD thesis, MIT Media Laboratory, 1993.

[52] F. R. Benucci, A. and M. Carandini, "Standing waves and traveling waves distinguish two circuits in visual cortex.," Neuron, vol. 55, pp. 103–117, 2007.

[53] C. F. G. L. Bringuier, V. and Y. Frégnac, "Horizontal propagation of visual activity in the synaptic integration field of area 17 neurons.," Science, vol. 283, pp. 695–699, 1999.

[54] F. Chavane, D. Sharon, D. Jancke, O. Marre, Y. Frégnac, and A. Grinvald, "Lateral spread of orientation selectivity in v1 is controlled by intracortical cooperativity.," Front. Syst. Neurosci, 2011.

[55] A. Alink, C. Schwiedrzik, A. Kohler, W. Singer, and L. Muckli, "Stimulus predictability reduces responses in primary visual cortex," Journal of Neuroscience, 2010.

[56] G. Benvenuti, S. Chemla, G. M. Arjan Boonman, and F. Chavane, "Anticipation of an approaching bar by neuronal populations in awake monkey v1," Journal of Vision, 2015.

[57] M. Subramaniyan, A. S. Ecker, S. S. Patel, R. J. Cotton, M. Bethge, X. Pitkow, P. Berens, and A. S. Tolias, "Faster processing of moving compared with flashed bars in awake macaque v1 provides a neural correlate of the flash lag illusion," Journal of Neurophysiology, 2018.

[58] D. Jancke, W. Erlaghen, G. Schöner, and H. Dinse, "Shorter latencies for motion trajectories than for flashes in population responses of primary visual cortex," Journal of Physiology, vol. 556, pp. 971–982, 2004.

[59] B. Ölveczky, S. Baccus, and M. Meister, "Segregation of object and background motion in the retina," Nature, vol. 423, pp. 401–408, 2003.

[60] P. Antinucci and R. Hindges, "Orientation-selective retinal circuits in vertebrates," Frontiers in Neural Circuits, vol. 12, 2018.

[61] J.-M. Geusebroek, A. Smeulders, and J. Weijer, "Fast anisotropic gauss filtering," IEEE Transactions on Image Processing, vol. 2350, 2003.

[62] W. Freeman and E. Adelson, "The design and use of steerable filters," IEEE Transactions on Pattern Analysis and Machine Intelligence, vol. 13, no. 9, pp. 891–906, 1991.

[63] M. Unser, "Fast gabor-like windowed fourier and continuous wavelet transforms," IEEE Signal Processing Letters, vol. 1, no. 5, pp. 76–79, 1994.

[64] R. Deriche, "Using Canny's criteria to derive a recursively implemented optimal edge detector," International Journal of Conputer Vision, vol. 1, pp. 167–187, May 1987.

[65] J. Snellman, T. Kaur, Y. Shen, and N. S. Prog, "Regulation of on bipolar cell activity," Progress in retinal and eye research, vol. 27, no. 4, pp. 450–63, 2008.

[66] T. Euler, P. Detwiler, and W. Denk, "Directionally selective calcium signals in dendrites of starburst amacrine cells," Nature, vol. 418, pp. 845–852, 2002.

[67] J. J. Tukker, W. R. Taylor, and R. G. Smith, "Direction selectivity in a model of the starburst amacrine cell," Visual Neuroscience, 2004.

[68] G. A. Enciso, M. Rempe, A. V. Dmitriev, K. E. Gavrikov, D. Terman, and S. C. Mangel, "A model of direction selectivity in the starburst amacrine cell network," Journal of Computational Neuroscience, vol. 18, pp. 567–578, June 2010.

[69] A. Destexhe, Z. Mainen, and T. Sejnowski, "Synthesis of models for excitable membranes, synaptic transmission and neuromodulation using a common kinetic

formalism," Journal of Computational Neuroscience, vol. 1, no. 3, pp. 195—230, 1994.

[70] E. Sernagor and M. Hennig, Retinal Waves: Underlying Cellular Mechanisms and Theoretical Considerations., ch. 1. Elsevier, 2012.

[71] R. Segev, J. Puchalla, and M. Berry, "Functional organization of ganglion cells in the salamander retina.," Journal of Neurophysiology, pp. 2277–92, 2006.

[72] Jacoby, J. and Zhu, Y. and DeVries, S. H. and Schwartz, G. W., "An amacrine cell circuit for signaling steady illumination in the retina.," Cell reports, vol. 13, no. 12, pp. 2663–2670, 2015.

[73] W. Heine and C. Passaglia, "Spatial receptive field properties of rat retinal ganglion cells," Visual Neuroscience, vol. 28, no. 5, pp. 403–17, 2011.

[74] E. Chen, J. Chou, J. Park, G. Schwartz, and M. Berry, "The neural circuit mechanisms underlying the retinal response to motion reversal.," Journal of Neuroscience, 2014.

[75] S. Sethuramanujam, G. B. Awatramani, and M. M. Slaughter, "Cholinergic excitation complements glutamate in coding visual information in retinal ganglion cells," The journal of physiology, pp. 464–475, May 2018.

[76] S. Sethuramanujam, A. J. McLaughlin, G. deRosenroll, A. Hoggarth, D. J. Schwab, and G. B. Awatramani, "A central role for mixed acetylcholine/gaba transmission in direction coding in the retina," Neuron, 2016.

[77] D. I. Vaney, B. Sivyer, and W. R. Taylor, "Direction selectivity in the retina: symmetry and asymmetry in structure and function," Nature Reviews Neuroscience, 2012.

[78] P. B. D. Thomas Euler and W. Denk, "Directionally selective calcium signals in dendrites of starburst amacrine cells," Nature, vol. 418, pp. 845–852, 2002.

[79] Y. Zerlaut, S. Chemla, F. Chavane, and A. Destexhe, "Modeling mesoscopic cortical dynamics using a mean-field model of conductance-based networks of adaptive exponential integrate-and-fire neurons.," Journal of Computational Neuroscience, 2018.

[80] S. Chemla, A. Reynaud, M. di Volo, Y. Zerlaut, L. Perrinet, A. Destexhe, and F. Chavane, "Suppressive traveling waves shape representations of illusory motion in primary visual cortex of awake primate," Journal of Neuroscience, vol. 39, no. 22, pp. 4282–4298, 2019.

[81] M. Buice and J. Cowan, "Field-theoretic approach to fluctuation effects in neural networks," Physical Review E, vol. 75, no. 5, 2007.

[82] S. ElBoustani and A. Destexhe, "A master equation formalism for macroscopic modeling of asynchronous irregular activity states," Neural computation, vol. 21, no. 1, pp. 46–100, 2009.

[83] A. Hodgkin and A. Huxley, "A quantitative description of membrane current and its application to conduction and excitation in nerve.," Journal of Physiology, vol. 117, pp. 500–544, 1952.

[84] C. Morris and H. Lecar, "Voltage oscillations in the barnacle giant muscle fiber.," Biophys J, vol. 35, no. 1, pp. 193–213, 1981.

[85] A. Papoulis, Probability, Random Variables and Stochastic Processes. McGraw-Hill, New York, 1965.

[86] Z. Piwkowska, M. Pospischil, R. Brette, J. Sliwa, M. Rudolph-Lilith, T. Bal, and A. Destexhe, "Characterizing synaptic conductance fluctuations in cortical neurons and their influence on spike generation," Journal of Neuroscience Methods, vol. 169, pp. 302–22, Apr. 2008. PMID: 18187201 DOI: S0165-0270(07)00557-2.

[87] D. Burr and P. Thompson, "Motion psychophysics: 1985–2010," Vision Research, 2011.

[88] A. T. Richard T. Born and T. Hartmann, "Cortical magnification plus cortical plasticity equals vision?," Vision Research, vol. 111, pp. 161–169, 2015.

[89] L. Bin, S. Wang, and M. Richard, "Retinal ganglion cell type, size, and spacing can be specified independent of homotypic dendritic contacts," Neuron, 2004.

[90] A. Wohrer, P. Kornprobst, and T. Viéville, "Virtual retina: a biological retina model and simulator, with contrast gain control," Research Report 6243, INRIA, July 2007.

[91] B. Cessac, P. Kornprobst, S. Kraria, H. Nasser, D. Pamplona, G. Portelli, and T. Vieville, "ENAS: A new software for spike train analysis and simulation." Bernstein conference, Sept. 2016. Poster.

[92] B. Cessac, P. Kornprobst, S. Kraria, H. Nasser, D. Pamplona, G. Portelli, and T. Viéville, "PRANAS: A new platform for retinal analysis and simulation," Frontiers in Neuroinformatics, vol. 11, p. 49, 2017.

[93] S. Amari, "Characteristics of random nets of analog neuron-like elements," Syst. Man Cybernet. SMC-2, 1972.

[94] P. A. Bromiley, "Products and convolutions of gaussian probability density functions," 2014.